FRACTURE MECHANICS Applied to BRITTLE MATERIALS

Proceedings of the Eleventh National Symposium on Fracture Mechanics: Part II

S. W. Freiman, *editor*

ASTM STP 678

AMERICAN SOCIETY FOR TESTING AND MATERIALS

FRACTURE MECHANICS APPLIED TO BRITTLE MATERIALS

Proceedings of the
Eleventh National Symposium
on Fracture Mechanics: Part II

A symposium sponsored by
ASTM Committee E-24 on
Fracture Testing of Metals
AMERICAN SOCIETY FOR
TESTING AND MATERIALS
Virginia Polytechnic Institute
and State University
Blacksburg, Va., 12-14 June 1978

ASTM SPECIAL TECHNICAL PUBLICATION 678
S. W. Freiman, National Bureau of
Standards, editor

List price $25.00
04-678000-30

AMERICAN SOCIETY FOR TESTING AND MATERIALS
1916 Race Street, Philadelphia, Pa. 19103

Library of Congress Catalog Card Number: 78-74564

NOTE

The Society is not responsible, as a body,
for the statements and opinions
advanced in this publication.

Printed in Baltimore, Md.
August 1979

Foreword

This publication, *Fracture Mechanics Applied to Brittle Materials,* contains papers presented at the Eleventh National Symposium on Fracture Mechanics which was held 12-14 June 1978 at Virginia Polytechnic Institute and State University, Blacksburg, Va. The American Society for Testing and Materials' Committee E-24 on Fracture Testing of Metals sponsored the symposium. S. W. Freiman, National Bureau of Standards, served as editor of this publication.

The proceedings have been divided into two volumes: Part I—*Fracture Mechanics* and Part II—*Fracture Mechanics of Brittle Materials.*

Related ASTM Publications

Developments in Fracture Mechanics Test Methods Standardization, STP 632 (1977), $24.75, 04-632000-30

Properties Related to Fracture Toughness, STP 605 (1976), $15.00, 04-605000-30

Fracture Analysis, STP 560 (1974), $22.75, 04-560000-30

A Note of Appreciation to Reviewers

This publication is made possible by the authors and, also, the unheralded efforts of the reviewers. This body of technical experts whose dedication, sacrifice of time and effort, and collective wisdom in reviewing the papers must be acknowledged. The quality level of ASTM publications is a direct function of their respected opinions. On behalf of ASTM we acknowledge with appreciation their contribution.

ASTM Committee on Publications

Editorial Staff

Jane B. Wheeler, *Managing Editor*
Helen M. Hoersch, *Associate Editor*
Ellen J. McGlinchey, *Senior Assistant Editor*
Helen Mahy, *Assistant Editor*

Contents

Introduction

The symposium on Fracture Mechanics Applied to Brittle Materials from which this volume was taken was organized to provide a state-of-the-art review of the various test techniques currently being used to obtain fracture mechanics data on a wide variety of brittle materials including ceramics, glasses, rocks, and concrete. This volume is a compilation of papers describing and reviewing most of the commonly used fracture toughness measurement techniques for brittle materials. Particular attention is given to the problems and discrepancies observed in making these measurements. The articles discuss not only critical fracture toughness measurements but also methods for determining crack growth rates in these materials as a function of stress intensity. In the latter case data are used to provide a basis for lifetime predictions for brittle components under stress. The papers in this volume cover a wide variety of test techniques which are now being used. Although the list of techniques discussed is clearly not complete, the papers should describe for the reader the kind of assumptions, problems, and unknown factors involved in making fracture toughness measurements in brittle materials and the reproducibility from one technique to another. One must remember in reading the papers in this volume that there is currently no "standard" test technique for obtaining fracture mechanics parameters on brittle materials. It is in fact the objective of Subcommittee E24.07 on Fracture Toughness of Brittle Nonmetallic Materials under whose direction this symposium was organized, to provide the experimental basis for establishing standard test procedures. However, this book should provide the reader with current guidelines for choosing a particular test technique, as well as being a basis for future experiments needed to establish the parameters important for the determination of accurate values of fracture toughness and crack velocity. It is hoped that this volume will be useful to workers in the fracture mechanics field as well as to those attempting to use this kind of data to predict the fracture behavior of brittle materials.

S. W. Freiman

Fracture and Deformation Division, National Bureau of Standards, Washington, D.C. 20234; editor.

E. R. Fuller, Jr.[1]

An Evaluation of Double-Torsion Testing—Analysis

REFERENCE: Fuller, E. R., Jr., **"An Evaluation of Double Torsion Testing—Analysis,"** *Fracture Mechanics Applied to Brittle Materials. ASTM STP 678.* S. W. Freiman, Ed., American Society for Testing and Materials, 1979, pp. 3-18.

ABSTRACT: The double-torsion test configuration has many advantages over conventional fracture mechanics configurations for the evaluation of subcritical crack growth parameters and fracture toughness. These advantages—such as crack-length independence, four-point loading, simple specimen geometry, and ease of precracking—have been responsible for the increased use of the double-torsion configuration in recent years. However, before double-torsion testing can be adopted as a standard configuration, a number of unresolved questions need to be answered about the double-torsion specimen and about the experimental techniques involved in its use.

The purpose of this paper is to address some of these questions and to indicate where further effort is needed to establish the validity of double-torsion testing. Assumptions of a compliance analysis for the double-torsion configuration are examined with particular attention given to the influence on experimental results that the violation of any of these assumptions may have. An analytical expression is derived for the compliance of a finite-thickness beam in torsion and is compared to the empirical compliance. Again the emphasis is on the assumptions of the derivation and how some of these restrictions might be relaxed.

KEY WORDS: double-torsion testing, compliance analysis, fracture toughness, curved crack profile, three-dimensional crack, torsional beam, side grooves, fracture (materials)

In recent years the double-torsion test configuration has received increased application in more brittle materials, as well as in polymers and metals, for the evaluation of fracture mechanics properties such as fracture toughness and subcritical crack growth parameters. Accompanying this increased use, however, a number of questions have arisen concerning the range of specimen dimensions and crack lengths over which valid data may be obtained. This has been the case particularly for brittle polycrystalline

[1]Physicist, Fracture and Deformation Division, National Bureau of Standards, Washington, D.C. 20234.

materials where microstructural interactions with the crack might be influenced by the specimen thickness and the state of stress. A companion paper [*1*][2] describes the use of the double-torsion configuration for obtaining fracture mechanics data and addresses some of these questions from an experimental viewpoint. This paper examines the analytical basis for the double-torsion configuration with the objective of explicitly indicating both the assumptions that have been made and how these assumptions might influence measured results. Areas are indicated where further consideration may have an impact on establishing the validity of double-torsion testing.

The basic geometry of the double-torsion specimen is illustrated in Fig. 1. It consists of a plate, which is partially cracked down the center to form two beams. Each of these beams is loaded in torsion, usually by four-point loading at the ends, causing the crack to propagate down the center of the specimen. The plate is sometimes notched, or side grooved, on one or both sides to help constrain the propagating crack to the center of the specimen. As illustrated in Fig. 2, the crack profile is not straight through the thickness, but extends further along the tensile side of the plate to form a curved crack front.

The concept of the double-torsion configuration was introduced by Outwater and Gerry of the University of Vermont [*2,3*]. Early development of double-torsion testing techniques proceeded independently from several dif-

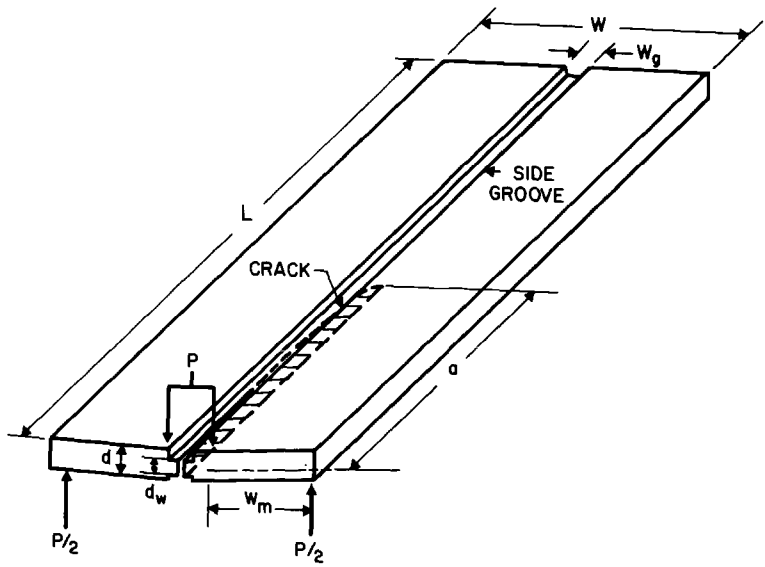

FIG. 1—*Schematic representation of the double-torsion test configuration.*

[2]The italic numbers in brackets refer to the list of references appended to this paper.

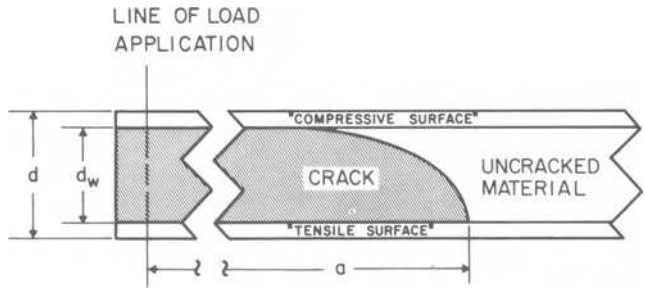

FIG. 2—*Schematic view of the curved crack front profile for the double-torsion specimen.*

ferent investigators. For example, Outwater and co-workers [*2–6*], Kies and Clark [*7*] and Beacham et al [*8*], Evans [*9,10*] and Williams and Evans [*11*], McKinney and Smith [*12*], and Weidmann and Holloway [*13*]. In contrast, analysis of the double-torsion configuration has not progressed much beyond its original forms [*2,6–8,11–13*]. The two notable exceptions are the inclusion of kinetic effects by Virkar and Johnson [*14*] and an important finite element stress analysis by Trantina [*15*]. Indeed, this paper will only examine the existing analytical basis and suggest possible extensions to explain some of the experimental questions and observations that have arisen. Some of these observations include: variations of the crack front profile [*11,15,16*]; dependence of the stress intensity factor on crack length [*1,6,12,13,15,17*]; apparent discrepancies in the stress intensity factor for thick specimens [*18*]; and influences of side notching and asymmetrical applied loading [*19,20*].

In the next section, the stress intensity factor for the double-torsion specimen is determined from a standard fracture mechanics analysis of the elastic strain energy release rate. The starting point for this analysis is an assumed form, either experimental or analytical, for the compliance relationship of the double-torsion configuration. The analysis is complicated mainly by the three-dimensional, curved crack profile that gives rise to questions concerning the mode of fracture [*9–11*] and how the profile might vary upon crack propagation. In the last section an analytical elastic solution is developed for the compliance relationship of the double-torsion configuration.

Energy-Rate Analysis for Stress Intensity Factor

The load-point displacement, Δ, of a linear elastic solid is related to the applied load, P, through the compliance relationship

$$\Delta = \lambda P, \tag{1}$$

where the compliance, λ, in general, will depend upon the specimen con-

figuration and the crack size. Experimental determinations of this compliance relationship for the double-torsion configuration have generally given a relationship

$$\lambda = \Delta/P = Ba + \lambda_o, \tag{2}$$

that varies linearly with the crack length, a, as measured by the longest extension of the curved crack profile (see, for example, [*1,9–13,17*]). This compliance relationship is illustrated schematically in Fig. 3. The parameters B and λ_o are found to depend on the elastic properties of the solid and on the specimen dimensions, but are found to be independent of the crack length. The notable exceptions to this linear relationship are near the ends of the specimen [*12,15,17*] (that is, for short crack lengths or short remaining ligament lengths). This nonlinearity is illustrated by the dashed line in Fig. 3, but discussion of effects related to these end regions is deferred to the next section.

The driving force for fracture, or strain energy release rate for crack extension, $\mathcal{G}$, is related to the specimen compliance by the Irwin relationship [*21,22*]

$$G = (P^2/2) \quad (\partial\lambda/\partial A)_P \tag{3}$$

where $(\partial A)_P$ is the increment of crack surface area that is produced upon crack extension at constant applied load P. An analogous expression

$$G = (M^2/2) \quad (\partial\lambda_t/\partial A)_M \tag{4}$$

has been developed by Outwater et al [*6*] for determining the strain energy release rate from the torsional compliance

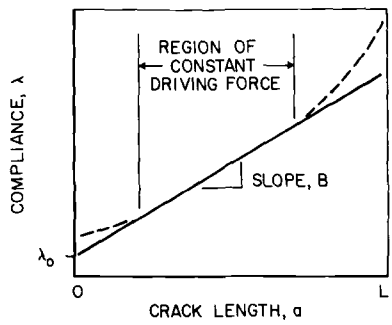

FIG. 3—*Schematic representation of the compliance relationship for the double-torsion test configuration. The solid line represents ideal linear behavior with the dashed line illustrating deviations from this linear behavior that result from end influences.*

$$\lambda_t = \Theta_t / M \tag{5}$$

where M is the applied torque on the specimen and Θ_t is the total load-plane twist, or rotation, between the two beams of the double-torsion specimen.[3] This expression can be shown to be equivalent to Eq 3 by relating the applied four-point load to the applied torque ($P/2 = M/w_m$) and by calculating the load-point deflection from the torsional deformation ($\Delta = w_m\theta = w_m\Theta_t/2$), as in the next section. The compliance then is related to the torsional compliance by

$$\lambda = \lambda_t (w_m/2)^2 \tag{6}$$

Using either Eq 3 or 4, the strain energy release rate is determined from a measured, or calculated, compliance relationship as

$$G = \frac{P^2 B}{2(\partial A/\partial a)_P} \tag{7}$$

Before this expression can be evaluated, it is necessary to determine the rate of change of crack surface area with an increment of crack extension. The usual assumption is that

$$(\partial A/\partial a)_P = d_w \tag{8}$$

where d_w is the web or specimen thickness on the crack plane. In its least restrictive sense, this condition requires that the crack front profile does not change on crack extension. This constancy of the crack profile implies that the crack velocity, as well as the strain energy release rate, vary along the crack front; being a maximum at the leading edge of the crack profile and decreasing back towards the trailing edge of the profile. This assumption and its implications remain to be verified experimentally and are subject to further theoretical analysis as they form an important part of the conclusion that the crack driving force is independent of crack length.

Using Eq 8 in Eq 7, the strain energy release rate for the double-torsion configuration is given by

$$G = \frac{P^2 B}{2 d_w} \tag{9}$$

[3]Note that the load-plane twist for each beam, θ, is one half of the rotation between the two beams; namely, $\theta = \Theta_t/2$. Part of the analysis by Outwater et al [6] is in error by this factor of 2; however, their final expressions are correct.

For Mode I fracture, the relationship between G and the stress intensity factor K_I is given by [23]

$$K_I = \sqrt{2\mu G/(1 \mp \nu)^{\pm 1}} \tag{10}$$

where μ is the elastic shear modulus, ν is Poisson's ratio, and the upper and lower signs refer to plane strain and plane stress, respectively. Substitution of Eq 9 into Eq 10 gives the stress intensity factor for the double-torsion configuration as

$$K_I = P \sqrt{\frac{\mu B}{(1 \mp \nu)^{\pm 1} d_w}} \tag{11}$$

where again the upper/lower signs refer to plane strain and plane stress, respectively. The appropriate choice between these two conditions is difficult to specify, since the crack profile is curved, or three dimensional. For brittle ceramic materials the distinction between plane strain and plane stress is seldom made. If the minimum thickness of $2.5(K_{Ic}/\sigma_y)^2$, where σ_y is the yield strength, that is recommended by the ASTM Test for Plane-Strain Fracture Toughness in Metallic Materials (E 399 - 76), is appropriate for these brittle materials, then most measured values have probably been plane-strain fracture toughness. Double-torsion experiments by Outwater et al [6] suggest that conditions, at least as determined at the leading edge of the crack profile, approximate plane strain in aluminum alloy specimens even at one half of the minimum thickness.

Another objection that has frequently been raised about the double-torsion configuration is the appropriateness of describing the mode of failure as Mode I, or an opening mode of fracture. However, this can be the only mode of crack deformation in an "ideal" double-torsion specimen, since the loading configuration and the specimen geometry are symmetrical about the crack plane. In support of this proposition Evans and co-workers [9–11] observe that measured values of G_c appear to agree with Mode I values as given by Eq 10, although they indicate that this could be a consequence of the relatively large values of K_{IIc} and K_{IIIc} compared to K_{Ic} for most materials.

The main assumptions of the analysis presented in this section are summarized in Table 1. The first assumption still requires further experimental investigation and theoretical analysis. The second assumption appears to be valid from symmetry arguments. Experimental data also support this assumption, but conclusive data have not been obtained on a material that exhibits "easy" Mode II or Mode III failure. The third entry is a question more than an assumption, and may not even be an appropriate question to ask. The next section provides an analytical calibration for the stress intensity factor through the development of an analytical expression for the constant B in the compliance relationship.

TABLE 1—*Assumptions in the stress intensity factor analysis for the double-torsion specimen and possible consequence of their invalidity.*

Assumption	Consequence of Invalidity
Crack profile independent of crack length $[(\partial A/\partial a)_P = d_w]$	stress intensity factor depends on crack length
Mode I failure	only G is given from analysis, K_I undetermined
Plane strain or plane stress (?)	

Analytical Compliance for Double-Torsion Specimen

The purpose of this analysis is to present an analytical solution for the linear elastic compliance of a double-torsion specimen of finite thickness. Such an analysis, although not unique, has not been presented specifically for the double-torsion specimen. The benefits of such a presentation are that assumptions of the analysis are stated explicitly, requirements on the imposed twisting torque are given in analytical form, and areas where the analysis may be improved are indicated. The present development follows an analysis by Timoshenko and Goodier [*24*] on the torsion of rectangular beams and the reader is referred to that text for further detail.

The double-torsion geometry for the analytical solution of linear elastic compliance is illustrated in Fig. 4. Since the existence of side grooves does not influence the following analysis, they are omitted for the sake of clarity. Possible consequences of side grooving, however, are discussed at the end of this section. From the outset it is assumed that the crack front is straight, not curved, and that the two beams of the double-torsion specimen twist independently. The restrictions that these assumptions place on the analysis are indicated below. The coordinate system for each of the retangular beams

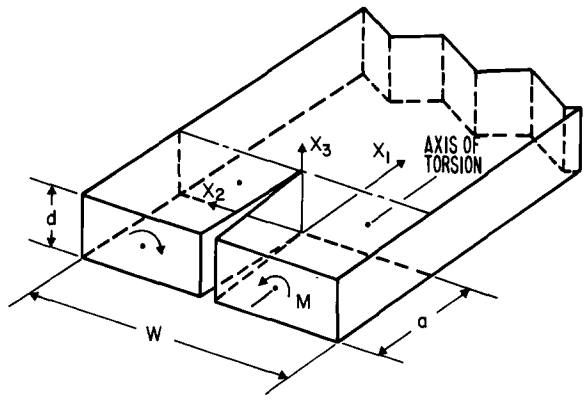

FIG. 4—*Geometry of the double-torsion test configuration for the analytical solution for the compliance. The specimen thinness ratio is defined by* $t = 2d/W$.

is illustrated in Fig. 5. The coordinate transformation between these beam coordinates and the crack-tip coordinate system is given by

$$b_1 = x_3 - (d/2)$$

$$b_2 = x_2 \pm (W/4)$$

$$b_3 = -x_1 \tag{12}$$

where the upper and lower signs, as will be the convention throughout this section, refer to the right and left beams, respectively.

A torque, or twisting moment, M is applied to each beam of the specimen so that the beam rotates through a total angular displacement of θ radians about the axis of torsion (b_3-axis). Accordingly, the beam rotation at a distance b_3 from its attachment to the plate, assuming for the present that the plate is perfectly rigid, is given by

$$\theta(b_3) = \pm b_3\theta/a = \mp x_1\theta/a \tag{13}$$

The upper and lower signs reflect the fact that the two beams rotate in opposite directions.

It should be noted that the applied torque is not specified as an input to the problem, but rather is determined from the required deformation that it produces. This deformation for each cross section of the beam is assumed to be composed of two components: (1) a pure torsional deformation, or twist of the cross section; and (2) an out-of-plane distortion, or warping, of the cross section. As illustrated in Fig. 5, the pure torsional deformation is described by the displacements

$$u_2 = b_1\theta(b_3) = \mp x_1[x_3 - (d/2)[\theta/a \tag{14}$$

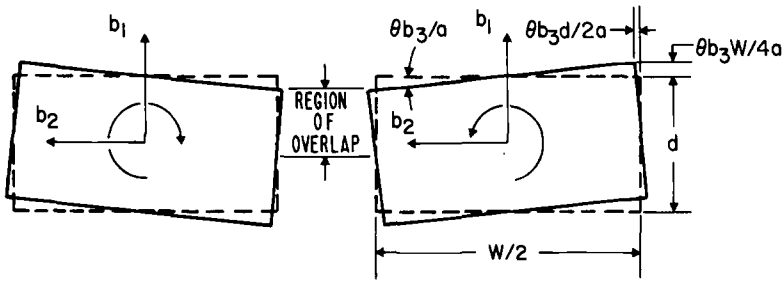

FIG. 5—*Schematic illustration of the beam coordinate systems and the torsional deformation of each beam. The beams are separated for clarity due to the region of interpenetration or overlap.*

$$u_3 = -b_2\theta(b_3) = \pm x_1[x_2 \pm (W/4)]\theta/a \tag{15}$$

in the $x_2 - x_3$ planes of each of the double-torsion beams. The out-of-plane distortion is described by an as-yet-undetermined function $F(x_2, x_3)$ according to

$$u_1 = (\theta/a)F(x_2, x_3) \tag{16}$$

This warping is assumed to be the same for all cross sections (that is, independent of x_1).

As seen from Fig. 5, and as can be calculated from Eq 14 through 16 there is a region where, if allowable, the two separate beams would interpenetrate each other. To obtain a proper solution, this region of interpenetration should be disallowed by the imposition of a displacement boundary condition for this region. This boundary condition would generate constraining contact stresses over the region. For the present, however, these contact stresses are assumed to have a negligible influence on the resulting solution and accordingly the region of overlap is ignored. This is probably a good approximation for thin beams, but may become more important for thicker specimens compared to the width.

For linear elasticity, the infinitesimal strain tensor is determined from the displacement gradients, $(\partial u_i/\partial x_j)$, according to[4]

$$\epsilon_{ij} = [(\partial u_i/\partial x_j) + (\partial u_j/\partial x_i)]/2$$

$$= (\theta/2a)\begin{bmatrix} 0 & \dfrac{\partial F}{\partial x_2} \mp \left(x_3 - \dfrac{d}{2}\right) & \dfrac{\partial F}{\partial x_3} \pm \left(x_2 \pm \dfrac{W}{4}\right) \\ \dfrac{\partial F}{\partial x_2} \mp \left(x_3 - \dfrac{d}{2}\right) & 0 & 0 \\ \dfrac{\partial F}{\partial x_3} \pm \left(x_2 \pm \dfrac{W}{4}\right) & 0 & 0 \end{bmatrix} \tag{17}$$

Since the deformation is a pure torsional shear, the stress tensor is given by

$$\sigma_{ij} = 2\mu\epsilon_{ij}, \tag{18}$$

where μ is the elastic shear modulus or modulus of rigidity.

[4]The (ij) indexes on the strain and stress tensor refer to the crack-tip coordinate system, (x_1, x_2, x_3).

The remaining problem consists of determining a warping function $F(x_2, x_3)$ that will satisfy both the equation of equilibrium,

$$(\partial\sigma_{12}/\partial x_2) + (\partial\sigma_{13}/\partial x_3) = 0 \tag{19}$$

(neglecting body forces) and the boundary condition that the sides of the double-torsion beams are unstressed,

$$\sigma_{12} = 0 \quad (\text{at } x_2 = 0 \text{ and } \mp W/2) \tag{20}$$

and

$$\sigma_{13} = 0 \quad (\text{at } x_3 = 0 \text{ and } d) \tag{21}$$

neglecting possible contact stresses at $x_2 = 0$, which influence Eq 20. The formulation of this problem is simplified greatly by the introduction of a stress function $\phi(x_2,x_3)$ according to

$$(\partial\phi/\partial x_3) \equiv \sigma_{12} = (\mu\theta/a)\{(\partial F/\partial x_2) \mp [x_3 - (d/2)]\} \tag{22}$$

and

$$-(\partial\phi/\partial x_2) \equiv \sigma_{13} = (\mu\theta/a)\{(\partial F/\partial x_3) \pm [x_2 \pm (W/4)]\} \tag{23}$$

so that Eq 19 is satisfied automatically, since $(\partial^2\phi/\partial x_2\partial x_3) = (\partial^2\phi/\partial x_3\partial x_2)$. From Eqs 22 and 23 it is easily shown that the stress function must satisfy the differential equation

$$(\partial^2\phi/\partial x_2^2) + (\partial^2\phi/\partial x_3^2) = \mp 2\mu\theta/a \tag{24}$$

subject to the boundary conditions that

$$(\partial\phi/\partial x_3) = 0 \quad (\text{at } x_2 = 0 \text{ and } \mp W/2)$$

and

$$(\partial\phi/\partial x_2) = 0 \quad (\text{at } x_3 = 0 \text{ and } d) \tag{25}$$

The solution to this differential equation (to within an arbitrary constant, which is unimportant) is given by

$$\phi(x_2,x_3) = \pm (8\mu\theta d^2/a) \sum_{n=1}^{\infty} \frac{1}{[(2n-1)\pi]^3}$$

$$\left\{1 - \frac{\cosh[(2n-1)\pi(4x_2/W \pm 1)/2t]}{\cosh[(2n-1)\pi/2t]}\right\} \sin[(2n-1)\pi x_3/d] \qquad (26)$$

The torsional shear stresses for every cross section of the double-torsion arms are given from Eqs 22 and 23 as

$$\sigma_{12} = \pm (8\mu\theta d/a) \sum_{n=1}^{\infty} \frac{1}{[(2n-1)\pi]^2}$$

$$\left\{1 - \frac{\cosh[(2n-1)\pi(4x_2/W \pm 1)/2t]}{\cosh[(2n-1)\pi/2t]}\right\} \cos[(2n-1)\pi x_3/d] \qquad (27)$$

and

$$\sigma_{13} = \pm (8\mu\theta d/a) \sum_{n=1}^{\infty} \frac{1}{[(2n-1)\pi]^2}$$

$$\left\{\frac{\sinh[(2n-1)\pi(4x_2/W \pm 1)/2t]}{\cosh[(2n-1)\pi/2t]}\right\} \sin[(2n-1)\pi x_3/d] \qquad (28)$$

The negatives of these stresses give the external shearing forces per unit area that must be applied to the ends of the double-torsion specimen at $x_1 = -a$ in order to produce the assumed torsional displacements. These external shearing forces have components in the x_2 and x_3 directions of

$$f_2 = -\sigma_{12} \quad \text{and} \quad f_3 = -\sigma_{13} \qquad (29)$$

In practice, the external forces applied to the ends of a double-torsion specimen are not distributed in this manner. By invoking Saint Venant's principle, the torsional deformation for "sufficiently long" crack lengths will depend only on the average applied force and applied torque at the loading end of the specimen. However, this requirement does impose a lower, and presently unspecified, limit on crack lengths for which valid data can be obtained.

The average applied force on the end of each beam is easily shown to be zero, that is,

$$\langle f_i \rangle = \pm \int_{\mp W/2}^{0} dx_2 \int_0^d dx_3 f_i = 0 \qquad (30)$$

Whereas the average torque applied to each arm of the specimen about an axis through the center of the beam is given by

$$M = \pm \int_{\mp W/2}^{0} dx_2 \int_0^d dx_3 \{[x_3 - (d/2)]f_2 - [x_2 \pm (W/4)]f_3\}$$

$$= \pm (\mu\theta/a)(Wd^3\psi/6) \tag{31}$$

where ψ is a function of the thinness ratio $t = 2d/W$ and is given by

$$\psi = 1 - 192t \sum_{n=1}^{\infty} \frac{\tanh[(2n-1)\pi/2t]}{[(2n-1)\pi]^5} \tag{32}$$

For computational purposes, a more rapidly converging form of this correction factor for a finite thickness specimen (that is, $t \neq 0$) is obtained by expanding $\tanh[(2n-1)\pi/2t]$ in a series of exponentials. After some manipulation one obtains

$$\psi = 1 - 186t\zeta(5)/\pi^5$$

$$- (384t/\pi^5) \sum_{n=1}^{\infty} \sum_{k=1}^{\infty} (-1)^k \cdot \frac{\exp[-(2n-1)k\pi/t]}{(2n-1)^5} \tag{33}$$

where $\zeta(5)$ is the Riemann zeta function given by [25]

$$\zeta(5) = \sum_{k=1}^{\infty} k^{-5} = 1.036\,927\,755 \tag{34}$$

This thickness correction factor, Eq 33, is given in Table 2 for several values

TABLE 2—*Correction factors from Eq 33 for a finite thickness double-torsion specimen as a function of the thinness ratio* t = 2d/W.

		Correction to B	Correction to K_I
t	$\psi(t)$	$1/\psi(t)$	$1/\sqrt{\psi(t)}$
1	0.4217	2.3712	1.5399
3/4	0.5414	1.8472	1.3591
1/2	0.6860	1.4576	1.2073
1/3	0.7900	1.2659	1.1251
1/4	0.8424	1.1870	1.0895
1/5	0.8740	1.1442	1.0697
1/6	0.8950	1.1174	1.0571
1/8	0.9212	1.0855	1.0419
1/12	0.9475	1.0554	1.0273
1/20	0.9685	1.0325	1.0161

of the thinness ratio, $t = 2d/W$. For ratios up to $t = 1$ (that is, a square beam cross section), a simplified expression which is accurate to better than 0.1 percent is given by

$$\psi = 1 - 0.6302t + 1.20te^{-\pi/t} \tag{35}$$

An alternate approximation has been given by Roark and Young [*26*] as

$$\psi = 1 - 0.63t\,[1 - (t^4/12)] \tag{36}$$

The required torsional compliance relationship between the average applied torque M and the angular displacement θ of each beam is given by Eqs 5 and 31; namely

$$\lambda_t = 2\theta/M = [12a/\mu W d^3 \psi\,(t)] \tag{37}$$

The load-point compliance is related to the torsional compliance, as in the previous section, according to

$$\begin{aligned} \lambda \equiv \Delta/P &= (w_m\theta)/(2M/w_m) \\ &= [3{w_m}^2/\mu W d^3 \psi\,(t)]a \end{aligned} \tag{38}$$

Thus, the analytical expression for the slope of the compliance relationship with respect to the crack length is given by

$$B = [3{w_m}^2/\mu W d^3 \psi\,(t)] \tag{39}$$

The intercept or constant compliance λ_o is not determined from the present analysis, but the origin of this term is indicated below.

For independent beams in torsion, Eq 38 is an exact expression for the load-point compliance with the correction for finite beam thickness given by the factor $\psi(t)$. The influence that this correction has on the value of B and K_I is given in Table 2 for select values of t. For the double-torsion configuration, however, the extent of overlap and the resulting contact stresses depend on the beam thickness. Accordingly, the correction for finite specimen thickness given by Eq 33 or 35 may not be the most important correction for thicker double-torsion specimens. This effect could possibly explain an experimental observation for polycrystalline alumina [*18*] where the analytical expression, Eq 11 with B given by Eq 39, underestimated K_{Ic} for specimens with a thinness ratio of $t = 2d/W \simeq 1/4$, but were in agreement with other measurements of K_{Ic} when $t \simeq 1/6$.

Another assumption made earlier in the analytical analysis was that the plate beyond the crack front was perfectly rigid. This plate has the same torsional shear stresses applied to it as the shear stresses on the end of each of

the double-torsion beams, namely, Eqs 27 and 28. If we relax the restriction that the plate is perfectly rigid, but still require that the remaining ligament length ($L - a$) is long, then the plate will have a constant compliance, λ_o, as is observed experimentally. Since this compliance is independent of crack length, it does not affect the K-calibration (Eqs 7 through 11) and only slightly influences crack velocity data, because for fairly long cracks, the compliance of the double-torsion beams is usually much larger than this constant correction (that is, $a \gg \lambda_o/B$). Accordingly, the elastic deflection of the uncracked portion of the double-torsion specimen is only of practical importance when the crack becomes long enough so that the remaining ligament length influences the K-calibration. Solving for this deflection also will probably depend on the importance of contact stresses and how they influence the crack front.

The existence of significant nonlinear end effects was first discussed quantitatively by McKinney and Smith [*12*]. They found a region, which was approximately a distance W from each end, where the data deviated from ideal behavior. This deviation has been quantified to a greater extent by the finite element stress analysis of Trantina [*15*] and by the recent experiments of Shetty and Virkar [*17*]. Both of these studies indicated that the analytical solution for K_I (Eq 11 with B given by Eq 39) gives a value that is too large for small cracks and is too small for long cracks. This result is a consequence of the nonlinear regions of the compliance relationship where the slope is less than B for short cracks (K_I decreased from the analytical value) and the slope is greater than B for long cracks (K_I increased from the analytical value). Between these two nonlinear end regions, there is a range of crack lengths for which the analytical solution is valid (see again Fig. 3). This linear range was determined to be

$$0.55W < a < L - 0.65W$$

from Trantina's finite element calculation [*15*], which used relative specimen dimensions of 1:10:20 for d, W, and L, respectively. Experimentally, Shetty and Virkar [*17*] obtained both

$$0.50W \lesssim a \lesssim L - 1.00W$$

and

$$0.40W \lesssim a \lesssim L - 0.80W$$

for specimens which had dimension ratios of 1:31.25:75 and 1:50:75, respectively. However, further systematic studies are required to determine this range of linearity and how it is influenced by specimen geometry.

Some final comments are made with regard to side notches or side grooves. Such grooves usually are employed to help constrain the crack to the center of the specimen. However, since these grooves introduce additional stress concentrations, they may substantially influence the double-torsion stress distribution and introduce further uncertainties into the analysis for stress intensity factor. Probably the best way to avoid these influences is to eliminate the side grooves, as advocated by Annis and Cargill [*19*]. With slight care in alignment of the applied load distribution [*19,20*], it is probably not necessary to have side grooves to guide the propagating crack. An additional consideration towards minimizing these effects may be to widen the width of the side groove [*1*].

In conclusion, the assumptions of the analytical analysis presented in this section are summarized in Table 3. This table along with Table 1 give the main assumptions in the analysis of the double-torsion test configuration.

TABLE 3—*Assumptions in the analytical compliance calculation for the double-torsion configuration and possible consequence of their invalidity.*

Assumption	Consequence of Invalidity
Crack profile straight through the thickness	unknown
Torsional deformation	. . .
Independent torsion beams with negligible contact stresses	influence stress intensity factor determination
Specified distribution of applied shear stresses on end of specimen	unimportant for "sufficiently long" crack lengths (Saint Venant's principle)
Specified applied forces and torques on end of specimen	deviation of crack from center of specimen
No deflections beyond crack tip	unimportant to K_I calibration for "sufficiently long" ligament lengths
	unimportant to compliance calibration and crack propagation data for long crack lengths [$a \gg \lambda_o/B$]
No side grooves	additional stress concentrations that may influence stress intensity factor

References

[*1*] Pletka, B. J., Fuller, E. R., Jr., and Koepke, B. G., this publication, pp. 19-37.

[*2*] Outwater, J. O. and Gerry, D. J., "On the Fracture Energy of Glass," *NRL Interim Contract Report.* Contract NONR 3219 (01) (x), AD 640848, University of Vermont, Burlington, Vt., Aug. 1966.

[*3*] Outwater, J. O. and Gerry, D. J., "On the Fracture Energy, Rehealing Velocity and Refracture Energy of Cast Epoxy Resin," 22nd Society of Plastic Industry Conference, Paper 13-D, 1967; also, *Journal of Adhesion,* Vol. 1, 1969, pp. 290-298.

[*4*] Outwater, J. O. and Austin, L. E. in *Materials Performance and the Deep Sea, ASTM STP 445,* American Society for Testing and Materials, 1969, pp. 41-54.

[*5*] Outwater, J. O. and Murphy, M. C., "On the Fatigue of Epoxy Resin," 26th Society of Plastic Industry Conference, Paper 10-A, 1971.

[*6*] Outwater, J. O., Murphy, M. C., Kumble, R. G., and Berry, J. T. in *Fracture Toughness*

and Slow-Stable Cracking, ASTM STP 559, American Society for Testing and Materials, 1974, pp. 127-138.

[7] Kies, J. A. and Clark, A. B. J. in *Fracture 1969 (Proceedings,* 2nd International Conference on Fracture, Brighton, April 1969), P. L. Pratt, Ed., Chapman and Hall Ltd., London, 1969, pp. 483-491.

[8] Beacham, C. D., Kies, J. A., and Brown, B. F., *Materials Research and Standards.* Vol. 11, 1970, p. 30.

[9] Evans, A. G., *Journal of Materials Science.* Vol. 7, No. 10, 1972, pp. 1137-1146.

[10] Evans, A. G., *International Journal of Fracture,* Vol. 9, No. 3, 1973, pp. 267-275.

[11] Williams, D. P. and Evans, A. G., *Journal of Testing and Evaluation,* Vol. 1, No. 4, 1973, pp. 264-270.

[12] McKinney, K. R. and Smith, H. L., *Journal of the American Ceramic Society,* Vol. 56, No. 1, 1973, pp. 30-32.

[13] Weidmann, G. W. and Holloway, D. G., *Physics and Chemistry of Glasses,* Vol. 15, No. 5, 1974, pp. 116-122.

[14] Virkar, A. V. and Johnson, D. L., *Journal of the American Ceramic Society,* Vol. 59, No. 5-6, 1976, pp. 197-200.

[15] Trantina, G. G., *Journal of the American Ceramic Society,* Vol. 60, No. 7-8, 1977, pp. 338-341.

[16] Virkar, A. V. and Gordon, R. S., *Journal of the American Ceramic Society,* Vol. 58, No. 11-12, 1975, pp. 536-537.

[17] Shetty, D. L. and Virkar, A. V., *Journal of the American Ceramic Society,* Vol. 61, No. 1-2, 1978, pp. 93-94.

[18] Evans, A. G., Linzer, M., and Russell, L. R., *Material Science and Engineering,* Vol. 15, 1974, pp. 253-261.

[19] Annis, C. G. and Cargill, J. S. in *Fracture Mechanics of Ceramics,* R. C. Bradt, D. P. H. Hasselman, and F. F. Lange, Eds., Plenum Press, New York, Vol. 4, 1978, pp. 737-744.

[20] Richter, H., Berichte Deutsche Keramisch Gesellschaft, Vol. 54, No. 12, 1977, pp. 405-409.

[21] Irwin, G. R., "A Critical Energy Rate Analysis of Fracture Strength," *Welding Journal* (Research Supplement), 1954.

[22] Irwin, G. R., in *Handbuch der Physik,* Vol. 6, Springer, Berlin, 1958, pp. 551-590.

[23] Paris, P. C. and Sih, G. C. in *Fracture Toughness Testing and Its Application, ASTM STP 381,* American Society for Testing and Materials, 1965, pp. 30-83.

[24] Timoshenko, S. and Goodier, J. N., *Theory of Elasticity,* McGraw-Hill, New York, 1951.

[25] *Handbook of Mathematical Functions,* M. Abramowitz and I. A. Stegun, Eds., National Bureau of Standards, Applied Mathematics Series 55, 1964.

[26] Roark, R. J. and Young, W. C., *Formulas for Stress and Strain,* McGraw-Hill, New York, 1975.

B. J. Pletka,[1] *E. R. Fuller, Jr.,*[2] *and B. G. Koepke*[3]

An Evaluation of Double-Torsion Testing—Experimental

REFERENCE: Pletka, B. J., Fuller, E. R., Jr., and Koepke, B. G., **"An Evaluation of Double-Torsion Testing—Experimental,"** *Fracture Mechanics Applied to Brittle Materials, ASTM STP 678,* S. W. Freiman, Ed., American Society for Testing and Materials, 1979, pp. 19-37.

ABSTRACT: Recently, the double-torsion (DT) technique has been widely used for fracture mechanics studies of brittle materials. The technique is popular for a number of reasons. First, the compliance analysis of a precracked DT specimen indicates the applied stress intensity factor, K_I, is independent of crack length. This allows tests to be run conveniently on opaque samples and in hostile environments. In addition, specimen and loading geometries are simple and easily adapted to most testing machines. Furthermore, specimens generally are precracked easily and slow crack growth data can be obtained using simple load relaxation tests. As in most testing techniques, however, experimental conditions may arise under which the validity of the data may be in question. For instance, the independence of K_I on crack length in a DT specimen occurs over only a limited range of crack lengths. The crack propagation characteristics have also been shown to be dependent on the specimen dimensions. Finally, irreproducibility of slow crack growth data occurs under certain testing conditions.

In this paper these and other experimental aspects of the DT test are examined in order to define the conditions under which the data are valid. Among the topics discussed are specimen and loading geometry, precracking techniques, data reproducibility, slow crack growth measurements, and comparisons of DT data with other techniques.

KEY WORDS: double torsion testing, fracture mechanics, slow crack growth, brittle materials, fracture (materials), crack propagation

Considerable interest has arisen in the acquisition of slow crack growth and fracture toughness data for ceramic materials because these data are

[1] Assistant professor, Department of Metallurgical Engineering, Michigan Technological University, Houghton, Mich. 49931.

[2] Physicist, Fracture and Deformation Division, National Bureau of Standards, Washington, D.C. 20234.

[3] Staff scientist, Honeywell Corporate Material Sciences Center, Bloomington, Minn. 55420.

necessary inputs in predictive analyses of the service lifetimes of brittle components [*1-4*].[4] Slow or subcritical crack growth parameters can be measured from breaking strength tests or from fracture mechanics tests. The latter usually are used to measure the fracture toughness, K_{Ic}.

Slow crack growth data are discussed most conveniently in terms of a three-stage crack velocity (V) versus stress intensity factor (K_I) curve exhibited by many ceramic materials and shown schematically in Fig. 1. In Region I the crack growth data are often described by the empirical equation

$$V = V_o(K_I/K_a)^n \tag{1}$$

where K_a is a constant used to normalize K_I and whose choice determines where the intercept will occur with respect to a log-log plot of V versus K_I;[5] V_o and n are material constants for a given environment. Characteri-

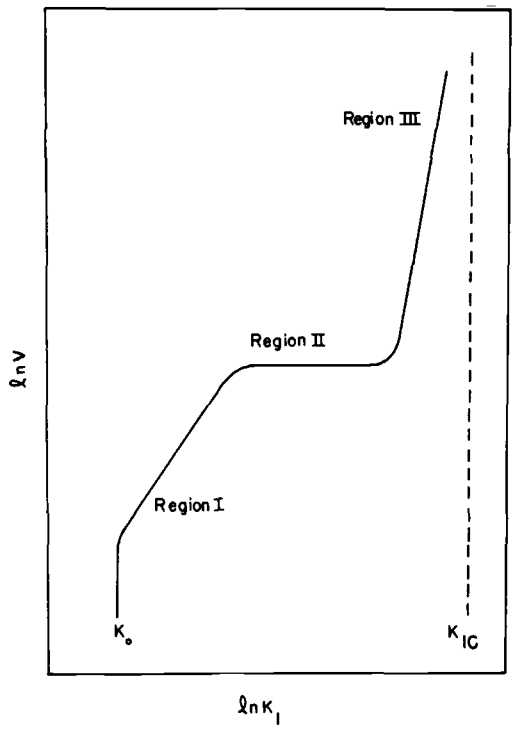

FIG. 1—*Schematic diagram showing variation of stress intensity factor with crack velocity during subcritical crack growth.*

[4] The italic numbers in brackets refer to the list of references appended to this paper.

[5] The usual expression for Eq 1 is $V = AK_I^n$. This form assumes $K_a = 1$ N/m$^{3/2}$ (when K_I is in units of N/m$^{3/2}$) and usually results in very large values for log A.

zation of slow crack growth in Region I is important because most of the subcritical crack growth occurs in this region before the onset of catastrophic fracture. Predictions of component lifetimes are based on Eq 1 and K_{Ic} [*1-4*].

A variety of fracture mechanics techniques for ceramics are available and one considered extremely versatile is the double-torsion (DT) technique [*5-7*]. The popularity of this technique stems from a number of reasons. Many specimen configurations have a crack length dependence on K_I, but the compliance analysis of the double torsion specimen indicates it is a "constant K" specimen, that is, K_I is independent of crack length [*8,9*] and is given by

$$K_I = P\, W_m \left[\frac{3}{W d^3 d_n (1-\nu)\xi}\right]^{1/2} \tag{2}$$

where P is the load, ν is the Poisson's ratio and the other terms are defined in the schematic showing a typical specimen and loading configuration in Fig. 2. Objections have been raised as to whether the mode of failure in the DT specimen is Mode I. Evans and co-workers [*8,9*] concluded that the correlation between G_c values measured by other techniques with values calculated from Eq 2 and the usual relationship between G and stress intensity factor [*10*] support the contention of a Mode I failure in the DT specimen. Equation 2 represents a plane strain condition at the crack tip and ξ is a correction factor for thick specimens obtained using elastic theory for thick plates [*11,12*]. A simplified expression for ξ in terms of

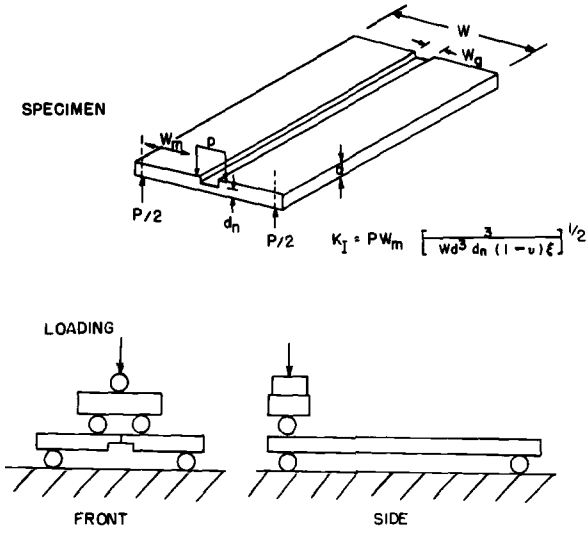

FIG. 2—*Schematic showing specimen and loading geometry of the double torsion specimen.*

a thickness ratio, $t = 2d/W$, which is accurate to better than 0.1 percent, is given by

$$\xi = 1 - 0.6302t + 1.20t\, e^{-\pi/t} \tag{3}$$

The independence of K_I on crack length allows crack growth data to be obtained on opaque specimens. The simple loading configuration shown in Fig. 2 results in these measurements being extended easily to high temperatures and hostile environments. The simple specimen geometry facilitates easy and rapid specimen preparation. Finally, a number of testing modes are available. In particular, during load relaxation under fixed grip conditions, provided the compliance is a linear function of crack length, it has been shown that the crack velocity is related to the instantaneous load and corresponding load relaxation rate (dP/dt) [*8,9*]. Thus, in a single load relaxation experiment, V is measured over a range of K_I.

A load relaxation technique can also be utilized with the double cantilever beam (DCB) specimen to measure V over a range of K_I [*13,14*]. However, compressive loading in the DT specimen is an advantage over the tensile loading system for DCB ceramic specimens. The use of a hard machine (small compliance) for DCB load relaxation experiments in order that catastrophic failure does not occur during the experiment is not a concern with the DT specimen [*14*].

The general procedure for conducting slow crack growth experiments and K_{Ic} measurements has been described previously [*8,9*]. However, certain precautions and special techniques are required to conduct the experiments properly and these are addressed in this paper. In addition, it has been determined that certain specimen and experimental conditions lead to data whose validity is questionable. These conditions also are examined. Furthermore, the assumption often has been made that fracture mechanics measurements and strength measurements yield identical failure prediction diagrams. This prediction is based on the equivalence of the propagation of large cracks in fracture mechanics specimens and small flaws in breaking strength specimens. This assumption is examined briefly in this paper.

General Review of DT Technique

The initial concept of the DT specimen is attributed to Outwater and Gerry [*5*]. They and several subsequent groups of workers subjected their specimens to constant load (from which K_I could be calculated) and directly measured crack velocities by monitoring crack lengths [*15,16,17*]. From these data it was confirmed that the crack velocity was constant for a constant load and that there was a good correlation between crack lengths derived from the compliance and crack lengths measured by other techniques.

The next advance in the DT technique arose from the work of Evans [*9*] and Williams and Evans [*8*]. In the latter, it was confirmed that there was a linear relationship between compliance, λ, and crack length, a, given by

$$\lambda = \Delta/P = (Ba + \lambda_o) \tag{4}$$

where Δ is the deflection, B the slope of the curve, and λ_o the intercept. Good agreement between analytical and experimental expressions for the stress intensity factor also was obtained. Starting with the expression for compliance, Williams and Evans also showed that for constant displacement, the crack growth rate was related to the instantaneous load and the corresponding load relaxation rate (dP/dt) as

$$V = -\frac{\Delta}{BP^2}\left(\frac{dP}{dt}\right) \simeq -\frac{(P_{i,f})(a_{i,f})}{P^2}\left(\frac{dP}{dt}\right) \tag{5}$$

where

P_i = initial load,
a_i = initial crack length,
P_f = final load, and
a_f = final crack length.

Thus, by measuring the instantaneous load and corresponding dP/dt, and the crack length before or after a load relaxation experiment, V can be measured over a range of K_I from a single experiment.

The crack front in a DT specimen is curved and extends further along the tensile surface than the compressive surface of the specimen. Evans [*9*] noted that in glass and alumina the crack shape is independent of crack length and the actual crack velocity can be approximated by multiplying Eq 5 by d_n/l where d_n is the web thickness and l is the length of the crack front. There are a number of problems associated with the curved front in a DT specimen. First, Virkar and Gordon [*18*] have pointed out that if slow crack growth is described by Eq 1, and the curved shape of the crack front does not change during propagation, then K_I must vary along the crack front. The exact variation in K_I has not been determined analytically at present. This point is discussed by Fuller [*12*] in this volume. Trantina [*19*] showed in a finite element analysis of the DT specimen, however, that a curved crack corresponding to those actually observed could have K_I equal to that given by Eq 2 to a depth of about one half of the specimen thickness. He also pointed up that although K_I must change along the crack front, since n in Eq 1 is large, the variation in K_I can be small. Thus, at this point in time the assumption is usually made that fracture in the DT specimen is occurring at values of K_I given by Eq 2. Further analysis will have to be made to verify this point completely.

A general description of the load relaxation technique is as follows. A precracked specimen is loaded at a relatively rapid crosshead speed (0.25 to 0.50 mm/min) to a load P, somewhat less than the critical load, P_{Ic}, necessary to initiate fast fracture of the specimen. If the load is sufficient such that the crack starts moving rapidly, that is a large relaxation is observed, the crosshead is arrested and the load is monitored as a function of time. The duration of most of our tests was 15 to 20 min since under ordinary testing conditions, slight oscillations in the load due to small thermal fluctuations obscures the data at low relaxation rates occurring at longer times. This limits the minimum crack velocity which can be measured with reasonable confidence to values of 10^{-6} to 10^{-7} m/s. After the test is completed, the specimen is removed from the loading fixture and the final crack length determined with a dye penetrant. By measuring P and the corresponding dP/dt, K_I is calculated from Eq 2 and V from Eq 5.

With extreme temperature control, crack velocity measurements using the load relaxation technique can be extended into the 10^{-8} to 10^{-9} m/s range. Evans [*9*] in fact has measured crack velocities as low as 10^{-11} m/s in glass with the technique. At low crack velocities, however, measurement of the resulting low load relaxation rates becomes a finite problem and other methods such as the constant load technique possibly may be more useful. However, Matsui et al [*20*] using the constant load technique to measure crack velocities in electrical porcelain *DT* specimens noted that when V was less than 10^{-6} m/s the crack decelerated and eventually stopped. They attributed this phenomenon to an interaction of the crack with the microstructure. Clearly, additional problems are to be expected when measuring extremely low crack velocities in polycrystalline ceramics.

In addition to obtaining crack velocities from constant load and load relaxation tests, a third method was suggested based on the observation that at a constant displacement rate, the crack propagates at a constant load [*9*]. Subsequently, Evans and Wiederhorn [*21*] showed that a load plateau should be obtained for a constant displacement rate, $\dot{y}$, and the crack velocity was given by

$$V = \frac{\dot{y}}{PB} \tag{6}$$

where B is obtained from the experimental compliance calibration or analytically as

$$B = \frac{3\,W_m^2}{Wd^3\,G} \tag{7}$$

where G is the shear modulus.

The load relaxation method is preferred since extensive crack growth is necessary in the other two techniques to obtain a single accurate measurement of V and K_I. Of course, this limits the number of individual $V - K_I$ data points that can be obtained from each specimen using either the constant load or constant displacement rate techniques. However, at high temperatures where the onset of plasticity or excessive extraneous relaxation may occur, the constant load condition is the only one that can be used.

Special Experimental Techniques

Specimen and Loading Geometry

A variety of DT specimen geometries can be used. Basically the specimen is a thin plate which usually has the dimensions of a microscope slide, that is, 2 by 25 by 75 mm. The variations in specimen geometry arise from two factors; the relative dimensions of the plate, for example, the ratio of specimen width to length, and in the geometry of the side groove(s) usually cut along the length of the specimen to guide the crack (see Fig. 2). Variations in the side groove geometry include one side groove versus side grooves on both sides of the specimen, and the width (W_g) and depth (web thickness d_n) of the side groove(s). Single side groove specimens can be placed on the test fixture with the side groove on the tensile or compressive surface of the specimen; the latter geometry facilitates the determination of the final crack length by dye penetration techniques.

The specimen is best loaded and supported by ball bearings; alternatively, the specimen can be supported by rollers, but the former are recommended since a definitive point loading system is obtained. The rear ball bearings shown in Fig. 2 serve only to position the specimen initially. Once the pure torque load is applied to the front of the specimen, the specimen lifts off of the rear ball bearings. For high temperature measurements, a similar loading device can be fabricated from hot-pressed silicon carbide [*21*]. In all cases, the use of high modulus materials is necessary to reduce extraneous relaxations during testing.

In some instances the crack may wander out of the side groove due to geometrical or material inhomogeneities, or both. Careful machining and specimen alignment minimize the problem. In some cases testing with the side groove on the tensile surface may help. In tests run on lead zirconate titanate (PZT), increasing the width of the side groove was found extremely beneficial [*22*]. It is suggested that with a wider groove, the crack is turned in the stress field of the specimen before it reaches the side of the groove; this appears to have been confirmed in photoelastic studies [*23*]. Annis and Cargill [*24*] have pointed out that by using a thinner specimen and by carefully aligning the specimen in the fixture, side grooves are not necessary.

In closing this section, several general recommendations are appropriate

for the design of DT specimens. The web thickness, d_n, should be approximately one half of the specimen thickness. Furthermore, based upon the discrepancies Evans et al [*25*] observed in K_{Ic} measurements on Lucalox,[6] the specimen thickness should be less than one twelfth of the specimen width. Finally, due to considerations of the constant K_I regime in the DT specimen (to be discussed later), the specimen length-to-width ratio should be greater than 2; it is not known what maximum value is appropriate.

Precracking Techniques

Precracking a DT specimen is necessary before performing any fracture mechanics studies, otherwise erroneously high stress intensity factors are obtained. (Precracking other specimen geometries usually is recommended, although some controversy exists as to the necessity of precracking.) For example, in a 7 μm grain size Wesgo alumina specimen containing a machined notch 35 mm in length, K_{Ic} was measured as 5.21 MN/m$^{3/2}$, compared to an average value of 4.35 MN/m$^{3/2}$ obtained from specimens of the same material containing precracks 43 to 54 mm in length. In all cases the specimens were 25 mm wide and 80 mm long. Two methods usually are used to precrack DT specimens and both require the same geometry of machined end notch from which the precrack initiates. In a 75-mm long specimen, a through notch typically 10 mm in length is cut in the middle of the side groove as shown in Fig. 3. At the end of the through notch, a tapered notch ~5 mm in length is cut such that the end of the tapered notch (*a* in Fig. 3) is on the compression side of the DT specimen.

The two precracking methods employ either a constant displacement rate or a fixed displacement of the testing machine crosshead. In the former, the specimen is loaded at a slow crosshead speed, for example, 5×10^{-3} mm/min, until a crack is initiated as noted by a rapid decrease in the load. The specimen in the latter method is also loaded at a slow crosshead speed, but periodically the crosshead displacement is fixed and a constant load is maintained on the specimen. Small increments to

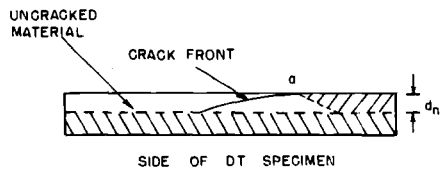

FIG. 3—*Schematic showing geometry of end notch and crack initiation. All cross hatched areas correspond to regions which have been removed by machining at W/2.*

[6]Trademark of General Electric. The use of these commercial trade names does not imply their endorsement for commerical applications by the National Bureau of Standards.

the load are added until crack initiation is noted again by a decrease in the load. In general, experience has shown that the maximum load for precracking is lower in the fixed displacement method and therefore smaller precracks are obtained. This is important for materials in which the precracking load exceeds P_{Ic}.

Extraneous Relaxations

Extraneous relaxations from the loading fixture and testing machine during a load relaxation experiment increase the relaxation rate at any load and increase the total load drop observed during the test. This effect is illustrated schematically in Fig. 4. Since the value of n in Eq 1 is computed from the slope of log V versus log K_I plots, that is, $n = \Delta \log V/\Delta \log K_I$, an increased relaxation rate implies a smaller change in V and a larger change in K_I. Both tend to decrease n.

There are two techniques that can be used to minimize this effect. First, a background relaxation can be recorded at a load of approximately ½ to ¾ P_{Ic} before a load relaxation test is conducted as shown in Fig. 4. The background relaxation then is subtracted from the total relaxation. The disadvantage of this technique concerns the uniqueness of the background relaxations, that is, background relaxations can vary due to changes in temperature, for example.

The second method seeks to minimize background relaxation. The fixture is first preloaded with a dummy specimen to approximately twice the anticipated peak load and held till relaxation ceases. This procedure then is repeated with a precracked specimen. The load is increased in increments until no relaxation is noted at about 90 percent of the load at which subcritical crack growth is expected. Using uncracked specimens

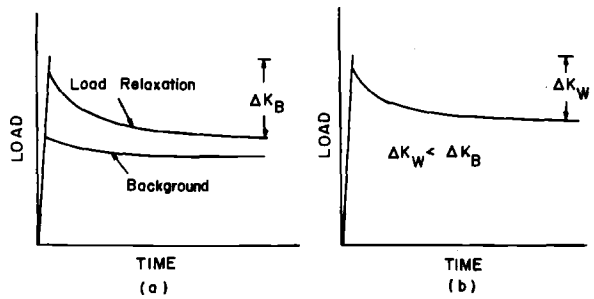

FIG. 4—(a) *Schematic of typical load relaxation and background curves.* (b) *After minimizing the background relaxation, the total range of* K_I *measured in the test,* ΔK_w *is smaller than when excessive background relaxations are present [that is,* ΔK_B *in* (a)]. *If uncorrected, the presence of the background relaxation results in low values of* n.

we have verified that this technique essentially eliminates background relaxations during subsequent load relaxation tests.

Crack Length Measurements

In load relaxation and constant load tests the crack length must be measured before or after the test. Since the crack front in a DT specimen is curved as shown in Fig. 3, the leading crack edge on the tensile surface is measured. The exact position of the trailing edge on the compressive surface is often difficult to ascertain. In opaque materials, crack measurements are performed with a dye penetrant. The criticism of this method is that the dye cannot penetrate near the crack tip. The accuracy of dye penetration is verified by making a measurement and then breaking the specimen opposite to the way it was originally loaded, that is, if it was tested with the side groove on the tensile surface of the specimen, it is broken with the side groove on the compressive surface. Since the crack profile at arrest can be observed on the fracture surface a comparison with the dye penetrant measurement can be made. This corroboration is recommended, particularly if the material is porous. In addition, the crack length measurement should be performed immediately after application of the dye penetrant. Allowing the specimen to remain in a room environment for a period of time, particularly when the humidity is high, causes the dye to smear around the crack trace.

An alternate technique for measuring crack lengths is to perform a compliance versus crack length calibration using specimens with various "crack lengths" sawn into them. Once the calibration is obtained, the crack length in precracked specimens can be determined by measuring the specimen compliance.

Data Collection and Reduction

A discussion of the collection and reduction of data is restricted to load relaxation experiments. dP/dt must be determined so that the velocity can be calculated. This involves measuring the time interval for a particular load decrement. While this can be performed directly from the strip chart, measurements at high crack velocities (large dP/dt values) and at low crack velocities (low dP/dt values) are difficult, and significant inaccuracies can result. A solution to this problem is provided by automated data acquisition systems. The data can be obtained by either measuring the time for a specific load decrement or the load decrement for a certain time interval. Systems employing both concepts have been built in our laboratories. The data are processed onto a file, for example, paper tape, and fed into a suitable program on a computer for the necessary computations of K_I and V. The value of n is evaluated from a least squares fit of ln K_I

upon ln V, minimizing the error in K_I. The load decrement or time interval between each measurement should be kept as small as possible. In the early stages of a load relaxation test where dP/dt is very large, using large load decrements or time intervals may result in erroneously low n values.

Conditions for Valid Data

Specimen Geometry Effects

As in most fracture mechanics tests, specimen geometry can strongly affect crack propagation and K_{Ic} data measured using DT tests. In what follows we discuss what currently is known about these effects. Since the DT specimen is a relatively new specimen much work remains to be done in this area.

The effects of specimen geometry on crack propagation have been evaluated by several different approaches. Evans [*9*] has shown that the DT specimen is a constant K specimen by demonstrating that K_{Ic} is independent of crack length in glass. However, the extent of the constant K_I regime along the specimen was not noted. This has been examined in our work by determining K_{Ic} as a function of the crack length, a, to specimen length, L, ratio in soda-lime-silicate glass microscope slides for ratios of a/L from 0.05 to 0.85. The results indicate an increase in K_{Ic} at short crack lengths and a decrease in K_{Ic} at long crack lengths as shown in Fig. 5.

A similar variation in K_{Ic} with crack length has been reported by Shetty and Virkar [*26*] who further showed that the valid range of crack lengths

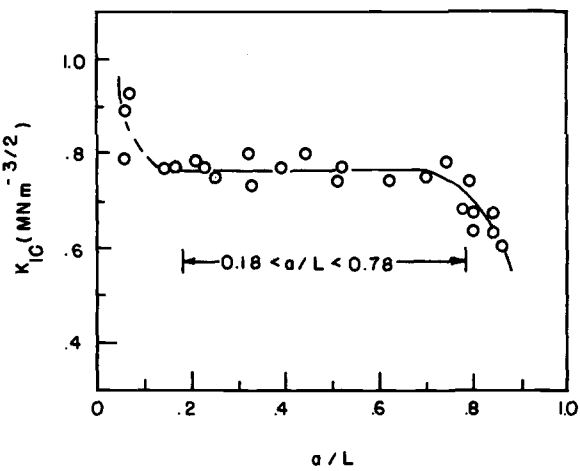

FIG. 5—K_{Ic} *measured in toluene on soda-lime-silicate glass slides as a function of crack length.*

(that is, the plateau in Fig. 5) decreased as the specimen length-to-width ratio decreased. These and the aforementioned results are in agreement with a three-dimensional elastic finite element stress analysis of the DT specimen performed by Trantina [*19*] who showed that K_I computed by the finite element analysis was less than that given by Eq 2 for short cracks (that is, a higher "apparent" value of K_I would be measured) and greater at long crack lengths. For a specimen with a length-to-width ratio $L/W = 3$, valid K_I measurements were predicted for $0.18 < a/L < 0.78$. These limits are indicated on Fig. 5 by arrows and are in excellent agreement with the experimental data.

Further confirmation of the increase in K_I at short crack lengths in a DT specimen has been obtained in load relaxation experiments performed on polycrystalline ceramics. Multiple load relaxation experiments on the same DT specimen can be performed when n is large ($n > 40$). Pletka and Wiederhorn [*27*] have noted that when the crack length was very short, that is, < 20 mm in 25 mm wide by 75 mm long magnesium aluminosilicate glass ceramic specimens, n values were invariable higher than n values obtained when the final crack length was between 25 and 50 mm long. Based upon these observations, it is proposed that the crack length should be greater than W and less than L-W to ensure that the crack is in the constant K_I regime.

As an extension of this work the dependence of side-groove geometry on crack propagation in soda-lime-silicate glass has been studied. The side groove geometry was varied in two series of glass specimens: one set were microscope slides with thicknesses of ~0.95 mm, and the other were plates 1.5 to 1.6 mm in thickness. All specimens were as-received with polished surfaces. With reference to Fig. 2, the variations in side groove geometry involved the number of side grooves (one side groove as well as side grooves on both sides of the specimen), the web thickness (d_n) and the width (W_g) of the side groove. The side groove geometry dependence in these specimens was evaluated by comparing the crack propagation parameter n determined from load relaxation experiments to data obtained in specimens which did not contain side grooves. All data were obtained with the specimens immersed in distilled water. The majority of single side groove specimens were placed on the test fixture so that the side groove was on the tensile surface of the specimen while the remaining specimens were placed with the side groove on the compressive surface of the specimen.

The results are summarized in Table 1, where the mean and standard deviation of n are given for each side groove geometry. There appears to be a slight difference in n when the two sets of specimens without side grooves are compared. However, the scatter bands of the two sets of specimens overlap and additional data are necessary to ascertain whether the difference is significant. Within each set of specimens, somewhat higher values of n and much larger standard deviations are obtained for specimens

TABLE 1—*Summary of crack propagation data for various side groove geometries in soda-lime-silicate glass.*

W_g, mm	Web Thickness[a]	Side Groove Type	No. of n Values	n Mean and Standard Deviation
		0.95 MM THICK MICROSCOPE SLIDES		
...	d	none	4	17.8 ± 1.7
0.4	3/4d	single	3	17.1 ± 2.2
0.4	1/2d	double	2	20.7 ± 9.8
		1.5–1.6 MM THICK SPECIMENS		
...	d	none	5	19.9 ± 1.3
1.7	1/2d	single	3	19.1 ± 1.3
1.7	1/2d	single[b]	3	16.1 ± 2.4
0.4	1/2d	single	3	18.0 ± 0.7
0.4	1/2d	double	4	23.8 ± 12.0
1.8	1/2d	double	3	19.6 ± 1.4
1.9	3/4d	single	2	18.5 ± 1.3
1.9	3/4d	single[b]	1	17.5
		1.5–1.6 MM THICK SPECIMENS ABRADED WITH 100 GRIT SiC		
...	d	none	3	19.5 ± 0.8

[a] In terms of specimen thickness.
[b] Side groove on the compressive surface of the specimen.

with double narrow (0.4 mm) side grooves. It can be concluded that this side groove geometry should be avoided. The remaining results indicate no significant side groove geometry dependence on crack propagation is apparent. Data for 1.5 to 1.6 mm thick specimens without side grooves which were abraded with 100 grit SiC also are included in Table 1. This treatment was performed to assess what influence surface finish might have on crack propagation. The data show that there is no effect.

It is important to realize, however, that soda-lime-silicate glass is an "ideal" material for crack propagation studies in that it does not contain any microstructural discontinuities such as grain boundaries or second phase particles. As a consequence there is a minimum interaction between the propagating crack and microstructure. Thus the next problem to be examined is whether the introduction of a microstructure promotes a specimen geometry dependence on crack propagation.

Constant displacement rate tests are one method in which rapid assessment of difficulties in crack propagation can be obtained. Our work on a series of six glass-ceramic and four electrical porcelain DT specimens suggests that narrow side groove widths promote an interaction between the crack and the side of the groove. Constant displacement rate tests conducted on glass in distilled water easily yielded the anticipated crack propagation at constant load. However such behavior was not observed in glass-ceramic and electrical porcelain specimens with narrow (0.4-mm)

side groove widths; instead, three different types of curves were observed of which two representative tracings are illustrated in Fig. 6. In the first type, a series of short plateaus, which occur at lower loads with increasing crack length, are obtained. For the moment, let us focus on the second type which is characterized by a series of discontinuities, in which a peak load is followed by a rapid decrease in load. The effect is attributed to the crack wandering into the wall of the side groove [*22,27*]. With wider side grooves or, equivalently, with thinner specimens [*24*] the crack will turn back toward the centerline before it intersects the wall of the groove. As a result, the crack remains perpendicular to the bottom of the specimen and propagation occurs in a geometrically stable manner. Similar effects also have been observed during our load relaxation tests on PZT specimens, in ZnSe by Evans and Johnson [*28*] and in graphite by Hodkinson and Nadeau [*29*]. The third type (not shown) is a continuous increase in load as the crack propagates. The fracture surface of these specimens clearly reveals the crack moving out of the side groove and into one of the arms of the specimen.

Is the DT Specimen a Constant K_I *Specimen?*

Measurements of K_{Ic} such as those shown in Fig. 5 indicate that within specific a/L ratios, K_{Ic} is independent of crack length. However, there are data taken during slow crack growth measurements which show that this may not always be the case. The Type I curve in Fig. 6 shows a series of plateaus occurring at lower loads with increasing crack length, suggesting that K_I is decreasing with increasing crack length. Additionally, since the value of n in Eq 1 is large for most ceramic materials, the amount of crack propagation that occurs during a single load relaxation test is limited. As a result, multiple relaxation tests can be performed on the same specimen. When multiple relaxations are performed on soda-lime glass speci-

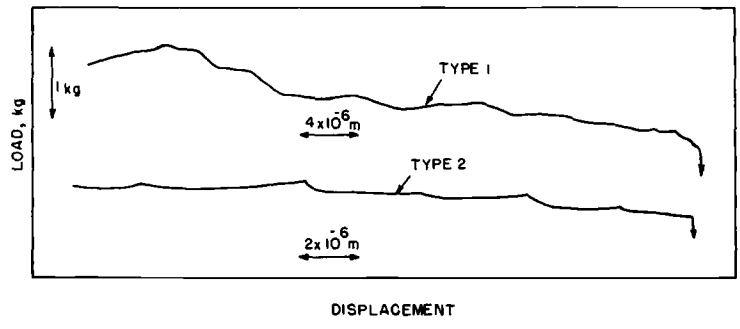

FIG. 6—*Tracings of portions of the load-displacement curves for two glass-ceramic DT specimens tested in distilled water at room temperature.*

mens tested in distilled water, the resulting $V - K_I$ curves invariably superimpose. When other ceramics are tested, superposition is not observed routinely. An example is shown in Fig. 7 which shows $V - K_I$ curves measured during subsequent relaxations on a glass-ceramic specimen. After the first relaxation the slope did not appreciably change but the curves shifted to lower values of K_I as the crack length increased. We have observed similar shifts in a number of materials including polycrystalline fine grained alumina and PZT ceramic.

The opposite effect has been observed in some alumina specimens in which the $V - K_I$ curve shifts to higher values of K_I during subsequent relaxations. An example showing three successive load relaxation runs on a Lucalox specimen is given in Fig. 8. Lucalox is a convenient material for these tests because it is semitransparent and any crack growth can be noted visually. The specimen contained a 2-mm wide side groove and was tested with the side groove on the tensile surface. After performing the first load relaxation on a precracked specimen, the load was decreased and then rapidly loaded to about 4 percent above the initial load in the first load relaxation. Very little crack growth could be detected either from the second load relaxation curve or optically. Again the load was decreased and then rapidly loaded to about 10 percent over the initial load in the first load relaxation. Although substantial crack growth occurred in the third

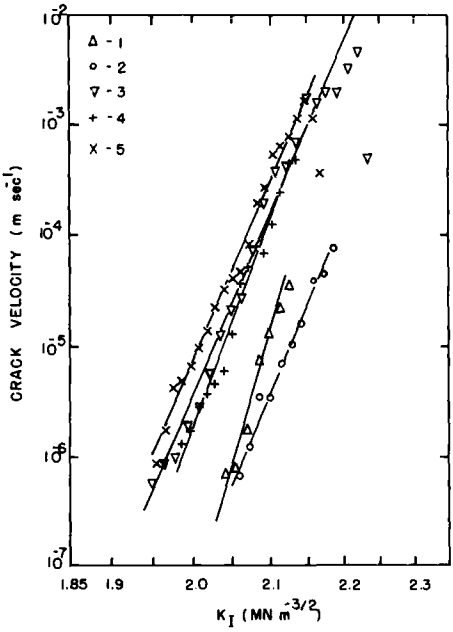

FIG. 7—V-K$_I$ *curves obtained during subsequent load relaxations (identified in upper left of figure) on the same glass-ceramic specimen.*

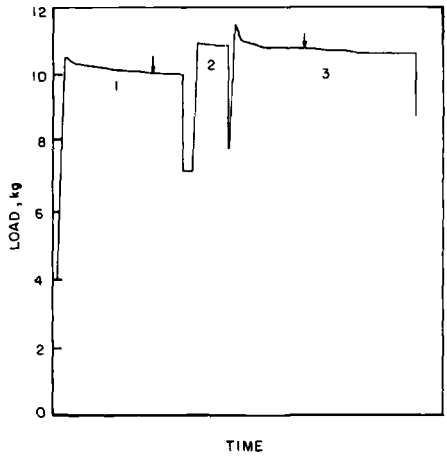

FIG. 8—*Load-time traces for three successive load relaxations run on a Lucalox DT specimen in water at room temperature. Initial chart speeds were 30 mm/min. In curves 1 and 3 the chart speed was reduced to 5 mm/min at the arrows.*

load relaxation test, the arrest load was about 6 percent higher than the arrest load in the first test. Throughout all three load relaxation tests, the crack remained in the center of the side groove.

The implications of these results are first that the DT specimen appears to be a constant K_I specimen within certain values of a/L. The reproducibility of $V - K_I$ data taken during successive load relaxations in glass specimens and data such as those shown in Fig. 5 support this. Secondly, microstructural effects appear to have a measurable effect on the data that are not completely understood. Work remains to determine for instance, if microstructural effects cause a change in the crack shape as a function of crack length.

Comparison of DT Data with Other Techniques

The intent of this paper was to focus on the experimental aspects of the DT specimen and not to dwell on a comparison of it with other fracture mechanics type specimens, such as the DCB. The existing data have demonstrated that there is good agreement between $V - K_I$ data obtained with the DT and DCB specimens for glass [*9,14*]; further work is needed to corroborate this for polycrystalline ceramics.

However, it has been assumed in failure prediction theories [*1-4*] that the propagation of large cracks in fracture mechanics specimens is equivalent to the propagation of small flaws in structural components. Therefore it has been proposed that data from either fracture mechanics or strength techniques may be used to generate failure prediction diagrams. This

assumption has been found to be valid in some ceramic materials and not in others by various workers; our work [*27*] as in agreement with this and will be discussed briefly. A detailed study of two glass-ceramics was undertaken in which the crack propagation paremeter n was determined using the DT specimen, and from stressing rate tests employing a four-point bend and a biaxial tension technique. The mean values of n and their standard deviation are summarized in Table 2. Differences in n were observed for the data of both the lithium aluminosilicate glass-ceramic (Cervit C-126) and the magnesium aluminosilicate glass-ceramic (Pyroceram 9606). Data obtained on other ceramic materials such as alumina have confirmed that a difference in the values of n may exist between crack propagation and breaking strength data. Thus the data raise doubt as to the equivalence between strength and fracture mechanics data for failure prediction purposes. A detailed discussion of why different crack propagation parameters are obtained with the different techniques is outside the scope of the present paper and will be discussed in a separate publication.

TABLE 2—*Summary of crack propagation parameter* (n) *data for two glass-ceramics.*

Glass-Ceramic	Biaxial Tension	Four-Point Bend	Double Torsion
Lithium aluminosilicate	37 ± 7	...	46 ± 10
Magnesium aluminosilicate	51 ± 5	52 ± 13	84 ± 7

Summary

1. The DT test is convenient to run and precracking is not difficult. The user should be aware of extraneous relaxations during load relaxation tests and to load, if possible, through ball bearings.

2. Increasing the width of the side groove eliminates the chance for the crack to interact with the side of the groove during propagation.

3. Measurements on glass specimens indicate, in agreement with analysis, that the DT specimen is a " constant K_I" specimen over a range of crack lengths that depend on specimen geometry.

4. Measurements of slow crack growth parameters on polycrystalline ceramic DT specimens indicate that the "constant K_I" condition may be affected by interactions of the propagating crack and the microstructure. Much more work is needed is this area.

Acknowledgments

The authors are indebted to J. G. Bruce for experimental assistance and to S. M. Wiederhorn for helpful and critical discussion during the course of this work. The support of the Office of Naval Research is gratefully acknowl-

edged by B.G.K. B.J.P. acknowledges the National Research Council for support as a post doctoral research associate at the National Bureau of Standards where much of this work was carried out.

References

[1] Wiederhorn, S. M. in *Fracture Mechanics of Ceramics*, Vol. 2, R. C. Bradt, D. P. H. Hasselman, and F. F. Lange, Eds., Plenum Press, New York, 1974, pp. 613-646.
[2] Evans, A. G. and Wiederhorn, S. M., *International Journal of Fracture*, Vol. 10, No. 3, Sept. 1974, pp. 379-392.
[3] Wiederhorn, S. M. in *Ceramics for High Performance Applications*, J. J. Burke, A. E. Gorum, and R. N. Katz, Eds., Brook Hill Publishing Company, Chestnut Hills, Mass. 1975, pp. 633-663.
[4] Wiederhorn, S. M., Tighe, N. J., and Evans, A. G., "New Design Techniques for Brittle Materials," Advisory Group for Aerospace Research and Development, Report No. 651, Dec. 1976, pp. 41-55.
[5] Outwater, J. O. and Gerry, D. J., "On the Fracture Energy of Glass," U.S. Naval Research Laboratory, Report Contract NONR 3219(01)(X), Aug. 1966.
[6] Outwater, J. O., Murphy, M. C., Kumble, R. G., and Berry, J. T. in *Fracture Toughness and Slow-Stable Cracking, ASTM STP 559*, American Society for Testing and Materials, 1974, pp. 127-138.
[7] Evans, A. G. in *Fracture Mechanics of Ceramics*, Vol. 1, R. C. Bradt, D. P. H. Hasselman, and F. F. Lange, Eds., Plenum Press, New York, 1974, pp. 17-48.
[8] Williams, D. P. and Evans, A. G., *Journal of Testing and Evaluation*, Vol. 1, No. 4, July 1973, pp. 264-270.
[9] Evans, A. G., *Journal of Materials Science*, Vol. 7, 1972, pp. 1137-1146.
[10] Paris, P. C. and Sih, G. C. in *Fracture Toughness Testing and Its Applications, ASTM STP 381*, American Society for Testing and Materials, 1965, pp. 30-83.
[11] Timoshenko, S. and Goodier, J. N., *Theory of Elasticity*, McGraw-Hill, New York, 1951.
[12] Fuller, E. R., Jr., this publication, pp. 3-18.
[13] Williams, D. P. and Nelson, H. G., *Metallurgical Transactions*, Vol. 3, No. 8, Aug. 1972, pp. 2107-2113.
[14] Virkar, A. V. and Gordon, R. S., *Journal of the American Ceramic Society*, Vol. 59, No. 1-2, Jan.-Feb. 1976, pp. 68-71.
[15] Kies, J. A. and Clark, A. B. J. in *Fracture-1969*, P. L. Pratt, Ed., Chapman and Hall, Ltd., London, 1969, pp. 483-491.
[16] Beachem, C. D., Kies, J. A., and Brown, B. F., *Materials Research and Standards*, Vol. 11, No. 4 April 1971, p. 30.
[17] McKinney, K. R. and Smith, H. L., *Journal of the American Ceramic Society*, Vol. 56, No. 1, Jan. 1973, pp. 30-32.
[18] Virkar, A. V. and Gordon, R. S., *Journal of the American Ceramic Society*, Vol. 58, No. 11-12, Nov.-Dec. 1975, pp. 536-537.
[19] Trantina, G. G., *Journal of the American Ceramic Society*, Vol. 60, No. 7-8, July-Aug. 1977, pp. 338-341.
[20] Matsui, M., Soma, T., and Oda, I. in *Fracture Mechanics of Ceramics*, Vol. 4, R. C. Bradt, D. P. H. Hasselman, and F. F. Lange, Eds., Plenum Press, New York, 1978, pp. 711-724.
[21] Evans, A. G. and Wiederhorn, S. M., *Journal of Materials Science*, Vol. 9, 1974, pp. 270-278.
[22] Bruce, J. G., Gerberich, W. W., and Koepke, B. G. in *Fracture Mechanics of Ceramics*, Vol. 4, R. C. Bradt, D. P. H. Hasselman and F. F. Lange, Eds., Plenum Press, New York, pp. 687-709.
[23] Fuller, E. R., Jr., National Bureau of Standards, Washington, D. C., unreported results.
[24] Annis, C. G. and Cargill, J. S. in *Fracture Mechanics of Ceramics*, Vol. 4, R. C.

Bradt, D. P. H. Hasselman, and F. F. Lange, Eds., Plenum Press, New York, pp. 737–744.

[25] Evans, A. G., Linzer, M., and Russell, L. R., *Materials Science and Engineering,* Vol. 15, 1974, pp. 253–261.

[26] Shetty, D. K. and Virkar, A. V., *Journal of the American Ceramic Society*, Vol. 61, No. 1–2, Jan.–Feb. 1978, pp. 93–94.

[27] Pletka, B. J. and Wiederhorn, S. M. in *Fracture Mechanics of Ceramics,* Vol. 4, R. C. Bradt, D. P. H. Hasselman, and F. F. Lange, Eds., Plenum Press, New York, 1978, pp. 745–759.

[28] Evans, A. G. and Johnson, H., *Journal of the American Ceramic Society,* Vol. 58, No. 5–6, May–June 1975, pp. 244–249.

[29] Hodkinson, P. H. and Nadeau, J. S., *Journal of Materials Science,* Vol. 10, No. 5, May 1975, pp. 846–856.

G. K. Bansal[1] *and W. H. Duckworth*[1]

Fracture Surface Energy Measurements by the Notch-Beam Technique

REFERENCE: Bansal, G. K. and Duckworth, W. H., **"Fracture Surface Energy Measurements by the Notch-Beam Technique,"** *Fracture Mechanics Applied to Brittle Materials, ASTM STP 678,* S. W. Freiman, Ed., American Society for Testing and Materials, 1979, pp. 38-46.

ABSTRACT: The notch-beam technique (NBT) for determining fracture surface energies (γ_i) of ceramic materials is discussed. Basic principles involved in the technique are reviewed, and effects of different test variables on measured γ_i values are examined. In addition, merits and limitations of the technique are discussed, and measured values are compared with those obtained by other techniques.

KEY WORDS: fracture (materials), crack propagation, ceramic materials, fracture mechanics methods, notch-beam test

This paper discusses the notch-beam technique (NBT) for determining fracture surface energies of ceramic materials. Merits and limitations of the technique are reviewed, and measured values are compared with those obtained by other techniques.

NBT can be used to measure a material's work of fracture, γ_f, as well as fracture surface energy, γ_i, and it is important to distinguish between the two properties. Both are measures of the energy required to form a unit area of new surface by crack propagation. However, they have different significances, and for the same material sometimes have different values.

γ_i is the energy term in the Griffith criterion for crack instability [*1,2*][2]

$$\sigma_f \simeq \frac{Z}{Y}\sqrt{\frac{2\gamma_i E}{a}} \tag{1}$$

[1]Principal research scientist and research leader, respectively, Battelle Columbus Laboratories, Columbus, Ohio 43201.

[2]The italic numbers in brackets refer to the list of references appended to this paper.

where

σ_f = applied tensile stress,
E = Young's modulus,
a = depth of the crack that becomes unstable, and
Z and Y = dimensionless parameters.

Z depends principally on the crack shape [2] and Y depends on crack depth relative to specimen thickness, type of loading, and crack location [3]. Equation 1 defines a local condition at the instant of fracture, when spontaneous growth of a sharp crack initiates. γ_i is related to the material's critical stress intensity factor or fracture toughness, K_{Ic}, as follows

$$\gamma_i = K_{Ic}^2/2E \tag{2}$$

γ_f is the total energy consumed per unit area of new surface formed in propagating a crack completely through a specimen. It is assessed from the relation [4]

$$\gamma_f = U/2A \tag{3}$$

where U is the total energy consumed by the material in fracturing and A is the projected area of the fracture face.

Fundamental understanding of fracture surface energy and work of fracture is lacking. The two terms account for irreversible energy transfer processes that occur during fracturing, but it is not possible at present to specify contributions of individual processes or interpret observed values in terms of the contributing processes. It is rather clear, however, that the material's thermodynamic free surface energy cannot account for a substantial portion of the energy required to fracture a ceramic.

Basic Principles

Fracture surface energy is determined using NBT by inducing a crack of known dimensions and orientation in a specimen and finding the stress at which it becomes unstable. γ_i is then calculated from equations similar to Eq 1.

A range of specimen geometries and loading configurations can be used, the most common being a single-edge notched beam (SENB) specimen loaded in bending as shown in Fig. 1. Either three- or four-point loading is used. Uniform tension loading could be used but is less satisfactory for brittle materials owing to the difficulties in gripping and alignment to eliminate spurious bending stresses.

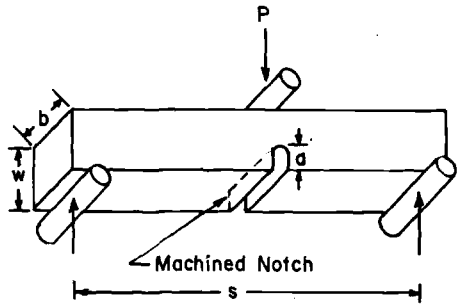

FIG. 1—*Schematic of notch-beam test in three-point bending.*

Using the specimen geometry and loading configuration shown in Fig. 1, K_{Ic} is calculated using the following form of the Griffith relation [*4*]

$$K_{Ic} = \frac{6M\,a^{1/2}}{bw^2} \cdot Y \tag{4}$$

where M is the applied bending moment at fracture, and a, b, and w are dimensions as shown in Fig. 1. Y is a dimensionless parameter which depends on a/w and on type of loading as follows

$$Y = A_0 + A_1(a/w) + A_2(a/w)^2 + A_3(a/w)^3 + A_4(a/w)^4$$

where the coefficients A have the values shown in Table 1. A graphical representation of Y values is given in Fig. 2.

Equation 4 assumes that the artificially induced crack which becomes unstable has zero width, extends the full breadth (b) of the specimen, and that its depth (a) is precisely known. Further, to obtain valid K_{Ic} values using NBT, cross sections of the specimen and of the precrack must be of sufficient size relative to microstructural features that the observed response to loading is representative of the bulk material. The reliability of NBT data depends on how closely these assumed conditions have been met experimentally. It

TABLE 1—*Values of coefficients* A.

Type of Loading	A_0	A_1	A_2	A_3	A_4
Four-point	+1.99	−2.47	+12.97	−23.17	+24.80
Three-point					
$s/w = 8$[a]	+1.96	−2.75	+13.66	−23.98	+25.22
$s/w = 4$	+1.93	−3.07	+14.53	−25.11	+25.80

[a] s is outer-span length (see Fig. 1).

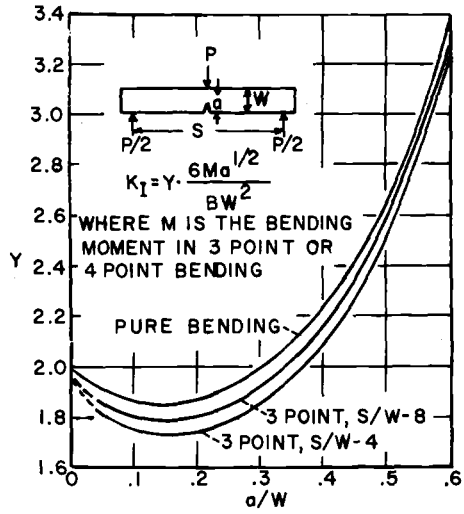

FIG. 2—Y *values as a function of notch depth and type of loading.*

should be noted that the kinds of experimental problems encountered with NBT also are encountered in other K_{Ic} measurement techniques.

In ultimate analysis, any K_{Ic} measurement technique must yield a value that is equivalent to that for crack instability from a natural flaw in the material. These flaws are intrinsic microstructural features, surface flaws from surface finishing or abuse in handling or service, or combinations of these. Accordingly, in appraising any technique, emphasis should be placed on determining how well it meets the criterion of providing for a given ceramic the same K_{Ic} value that governs fractures from real flaws.

Comparison of NBT with Other Data

NBT, as described previously, has been used to measure fracture surface energies of a wide variety of ceramic materials. In a few cases, data are available to permit comparison of values with those obtained by other techniques, including strength tests. Table 2 gives these comparisons, and it will be noted that the agreement among values is generally good. As an exception, NBT values for the hot-pressed silicon nitride (Si_3N_4) are in a higher range and more in accordance with the values from strength tests than are those given by double-cantilever beam (DCB) and double-torsion tests. It will be noted also that unlike the measurements on the three polycrystalline ceramics, valid NBT determinations for glass were obtained only when specimens were precracked deliberately at the root of the saw-cut notch.

Table 3 compares NBT and DCB values for four alumina (Al_2O_3) ceramics, two fine-grained, and two coarse-grained. The NBT data reflect

TABLE 2—*Comparison of room temperature fracture surface energies obtained by different test techniques.*

Material	Fracture Surface Energy, J/m^2					
	Notch Bend				Strength Tests	
	Notched Only	Precracked	Cantilever [5]	Double Torsion [6]	From Flaw Size [7]	From Fracture Mirror [8]
Soda-Lime Glass	12 to 20	4.1	3.9	3.8	4	4
Glass-Ceramic (Corning PyroCeram 9606)	24	...	22	25	25	25
Sintered Al_2O_3 (3-M Alsimag 614)	26	...	25	23	24	23
Hot-Pressed Si_3N_4[a] (Norton NC-132)	40 to 60	...	26 to 40	25 to 40	48	48

[a]Fracture surface energy is anisotropic, that is, depends on direction of crack propagation with respect to hot-pressing direction.

Table 3—*Fracture energies of fine- and coarse-grained alumina ceramics measured by NBT and DCB techniques* [9].

Material	Grain Size, μm	Fracture Energy, J/m^2	
		Notch Beam[a]	Double Cantilever[b]
Coors AD999	3	20	19
GE Lucalox	35	20	32
Experimental	3	23	21
Experimental	20	21	39

[a]Specimens notched only.
[b]Specimens precracked.

little difference in fracture energies, while the DCB measurements give appreciably higher values for the coarse-grained bodies but agree with the NBT values for the fine-grained bodies. No *a priori* basis exists for judging which test technique, if either, gave valid fracture-energy determinations. A possible factor here is the finding [*10*] that K_{Ic} of some Al_2O_3 ceramics exhibit a dependence on the extent of subcritical crack growth. In a recent review of microstructural effects on ceramic fracture energies, Rice [*11*] observes that effects of both porosity and grain size tend to be less pronounced in NBT data than in data obtained by other measurement techniques, as is reflected in Table 3.

Effects of Test Variables

A few investigations have been made of effects of NBT test variables on measured values of ceramic fracture surface energies. Simpson [*12*] investigated the effects of width and depth of saw-cut notches in measurements on three materials, an Al_2O_3 and a silicon carbide (SiC) ceramic and a bulk graphite. His data, given in Fig. 3, show that the values were affected by both notch width and notch depth, and those obtained with the narrower notches of 0.20 mm approached smaller values measured using the DCB technique.

Davidge and Tappin [*13*] have reported that saw cutting of thin (0.25 mm wide) notches can introduce limited cracking at the notch root which in case of a coarse-grained Al_2O_3 ceramic was sufficient to yield results that agree with those on specimens further cracked by wedging the notch. Barnby and Taylor [*14*] have reported the same phenomenon in specimens of a reaction-sintered Si_3N_4. Thus, it would appear that if the saw-cut notch is made sufficiently thin, less than 0.25 mm, and the material precracks upon saw cutting the notch, valid fracture energy measurements can be made without the need for deliberate precracking.

Since saw cutting the notch can introduce a cracked zone at the notch root

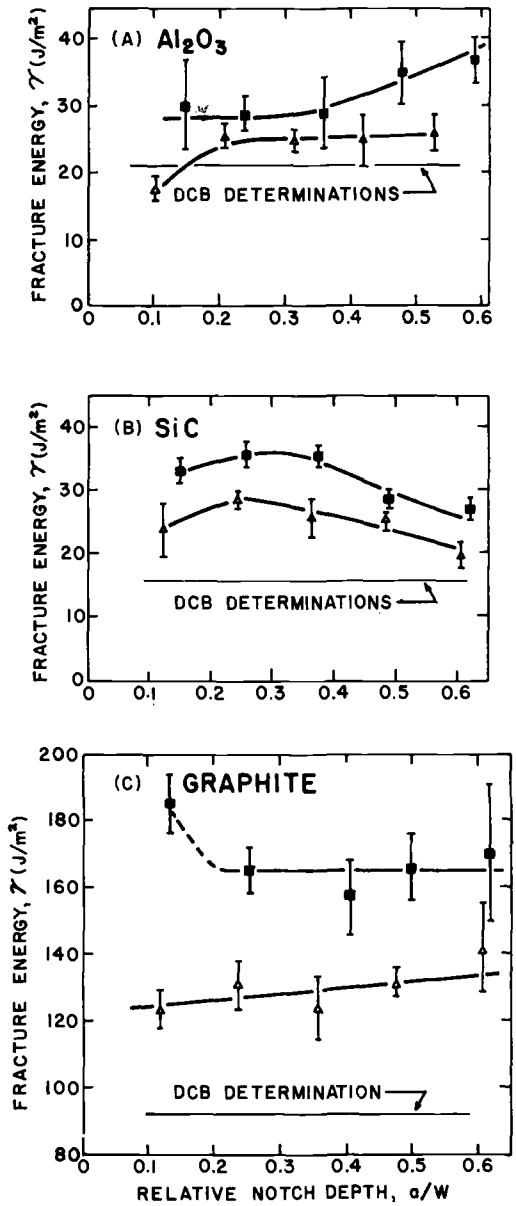

FIG. 3—*Fracture surface energies as measured using two notch widths on as-sawed specimens and on precracked double-cantilever beams (■0.75-mm notch width, Δ0.20-mm notch width.* [12]).

which acts like a deliberately introduced precrack, failure to consider the depth of the cracked zone in the value used to calculate K_{Ic} (Eq 4) could result in an erroneous value [*15*]. This error can be minimized by preloading the specimen to about 90 percent of the fracture load to cause crack linkage in the cracked zone, unloading and measuring the crack depth, and then reloading to failure.

If crack depth is determined prior to fracturing the specimen, an erroneous result will be obtained, of course, if significant stable crack growth occurs during loading. This suggests the use of fast loading or testing in an inert (for example, moisture free) environment to eliminate this source of possible error. Also, the possibility exists of crack healing in elevated temperature tests which would lead to erroneously large values of fracture surface energy if the initial crack depth is used in Eq 4.

We have noted above that the NBT specimen should be of sufficient size that the cross section is representative of the bulk material. The size should allow the crack which becomes unstable to have a depth that extends many (for example, 20 to 50) grain diameters. Effects on the fracture surface energy of rocks [*16*] and alumina ceramics [*10*] have been attributed to a microcracked volume that surrounds the crack tip, which suggests that the crack depth and specimen size must be sufficient to establish an equilibrium three-dimensional network of cracks at the tip of the unstable crack in order to obtain a valid fracture surface energy measurement for such materials. Because of the limited volume of material subjected to maximum tension with three-point bending [*17*], it is questionable whether it will yield valid measurements for materials in which a microcracked volume surrounds the unstable crack tip. This indicates the need to use four-point bending for NBT measurements on these materials.

Thus it can be seen that test conditions which yield valid measurements on one ceramic may give erroneous values if used for another ceramic having a different microstructure. This precludes a general specification of such factors as specimen size, crack depth, and use of three- or four-point bending. The investigator must be aware of peculiarities of the material on which measurements are being made to obtain error-free data from NBT. In this connection, the forementioned fact that K_{Ic} of Al_2O_3 ceramics have been observed to vary with depth of the crack that becomes unstable obviously means that K_{Ic} of some ceramics cannot be expressed as a single value. In these cases, K_{Ic} must be assessed as a function of crack depth or fracture stress, and measurements must be made to provide the functional relation.

The fact that saw-cutting of the notch in NBT specimens sometimes introduces cracking at the notch root suggests that residual thermally induced stresses at the root also are possible. If residual stresses are present, Eq 4 would give an erroneous K_{Ic} value. Annealing of specimens might be used to eliminate this error.

Conclusions

A main conclusion from this review is that NBT can be used for valid fracture surface energy measurements on ceramic materials. The technique offers the advantages of requiring a rather simple specimen geometry, loading configuration, and testing procedure. Precautions must be exercised in its use, particularly with respect to inducing the crack which becomes unstable and defining its depth. Correct use of the technique suffers from insufficient study of effects of test variables on results.

References

[1] Griffith, A. A., *Philosophical Transactions*, Royal Society, London, Vol. A 221, 1921, p. 163.
[2] Bansal, G. K., *Journal of the American Ceramic Society*, Vol. 59, No. 1-2, 1976, p. 87.
[3] Brown, W. F., Jr. and Srawley, J. E. in *Plane Strain Crack Toughness Testing of High-Strength Metallic Materials, ASTM STP 410*, American Society for Testing and Materials, 1967.
[4] Tattersall, H. G. and Tappin, G., *Journal of Materials Science*, Vol. 1, 1966, p. 296.
[5] Wiederhorn, S. M., Shorb, A. M., and Moses, R. L., *Journal of Applied Physics*, Vol. 39, 1968, p. 1572.
[6] Evans, A. G., *Journal of Materials Science*. Vol. 7, 1972, p. 1137.
[7] Bansal, G. K. and Duckworth, W. H., *Journal of the American Ceramic Society*, Vol. 60, No. 7-8, 1977, p. 304.
[8] Bansal, G. K., *Philosophical Magazine*, Vol. 35, No. 4, 1977, p. 935.
[9] Simpson, L. A. in *Fracture Mechanics of Ceramics*, Vol. 2, R. C. Bradt et al, Eds., Plenum Press, New York, 1974.
[10] (a) Hubner, H. and Jillek, W., *Journal of Materials Science*, Vol. 12, 1977, p. 117.
(b) Bansal, G. and Duckworth, W., *Journal of Materials Science*, Vol. 13, 1978, p. 215.
[11] Rice, R. W. in *Treatise on Materials Science and Technology*, Vol. 11 R. K. MacCrome, Ed., Academic Press, New York, 1977.
[12] Simpson, L. A., *Journal of the American Ceramic Society*, Vol. 57, No. 4, 1974, p. 151.
[13] Davidge, R. W. and Tappin, G., *Proceedings*, British Ceramic Society, Vol. 15, 1970, p. 47.
[14] Barnby, J. T. and Taylor, R. A. in *Special Ceramics 5*, P. Popper, Ed., British Ceramic Research Association, 1972, pp. 311-328.
[15] Simpson, L. A., Ritchie, I. G., and Lloyd, D. J., *Journal of the American Ceramic Society*, Vol. 58, No. 11-12, 1975, p. 537.
[16] Cooper, G. A., *Journal of Materials Science*, Vol. 12, 1977, p. 277.
[17] Duckworth, W. H., *Journal of the American Ceramic Society*, Vol. 34, No. 1, 1951, p. 1.

W. L. Fourney[1] *and T. Kobayashi*[1]

Influence of Loading System on Crack Propagation and Arrest Behavior in a Double-Cantilever Beam Specimen

REFERENCE: Fourney, W. L. and Kobayashi, T., **"Influence of Loading System on Crack Propagation and Arrest Behavior in a Double-Cantilever Beam Specimen,"** *Fracture Mechanics Applied to Brittle Materials, ASTM STP 678,* S. W. Freiman, Ed., American Society for Testing and Materials, 1979, pp. 47-59.

ABSTRACT: Design and analysis procedures which include dynamic crack propagation and crack arrest are currently under development in order to assure the safety of such structures as nuclear pressure vessels. This type of design and analysis procedure requires a knowledge of the relationship of stress intensity factor (K) as a function of crack speed ($\dot{a}$). The minimum value of stress intensity factor (designated as K_{I_m}) on the K versus $\dot{a}$ relationship is of particular importance because crack arrest will occur if the stress intensity factor falls below this minimum value.

Direct determination of the K versus $\dot{a}$ relationship and of the value of K_{I_m} for pressure vessel grade steels is an extremely difficult and complex task. For this reason methods have been developed to approximate K_{I_m} values. One such method was developed by Battelle Columbus Laboratory (BCL) and another by Materials Research Laboratory in Chicago. One difficulty involved in an analysis of dynamic crack propagation and arrest is the interaction of the specimen and loading system, and its effect on crack behavior.

This paper describes a series of experiments conducted to determine the influence of loading system on crack jump length and stress intensity as a function of velocity. Rectangular double-cantilever models made from Homalite 100, a birefringent polymer, were tested with two different wedge loading systems. One system used steel loading pins and aluminum wedge. The second system used both plastic pins and plastic wedge. A Cranz-Schardin high speed camera was used to photograph isochromatic fringe patterns associated with propagating and arrested cracks. Dynamic stress intensity factors were determined from the isochromatic fringe loops using a three-parameter Westergaard stress function.

The high speed photographs also were used to determine crack length as a function of time. From this relationship the crack velocity was determined. The results were compared with the predictions of a one dimensional finite difference computer code written

[1]Professor and associate professor, respectively, Mechanical Engineering Department, University of Maryland, College Park, Md. 20742.

by BCL. The crack jump for the models loaded with the plastic pins and wedge was found to be about twice the crack jump for the models loaded by metal pins and wedge for the same initial pin displacement. The amount of energy stored in pin contact stress was computed and when this additional energy was added to the computer input it was found that the proper crack length as a function of time was predicted by the BCL code.

KEY WORDS: dynamic photoelasticity, crack propagation, crack arrest, stress intensity factor, rectangular-DCB specimen, fracture (materials)

Dynamic crack propagation and crack arrest behavior is an important consideration in analyses such as loss-of-coolant accident (LOCA) in the nuclear pressure vessel. Analysis of dynamic crack propagation and crack arrest requires the full understanding of the relationship between the instantaneous stress intensity factor (K) and the crack velocity ($\dot{a}$), and the minimum value of the stress intensity factor (K_{I_m}) on the K versus $\dot{a}$ relationship. The K_{I_m} value is of particular importance in the analysis of crack arrest since crack arrest occurs if the stress intensity factor falls below the K_{I_m} value.

Several research groups have published results relating to the determination of such a relationship [*1-5*][2] and there appears to be some disagreement as to the dependence or independence of the K versus $\dot{a}$ relationship on specimen geometry. Direct determination of this relationship and the value of K_{I_m} for pressure vessel grade steels is extremely difficult. For this reason methods have been developed to approximate K_{I_m} values. Two such methods have been proposed to ASTM Committee E24.03 on Dynamic Testing as standard crack arrest toughness procedures and these methods are currently under examination. One of the methods was developed by Battelle Columbus Laboratory (BCL) and uses an energy balance criteria and a two-dimensional finite difference computer code to find crack arrest toughness values (K_{ID_m}) from crack jump lengths and crack speeds. Material Research Laboratory in Chicago uses the load on the specimen after arrest, the arrested crack length, and a static analysis to approximate stress intensity factor required for arrest (K_{I_a}).

One of the difficulties involved in an analysis of dynamic crack propagation and arrest is the interaction of the specimen and loading system and its effect on crack behavior. This paper describes a series of experiments conducted to determine the influence of loading system on crack jump length and stress intensity as a function of crack speed. The experimental results also were compared with a one-dimensional version of the finite difference code developed by BCL, which is described in the Abstract.

Experimental Procedure

Rectangular double-cantilever-beam specimens (R-DCB) made from

[2]The italic numbers in brackets refer to the list of references appended to this paper.

Homalite 100 (12.7 mm thick) were examined in this test. Homalite 100 is a birefringent brittle thermosetting polyester and its properties have been well documented [2,6]. The specimen geometry of the models is shown in Fig. 1. The specimens were loaded by forcing a 31-deg wedge between the loading pins with a hydraulic cylinder as shown in Fig. 2. Two different systems of pins and wedges were used in order to vary the compliance of the loading system. The stiffer of the two systems used steel pins 25.4 mm (1 in.) in diameter and 75 mm (3 in.) in length together with a 31-deg aluminum wedge. The other system used Plexiglas pins and a Plexiglas wedge of the same geometry and dimensions as the first system.

The load on the wedge was measured with a quartz load cell with a resonant frequency of 70 kHz. The crack opening displacement at the pins was monitored by a linear variable differential transducer (LVDT) with a frequency response of up to 14 kHz. The load and pin-displacement signals were recorded on an X-Y recorder and also on oscilloscopes.

Isochromatic fringe patterns during dynamic crack propagation and crack arrest phenomena were observed and recorded with a Cranz-Schardin type multiflash camera capable of photographing 16 frames at rates from 30 000 to 850 000 frames per second. Timings of 16 spark gap firings were monitored by a high frequency photodiode (Lite-Mike) and recorded on an oscilloscope. A typical set of 16 photographs showing the fringe patterns associated with high speed crack propagation is shown in Fig. 3. An enlargement of one of the photographs is shown in Fig. 4*a*. From these enlargements, the radius of the fringe loop (r_m) and the tilt (θ_m) were measured for a specific fringe loop of order N as shown in Fig. 4*b* schematically. This information was used in the three-parameter

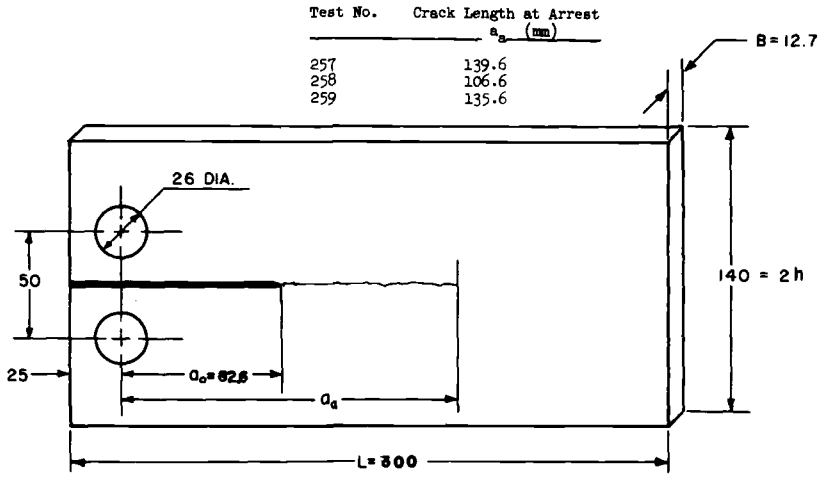

FIG. 1—*Specimen geometry for R-DCB models.*

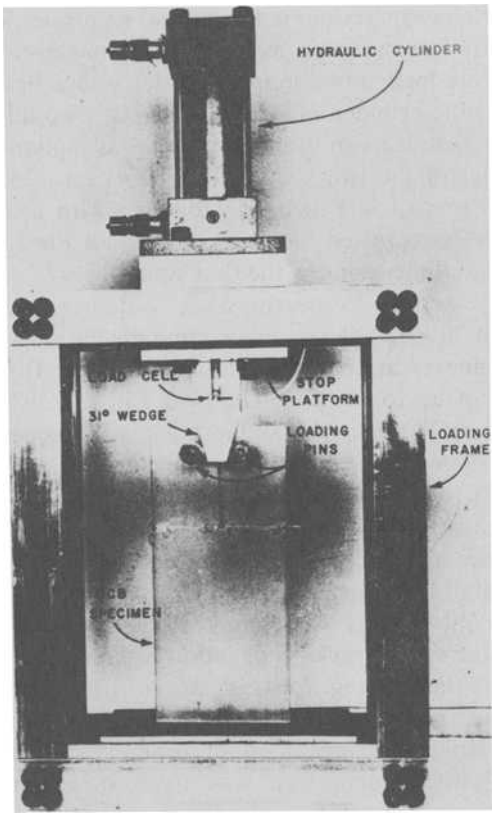

FIG. 2—*Loading system for R-DCB specimens.*

Westergaard stress function method developed by Etheridge and Dally [*7*] to obtain the dynamic stress intensity factor. In addition, crack position information was also obtained from the photographs.

Results

The results of three tests are presented in this paper. Tests 257 and 259 were run with plastic pins and a plastic wedge and Test 258 with an aluminum wedge and steel pins. The conditions for these three tests were identical in all respects except for loading pins and wedges. In all cases, the models were loaded by applying a compressive force to the wedge to a pin-displacement of 0.29 mm (0.0114 in.), then the cracks were initiated by pulling a solenoid activated saw blade across the blunted crack tip. Detailed results are presented in the following sections.

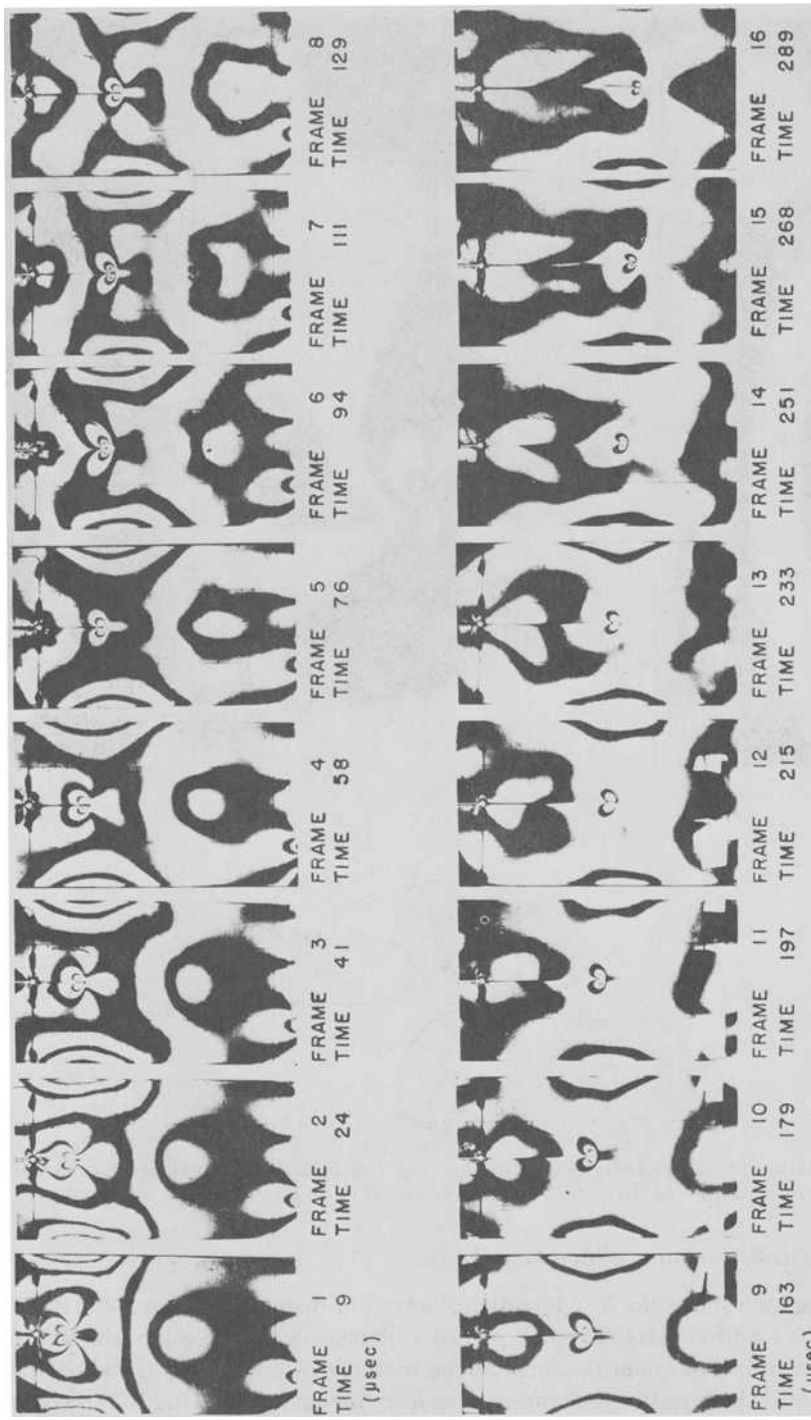

FIG. 3—*Sequence of 16 frames showing isochromatic loops associated with high velocity crack propagation in a R-DCB specimen.*

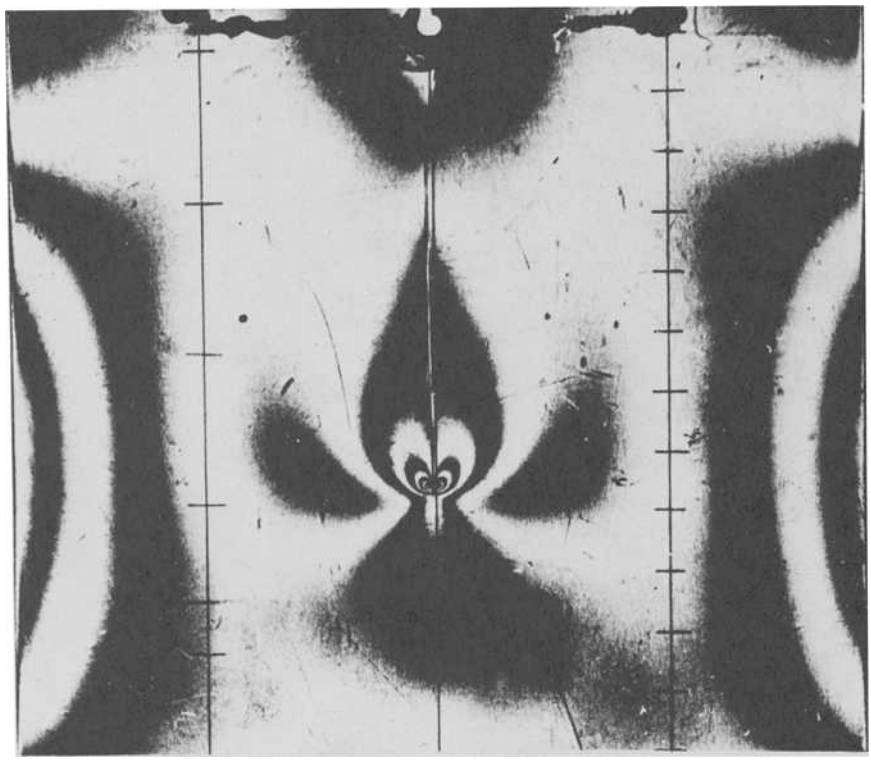

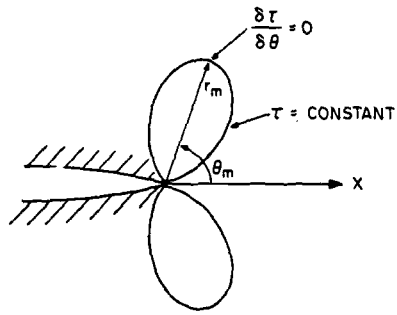

FIG. 4—(a) *Enlarged photograph showing fringe loop geometry for a propagating crack in a R-DCB specimen,* and (b) *position parameters* θ_m *and* r_m *on a fringe loop.*

Pin-Displacement and Load on Wedge

Figure 5 shows the X-Y recorder plots of pin-displacement and load on the wedge for three tests. The X-Y recorder plots were used to establish the load and pin-displacement readings at the moment of crack propagation initiation and shortly after the crack arrest since the response of the X-Y recorder was too slow to follow the rapid changes of the signals during the crack prop-

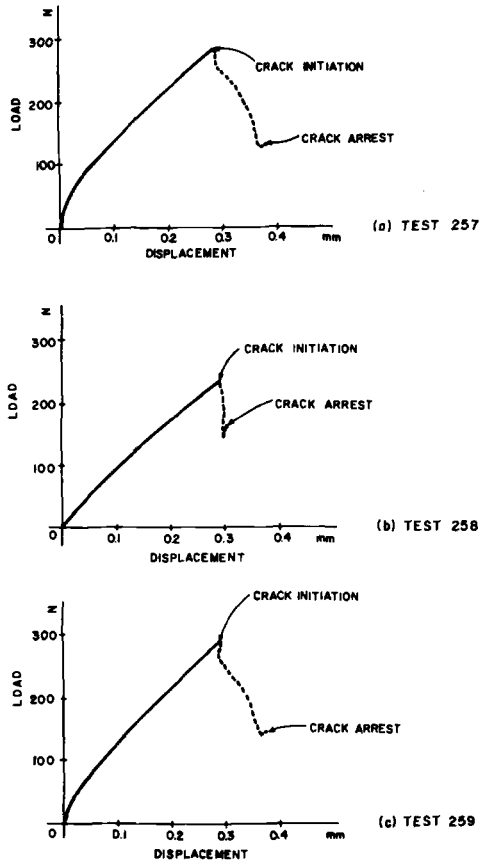

FIG. 5—*X-Y recorder plots for load versus pin displacement for three tests conducted.*

agation. The changes of the pin-displacement and the load on the wedge during the crack propagation and shortly after crack arrest were monitored and recorded on the oscilloscopes. Figure 6 shows the oscilloscope records of the load and the pin-displacement as a function of time for Tests 258 and 259. Examination of Fig. 5 shows that the pin-displacement change after the crack jump, when loaded with the steel pins and aluminum wedge, was extremely small (of the order of 0.015 mm); however, with the plastic pins and plastic wedge, the pin-displacement change increased up to 0.081 mm. The oscilloscope traces of pin-displacement shown in Fig. 6 also indicate the same result. Furthermore, these traces show that when the specimen was loaded with the steel pins and aluminum wedge system, the pin-displacement exhibited a large oscillation, but the load on the wedge showed only a small variation. On the other hand, when the specimen was loaded with the plastic pins and plastic wedge, the pin-displacement exhibited a rather gradual motion, but the load on the wedge indicated a large oscillation. The oscilloscope

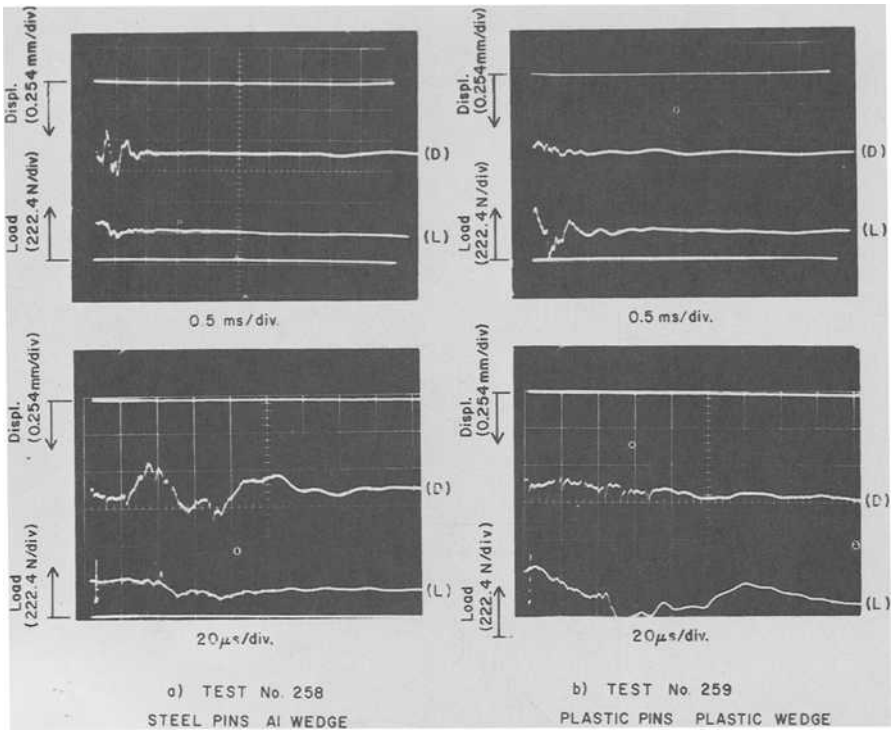

FIG. 6—*Oscilloscope traces for load and pin displacement versus time records for the two different types of tests conducted.*

traces in Fig. 6 also indicated that the oscillations on the load and the pin-displacement damped out much faster when the specimen was loaded with the stiffer system.

High Speed Photographic Observation

From the 16 photographs obtained with the Cranz-Schardin camera, the crack position and the dynamic stress intensity factor were determined. Figure 7 shows the plots of the crack position versus time from three models (Nos. 257, 258, and 259). The plots indicate that when the specimen was loaded with the plastic pins and plastic wedge (Nos. 257 and 259), the crack propagated at higher velocity (approximately $\dot{a} = 172$ m/s) and longer distance ($\Delta a = 57$ mm for No. 257 and $\Delta a = 53$ mm for No. 259) than those with the steel pins and aluminum wedge ($\dot{a} = 96$ m/s and $\Delta a = 24$ mm). Furthermore, the plots in Fig. 7 indicate that the crack reinitiation occurred in both models Nos. 257 and 259, but the crack remained arrested in the model No. 258.

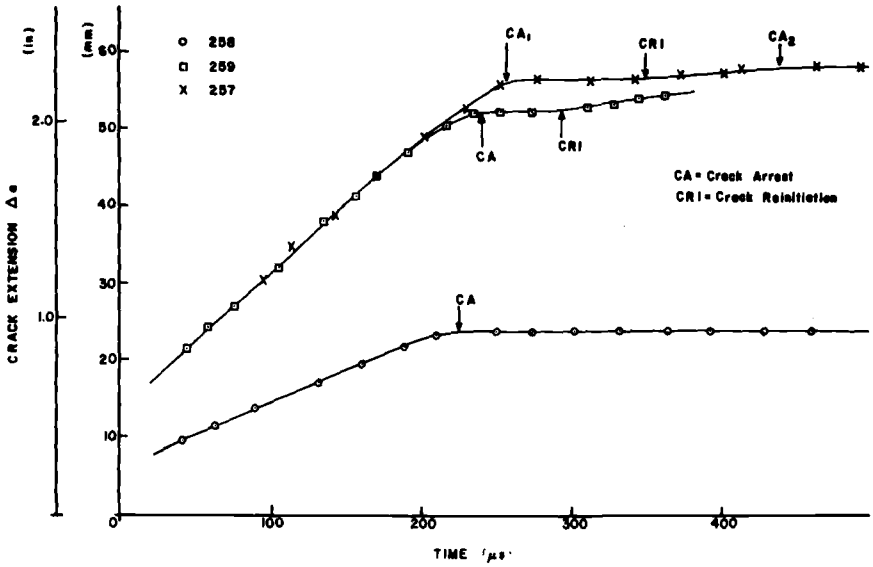

FIG. 7—*Experimentally determined crack position as a function of time for the three tests conducted.*

Figure 8 shows the plots of the instantaneous stress intensity factor K as a function of time for the three models. The arrows were placed on the curve to correspond to the time of crack arrest and crack reinitiation established from the a versus t curves in Fig. 7. It is of interest to note that in all three cases oscillation in the K values were observed. The K versus t curves for three models during the crack propagation phases did not show any significant differences and in all cases the crack arrest was observed at 225 ~ 255 μs time range; however, the major differences in the K versus t curve for two types of loading system appeared after crack arrest. The K versus t curve for Model No. 258 (with stiff loading system) shows that after the crack arrest the stress intensity factor dropped from about 0.39 MPa$\sqrt{m}$ to 0.36 MPa$\sqrt{m}$ and during the remaining observation period the stress intensity factor remained at around 0.36 MPa$\sqrt{m}$. In the case of models Nos. 257 and 259 after the crack arrest, the stress intensity factor reached 0.36 MPa$\sqrt{m}$; then started to increase again and reached a peak value of 0.41 MPa$\sqrt{m}$. In these two models a crack reinitiation occurred during the K-increase phase. The K value at the reinitiation was about 0.39 MPa$\sqrt{m}$ for both cases. The crack arrest time periods were about 90 μs for No. 257 and 55 μs for No. 259. In the case of model No. 257, a second crack arrest was observed approximately 90 μs after crack reinitiation. The K value at the second arrest was 0.39 MPa$\sqrt{m}$.

From the information presented in Figs. 7 and 8, the K versus crack velocity ($\dot{a}$) relationship is developed and is represented by the plotted points in

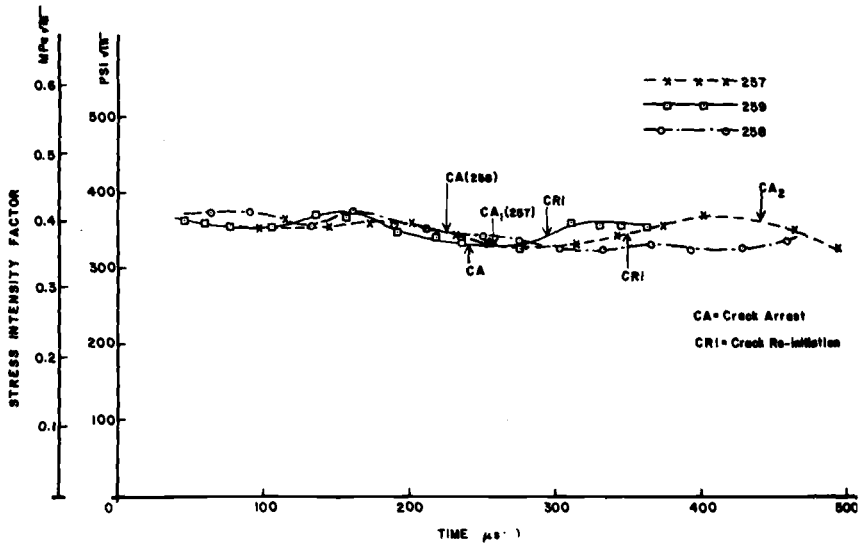

FIG. 8—*Instantaneous stress intensity factor as a function of time for the three models.*

Fig. 9. The resulting K versus $\dot{a}$ behavior from those three tests show good agreement among themselves; furthermore, these results exhibit good agreement with the K versus $\dot{a}$ relationship established with other specimen geometries [*8*]. One of these curves from SEN specimen also is shown in Fig. 9 by a solid line.

Numerical Analysis of Crack Behavior with the BCL Computer Code

Using the data presented in the previous section, a one-dimensional finite difference computer code developed by BCL was used to predict crack growth as a function of time. The computer code uses an energy balance criterion to determine crack growth behavior. The program is described in detail in Ref *4*. A two-dimensional version of this program is being proposed as one of the ASTM standard procedures for a crack arrest toughness measurement. It is noted that these computer codes assume a perfectly rigid loading fixture.

The properties of Homalite 100 including the K versus $\dot{a}$ relationship, specimen geometry and dimensions, and initial loading condition (a pin-displacement at the moment of crack initiation) were input in the computer code. Curve I in Fig. 10 shows the predicted crack position as a function of time by the BCL code. The a versus t curve shows a good agreement with the experimentally observed a versus t in model No. 258. This indicates that the steel pins and aluminum wedge system for plastic DCB specimens can be considered a fully rigid loading system. The plastic pins and plastic wedge

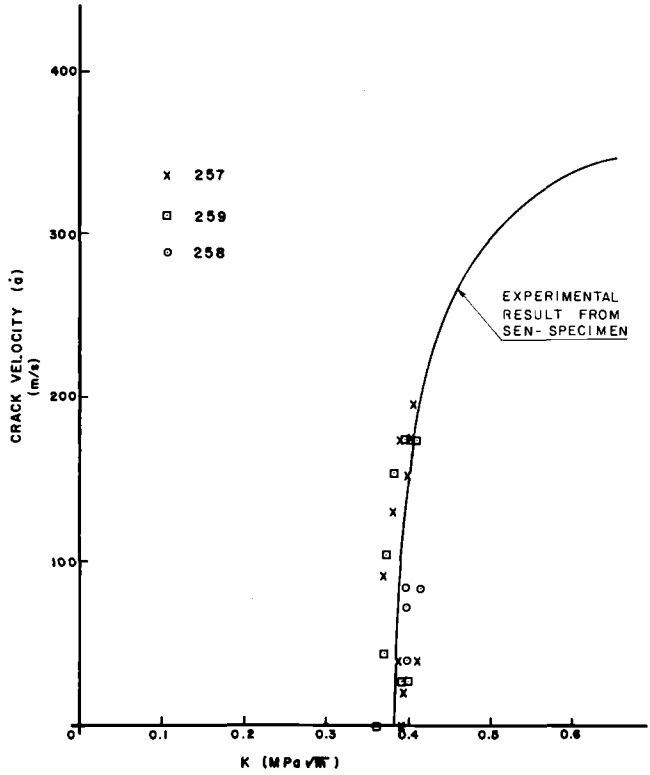

FIG. 9—K *versus* ȧ *relationship obtained from experiments conducted.*

whose modulus of elasticity is close to that of DCB specimen cannot be considered as a rigid loading system and the strong interaction between the loading system and the specimen would be observed. This may be a problem when the BCL computer code is applied to the steel DCB specimen loaded with steel pins and steel wedge since the BCL underestimates the crack jump distance by as much as a factor of two.

The additional crack growth obtained in the model when the plastic loading system was used was attributed to additional energy added to the model from the pins once the crack began propagating. A calculation was made to determine the amount of energy stored in the two loading systems in the form of both bending and Hertzian contact stresses. For the steel pins and aluminum wedge the values calculated were 6.21×10^{-5} NM (5.5×10^{-3} lb·in.) in contact and 2.94×10^{-6} NM (2.6×10^{-5} lb·in.) in bending energy. For the plastic pins and plastic wedge systems the values were 1.37×10^{-2} NM (1.21×10^{-1} lb·in.) in contact and 4.52×10^{-4} NM (4.0×10^{-3} lb·in.) in bending energy. The calculations were according to the formulae given in Ref. *9*.

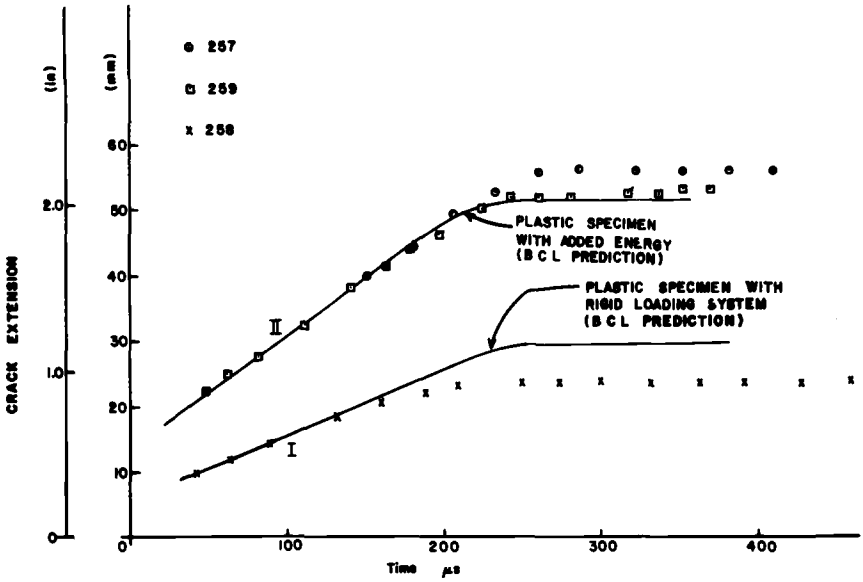

FIG. 10—*Comparison of predicted crack growth as a function of time according to BCL finite difference code with experimentally determined values.*

Using the load on the pins from the hydraulic ram and the pin-displacement during loading and assuming elastic loading, the amount of potential energy stored in the model was calculated. The results show that for the metal loading system an additional 2 percent of the potential energy in the model was stored in the wedge and pins due to contact stresses. For the plastic loading system the contact and bending energy in the loading system was equivalent to 43 percent of the potential energy in the model. If all this energy were imparted to the model as the crack propagated it would mean that K_Q for the plastic system should be 19 percent greater than for the metal system.

To permit some of this additional energy to be fed into the model in the plastic case as the crack propagates, the initial value of stress intensity factor before crack initiation was increased by 13 percent. That is, the K_Q for the plastic pins and wedge was 1.13 times as large as the K_Q for the metal pins and wedge. When this larger value of K_Q was used as input in the computer the resulting curve for crack length as a function of time is given as Curve II in Fig. 10. It is seen that the computed results now agree quite nicely with those obtained experimentally. The crack jump predicted, as well as the crack velocity are in agreement with the experimental values obtained with the plastic pins and wedge.

Summary and Conclusions

The compliance of the loading system has been shown to have a pronounced effect on the crack jump length and velocity of crack propagation in a rectangular DCB specimen.

When a very compliant loading system with plastic pins and wedge was used ($E \simeq 40\ 000$ psi), the crack jump distance and crack speed were found to be about twice those values observed for the same situation where steel loading pins and an aluminum wedge were used.

The experimental results were compared with the output from a computer program written by BCL and agreement was found to be good when energy was added to the input to simulate the energy which finds its way into the specimen from contact stresses once the crack begins to propagate.

One should be extremely careful then in predicting stress intensity factors from experimental measurements of crack jump length and crack velocity unless the loading train is extremely stiff when compared to the specimen compliance.

Acknowledgment

This work was funded in part by NRC grant No. AT(49-24)-0172. The use of the BCL Computer Code as generated by M. F. Kanninen, P. C. Gehlen, and G. T. Hahn is gratefully acknowledged.

References

[1] Kobayashi, A. S., Mall, S., and Lee, M. H. in *Cracks and Fracture, ASTM STP 601*, American Society for Testing and Materials, 1976, pp. 274-290.

[2] Kobayashi, T. and Dally, J. W. in *Fast Fracture and Crack Arrest, ASTM STP 627*, American Society for Testing and Materials, 1977, pp. 257-273.

[3] Kalthoff, J. F., Bernert, J., and Winkler, S. in *Fast Fracture and Crack Arrest, ASTM STP 627*, American Society for Testing and Materials, 1977, pp. 161-176.

[4] Hahn, G. T., Gehlen, P. C., Hoagland, R. G., Kanninen, M. F., Popelar, C., and Rosenfield, A. R., "Critical Experiments, Measurements and Analyses to Establish a Crack Arrest Methodology for Nuclear Pressure Vessel Steels," 4th Quarter Progress Report, Task 62, Battelle Columbus Laboratories, BMI-1939, Nov. 1975.

[5] Crosley, P. B. and Ripling, E. J. in *Fast Fracture and Crack Arrest, ASTM STP 627*, American Society for Testing and Materials, 1977, pp. 372-391.

[6] Kobayashi, A. S., Wade, B. G., and Bradley, W. G. in *Deformation and Fracture of High Polymers*, by Kansch, et al Eds., Plenum Press, New York, 1973, pp. 487-500.

[7] Etheridge, J. M. and Dally, J. W., "A Three Parameter Method for Determining Stress Intensity Factors from Isochromatic Fringe Loops," to appear in *Engineering Fracture Mechanics*.

[8] Kobayashi, T., Dally, J. W., and Fourney, W. L., "Influence of Specimen Geometry on Crack Propagation and Arrest Behavior," presented at the 6th International Conference on Experimental Stress Analysis, Munich, West Germany, Sept. 1978.

[9] Seeley, F. B. and Smith, J. O., *Advanced Mechanics of Materials*, 2nd ed. Wiley, New York, 1960.

F. P. Champomier[1]

Crack Propagation Measurements on Glass: A Comparison Between Double Torsion and Double Cantilever Beam Specimens

REFERENCE: Champomier, F. P., **"Crack Propagation Measurements on Glass: A Comparison Between Double Torsion and Double Cantilever Beam Specimens,"** *Fracture Mechanics Applied to Brittle Materials, ASTM STP 678*, S. W. Freiman, Ed., American Society for Testing and Materials, 1979, pp. 60-72.

ABSTRACT: A simple and rapid method of measuring crack propagation in glass was sought. Double torsion (DT) and double cantilever beam (DCB) specimens that allow K_{Ic} values as well as (K, V) diagram determinations were tested successively, using relatively large testpieces (250 by 100 by 6 mm).

In the case of DT specimens, it is shown that relaxation experiments do not require the prior determination of specimen compliance. Excellent reproducibility thus is obtained. The technique is easy to master, but the crack front profile is not taken readily into account.

Relaxation of DCB specimens reveals the important role played by the specimen compliance compared to the testing machine compliance. Experiments are not conducted as easily as in the previous case.

In both cases, it is shown that the minimum speed that can be achieved practically during a relaxation experiment on glass is of the order of 10^{-7} ms^{-1}.

Results were obtained on float glass in ambient air. They are in satisfactory agreement and compare favorably with published data.

KEY WORDS: test method, fracture mechanics, double torsion, double cantilever beam, critical stress intensity factor, crack propagation, load relaxation, float glass, fracture (materials)

Fracture mechanics methods are now used increasingly in metallurgy (fracture toughness determinations of steel and aluminum alloys are com-

[1] Ingénieur des Arts et Manufactures, Service Central de Recherche, Saint-Gobain Industries, Aubervilliers, France.

mon practice). In contrast, application of such methods to very brittle materials (glass, ceramics, carbides, etc.) has been given attention only recently and still requires development.

Yet, it appears that the fracture toughness concept is essential to characterize brittle materials (glass in particular) for which the notions of elastic limit, yield strength, or ultimate tensile strength are often unsatisfactory. Also, it is now well established [*1,2*][2] that the dynamics of crack propagation can be described adequately by the stress intensity factor, crack velocity (K, V) diagram for a material in a given environment. Practical applications include prediction of times to failure [*3,4*] and require knowledge of the (K, V) diagram up to the critical stress intensity factor, K_{Ic}, that leads to catastrophic failure. In particular, accurate determination of n, the slope of log V versus log K_I, is essential for correct service life calculations [*5*].

Glass is ideally suited to fracture mechanics theories since it can be considered as an homogeneous and purely elastic medium in most instances. Moreover, very long service life (usually 10 years) is required in many building applications. In view of these considerations, it appears desirable to develop routine procedures of (K, V) diagram determination. A precise, yet simple and rapid method would supplement the usual bend tests advantageously, since the results of such tests have only relative meaning.

This paper describes the experiments undertaken in our laboratories with the aim of comparing double torsion (DT) and double cantilever beam (DCB) specimens for rapid (K, V) diagram determination of industrial glass.

Double Torsion Technique

This technique has been designed by Outwater [*6*] and developed by Evans [*7,8*]. The specimen is a rectangular plate (Fig. 1).

Since large samples of industrial glass of practically constant thickness, t_o, are easily available, appreciable dimensions were chosen (250 by 100 by 6 mm). The specimen is supported on two parallel rollers or else on four steel balls (12 mm in diameter). The load is applied by a loading ball (12 mm in diameter) fixed to the crosshead of a testing machine above the specimen axis. To ensure that the crack propagates along this axis, the lower face of the specimen bears a cutting wheel score. The axial fissure caused by this score shows a fairly constant depth (typically 300 μm) which is determined by a microscope measurement after test completion. Crack initiation is performed by thermal shock, that is, by the sudden application of a small red-hot glass bead on the score line in the vicinity of point M.

The way the specimen is supported (rollers or balls) has no appreciable

[2]The italic numbers in brackets refer to the list of references appended to this paper.

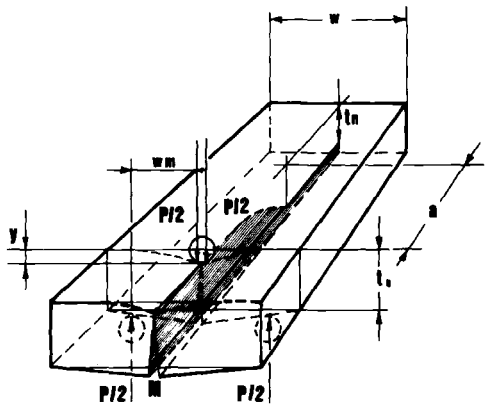

FIG. 1—*DT specimen configuration.*

influence on numerical results. In neither case, however, could the weight of the specimen be satisfactorily accounted for. Nevertheless, care was taken to use good quality rollers or to keep the loading ball and two supporting balls in a plane perpendicular to the specimen axis. Although the exact loading points slightly change with the deflection, y, this effect is negligible and w_m was always taken as half the distance between the supporting balls or rollers.

The critical stress intensity factor, K_{Ic}, may be defined in various ways. The most precise way involves stipulating the corresponding crack speed, V (usually between 0.1 and 1 ms^{-1}) [*4*]. The DT specimen for which V is proportional to the crosshead speed, $\dot{y}$, through [*8, 9*]

$$\dot{y} = \text{BPV}, \quad B = \frac{3\,w_m^2}{wt_o^3 G}, \quad G = \text{shear modulus of test material}$$

is particularly convenient here since the critical value, P_c, usually can be estimated from the expected K_{Ic} value [*8, 9*]:

$$K_{Ic} = \left[\frac{3(1+\nu)}{wt_o^3 t_n}\right]^{1/2} w_m P_c, \quad \nu = \text{Poisson's ratio of test material}$$

Table 1 gives results obtained on float glass from three different European plants.

In order to achieve a crack speed in the neighborhood of 0.4 ms^{-1}, $\dot{y}$ was chosen equal to 20 mm/min. At such a speed, the test leads to the complete breakage of the specimen, but K_{Ic} is estimated quite accurately. There appears to be no significant difference between the three glasses tested, the compositions of which were very similar.

TABLE 1—K_{Ic} *results for float glass. DT specimens in ambient laboratory air.* $\nu = 0.25$, $w_m = 0.040$ *m, initial crack length* $\simeq$ *0.10 m.*

Plant	Scored Face	K_{Ic} MNm$^{-3/2}$
A	Top	0.750
	T	0.746
	T	0.744
	Bottom (Sn)	0.746
	B	0.751
	B	0.750
B	T	0.759
	T	0.750
	T	0.749
	B	0.735
	B	0.741
	B	0.746
C	T	0.745
	T	0.755
	T	0.755
	B	0.740
	B	0.752

The mean value for K_{Ic} is 0.748 MNm$^{-3/2}$ with an overall standard deviation of 0.006 MNm$^{-3/2}$. This is almost identical to Wiederhorn's result on microscope slides (DCB specimens in dry nitrogen, 300 K): 0.749 MNm$^{-3/2}$ [*10*].

Relaxation tests were also conducted in ambient laboratory air (20°C, 40 percent relative humidity). To keep the experimental procedure simple, it appeared desirable to avoid crack growth rate monitoring through displacement gages. In such a case, compliance calibration, as described by Evans [*7,8*], is suitable but requires additional experiments under perfectly identical conditions (as to the specimen size and position and to the loading system stiffness). The use of the following equation to calculate V during a relaxation test eliminates this need

$$V = -\frac{P_i P_f (a_f - a_i)}{P_i - P_f} \frac{1}{P^2} \frac{dP}{dt}, \quad t = \text{time},$$

indexes i and f refer to initial and final conditions. The only requirement here is the measurement of a_i and a_f. It is realized that this can cause a problem in the case of nontransparent materials despite the fact that the specimen is available for manipulation both in initial and final conditions.

The preceding formula is derived easily under the usual assumption that the compliance, C, is a linear function of crack length, a, ($C = Ba + D$) [*7–9*]. It was checked against compliance calibration as well as actual crack length measurements made during relaxation experiments; the agreement proved excellent.

It is of primary interest to determine (K, V) diagrams in the low speed region. The question was raised as to whether the DT relaxation technique was suitable for this purpose. To answer, the following approach was considered [9]. If V can be represented by AK_I^n (A and n constant) [2–5], one may write

$$V = A\alpha^n P^n, \quad \alpha \text{ constant for relaxing DT specimens}$$

$$= -\frac{y}{B}\frac{1}{P^2}\frac{dP}{dt}, \quad \begin{array}{l} y = \text{deflection at the loading point} \\ \quad = \text{constant} \end{array}$$

Integrating and rearranging yields

$$\left[\frac{V}{V_i}\right]^{(n+1)/n} = \frac{1}{1 + \dfrac{(n+1)V_i t}{a_i + D/B}}$$

In the case of glass, n can be estimated to be around 14 [7] and therefore, as a first approximation, the aforementioned formula describes a hyperbola [9]. Numerically, it is clear that, in order for the speed to drop from V_i to $V_i/10$, $[(n+1)V_i t]/(a_i + D/B)$ must equal 10.8. As $(a_i + D/B)$ cannot be much lower than 0.05 m, this entails $V_i t \simeq 0.036$ m. In other words, relaxation from 10^{-6} to 10^{-7} ms^{-1} takes several hours (10 in the present case) whatever the specimen geometry and machine stiffness (machine compliance is present implicitly in D and thus partly controls time and crack growth during the experiment). As longer tests seem impractical and, in any case, require drastic precautions (humidity, temperature, machine zero, and calibration need to be kept constant), the minimum speed that can be achieved, at least in routine testing, appears to be of the order of 10^{-7} ms^{-1}.

As an example, Fig. 2 shows results obtained on float glass from Plant C. Points from three different relaxation experiments are plotted. The longest relaxation lasted 6 h. The solid line represents the least square fit of an expression of the form

$$\log V = n \log K_I + \log A,$$

that is,

$$\log V = 14.3 \log K_I - 86.4$$

It should be emphasized that no correction allowing for crack profile has been introduced in the results presented here.

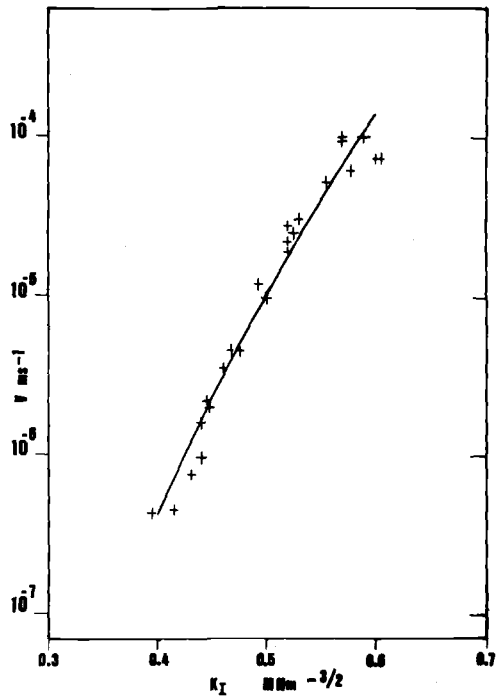

FIG. 2—(K, V) *diagram for float glass (Plant C). Relaxation of DT specimens in ambient laboratory air. Scored face is float top side.*

Numerous other experiments were conducted and practically all experimentally determined crack velocities were found to fall within a factor two of the most probable value. This scatter appears quite reasonable considering that the graphic determination of a slope (dP/dt) is an intrinsically imprecise operation. According to our measurements, the best value for n would be 14, but it should be kept in mind that this parameter is extremely sensitive to small variations in the data.

Double Cantilever Beam Technique

Plates of float glass can also be turned into DCB specimens (Fig. 3).

Loading holes are formed by diamond drills. In order to confine the crack to the plane of symmetry, the specimen is scored on *each* face. Indeed, the crack is found to deviate readily if not guided by such a measure. Initial fissuration is performed again by thermal shock, eventually extended in double torsion, the crack profile being straightened in DCB mode.

The torque caused by the weight of a DCB specimen, loaded on a verti-

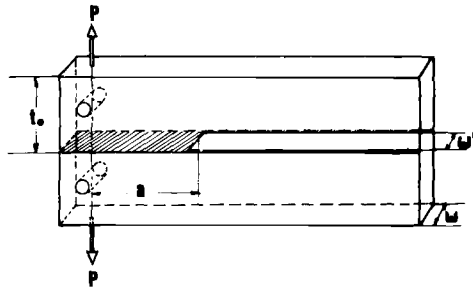

FIG. 3—*DCB specimen configuration.*

cal testing machine, normally is balanced by that of the force exerted by the pin located in the upper loading hole. Depending on specimen dimensions, this force may prove considerable. Therefore, it was useful to support the specimen by an auxiliary bearing located under the end opposite the holes. The vertical position of the bearing is adjusted so that the specimen is horizontal while only resting on the bearing and upper loading pin; the loading force is then considered to be zero.

K_{Ic} tests were conducted on two specimen geometries (250 by 100 by 6 mm and 250 by 50 by 6 mm). Various crack lengths were used but, to follow Wiederhorn's conclusions [*11*], they were always greater than 1.5 t_o. Rapid loading invariably resulted in the complete breakage of the specimen and gave the K_{Ic} values listed in Table 2. The following equation was used [*11,12*]

$$K_I = \left[\frac{12\,F'(a)}{ww'{t_o}^3}\right]^{1/2} P$$

where $F'(a) = a^2 + 1.32\,at_o + 0.542\,{t_o}^2$.

Typical loading speeds were around 5 mm/min, leading to loading times of 2 to 3 s. In contrast to DT tests, no definite V value can be attributed to these experiments; it nevertheless appears that a correct estimation of K_{Ic} is obtained.

Relaxation experiments were performed using essentially the method and formulae of Virkar and Gordon [*12*]. These authors pointed up that machine stiffness must be taken into account and a loading system that is not hard enough leads to catastrophic failure. Indeed, during the relaxation of a DCB specimen, K_I is proportional to $P\,[F'(a)]^{1/2}$ where P is a decreasing function of time while a, and hence $[F'(a)]^{1/2}$, increases with time. Depending on machine compliance as compared to specimen compliance, the product may prove to increase or decrease with time. As stated by Jones and West [*13*], a perfectly soft machine will always produce catastrophic failure whereas an ideally hard machine will lead to crack arrest.

TABLE 2—K_{Ic} *results for float glass (Plant C). DCB specimens in ambient laboratory air.*

Specimen Dimensions	K_{Ic} MNm$^{-3/2}$
250 by 100 by 6 mm	0.76
	0.76
	0.69
	0.69
	0.79
	0.72
	0.72
250 by 50 by 6 mm	0.78
	0.74
	0.73
	0.76
	0.75
Mean value	0.74
Standard deviation	0.03

The intermediate case is also of interest since a correct balance between machine and specimen compliances results in propagation at nearly constant K_I. For a fixed deflection, the DCB specimen then behaves like a tapered double cantilever beam (TDCB) specimen under constant load. A relaxation experiment thus yields one and only one point of the (K, V) diagram but with high precision.

Conditions for nearly constant K_I propagation may be derived in the following way. Let X be the total deflection

$$X = [C_M + C(a)] \cdot P = \text{constant}$$

where

C_M = machine compliance,
$C(a)$ = specimen compliance [*12*] $\simeq [24/(Ewt_o^3)]\, F(a)$, and
E = Young's modulus of test material.

Differentiating X with respect to time, t, and introducing the result in the expression of dK_I/dt yields

$$\frac{dK_I}{dt} = K_I \frac{F''(a)}{2F'(a)} - \left[\frac{F'(a)}{\frac{Ewt_o^3}{24} C_M + F(a)}\right] \frac{da}{dt}$$

Now, $F(a)$ is conveniently approximated by $1/3\ (a + 0.66\ t_o)^3$, $F'(a)$ by $(a + 0.66\ t_o)^2$, ... [*11*]. Hence,

$$\frac{dK_I}{dt} \simeq -K_I \left[\frac{2C(a) - C_M}{[C_M + C(a)](a + 0.66\ t_o)}\right] \frac{da}{dt}$$

Constant K_I propagation will therefore occur if, during an appreciable length of time, $2C(a) \simeq C_M$. While, strictly speaking, this relation is true for only one a value, it holds approximately over a fairly large domain.

The value of C_M for the particular experimental arrangement used was $\simeq 1 \times 10^{-6}$ mN^{-1} and it was found that propagation at nearly constant K_I occurred during relaxation of the specimens 250 by 100 by 6 mm. In fact, with this geometry, when a increases from 8 to 15 cm, $C(a)$ changes from $\simeq C_M/4$ to $\simeq C_M$, but this variation is small enough to retain nearly constant K_I propagation.

In such a case, (K, V) diagram determination implies successive experiments at various K_I values. Following the crack optically allows precise V measurements, although the usual V formula (involving the estimation of dP/dt) is still applicable.

To obtain crack arrest during relaxation, it appeared easier to modify $C(a)$ rather than C_M and, consequently, specimens half as thick as those previously used (250 by 50 by 6 mm) were tested successfully in this manner.

Data obtained by both methods are plotted on Fig. 4; they appear entirely consistent.

An argument very similar to that used for DT specimens, allows an estimation of the lowest velocity attainable by relaxation of a DCB specimen. The best conditions for low speed measurements involve using a very stiff machine. Hence, in this case, $C_M \ll C(a)$

$$\frac{dK_I}{dt} \simeq -K_I \left(\frac{2}{a + 0.66\, t_o}\right) \frac{da}{dt}$$

Assuming $da/dt = V = AK_I{}^n$, leads to

$$-\frac{dV}{V^2} = \frac{2n}{a + 0.66\, t_o}\, dt$$

As an approximation, integration may be performed considering $(a + 0.66\ t_o)$ to be constant

$$\frac{V}{V_i} = \frac{1}{1 + \dfrac{2nV_i t}{a + 0.66\, t_o}}$$

Taking $(a + 0.66\ t_o) = 0.05$ m, $n = 14$, relaxation from 10^{-6} to 10^{-7} ms^{-1} is found to last 4.5 h which is only slightly better than the DT result.

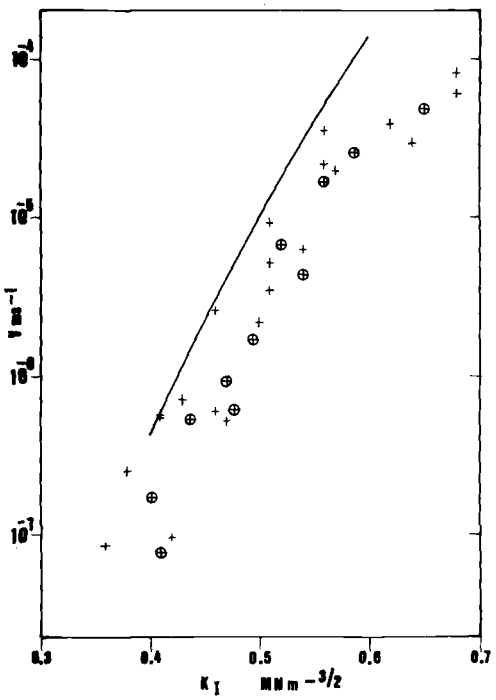

FIG. 4—(K, V) *diagram for float glass (Plant C). DCB specimens in ambient laboratory air. Specimen dimensions:* +250 by 100 by 6 mm (*constant* K_I *propagation*), ⊕250 by 50 by 6 mm. *Solid line represents DT results.*

Discussion

DT and DCB specimens have been proved to yield (*K*, *V*) diagrams in essentially the same range. Their potentials are, *a priori*, very similar:

1. Rapid loading leads to catastrophic failure and determines K_{Ic}.
2. Relaxation experiments at constant deflection yield (*K*, *V*) values from $V \simeq 10^{-7}$ to $\simeq 10^{-4}$ ms^{-1}.
3. If necessary, additional points in the vicinity of 10^{-3} ms^{-1}, may be obtained by the incremental method [7], not discussed here, for the DT specimen, or in the constant K_I mode for the DCB configuration.

However, the results obtained must be examined carefully and compared to determine the ultimate value of the two methods.

From an experimental point of view, the simplest method uses the DT specimen. Little or no machining is required for specimens, the specimen fixture is simple and, above all, numerical calculations are straightforward.

The DT specimen, however, appears to have two major drawbacks. The first lies in connection with the crack front curvature. The strength of

materials analysis of the DT specimen [*8*] assumes that the crack front is orthogonal to the plane of the specimen, which is not true. Consequently, velocity measurements usually refer to the leading edge of the crack along the lower face [*7,8*], as is the case for the results presented here. It nevertheless appears quite impossible to reconcile, within a simple analysis, the three following considerations: (a) stress intensity is independent of crack length [*6–8.15*], (b) crack shape is independent of crack length [*6–8,14,15*], and (c) crack propagation is orthogonal to the crack front [*14,15*]. Attempts to solve this problem have been made [*14,15*], but should be pursued if all ambiguities are to be resolved.

Evans [*7,8*] came to the conclusion that measured velocities should be divided by a factor Φ. Accordingly, in most of Fig. 2, plotted points may be considered too high by a factor of five. Indeed, examination of Fig. 4 discloses that DT velocities are consistently greater than the DCB results by a factor of this order of magnitude. This correction nevertheless has been questioned recently [*14*], although no definite answer was given to the problem.

The second point that casts a shadow on DT results is the problem of the rupturing mode. Crack growth may not occur in pure Mode I opening [*8*]. Additional studies need to be performed to establish to what amount is Mode III failure present.

In case of K_{Ic} tests, these points are not so important, as proved by the good agreement between values obtained with the DT and DCB techniques. Still, the DT specimen has the considerable advantage of allowing the simultaneous determination of a precise reference velocity.

The DCB specimen does fracture in pure Mode I and has a reasonably straight crack front. This is theoretically satisfying. However, data in Fig. 4 are definitely more scattered than in Fig. 2, and K_{Ic} results show a similar trend. It is felt that this scatter is primarily due to uncertainties in measured K_I values. In the DCB case, K_I is a function of crack length, a; this is undoubtedly a reason for poorer precision in K_I determination during relaxation or even in rapid loading tests. In such a case, data may be best fitted by straight lines using the method of least squares and minimizing the error along the log K_I axis [*1*].

This gives additional value to experiments conducted at nearly constant K_I. It is felt that K_I as well as V are determined more accurately in this manner than in conventional relaxation experiments.

Applying a constant moment on each arm of a DCB specimen converts it into the so-called modified DCB specimen [*16*]. In this case, K_I turns out to be independent of crack length. Despite the potential advantages of this result, the evaluation of such a configuration was not undertaken as its experimental complexity seems to render it unsuitable for routine testing.

In view of the aforementioned considerations, it appears that DT and DCB specimens are practically equivalent and can be used indifferently as

a matter of convenience for the experimenter. However, the questions raised in the preceding discussion should be resolved before either method is promulgated in a formal standard.

Conclusion

Experiments described here were undertaken with the aim of defining a simple, rapid, and inexpensive method of determining K_{Ic} values as well as (K, V) diagrams of industrial glass. Therefore, an elaborate set up involving displacement gages was rejected and instead, attention was focused on crack length evaluation through indirect compliance determination during specimen relaxation. This appears possible because first, glass can be considered as a homogeneous and purely elastic material, and second, glass is a transparent medium.

DT and DCB techniques were tested in parallel. It was demonstrated that they are potentially equivalent for routine determination of K_{Ic} values and (K, V) diagrams. Because of its simplicity, the DT specimen appears very attractive. Reproducibility is also excellent. Uncertainties concerning the effect of crack front shape on crack growth remain and should be resolved if the specimen is to be used in absolute standard testing.

The DCB specimen is not as easy to use. The geometry implies that K_I is a function of crack length, giving rise to more complicated calculations and poorer reproducibility. In this case, however, interaction between machine and specimen compliances plays an important role in relaxation experiments and may be taken advantage of since nearly constant K_I propagation may be obtained.

Acknowledgments

The writer is indebted to P. Fournier for experimental work as well as helpful discussions on the subject reported here. The financial assistance provided by the Délégation Générale à la Recherche Scientifique et Technique is also acknowledged.

References

[1] Wiederhorn, S. M., *Journal of the American Ceramic Society*, Vol. 50, No. 8, 1967, pp. 407-414.

[2] Freiman, S. W., *Ceramurgia International*, Vol. 2, No. 3, 1976, pp. 111-118.

[3] Wiederhorn, S. M., *Journal of the American Ceramic Society*, Vol. 56, No. 4, 1973, pp. 227-228.

[4] Wiederhorn, S. M., in *Proceedings*, 10th International Congress on Glass, Vol. 11, 1974, pp. 1-15.

[5] Wilkins, B. J. S. and Simpson, L. A., *Journal of the American Ceramic Society*, Vol. 57, No. 11, 1974, p. 505.

[6] Outwater, J. O. and Gerry, D. J., "On the Fracture Energy of Glass," U.S. Naval Research Laboratory, Contract NONR 3219(01)X, Report AD 640 848, 1966.
[7] Evans, A. G., *Journal of Material Science*, Vol. 7, No. 10, 1972, pp. 1137-1146.
[8] Williams, D. P. and Evans, A. G., *Journal of Testing and Evaluation*, Vol. 1, No. 4, 1973, pp. 264-270.
[9] Fournier, P. and Naudin, F., *Revue de Physique Appliqueé*, Vol. 12, No. 5, 1977, pp. 797-802.
[10] Wiederhorn, S. M., *Journal of the American Ceramic Society*, Vol. 52, No. 2, 1969, pp. 99-105.
[11] Wiederhorn, S. M., Shorb, A. M., and Moses, R. L., *Journal of Applied Physics*, Vol. 39, No. 3, 1968, pp. 1569-1572.
[12] Virkar, A. V. and Gordon, R. S., *Journal of the American Ceramic Society*, Vol. 59, No. 1-2, 1976, pp. 68-71.
[13] Jones, A. T. and West, A. J., *Engineering Fracture Mechanics*, Vol. 9, No. 1, 1977, pp. 5-15.
[14] Virkar, A. V. and Gordon, R. S., *Journal of the American Ceramic Society*, Vol. 58, No. 11-12, 1975, pp. 536-537.
[15] Trantina, G. G., *Journal of the American Ceramic Society*, Vol. 60, No. 7-8, 1977, pp. 338-341.
[16] Freiman, S. W., Mulville, D. R., and Mast, P. W., *Journal of Materials Science*, Vol. 8, No. 11, 1973, pp. 1527-1533.

L. M. Barker[1]

Short Bar Specimens for K_{Ic} Measurements

REFERENCE: Barker, L. M., **"Short Bar Specimens for K_{Ic} Measurements,"** *Fracture Mechanics Applied to Brittle Materials. ASTM STP 678.* S. W. Freiman, Ed., American Society for Testing and Materials, 1979, pp. 73-82.

ABSTRACT: The new short rod fracture toughness specimen with a circular cross section has already been used successfully for K_{Ic} measurements on a wide variety of materials, including brittle nonmetals. Now, a rectangular shaped "short bar" specimen which is comparable in every respect to the short rod has been developed and tested. The short bar dimensions were selected so that the geometrical constant relating K_{Ic} to the peak load in the experiment should be the same for both short rod and short bar configurations, according to a simplified compliance calculation. Careful comparison testing of short rod and short bar specimens of aluminum, aluminum oxide, and fused quartz have shown no experimentally significant difference in the geometrical constant. Therefore, these tests indicate that the short rod and short bar specimens can be used interchangeably, with no difference in the equation relating the peak load to K_{Ic}.

KEY WORDS: crack propagation, fracture tests, notched specimens, toughness, fracture (materials)

A new short rod fracture toughness specimen (Fig. 1) has been introduced recently [*1-5*].[2] The advantages of testing for the plane strain critical stress intensity factor (K_{Ic}) with the short rod specimen include its economical use of specimen material, the fact that a stable crack is obtained in the specimen as a matter of course during the test for K_{Ic}, the dependence of K_{Ic} on the peak load alone (no measurement of crack length is necessary), the simplicity of the data reduction, and the applicability of the specimen to both ductile and brittle materials.

Although the cylindrical shape of the short rod specimen has an advantage in ease of fabrication in many instances, a rectangular shaped specimen with similar test characteristics would often be easier to make. There-

[1] Staff consultant, Terra Tek, Inc., Salt Lake City, Utah 84108.

[2] The italic numbers in brackets refer to the list of references appended to this paper.

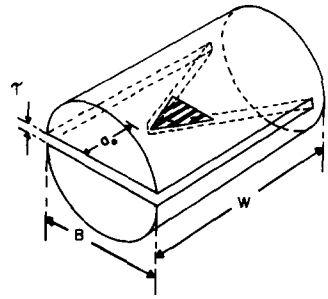

FIG. 1—*Short rod specimen.*

fore, a "short bar" rectangular shaped fracture toughness specimen (Fig. 2) has been designed to have the same testing characteristics as the circular short rod specimen. This paper first briefly reviews the short rod/short bar test methods, and then presents the short bar design considerations which give it the same characteristics as the short rod. The results of carefully controlled tests which have shown that the short bar calibration constant can be considered the same as that of the short rod then are described. The K_{Ic} values obtained by the short rod and short bar tests also are compared with published values for the same materials.

Test Methods

The short rod and short bar specimens can be loaded by machining shallow grip grooves in the face of the specimen and using grips to pull the specimen halves apart [*1*]. Alternatively a thin inflatable bladder (called a "flatjack") can be placed inside the slot in the mouth of the specimen. Inflating the flatjack then brings it into contact with the inside of the slot, thus loading the specimen in proportion to the pressure in the flatjack [*4*]

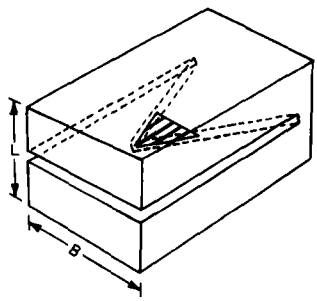

FIG. 2—*Short bar specimen.*

(Fig. 3). Note that no grip grooves are required for flatjack loading of specimens.

The crack growth from the point of the V-shaped slot in the specimen is initially stable, even for the most brittle materials. Thus, a real crack is obtained during the initial loading of the specimen, and an ever-increasing load is required for continued crack growth until the crack reaches a certain critical length, a_c. Thereafter, the load to produce further crack growth decreases. It is shown in Ref *1* that a_c depends upon the specimen geometry, but is independent of the specimen material, provided only that the specimen behaves according to linear elastic fracture mechanics (LEFM) principles. Thus, once a particular geometry and loading configuration has been calibrated, the crack location at the time of the peak load is a known constant, and the equation for K_{Ic} becomes [*4*]

$$K_{Ic} = A_F P_c \sqrt{B} \tag{1}$$

for the case of short rod specimens loaded by the flatjack method. In Eq 1, P_c is the peak pressure in the flatjack during the test, B is the specimen diameter, and A_F is a dimensionless constant of the specimen geometry and loading configuration.

Short Rod Dimensions and Calibration for Flatjack Loading

Short rod specimens can be scaled to any size without affecting the dimensionless calibration constant, A_F, provided the specimen behavior is still linear elastic. The dimensions of the calibrated short rod specimen configuration, in terms of the diameter, B, are

$$W/B = 1.500 \pm 0.006$$
$$\tau/B = 0.030 \pm 0.002$$
$$a_o/B = 0.531 \pm 0.006 \text{ (for straight slots)}$$
$$a_p/B = 0.482 \pm 0.002$$
$$\theta = 55.2 \pm 0.5 \text{ deg}$$

The dimensions are labeled in Fig. 4, except for τ, which is the slot thickness. The dimension a_p is the height of the flatjack which is inserted into the sawed slot. For specimens of these dimensions it has been found experimentally that a_c/B is about 0.85 for both grip-loaded and flatjack-loaded short rod specimens, although there is no obvious reason why a_c should be the same in both cases.

The specimen's calibration constant, A_F in Eq 1, is of course dependent upon the particular loading configuration used in the test. The specimen has been calibrated using flatjacks which uniformly pressurize the entire inside of the specimen slot to a scaled depth of 0.467. This is less than

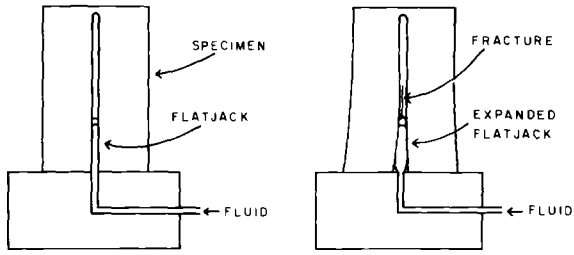

FIG. 3—*Flatjack method of loading specimens. In* (a), *the specimen is seated over the flatjack. In* (b), *fluid pressure in the flatjack is producing fracture. The specimen deflection is greatly exaggerated.*

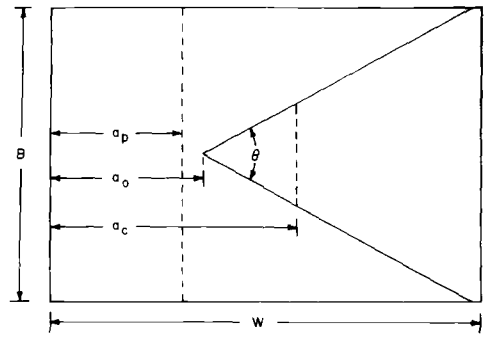

FIG. 4—*Short rod and short bar dimension nomenclature.*

a_p/B by an amount equal to $\frac{1}{2}\tau/B$, because the end of the flatjack has the shape of a half-cylinder, such that it contacts the inside of the slot only to a point which is half of the slot thickness less than the full height of the flatjack. The flatjack dimensions are B by a_p, and its thickness is τ. Since it is difficult to maintain a constant flatjack contact area in specimens that require relatively large mouth opening displacements to produce fracture, the flatjack method of loading has been restricted to relatively brittle, low-toughness materials such as ceramics, tungsten carbides, glass, and bearing steels.

Figure 4 depicts a specimen with slots having straight bottoms. Many such specimens have been tested, while many others have had their slots cut by letting them come straight down onto a circular saw blade, such that the resulting slots have a curvature equal to that of the periphery of the saw blade. It has been found experimentally that the straight-slotted and curved-slotted specimens have the same calibration constant if the latter are made so that their slot bottoms are tangent to the straight-slotted

configuration at the distance a_c from the specimen mouth, as indicated in Fig. 5.

For the specimen dimensions and for the aforementioned flatjack loading, the calibration constant has been evaluated as

$$A_F = 7.51 \tag{2}$$

The calibration is based on two sets of experiments, the first of which was used to evaluate the calibration constant for grip-loaded short rod specimens, as detailed in Ref *1*. The second set of experiments consisted of a large number of tests on various kinds of tungsten carbide, alumina, and fused quartz. In these experiments, A_F was adjusted to cause flatjack-loaded short rod specimens to produce the same K_{Ic} as grip-loaded short rod specimens.

Improvements in calibration are undoubtedly possible by direct accurate measurements or calculations of the compliance versus crack length relation, or both, so that the calibration can be determined from basic principles rather than from comparison testing.

Short Bar Specimen Design

Since the short rod specimen configuration has already proved valuable for testing a wide range of materials, and since the calibration of the short rod has been established reasonably well, it would appear valuable to design the short bar specimen to have the same characteristics and calibration as the short rod. This was accomplished by making the plan view of the short bar identical to that of the short rod, and by keeping all of the specimen proportions the same as those listed in the previous section. Having fixed these aspects of the short bar specimen configuration, only the specimen height, L, (Fig. 2) remained to be assigned. So that the short bar specimen would have nearly the same characteristics and calibration as the short rod, L was chosen so that the compliance of the two specimens would be essentially the same for any given crack length, a. By consulting the beam bending equations in Roark [*6*] for both semicircular and

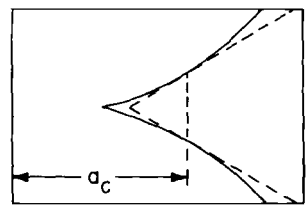

FIG. 5—*Straight-slotted and curved-slotted specimen configurations.*

rectangular cross-section beams, it was found that the compliances should be equal if the scaled height were given by

$$L/B = 0.870 \tag{3}$$

Assuming the relation of Eq 3 does indeed make the compliances of the two specimen types essentially equal for equal crack lengths, the first and second derivatives of the compliance with respect to the crack length should also be equal. Thus, the relation between K_I and the load applied to the specimen should be the same for both configurations, and the crack location at peak load also should be the same. Therefore, the calibration constant, A_F, in Eq 1 should be the same for the two specimen types, assuming equivalent loading.

Equation 3 was derived under the assumption that the specimen mouth opening can be calculated by approximating half of either specimen configuration as a cantilever beam of uniform cross section whose length was equal to the distance from the front of the specimen to the crack tip (Fig. 6). It also was assumed that the saw-cut thickness, τ, could be considered to be zero for purposes of the calculation. The situation is actually more complicated because the specimen arms are not cantilevered perfectly at the crack tip—the width of the crack front is much less than the width, B, of the specimen. Furthermore, the saw-cut thickness is not zero, and because the cracked surfaces have had no material removed by the saw cut, the beam cross section is not quite constant. Therefore, an experimental verification of the essential equivalence of the short rod and short bar specimens was considered essential.

Experiments

The short bar fracture toughness specimen configuration was tested using 7075-T651 Al, AD-94 Al_2O_3 (a 94 percent alumina (Al_2O_3) product of Coors Porcelain), and fused quartz. In order to assure material uniformity, both the short bar and short rod specimens were cut from single

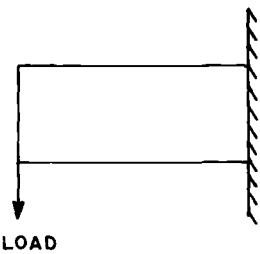

FIG. 6—*Beam-bending approximation assumed for the compliance equalization calculation.*

19-mm diameter rods of each specimen material. The crack orientation was always in the C-L direction as defined by the ASTM Test for Plane-Strain Fracture Toughness of Metallic Materials (E 399-76). The B-dimension of all specimens was 12.7 ± 0.025 mm (0.500 ± 0.001 in.). The other dimensions follow from the dimension proportions listed previously, with the exception of a_o/B. Because the curved-slot configuration was used with a radius of curvature of $5B$, a_o/B was made equal to 0.500 to achieve the specimen equivalency discussed previously (see Fig. 5).

The behavior of the two specimen types during the tests seemed to be the same, with the possible exception that in aluminum the crack initiation at the point of the V seemed to occur at a slightly higher "pop-in" load, on the average, in the short bar specimens. In both aluminum specimen types, the crack advanced in a number of small audible jumps. It seemed to become "pinned" at several crack locations near a_c, and the degree of pinning at different positions varied widely even within a single specimen. This caused larger standard deviations in the aluminum data than in the data from the other two materials, in which the crack growth was quite smooth. Nevertheless, the standard deviations of the aluminum data were only about 3 percent. The value of 2.5 $(K_{Ic}/\sigma_{ys})^2$ was 5.3 mm for the aluminum, and much smaller for the other two materials.

The Al_2O_3 and fused quartz specimens were tested in air, where moisture due to humidity can cause stress corrosion cracking. However, rapid loading was used to make the crack velocity high enough to preclude significant stress corrosion cracking effects. From visually observing the crack in the fused quartz specimens, the crack velocities are estimated to have been at least 10 mm/s as the crack passed through the critical length, a_c.

The test results summarized in Table 1 were obtained using the same specimen geometry calibration constant, A_F (see Eqs 1 and 2), for both the short bar and short rod specimens. The differences in measured K_{Ic} are not statistically significant. Note that the standard deviation obtained by lumping the short bar and short rod data together is always smaller than the standard deviation of one of the two data sets. Furthermore, the short bar average K_{Ic} values for the three materials are neither consistently larger nor smaller than those measured by the short rod. Thus, within the accuracy of these experiments, it can be stated that the calibration constant, A_F, is the same for both the short rod and short bar specimen geometries.

Finally, it is interesting to compare the K_{Ic} values measured here with those for similar materials from the literature. No measurements of K_{Ic} in 7075-T651 aluminum using the C-L crack orientation were found in the literature, however, data have been published for the same material with the T-L crack orientation, which should produce similar K_{Ic} values. Kaufman et al [7] obtained 20.8 and 27.5 MPa$\sqrt{\text{m}}$ for specimens from 12.77 and 44.5-mm-thick plate stock, respectively. Kaufman et al [8]

TABLE 1—*Summary of experiments.*

Material	Specimen Type	No. of Tests	Average K_{Ic} (MPa$\sqrt{m}$)	Standard Deviation, percent	Total Group Values[a]		
					No. of Tests	Average K_{Ic} (MPa$\sqrt{m}$)	Standard Deviation, percent
7075-T651 Al	short bar	6	23.42	2.5	12	23.17	2.9
7075-T651 Al	short rod	6	22.91	3.1			
AD-94 Al_2O_3	short bar	5	3.82	0.8	10	3.83	0.7
AD-94 Al_2O_3	short rod	5	3.84	0.4			
Fused quartz	short bar	5	0.738	0.6	10	0.735	1.3
Fused quartz	short rod	5	0.732	1.8			

[a] Averaging both short bar and short rod data together.

obtained K_{Ic} values from 24.5 to 28.5 MPa$\sqrt{m}$ for T-L specimens made from plate stock, and 23.6 to 30.6 MPa$\sqrt{m}$ for T-L specimens made from extrusions. Nelson and Kaufman [*9*] found an average K_{Ic} of 22.6 MPa$\sqrt{m}$ for T-L specimens of 35 mm thickness. These values agree quite well with the 23.2 MPa$\sqrt{m}$ average K_{Ic} found for the C-L specimens of this study.

No fracture toughness data on Coors AD-94 alumina were found in the literature. However, K_{Ic} measurements on somewhat similar aluminum oxide formulations have been made [*4,10–12*]. These would seem to suggest a K_{Ic} value for AD-94 of perhaps 10 percent less than the 3.83 MPa$\sqrt{m}$ obtained here. In this regard, it is interesting that in earlier short rod tests of six specimens of AD-94 material from a different production run, the author measured an average K_{Ic} of 3.39 MPa$\sqrt{m}$ with a standard deviation of 2.3 percent. This value seems to compare more favorably with other published results. Apparently the AD-94 rod which supplied the material for the present test series was somehow tougher than might be expected generally.

Fused quartz K_{Ic} measurements have been made by Mecholsky et al [*13*] (0.73 MPa$\sqrt{m}$); Wiederhorn [*14*] (0.798 and 0.789 MPa$\sqrt{m}$); and Wiederhorn et al [*15*] (0.729 to 0.753 MPa$\sqrt{m}$). It is apparent that the 0.735 MPa$\sqrt{m}$ obtained in the present study is in very good agreement with these values.

Conclusions

A new short bar fracture toughness specimen with a rectangular cross section has been designed to have essentially the same characteristics as the recently introduced short rod specimen which has a circular cross section. Comparison tests on aluminum, alumina, and fused quartz have been unable to distinguish any difference in the calibration constant for the two specimen types, and have shown the specimen behaviors during testing to be essentially the same. Comparisons of the short bar and short rod K_{Ic} measurements of aluminum, alumina, and fused quartz with published data show good agreement.

Acknowledgment

The idea of how to make the short bar calibration constant essentially the same as that of the short rod was sparked by a short presentation by J. Srawley of NASA-Lewis in a recent meeting of ASTM Subcommittee E24.07 on Fracture of Brittle Nonmetallic Materials at National Bureau of Standards. The author is also grateful to G. Kaufman for helpful consultation, to R. Schmidt for reviewing the manuscript, and to A. Rodgers for excellent specimen preparation. This work was supported by the National Science Foundation.

References

[1] Barker, L. M., *Engineering Fracture Mechanics*, Vol. 9, 1977, p. 361.

[2] Barker, L. M. in *Proceedings*, ICM-II Conference, Boston, 1976, p. 1547.

[3] Barker, L. M. and Leslie, W. C. in *Fracture 1977*, Vol. 2, 4th International Conference on Fracture, Waterloo, Canada, 1977, p. 305.

[4] Barker, L. M., *Fracture Mechanics of Ceramics*, Vol. 3, 1978, p. 483.

[5] Koblitz, F. F., Luna, V. R., Glenn, J. E., and DeVries, K. L., "Fracture Toughness Testing of Dental Biomaterials," 175th National Meeting of the American Chemical Society, 15 March 1978.

[6] Roark, R. J., *Formulas for Stress and Strain*, 4th Ed., McGraw-Hill, New York, 1971.

[7] Kaufman, J. G., Schilling, P. E., and Nelson, F. G., *Metals Engineering Quarterly*, Vol. 9, 1969, p. 39.

[8] Kaufman, J. G., Moore, R. L., and Schilling, P. E., *Engineering Fracture Mechanics*, Vol. 2, 1971, p. 197.

[9] Nelson, F. G. and Kaufman, J. G. in *Fracture Toughness Testing at Cryogenic Temperatures, ASTM STP 496*, 1971, pp. 27-39.

[10] Freiman, S. W., McKinney, K. R., and Smith, H. L., in *Fracture Mechanics of Ceramics*, Vol. 2, R. C. Bradt, D. P. H. Hasselman, and F. F. Lange, Eds., Plenum Press, New York, 1974, p. 659.

[11] Bertolotti, R. A., *Journal of the American Ceramic Society*, Vol. 56, 1973, p. 107.

[12] Swanson, G. D. and Gross, G. E., *Journal of the American Ceramic Society*, Vol. 54, 1971, p. 382.

[13] Mecholsky, J. J., Rice, R. W., and Freiman, S. W., *Journal of the American Ceramic Society*, Vol. 57, No. 10, 1974, p. 440.

[14] Weiderhorn, S. M., *Journal of the American Ceramic Society*, Vol. 52, No. 2, 1969, p. 99.

[15] Weiderhorn, S. M., Evans, A. G., and Roberts, D. E. in *Fracture Mechanics of Ceramics*, Vol. 2, R. C. Bradt, D. P. H. Hasselman, and F. F. Lange, Eds., Plenum Press, New York, 1974, p. 829.

J. J. Petrovic[1] *and M. G. Mendiratta*[2]

Fracture from Controlled Surface Flaws

REFERENCE: Petrovic, J. J. and Mendiratta, M. G., **"Fracture from Controlled Surface Flaws,"** *Fracture Mechanics Applied to Brittle Materials, ASTM STP 678.* S. W. Freiman, Ed., American Society for Testing and Materials, 1979, pp. 83-102.

ABSTRACT: The use of controlled surface flaws to examine fracture properties of brittle materials is reviewed. Surface flaws are introduced by microhardness indentation. Such flaws are semi-elliptical in shape, with dimensions dictated by the indentation load.

A single flaw of proper size placed on the tensile surface of a conventional four-point bend specimen initiates fracture because it is the "worst flaw" in the specimen. Presence of the flaw reduces both the fracture strength and its associated scatter. Because controlled surface flaw dimensions are generally visible on the fracture surface, the critical stress intensity factor, K_{Ic}, may be calculated using fracture mechanics analyses for surface flaws in bending.

Such a fracture mechanics test is experimentally convenient, adaptable to testing in severe environments, and requires a relatively simple test specimen geometry. Also of importance is the fact that the fracture flaw dimensions are close to those of the natural flaws in the material. For silicon nitride (Si_3N_4) and silicon carbide (SiC) the technique has been employed to determine K_{Ic} at room and elevated temperatures, as well as under dynamic loading conditions. It has also been used to study slow crack growth, environmental effects, and mixed-mode fracture in these materials. Disadvantages of the controlled surface flaw technique as well as potential new applications are discussed.

KEY WORDS: controlled surface flaws, microhardness indentation precracking, semi-elliptical surface crack, brittle materials, fracture (materials), fracture toughness, bend test, crack propagation

In recent years, the crack patterns produced in the vicinity of microhardness indentations in brittle materials have been the subject of increasing

[1] Materials scientist, Group CMB-5, Los Alamos Scientific Laboratory, Los Alamos, N. Mex. 87545.

[2] Materials scientist, Systems Research Laboratories, Inc., Dayton, Ohio 45440.

scrutiny [*1–5*].[3] Whereas in the past such cracking has been viewed as a generally undesirable element associated with the hardness testing of brittle materials, it is now recognized that indentation-produced cracks can play a valuable role in examining the fracture behavior of these materials.

One aspect of the use of indentation cracking to investigate brittle fracture is the area of fracture from controlled surface flaws. The term "indentation precracking" has also been used to describe the approach [*6*]. In this technique, surface flaws of controlled size and shape are introduced into a mechanical test specimen by microhardness indentation. Subsequent fracture of the specimen initiates from the site of the controlled surface flaw, and the resultant fracture may be analyzed to derive fracture mechanics parameters. The present discourse reviews this method, its applications to date, its advantages and disadvantages, and its potential for future application.

Microhardness Indentation Cracking

Typical surface crack patterns around microhardness indentations are shown in Figs. 1 and 2, for a diamond pyramid indentation and a Knoop indentation. On the surface, sharp cracks radiate from the corners of the diamond pyramid indentation, while for the Knoop indentation a sharp crack is formed along the long diagonal.

The cracks visible on the surface actually extend below the surface with a semi-elliptical shape, as shown in Fig. 3 for a 2600-g Knoop indentation in hot-pressed silicon nitride (Si_3N_4). These cracks correspond to the "median vents" described by Lawn et al [*1–3*]. Thus, with microhardness indentation it is possible to introduce semi-elliptical surface flaws into brittle materials.

In our work, we have preferred to use flaws produced by Knoop indentations as opposed to diamond pyramid indentations, for the following reasons. First, with the Knoop indentation there is no crack perpendicular to the primary surface flaw, as is the case with the diamond pyramid indentation. This is a more desirable situation from a fracture mechanics analysis viewpoint. Second, orientation of Knoop surface flaws is more convenient and controllable, since alignment is achieved by aligning the long axis of the Knoop indentation.

Surface flaws produced by Knoop indentation are "controlled" in the sense that their basic shape is semi-elliptical, and their size is determined by the applied Knoop microhardness load.

Surface Flaws in Four-Point Bending

If a single controlled surface flaw of suitable size is placed on the tensile

[3]The italic numbers in brackets refer to the list of references appended to this paper.

surface of a four-point bend specimen and accurately aligned perpendicular to the tensile stress direction as shown schematically in Fig. 4, fracture initiates at the site of this flaw because it is the "worst flaw" in the specimen. There is a consequent reduction in the fracture stress as compared to the "unflawed" condition, and the surface flaw profile is visible on the fracture surfaces.

Table 1 shows the effect of a single surface flaw on the fracture stress in four-point bending of three structural ceramic materials. Twenty tests were performed for each material. Taking HS-130 hot-pressed Si_3N_4 as an example, the room temperature as-received fracture stress was 661 MN/m^2. The surface flaw produced by a 2600-g Knoop indentation had a depth, a, of 68.5 μm and a surface length, $2c$, of 154 μm. Thus, this was quite a small flaw as compared to the bend specimen thickness of 3175 μm. For HS-130 Si_3N_4, the presence of this flaw reduced the fracture stress to 322 MN/m^2, approximately a factor of two reduction. It is also important to notice that the scatter in fracture stress was reduced by a factor of four as a result of the flaw being present. This indicates that the flaws introduced by microhardness indentation were highly reproducible. Similar effects are evident for the other materials in Table 1.

Fracture Mechanics of Surface Flaws

A review of fracture mechanics expressions for surface and internal cracks has been compiled by Keays [7]. Green and Sneddon [8] and Irwin [9] addressed the question of stresses in the vicinity of an elliptical crack in an infinite medium subjected to tensile loading. The derived stress intensity factor for the elliptical crack is of the form

$$K_I = \frac{\sigma(\pi a)^{1/2}}{\Phi}\left(\frac{a^2}{c^2}\cos^2\phi + \sin^2\phi\right)^{1/4} \tag{1}$$

where

σ = applied tensile stress,
a = minor half-axis of ellipse,
c = major half-axis of ellipse, and
ϕ = angle as defined in Fig. 5.

The term Φ is given by

$$\Phi = \int_0^{\pi/2}\left[\sin^2\phi + \frac{a^2}{c^2}\cos^2\phi\right]^{1/2} d\phi \tag{2}$$

Φ is a complete elliptic integral of the second kind, and its value increases as the a/c ratio of the elliptical crack increases, reaching a value of $\Phi = \pi/2$ for $a/c = 1$. Φ is given as a function of a/c ratio in Table 2. For the

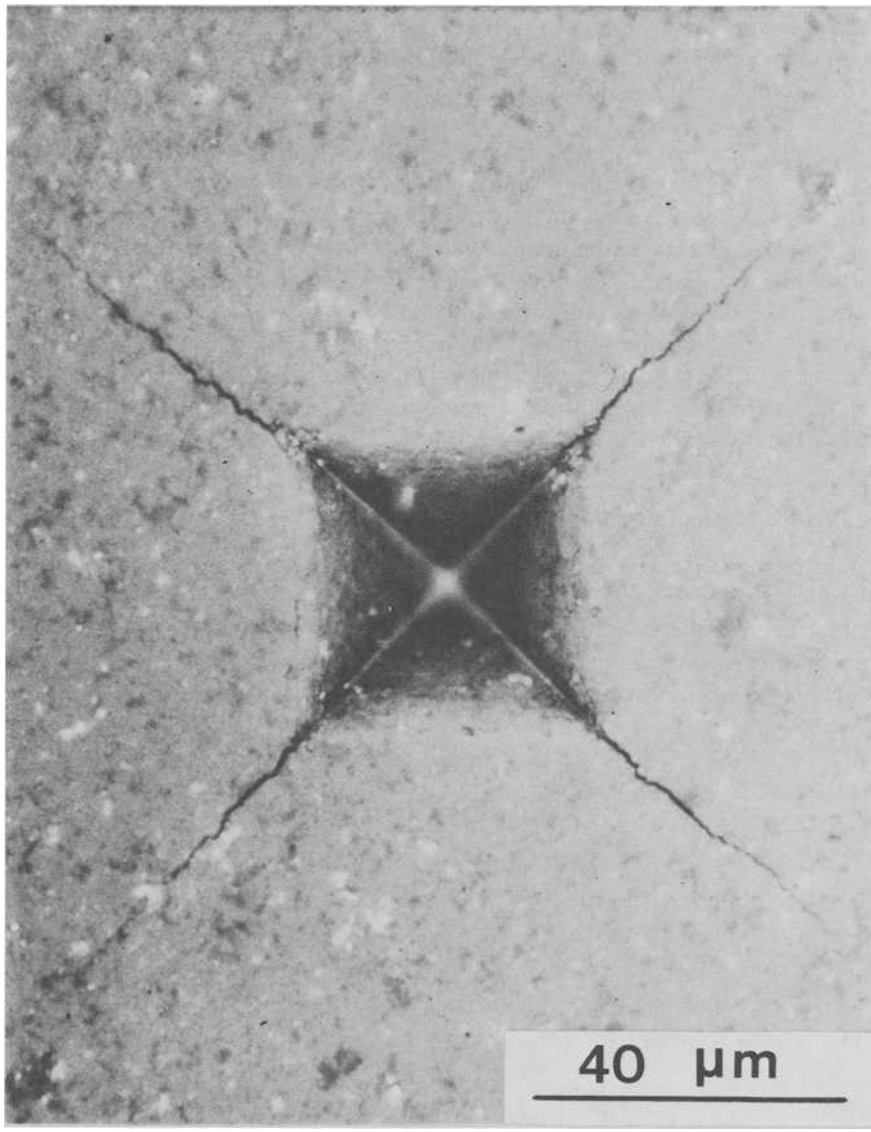
40 µm

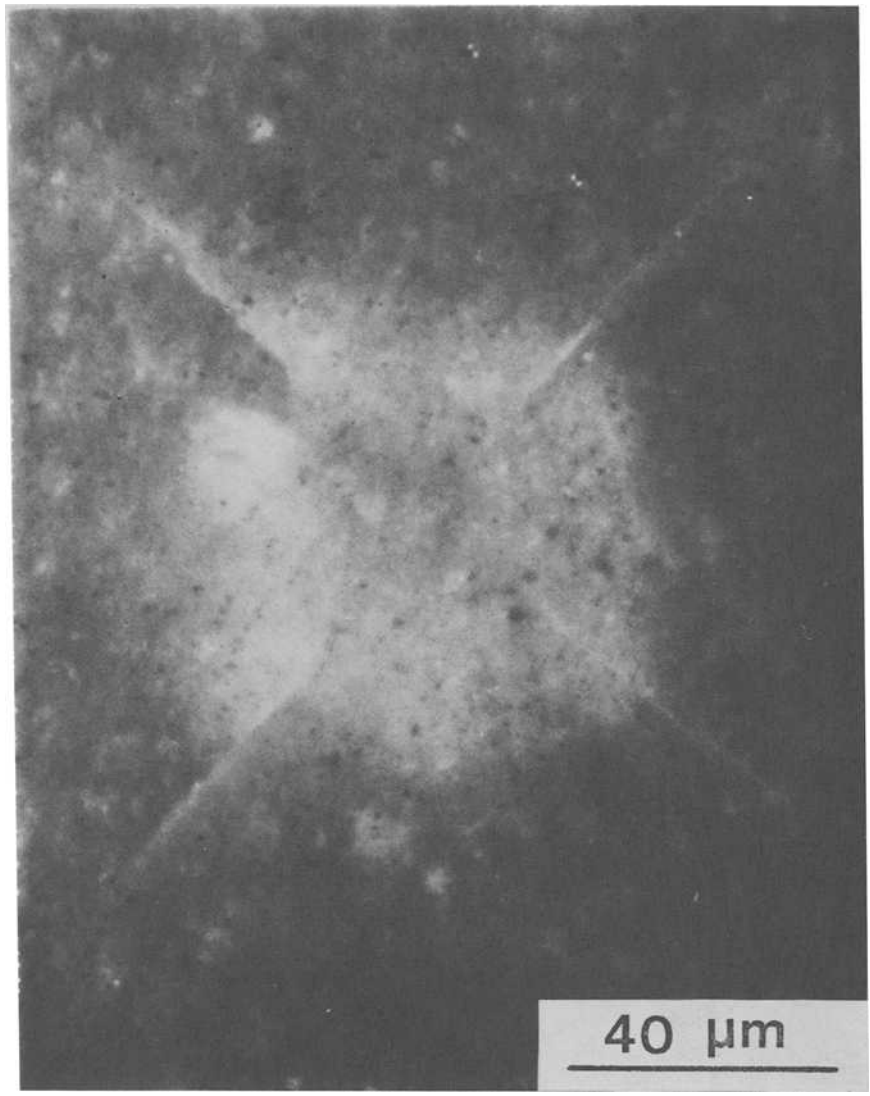

FIG. 1—*2600-g Diamond Pyramid indentation in hot-pressed Si_3N_4.* (a) *Indentation on polished surface, and* (b) *crack pattern after 8 μm surface removal.*


40 μm

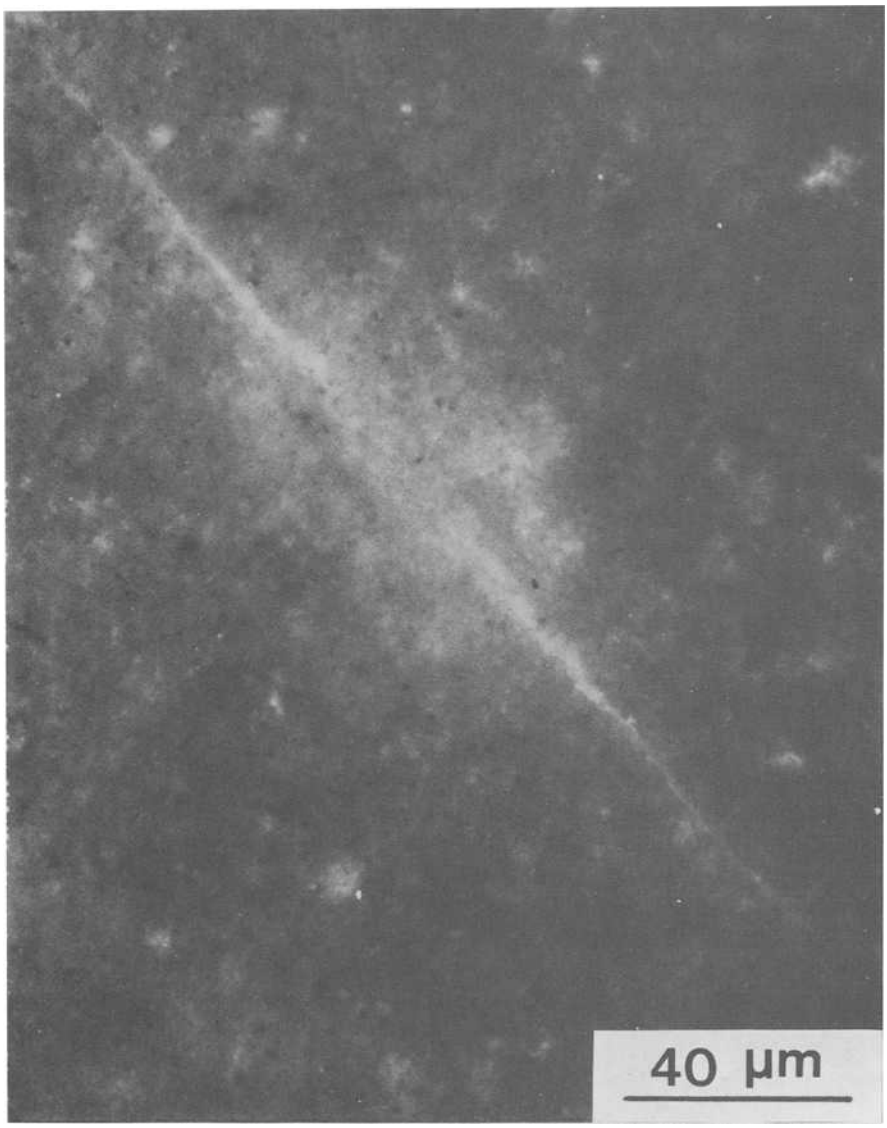

FIG. 2—*2600-g Knoop indentation in hot-pressed Si_3N_4.* (a) *Indentation on polished surface, and* (b) *crack pattern after 8-μm surface removal.*

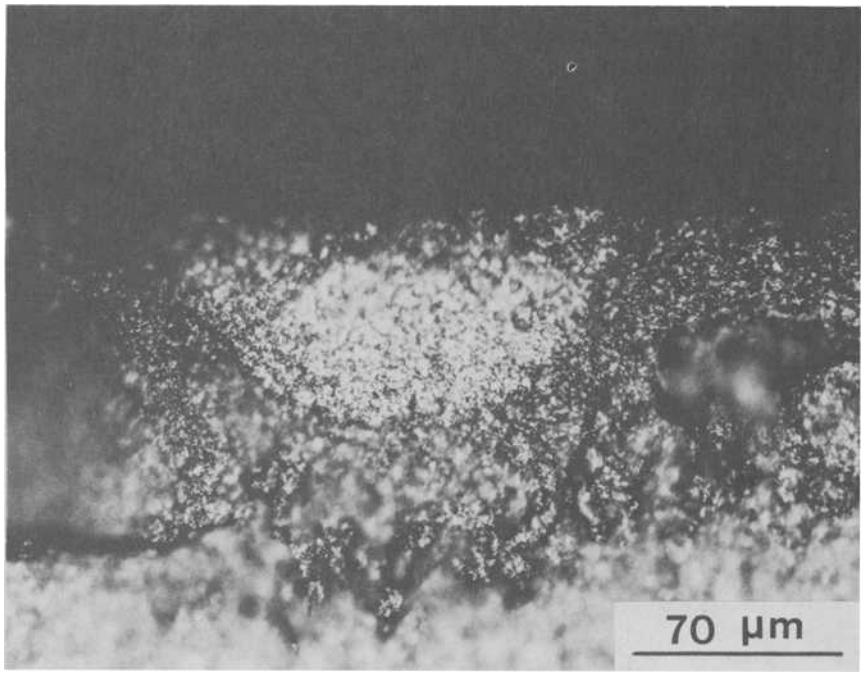

FIG. 3—*Surface flaw produced by a 2600-g Knoop indentation in hot-pressed Si_3N_4. Flaw profile as seen on a fracture surface.*

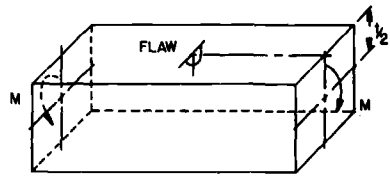

FIG. 4—*Schematic of controlled surface flaw on the tensile surface of a four-point bend specimen.*

elliptical crack in an infinite medium under tensile loading, the point of maximum stress intensity occurs at the intersection of the minor axis with the ellipse (Fig. 5), where the stress intensity factor is

$$K_I = \frac{\sigma(\pi a)^{1/2}}{\Phi} \tag{3}$$

If the elliptical crack in the infinite solid is sectioned along its midplane (Fig. 5), a semi-elliptical surface crack results. Irwin [9] suggested that the

TABLE 1—*Effect of one controlled surface flaw on the four-point bend strength of three hot-pressed structural ceramics.*

Material	Room Temperature As-Received Fracture Stress, MN/m^2	2600-g Knoop, Flaw Dimensions $2c$ ($\times 10^{-3}$ m)	Flaw Dimensions a ($\times 10^{-3}$ m)	Room Temperature Flawed Fracture Stress, MN/m^2
HS-130 Si_3N_4	661 (9.48 percent SD)	0.154 (7.05 percent SD)	0.0685 (3.34 percent SD)	322 (2.16 percent SD)
NC-132 Si_3N_4	614 (14.24 percent SD)	0.170 (5.97 percent SD)	0.0745 (3.48 percent SD)	329 (1.19 percent SD)
NC-203 SiC	480 (5.27 percent SD)	0.159 (3.49 percent SD)	0.0927 (4.27 percent SD)	229 (1.35 percent SD)

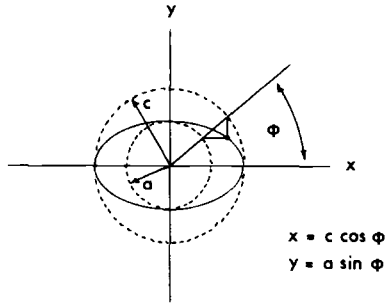

ELLIPTICAL CRACK

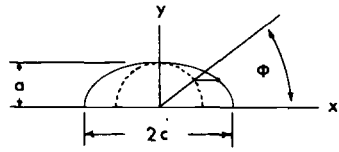

SEMI-ELLIPTICAL CRACK

FIG. 5—*Schematic representation of the elliptical crack and semi-elliptical crack, showing definitions of crack parameters.*

TABLE 2—*Value of the elliptical integral Φ as a function of* a/c *ratio.*

a/c Ratio	Φ	*a/c* Ratio	Φ
0	1.0000	0.55	1.2432
0.05	1.0049	0.6	1.2764
0.1	1.0160	0.65	1.3105
0.15	1.0316	0.7	1.3456
0.2	1.0506	0.75	1.3815
0.25	1.0723	0.8	1.4181
0.3	1.0966	0.85	1.4553
0.35	1.1227	0.9	1.4933
0.4	1.1506	0.95	1.5318
0.45	1.1802	1.00	1.5708
0.5	1.2111		

stress intensity factor for the surface flaw could be described by insertion of a numerical free surface correction factor, M, into Eq 3 so that

$$K_1 = \frac{\sigma M(\pi a)^{1/2}}{\Phi} \tag{4}$$

He also developed a plasticity correction factor by adding a yield zone

radius, $Ry = K_I^2/(4\sqrt{2}\pi\sigma_{ys}^2)$, to the crack length in the computation of K_I, giving

$$K_I = \frac{\sigma M(\pi a)^{1/2}}{\left\{\Phi^2 - 0.212\left(\frac{\sigma}{\sigma_{ys}}\right)^2\right\}^{1/2}} \tag{5}$$

where σ_{ys} is the tensile yield stress. Thus, the final form of K_I for the semi-elliptical surface flaw is

$$K_I = \sigma M\left(\frac{\pi a}{Q}\right)^{1/2} \tag{6}$$

where $Q = \Phi^2 - 0.212\,(\sigma/\sigma_{ys})^2$.

Equation 6 is the most commonly used expression for the stress intensity factor of semi-elliptical surface flaws (see Ref *7* for other functional forms of K_I). Although this expression was derived originally for tensile loading conditions, subsequent analyses [*10–16*] have extended its application to bending conditions as well.

No exact theoretical solution has yet been formulated for the free surface correction factor M in Eq 6, and as a result much effort has been and continues to be directed towards the refinement of numerical approximation solutions for this term. In general, M is a function of the a/c ratio (flaw shape), the a/t ratio (flaw size with respect to the test specimen dimensions), the angle ϕ (position along the flaw periphery), and the mode of loading (for example, tension, bending).

Under tensile loading conditions, the value of M increases with increasing a/t [*16–18*]. At the flaw depth ($\phi = \pi/2$) M increases with decreasing a/c ratio, while at the flaw surface ($\phi = 0$) the opposite occurs [*18*]. Under bending conditions, M values generally decrease with increasing a/t [*16*], while the dependency on a/c ratio is the same as for the tension case.

For controlled surface flaws in brittle materials, the commonly encountered flaw conditions are small flaws (a/t near zero) and nearly semi-circular flaws (a/c near 1). For small, semi-circular surface flaws, Smith et al [*10*] indicated that M varied from a value of 1.03 at the flaw depth ($\phi = \pi/2$) to 1.21 at the flaw surface ($\phi = 0$), for both tension and bending conditions. Recent analyses of Raju and Newman [*18*] for the semi-circular surface flaw in tension ($a/t = 0.2$) yielded M values of 1.036 at the flaw depth and 1.166 at the flaw surface. For small, nearly semi-circular ($a/c = 0.98$) surface flaws in bending, Kobayashi [*16*] derived an M value of 1.03 at the flaw depth and a value of 1.24 at the flaw surface. These data also indicate that for small flaws in bending, M values at the flaw depth and flaw surface are equal ($M \cong 1.06$) for an a/c ratio of 0.8.

The previous discussion illustrates the fact that some uncertainty in the value of K_I calculated from Eq 6 for small, nearly semi-circular surface flaws currently exists, especially with regard to the position along the flaw periphery where fracture initiates. Although the fracture mechanics analyses suggest that fracture will initiate at the flaw surface (since this location has the highest value of K_I), there is currently no evidence that this is actually the case for the fracture of controlled surface flaws. Thus, at present, the uncertainty in K_I values for small, nearly semi-circular surface flaws is of the order of 15 percent. This uncertainty can be expected to diminish as numerical approximations for K_I continue to be refined.

Equation 6 has been applied to fracture from indentation-produced controlled surface flaws to calculate K_{Ic} values. Specimens containing a surface flaw are fractured in four-point bending, and the maximum outer fiber tensile stress determined. Since flaw dimensions can be measured on the fracture surface, this provides the necessary information to calculate K_{Ic} from Eq 6. For brittle fracture, the plasticity correction term usually is neglected.

Current Applications of the Controlled Surface Flaw Technique

The controlled surface flaw technique has been applied to measure K_{Ic} values at both room temperature and elevated temperatures for the structural ceramics Si_3N_4 [*19-21*] and silicon carbide (SiC) [*22*]. For the case of SiC, this technique was able to distinguish differences in fracture behavior associated with air and vacuum environments. Ingelstrom and Nordberg [*23*] used the method to determine K_{Ic} values for tungsten carbide-cobalt (WC-Co) composite materials at room temperature. Govila [*24*] has examined the fracture behavior of vanadium carbide (VC) single crystals, measuring fracture surface energy as a function of temperature.

A slight modification of the technique was employed by Petrovic and Mendiratta to study mixed-mode fracture in hot-pressed Si_3N_4 [*25,26*]. Rather than orienting the surface flaw perpendicular to the bending tensile stress direction, it was positioned accurately at various different angles. Doing so leads to mixed-mode fracture conditions, with Modes I, II, and III present. This technique was found to be an experimentally convenient one for the observation of mixed-mode fracture.

Mendiratta, Wimmer, and Bransky [*27*] and Gonczy and Johnson [*28*] used the controlled surface flaw technique to obtain dynamic K_{Ic} values both at room temperature and 1300°C for hot-pressed Si_3N_4. Flawed bend bars were employed in conjunction with dynamic loading methods. Dynamic K_{Ic} values were less temperature dependent than static K_{Ic} values in this material.

The elevated temperature slow crack growth behavior of hot-pressed Si_3N_4 was investigated by Mendiratta and Petrovic [*29*]. In this case, arrays

of differently sized surface flaws were placed on a single four-point bend bar, then subjected to stress at elevated temperatures for various times. Average crack velocities and K_I values were determined by observation of surface crack extension. Slow crack growth from individual flaws was erratic and not well described by the empirical relationship $V = A K_I^n$. Land and Mendiratta [*30*] have put forward a theoretical framework which explains such behavior in terms of flaw interactions with material inhomogeneities.

Strength degradation in untempered and tempered glasses has been examined by placing diamond pyramid indentations in four-point bend specimens and interpreting the subsequent fracture behavior [*31–33*]. The thermal shock [*34*] and thermal fatigue [*35*] responses of soda-lime-silica glass have been investigated using diamond pyramid and Knoop indentation surface flaws, respectively, in specimens of rod geometry which were subjected to the thermal exposures and then fractured in four-point bending.

Tappin, Davidge, and McLaren [*36*] used the controlled surface flaw technique to investigate fracture of silicon carbide under biaxial stress conditions. In this case, a Knoop indentation was placed on the surface of a tube specimen, which was then pressurized to achieve biaxial loading. Fracture initiated from the controlled surface flaw, and results were analyzed in terms of multiaxial fracture theories.

It is evident from the preceding discussion that the applications to date of the controlled surface flaw technique cover a wide range. This technique is useful for examining a number of phenomena associated with the fracture behavior of brittle materials, and the full extent of potential applications for this method has yet to be explored.

Disadvantages of the Controlled Surface Flaw Technique

As is the case with all fracture mechanics tests for brittle materials, there are certain disadvantages associated with the use of the controlled surface flaw method. These disadvantages are the following: (*a*) residual stress effects, (*b*) flaw "healing" at elevated temperatures, (*c*) difficulty in observation of the flaw profile on fracture surfaces, and (*d*) possible applicability of the technique to a limited range of brittle materials. Each of these disadvantages will now be discussed in more detail.

In Fig. 6, surface flaws were placed on bend bars of hot-pressed Si_3N_4, then subjected to an elevated temperature air annealing treatment prior to subsequent fracture at room temperature [*37*]. Although fracture always initiated at the flaw site, room temperature K_{Ic} values increased as a result of the annealing treatment. This effect was independent of annealing environment, since it also occurred for vacuum annealing. Ingelstrom and Nordberg [*23*] have observed similar effects in WC-Co alloys.

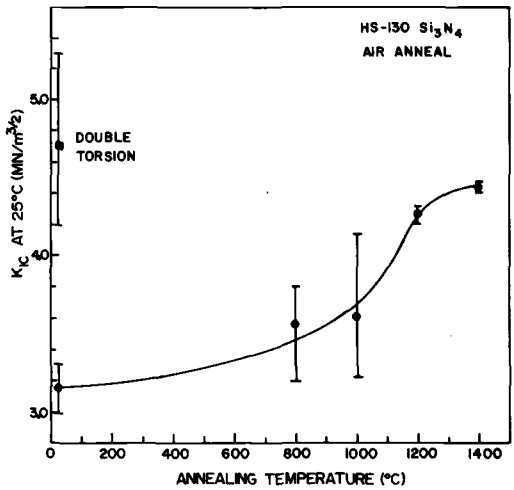

FIG. 6—*Effect of annealing on room temperature* K_{Ic} *values obtained by the controlled surface flaw technique for hot-pressed* Si_3N_4. *Double torsion data are from Ref* 41.

This increase in K_{Ic} with annealing has been attributed to a reduction in residual stresses associated with the microhardness indentation used to produce the controlled surface flaw [*19,20,23*]. If such is the case, then careful surface polishing to remove the indentation zone and associated tensile residual stresses at the crack tip (shown schematically in Fig. 7) should lead to an increase in K_{Ic} values. Results of such polishing experiments for hot-pressed Si_3N_4 [*37*] are shown in Fig. 8. K_{Ic} (compensated for changes in flaw size produced by polishing) increased with increasing surface removal, reaching a constant value at a surface removal of about three indentation depths. This result strongly supports the contention that residual stresses can affect K_{Ic} values obtained from the surface flaw technique.

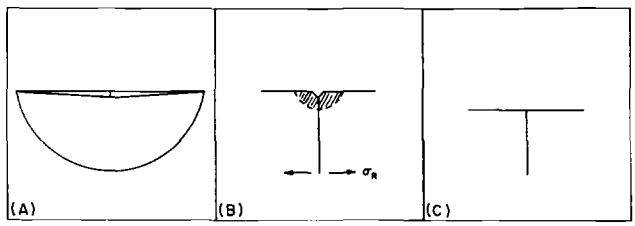

FIG. 7—*Schematic of surface polishing to remove residual stresses associated with the microhardness indentation.* (a) *Profile of controlled surface flaw and associated Knoop microhardness indentation,* (b) *side view of indentation and crack below it. A surface deformed region produced by the microhardness indentation is presumed to generate tensile residual stresses at the crack tip, and* (c) *if the surface deformed region is polished away, residual stresses at the crack tip should be eliminated.*

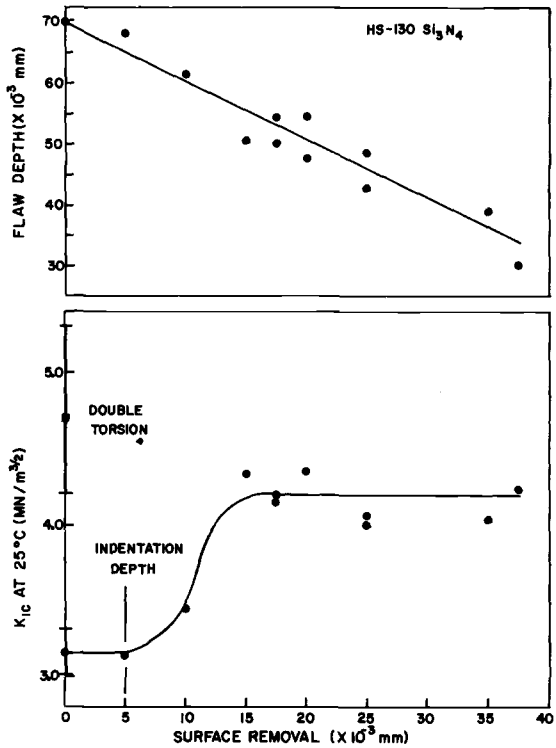

FIG. 8—*Effect of surface polishing on room temperature* K_{Ic} *values obtained by the controlled surface flaw technique for hot-pressed* Si_3N_4. *Double torsion data are from Ref* 41.

Residual stress effects must be eliminated in order to derive true K_{Ic} values for a given material. This would appear to be the major disadvantage with the technique. As indicated previously, two methods for achieving this end are annealing of the indented/flawed material, or polishing away of the indentation. If attempts are not made to correct for residual stress effects, K_{Ic} values will be low in comparison to actual values. Table 3 shows the effect of surface polishing on K_{Ic} values obtained for three structural ceramic materials. In all cases, K_{Ic} increased when the indentation was removed.

For some brittle materials, surface flaws can "heal" when exposed to elevated temperatures. Figure 9 shows an example of such flaw "healing" in hot-pressed SiC [*22*]. Specimens were indented, exposed to an elevated temperature annealing treatment, then subsequently tested at room temperature and the flawed fracture stress measured. The as-indented fracture stress was 225 MN/m^2. With air annealing, this fracture stress increased until at 1000°C and above, fracture no longer occurred at the site of the controlled surface flaw. The flaw had been "healed" by this air annealing

TABLE 3—*Effect of surface polishing on room temperature K_{Ic} values for three structural ceramics. Surface removal corresponded to three indentation depths in all cases. K_{Ic} at 25°C, $MN/m^{3/2}$.*

	NC-350 Si_3N_4	HS-130 Si_3N_4	NC-203 SiC
As-Indented	1.15	3.16	2.57
Ground	1.86	4.20	2.91

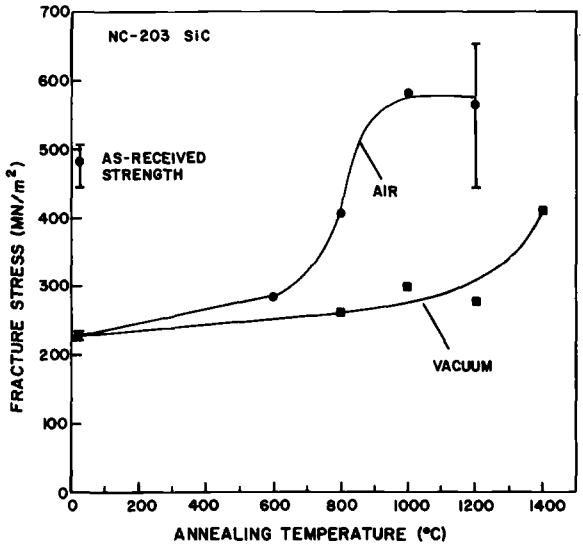

FIG. 9—*Flawed fracture stresses (2600-g Knoop flaw) of hot-pressed SiC at room temperature, after elevated temperature annealing.*

treatment. Note that fracture stresses observed for cases where the flaw had "healed" (1000°C and above) were higher than as-received strengths for the material, suggesting that flaw "healing" mechanisms also influenced the nature of as-fabricated surface defects.

In Fig. 9, flaw "healing" was not observed when annealing treatments were performed in a vacuum environment, illustrating that such "healing" phenomena can be sensitive to environmental effects. Under vacuum conditions, fracture always occurred at the site of the flaw, even for annealing treatments at the highest annealing temperatures. For hot-pressed SiC, the presence of a small pre-load on the specimen during the air annealing treatment eliminated the flaw "healing" effects, a result possibly related to small displacements of the flaw surfaces produced by the pre-load.

One of the attractive features of the controlled surface flaw technique is that fracture flaw profiles are visible on the fracture surfaces. With a knowledge of the fracture stress, these dimensions allow ready calculation

of K_{Ic} from Eq 6. The question must be asked: Why is the flaw visible at all on the fracture surfaces? The fact of its visibility certainly suggests differences between the nature of indentation fracture and subsequent fast, catastrophic fracture from the flaw site. To the author's knowledge, however, the reasons for such differences have not been addressed in any definitive way.

Surface flaw profiles were readily visible on fracture surfaces in hot-pressed Si_3N_4 [*20*] and hot-pressed SiC [*22*]. However, flaws were somewhat harder to see in reaction sintered Si_3N_4 [*21*], a lower density material. This suggests the possibility that, in some brittle materials, flaws may be essentially invisible on fracture surfaces.

If this were the case, flaw profiles might be enhanced by liquid penetration techniques, such as dye penetrants or etching solutions. In addition, laborious but definitive incremental polishing techniques could be employed to establish the flaw profile dimensions [*20*]. Finally, the assumption could be made that flaws were essentially semi-circular in shape, in which case flaw dimensions could be derived from measurement of surface length.

An appropriate question to put forward is the following: Can semi-elliptical surface flaws of reproducible sizes be introduced into all brittle materials using microhardness indentation? For example, are there grain size and density limits to the production of controlled surface flaws, such that the size and shape of these flaws are no longer well-defined or reproducible? It seems likely that such limits may exist, but the range of these possible limits has not yet been defined.

Evans [*38*] has indicated that controlled surface flaws cannot be produced by microhardness indentation in relatively coarse grained materials (approximately 20 μm grain size) which are sintered to full density with the aid of specific additives. Two of these materials are alumina sintered with magnesium oxide (MgO) (Lucalox) and MgO sintered with lithium fluoride (LiF). For these materials, networks of grain boundary cracks occur at the indentation and semi-elliptical surface flaws are not formed.

Advantages of the Controlled Surface Flaw Technique

The controlled surface flaw method presents some distinct advantages with regard to examinations of fracture in brittle materials. Foremost among these are the following: (*a*) a simple bend bar specimen geometry is used, (*b*) potential exists for adaptation of the technique to other specimen geometries, and (*c*) the controlled surface flaw approximates natural failure defects in brittle materials.

Almost all applications of the controlled surface flaw technique to date have employed a four-point bend bar specimen geometry. This is a small,

inexpensive specimen which can be obtained readily in most situations. Furthermore, bend tests are experimentally convenient to perform. Because of this fact, controlled surface flaw experiments can be conducted under severe environmental conditions, such as high temperature, controlled atmospheres, corrosive environments, and high strain rates. Thus, the controlled surface flaw technique possesses a high degree of versatility with regard to potential applications.

Controlled surface flaws have the potential for use with specimen geometries other than the bend bar. A controlled surface flaw might be placed on the surface of a disk specimen, and the disk fractured in biaxial flexure [*39*]. Often in brittle material development programs, only small quantities of material are produced. In such instances, bend bars may not always be available, although right cylinders can usually be made. With a right cylinder, the diametral compression test [*40*] could be used in conjunction with a properly oriented controlled surface flaw on the flat end of the cylinder (where tensile stresses exist), to fracture the material in tension using a compressive loading mode, and thus derive values of K_{Ic}.

An interesting question arises with regard to the use of controlled surface flaws in conjunction with the direct compression test. The controlled surface flaw is the "worst flaw" in tension, but will it be the "worst flaw" in compression? If it is not, then this would constitute a significant observation in itself. However, if it is, controlled surface flaws might be used to examine details of compressive fracture. Such flaws could be placed, suitably inclined, on the circumferential surface of a right cylindrical compression specimen and thus be subjected to compressive loading.

Surface flaws also could be loaded in torsion. In such cases, fracture would be a combination of Modes II and III, with no Mode I present. The possibilities of investigating mixed-mode fracture using combinations of tension/torsion and compression/torsion also present themselves.

Controlled surface flaws approximate actual failure defects in brittle materials. Fracture initiates from a very small crack which is well characterized in terms of its size and shape. Although this crack is the "worst flaw" in the material, its size is still close to the size range of the naturally occurring material defects.

The following question needs to be addressed. Are small flaws the same as large cracks with respect to the fracture of brittle materials? It seems possible that small flaws might interact more directly than large cracks with local material inhomogeneities such as porosity, grain boundaries, and compositional variations, to produce differences in fracture behavior related to the size of the fracture initiating crack. Recent work [*29,30*] has indicated that this may be true with respect to elevated temperature slow crack growth.

Conclusions

Controlled surface flaws associated with microhardness indentations can be a valuable tool for the examination of various aspects of brittle fracture. Semi-elliptical surface flaws of controlled size and shape produced by Knoop indentation initiate fracture in four-point bend specimens. Fracture mechanics analyses for surface flaws in bending may be applied to this fracture to obtain the critical stress intensity factor K_{Ic}. The technique, which employs a simple specimen geometry and is experimentally convenient, has been used to derive both static and dynamic K_{Ic} values at both ambient and elevated temperatures, as well as to examine mixed-mode fracture and elevated temperature slow crack growth. Effects of residual stresses associated with the microhardness indentation required to produce the controlled surface flaw are the major disadvantage of the technique. Its advantages include simplicity, versatility, and the fact that the fracture initiating crack approximates natural defects in brittle materials.

References

[1] Lawn, B. and Wilshaw, R., *Journal of Materials Science*, Vol. 10, 1975, pp. 1049-1081.

[2] Lawn, B. R. and Swain, M. V., *Journal of Materials Science*, Vol. 10, 1975, pp. 113-122.

[3] Lawn, B. R. and Fuller, E. R., *Journal of Materials Science*, Vol. 10, 1975, pp. 2016-2024.

[4] Lawn, B. R., Fuller, E. R., and Wiederhorn, S. M., *Journal of the American Ceramic Society*, Vol. 59, 1976, pp. 193-197.

[5] Evans, A. G. and Wilshaw, T. R., *Acta Metalurgica*, Vol. 24, 1976, pp. 939-956.

[6] Govila, R. K., "Comparison Between Indentation Precracking and Double Torsion Techniques for Measuring Fracture Mechanics Parameters in Hot-Pressed Si_3N_4," Basic Science Division presentation No. 131, 80th Annual American Ceramic Society Meeting, Detroit, 6-11 May 1978.

[7] Keays, R. H., "A Review of Stress Intensity Factors for Surface and Internal Cracks," Structures and Materials Report 343, Department of Supply, Australian Defence Scientific Service, Aeronautical Research Laboratories, April 1973.

[8] Green, A. E. and Sneddon, I. N., in *Proceedings*, Cambridge Philosophical Society, Vol. 46, 1950, pp. 159-163.

[9] Irwin, G. R., *Journal of Applied Mechanics*, Vol. 29, No. 4; *Transactions*, American Society of Mechanical Engineers, Vol. 84, Series E, 1962, pp. 651-654.

[10] Smith, F. W., Emery, A. F., and Kobayashi, A. S., *Journal of Applied Mechanics*, Vol. 34, No. 4; *Transactions*, American Society of Mechanical Engineers, Vol. 89, Series E, 1967, pp. 953-959.

[11] Rice, J. R. and Levy, N., *Journal of Applied Mechanics*, Vol. 39, *Transactions*, American Society of Mechanical Engineers, Vol. 94, 1972, pp. 185-194.

[12] Grandt, A. F., Jr. and Sinclair, G. M. in *Stress Analysis and Growth of Cracks, ASTM STP 513;* American Society for Testing and Materials, 1972, pp. 37-58.

[13] Shah, R. C. and Kobayashi, A. S. in *Stress Analysis and Growth of Cracks, ASTM STP 513;* American Society for Testing and Materials, 1972, pp. 3-21.

[14] Schroedl, M. A. and Smith, C. W., in *Progress in Flaw Growth and Fracture Toughness Testing, ASTM STP 536*, American Society for Testing and Materials, 1973, pp. 45-63.

[15] Kobayashi, A. S., Polvanich, N., Emery, A. F., and Love, W. J. in *Proceedings*, 12th Annual Meeting of the Society of Engineering Science, University of Texas at Austin, Oct. 1975, pp. 343-352.

[16] Kobayashi, A. S., in *Proceedings*, 2nd International Conference on Mechanical Behavior of Materials, 16-20 Aug. 1976, Boston, pp. 1073-1077.
[17] Smith, F. W. and Sorensen, D. R., *International Journal of Fracture*, Vol. 12, No. 1, 1976, pp. 47-57.
[18] Raju, I. S. and Newman, J. C., Jr., "Improved Stress-Intensity Factors for Semi-Elliptical Surface Cracks in Finite-Thickness Plates," Report No. TMX-72825, National Aeronautics and Space Administration, 1977.
[19] Petrovic, J. J. and Jacobson, L. A. in *Ceramics For High-Performance Applications*, J. J. Burke, A. E. Gorum, and R. N. Katz, Eds., Brook Hill Publishing Co., 1974; *Proceedings*, 2nd Army Materials Technology Conference, Hyannis, Mass., 13-16 Nov. 1973.
[20] Petrovic, J. J., Jacobson, L. A., Talty, P. K., and Vasudevan, A. K., *Journal of the American Ceramic Society*, Vol. 58, 1975, pp. 113-116.
[21] Wills, R. R., Mendiratta, M. G., and Petrovic, J. J., *Journal of Materials Science*, Vol. 11, 1976, pp. 1330-1334.
[22] Petrovic, J. J. and Jacobson, L. A., *Journal of the American Ceramic Society*, Vol. 59, 1976, pp. 34-37.
[23] Ingelstrom, N. and Nordberg, H., *Engineering Fracture Mechanics*, Vol. 6, 1974, pp. 597-607.
[24] Govila, R. K., *Acta Metalurgica*, Vol. 20, 1972, pp. 447-457.
[25] Petrovic, J. J. and Mendiratta, M. G., *Journal of the American Ceramic Society*, Vol. 59, 1976, pp. 163-167.
[26] Petrovic, J. J. and Mendiratta, M. G., *Journal of the American Ceramic Society*, Vol. 60, 1977, p. 463.
[27] Mendiratta, M. G., Wimmer, J., and Bransky, I., *Journal of Materials Science*, Vol. 12, 1977, pp. 212-214.
[28] Gonczy, S. T. and Johnson, D. L. in *Fracture Mechanics of Ceramics*, Vol. 3, R. C. Bradt, D. P. H. Hasselman, and F. F. Lange, Eds., Plenum Press, New York, 1978, pp. 495-506.
[29] Mendiratta, M. G. and Petrovic, J. J., *Journal of the American Ceramic Society*, Vol. 61, 1978, pp. 226-230.
[30] Land, P. L. and Mendiratta, M. G., *Journal of Materials Science*, Vol. 12, 1977, pp. 1421-1425.
[31] Lawn, B. R. and Marshall, D. B. in *Fracture Mechanics of Ceramics*, Vol. 3, R. C. Bradt, D. P. H. Hasselman, and F. F. Lange, Eds., Plenum Press, New York, 1978, pp. 205-229.
[32] Marshall, D. B. and Lawn, B. R., *Journal of the American Ceramic Society*, Vol. 61, 1978, pp. 21-27.
[33] Swain, M. V., Hagan, J. T., and Field, J. E. in *Fracture Mechanics of Ceramics*, Vol. 3, R. C. Bradt, D. P. H. Hasselman, and F. F. Lange, Eds., Plenum Press, New York, 1978, pp. 231-243.
[34] Soltis, T. R., Urick, P. A., and Hasselman, D. P. H., *Journal of the American Ceramic Society*, Vol. 61, 1978, pp. 89-90.
[35] Hasselman, D. P. H., Chen, E. P., and Urick, P. A., *Ceramic Bulletin*, Vol. 57, 1978, pp. 190-192.
[36] Tappin, G., Davidge, R. W., and McLaren, J. R. in *Fracture Mechanics of Ceramics*, Vol. 3, R. C. Bradt, D. P. H. Hasselman, and F. F. Lange, Eds., Plenum Press, New York, 1978, pp. 435-449.
[37] Petrovic, J. J., Dirks, R. A., Jacobson, L. A., and Mendiratta, M. G., *Journal of the American Ceramic Society*, Vol. 59, 1976, pp. 177-178.
[38] Evans, A. G., this publication, pp. 112-135.
[39] Wachtman, J. B., Jr., Capps, W., and Mandel, J., *Journal of Materials*, Vol. 7, 1972, pp. 188-194.
[40] Rudnick, A., Hunter, A. R., and Holden, F. C., *Materials Research and Standards*, Vol. 3, 1963, pp. 283-289.
[41] Evans, A. G. and Wiederhorn, S. M., *Journal of Materials Science*, Vol. 9, 1974, pp. 270-278.

R. H. Marion[1]

Use of Indentation Fracture to Determine Fracture Toughness

REFERENCE: Marion, R. H., **"Use of Indentation Fracture to Determine Fracture Toughness,"** *Fracture Mechanics Applied to Brittle Materials, ASTM STP 678,* S. W. Freiman, Ed., American Society for Testing and Materials, 1979, pp. 103-111.

ABSTRACT: In recent studies on indentation fracture in brittle materials, use of the cracks which form beneath a pointed indenter and grow stably with load has been suggested as a simple technique for the determination of fracture toughness (K_c). The applicability of this technique has been assessed by performing tests on a number of polycrystalline ceramics, glass-ceramics, and glasses which span a range of fracture toughness from 0.7 to 4.5 MN $m^{-3/2}$. Various sharp indenter geometries were tested and it was concluded that cracks produced with the Vickers indenter were the easiest to measure. The existing theories for calculating K_c from experimental measurements (crack length, load, etc.) have been evaluated and their applicability has been determined. The results demonstrate the usefulness of a Vickers pyramid in obtaining a qualitative ranking of K_c for a wide range of brittle materials. A number of practical problems associated with this technique are discussed.

KEY WORDS: fracture toughness, indentation fracture, brittle materials, brittle materials testing, sharp indenters, fracture (materials)

A number of studies have shown that the extent of surface cracking that originates from indentations made with a sharp indenter reflects the toughness of materials [*1-4*].[2] These early investigators used a theory based on the work required for crack formation to rank the crack resistance of various materials. Recently, two fracture mechanics analyses of indentation fracture have been formulated [*5,6*]. Both of these analyses consider the penny-shaped median crack which forms beneath a pointed indenter and grows stably as the load is increased. These theories provide a basis for obtaining the fracture toughness (K_c) from tests using sharp indenters. The ad-

[1]Member of technical staff, Sandia Laboratories, Albuquerque, N. Mex. 87185.
[2]The italic numbers in brackets refer to the list of references appended to this paper.

vantages of this approach are: (1) many tests can be performed on a small specimen not suitable for conventional fracture toughness testing; (2) the results are not influenced unduly by the preexisting flaw distribution (as they are with a spherical indenter) [5,6]; and (3) the simplicity and ease of this test. This method could be very useful in material development studies or in process control.

The use of sharp indenters to obtain K_c has been discussed recently by Mendiratta and Petrovic [7] and Evans and Charles [8]. Mendiratta applied the theory of Lawn and Swain [5] to data obtained for silicon nitride (Si_3N_4) and silicon carbide (SiC) with a Knoop indenter. They used indenter loads up to 30.4 N which produced cracks not much longer than the indent diagonal. Evans et al [8,9] used a Vickers indenter at loads up to approximately 70 N to study a wide range of ceramic materials. They did not use the aforementioned fracture mechanics analyses but derived a semi-empirical equation describing indentation fracture. Their analysis successfully spanned a large range of toughness and hardness. If a correction for hardness was not included in their analysis the correlation was not as good. Also, they found [9] that data on glass did not conform well with data on other ceramics.

The goal of the present work was to establish the validity of the indentation fracture technique for measuring K_c of glasses and polycrystalline ceramics (or, at least to accurately rank toughness of different materials) and to apply the technique to developmental glass-ceramic materials. We also sought to determine whether the special surface preparation described in Refs 7-9 was necessary or whether reliable data could be obtained on an as-received specimen surface. To accomplish these goals, tests have been performed on two polycrystalline ceramics, two glasses, and three glass-ceramics. The effects of various indenter geometries have been studied, the various theories for calculating K_c have been tested and the accuracy in determining K_c examined.

Theory

As mentioned previously, the fracture mechanics analyses in Refs 5 and 6 are based on the propagation of the penny-shaped median crack which forms beneath a pointed indenter (see Fig. 1). At some critical load the crack breaks through spontaneously to the free surface ("pop-in") and transforms into a well-developed, center loaded half-penny crack. If the specimen is unloaded before the critical load is reached, "pop-in" will be produced by the residual stresses developed during unloading and the dimensions of the radial traces produced will reflect the depth of cracking one would have obtained if the half-penny configuration had been realized prior to maximum loading [6]. Lawn and Fuller [6] found that the surface trace length, (2D'), was approximately twice the subsurface depth, D, of the cracks. Therefore, (in Fig. 1) $D \cong D'$. Both of the analyses to be presented apply only to "well-developed" cracks with $D/a \geq 2$ ($2a$ = indent diagonal (see Fig. 1)).

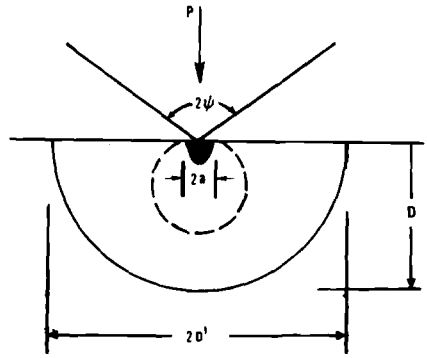

FIG. 1—*Illustration of parameters defining the median crack which forms during indentation.*

The crack configuration during indentation presents a complex elastic-plastic problem. Using a simplified fracture mechanics analysis, Lawn and Swain [5] obtained the equation for K_c

$$K_c = \frac{(1 - 2\nu)(\alpha p_o)^{1/2}}{2^{1/2}\pi^2\beta}\left(\frac{P}{D}\right)^{1/2} \tag{1}$$

where

P = indenter load,
D = crack depth,
ν = Poisson's ratio,
p_o = mean contact pressure,
α = dimensionless constant determined by the indenter geometry (typically, for a Vickers indenter $\alpha = 2/\pi$, and for an axially symmetric indenter $\alpha = 1$), and
β = dimensionless constant determined by the deformation zone geometry (for a Vickers or Knoop indenter [5, 7], $\beta \sim 2$).

For a pointed indenter which leaves geometrically similar impressions in a homogeneous specimen at all loads, the mean indentation pressure remains invariant and is equal to the hardness of the material [10]. Equation 1 predicts that for a given material a plot of P versus D will be a straight line. By measuring the hardness and the dependence of D (or D') on P, the fracture toughness can be calculated.

A second analysis, based on dimensional arguments for general penny-shaped cracks, predicts a different relation between the parameters [6]. This treatment yields a much simpler equation for calculating K_c

$$K_c = \frac{1}{\pi^{3/2}\tan\psi}\left(\frac{P}{D^{3/2}}\right) \tag{2}$$

where ψ is the indenter cone half angle. Equation 2 is strictly valid only for conical indenters, but it has been shown to yield a good fit to crack growth data obtained with a Vickers indenter [6]. In this case ψ is assumed to be 68 deg, the half-angle between the indenter faces. When there is friction between the indenter and specimen, ψ may be replaced by ψ plus arctan μ, where μ is the coefficient of friction. This analysis predicts that for a given material, a plot of P versus $D^{3/2}$ will be a straight line and that the hardness is not needed to calculate K_c.

Experimental Procedure

The materials studied are described in Table 1. All specimens had negligible surface residual stresses and thickness dimensions at least three times greater than the maximum crack depth (D) studied. For soda-lime glass, where both D and D' were measured, the back surface was found not to affect crack propagation when crack depths did not exceed one third of the specimen thickness (that is, the dependence of crack length on load did not change significantly as the crack depth increased). The crack lengths studied were always ten times greater than the maximum grain size or crystallite size for the crystalline or partly crystalline materials.

The effects of various indenter geometries, loading rate effects and a comparison of D and D' were all performed on soda-lime glass. Standard Knoop and Vickers indenters were used in addition to conical indenters with a half-

TABLE 1—*Materials tested and their properties.*

Material	Surface Condition	Vickers Hardness (GN/m^2)	K_c ($MN/m^{3/2}$)
Soda-lime silica float glass	as received (annealed)	5.5	0.75 [11]
Sodium borosilicate glass (B/Na = 0.2)	as poured (and annealed)	5.5	0.75 [12]
HR66B + CoO, a lithia-baria-silica glass-ceramic[a]	polished[b]	5.7	...
MS011, a zinc silicate glass ceramic (~30 volume % crystalline)[a]	polished[b]	6.9	1.0 [13]
Corning 0337 glass ceramic (~60 volume % crystalline)	as-fired[c] (to crystallize)	12.7	1.6 [14]
Wesgo Al-500 alumina	as-fired[c]	14.2	3.5 [15]
Diamonite P3142-1 alumina	as-fired[c]	15.7	4.5 [15]

[a]Glass-ceramic developed at Sandia Laboratories.
[b]Diamond sawn and then polished to decrease depth of surface residual stresses. Crack length measurements performed between final polishing increments indicated negligible surface residual stress.
[c]Machined prior to final firing.

angle $\psi = 30, 50, 70$ deg. The conical indenters were tungsten carbide with a tip radius <25 μm. The crack depth tests were performed on an Instron Testing Machine at crosshead rates of 0.05 mm/min to 0.5 mm/min. All the indents on soda-lime glass were performed with paraffin oil on the surface to decrease rate-dependent environmental effects. The growth of the cracks in the crack depth studies was followed with a traveling microscope; inaccuracies in the measuring technique were found to be insignificant in comparison to the scatter in results from crack to crack.

All the tests on the other materials listed in Table 1 were performed at a crosshead rate of 5.0 mm/min with a Vickers indenter. Oil was not used on the surface. Also, only surface crack length measurements were performed on these materials because all of them except the sodium borosilicate glass are opaque. All the surface crack length measurements (including those on soda-lime glass) were obtained from photographs taken of the cracks. The cracks on opaque specimens were made visible by use of a dye penetrant. The photographs of cracks in the transparent glasses were taken in transmission with polarized light.

Data were collected on each sample at four or more indenter loads, P, with a minimum of three indents made at each load. Data were gathered only for well-developed cracks ($D'/a \geq 2$). Cracks with $D'/a < 2$ fall within the realm of "elastic/plastic" indentation fields [*8,9*] and, accordingly, tend to be less reliable. Occasionally, cracks formed which were not collinear with the Vickers indent diagonal and sometimes extensive spalling occurred. Indents with these characteristics were not included in the results. Since residual stresses form upon unloading, the indents were spaced a few diameters (D or D') apart when repeated tests were performed on the same sample. The indenter tips were checked periodically to ensure their integrity and geometry.

Vickers hardness measurements were performed on a Shimadzu microhardness tester using a 15 s load time. The hardness was measured as a function of load to ensure that the value obtained was in the load-independent regime.

Results

A comparison of cracks produced with various indenter types on soda-lime glass demonstrated that those produced with the Vickers indenter were the easiest to measure and had the smallest scatter. The Knoop indenter produced surface cracks which were not much longer than the long indent diagonal and they were difficult to measure. Also, a comparison of the slopes of P versus D (or P versus $D^{3/2}$) with P versus D' for $P(D')^{3/2}$) for a Knoop indenter indicated that either $D \neq D'$ or the measurements of D' were incorrect. (D and D' were not measured simultaneously for the same crack; they were measured for different indents on the specimen. Because there are two possible sources of error ($D \neq D'$ and difficulty in measuring D'), it

seemed best to compare slopes.) The $\psi = 70$ deg conical tip gave results approximately the same as the Vickers indenter (angle between faces = 68 deg) but the surface crack lengths had larger scatter and were more difficult to measure than for the Vickers indenter. The Knoop and conical indenters need higher loads than a Vickers point to produce cracks of the same length.

A comparison of the data obtained using crack depth (D) and surface crack length (D') on soda-lime glass indicated that for a Vickers indenter $D = D'$, in agreement with Ref *6*. In the tests where crack depth was measured it was found that the dependence of D on P was a function of the loading rate (for slow loading rates) even with oil on the surface. At loading rates greater than 0.2 to 0.5 mm/min, variations due to kinetic effects (caused by rate-dependent environmental effects) were within the accuracy of measurement of D. The effect of loading rate was not as pronounced in the surface crack length (D') studies on soda-lime glass. Based on these results on soda-lime glass, a loading rate of 5 mm/min was chosen for obtaining surface crack length data on the other materials. As mentioned previously, a Vickers indenter was used in all these experiments.

Typical examples of the data obtained are given in Figs. 2 and 3 where P versus D' and P versus $(D')^{3/2}$ are plotted for Diamonite alumina and MS 011 glass-ceramic. These types of plots were made for all materials and a least-squares straight line was fitted to the data. The root-mean-square error in the fit was approximately the same for P versus D' and P versus $(D')^{3/2}$. Therefore, it appears that neither theory fits the data better than the other. Summary plots of the least-squares fit line for all materials are given in Figs. 4 and 5. It can be seen that as K_c of the material increases (compare with Table 1), the slopes of the lines increase. This is in qualitative agreement with Eqs 1 and 2.

The quantitative accuracy of K_c calculated with Eqs 1 and 2 is shown in Fig. 6. The correlation between K_c obtained from indentation fracture and

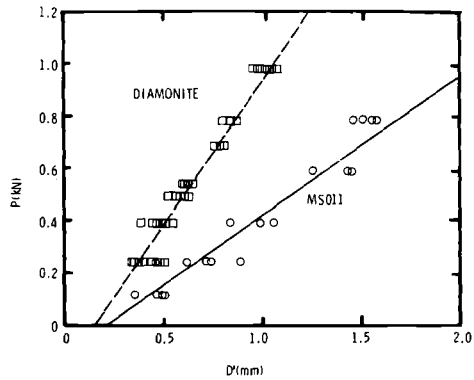

FIG. 2—P *versus* D' *for diamonite P 3142-1 alumina and MS 011, a zinc silicate glass ceramic. The straight lines are least squares fit to the data.*

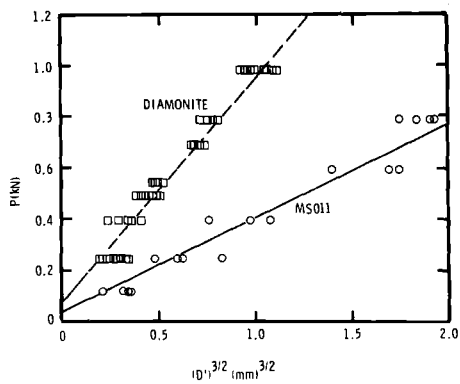

FIG. 3—P *versus* $(D')^{3/2}$ *for Diamonite P3142-1 alumina and MS 011, a zinc silicate glass ceramic. The straight lines are least squares fit to the data.*

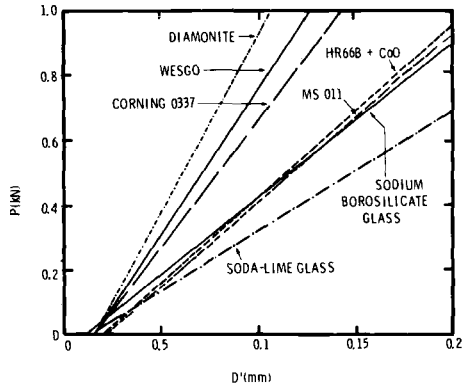

FIG. 4—P *versus* D′ *composite plot for all materials studied (see Table 1). Only the least-squares straight line fits obtained from plots similar to Fig. 2 are plotted.*

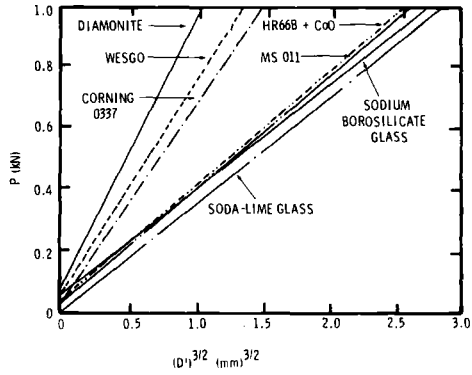

FIG. 5—P *versus* $(D')^{3/2}$ *composite plot for all materials studied (see Table 1). Only the least-squares straight line fits obtained from plots similar to Fig. 3 are plotted.*

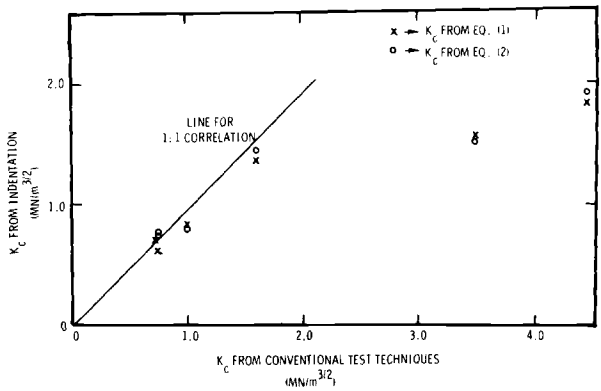

FIG. 6—K_c *calculated by methods described in this paper versus* K_c *calculated by conventional fracture mechanics techniques. The straight line indicates the locus for a 1:1 correlation between the two methods.*

K_c obtained by conventional test techniques is good for the lower toughness materials, but it is only qualitatively correct for the alumina ceramics. The results for HR 66B + CoO glass ceramic are not shown in this figure because K_c determined by conventional techniques is unknown (it is estimated to be similar to MS 011). For this material K_c from indentation fracture was 0.8 and 0.85 MN/m$^{3/2}$ from Eqs 1 and 2, respectively.

An attempt was made to apply the empirical analysis of Evans et al [*8*] to the data obtained in this study. They present a master curve in a plot of $K_c\phi/p_o\sqrt{a}\,(p_o/\phi E)^{0.4}$ versus D'/a which described the behavior of all their results except glasses (ϕ is a constraint factor). The loads used in the present study are approximately ten times higher than in Ref *9* (which contains the data for Ref *8*). With these high loads, the lateral cracking near the indent caused by the residual stresses formed on unloading [*5,6*] made it difficult to measure a, the indent half diagonal. However, for the sparse data available it appears that it does not fit their master curve.

Discussion and Conclusions

The results presented in the preceding section demonstrate that indentation fracture may be very useful in obtaining a ranking of the fracture toughness but that the magnitudes of the values obtained may differ from values obtained by conventional fracture mechanics methods. As Evans and Charles [*8*] have observed, the problems appear most pronounced in specimens of high hardness. Hardness is important in crack propagation because it affects the stresses produced by the indenter.

It appears that Eqs 1 and 2 are equally reliable for calculating K_c. Due to the simplicity of Eq 2, it is preferable for rapid determination of fracture toughness. From Figs. 4 and 5 it is obvious that a ranking of the toughness of

materials can be obtained by measuring P and D' at one load, preferably a high load. Therefore, by making a 5 to 10 indents at one load on each material, the toughness values can be ranked. This can be done with any simple loading apparatus.

The results presented on experimental technique suggest that one should use a Vickers indenter and a fairly fast loading rate. One needs the fairly fast loading rate to eliminate rate dependent environmental effects such as those described in this paper for soda-lime glass. The use of large loads (and the resulting large cracks) eliminates the need for a highly polished surface. Another advantage of large cracks is that residual stresses very near the surface do not have as large an effect on the propagation of the median crack as they do for small cracks. Therefore, more representative results can be obtained on samples containing small amounts of residual stress which may have been caused by surface finishing. However, one must be aware that residual stresses can change the slope and intercept of plots of P versus D' or P versus $(D')^{3/2}$.

Acknowledgment

This work is supported by the United States Department of Energy.

References

[1] Palmqvist, S., *Jernkontorets Annaler,* Vol. 141, No. 5, 1957, pp. 300-307.
[2] Palmqvist, S., *Archiv für das Eisenhüttenwesen,* Vol. 33, 1962, pp. 629-634.
[3] Dawihl, W. and Altmeyer, G., *Zeitschrift für Metallkunde,* Vol. 55, No. 5, 1964, pp. 231-237.
[4] Exner, H. E. in *Transactions of the Metallurgical Society,* American Institute of Mining, Metallurgical, and Petroleum Engineers, Vol. 245, No. 4, 1969, pp. 677-683.
[5] Lawn, B. R. and Swain, M. V., *Journal of Materials Science,* Vol. 10, 1975, pp. 113-122.
[6] Lawn, B. R. and Fuller, E. R., *Journal of Materials Science,* Vol. 10, 1975, pp. 2016-2024.
[7] Mendiratta, M. G. and Petrovic, J. J., *Journal of Materials Science,* Vol. 11, 1976, pp. 973-976.
[8] Evans, A. G. and Charles, E. A., *Journal of the American Ceramic Society,* Vol. 59, No. 7-8, 1976, pp. 371-372.
[9] Evans, A. G. and Wilshaw, T. R., *Acta Metallurgica,* Vol. 24, 1976, pp. 939-956.
[10] Tabor, D., *Hardness of Metals,* Clarendon, Oxford, 1951.
[11] Wiederhorn, S. M., *Journal of the American Ceramic Society,* Vol. 52, No. 2, 1969, pp. 99-105.
[12] Eagan, R. J. and Swearengen, J. C., *Journal of the American Ceramic Society,* Vol. 61, No. 1-2, 1978, pp. 27-30.
[13] Swearengen, J. C. and Eagan, R. J., *Journal of Materials Science,* Vol. 11, 1976, pp. 1857-1866.
[14] Beauchamp, E. K., "Crack Propagation and Failure Prediction in a Glass-Ceramic," Technical Report No. SAND 75-0273, Sandia Laboratories, Albuquerque, N. Mex., 1975.
[15] Swearengen, J. C., unpublished results, Sandia Laboratories, Albuquerque, N. Mex.

A. G. Evans[1]

Fracture Toughness: The Role of Indentation Techniques

REFERENCE: Evans, A. G., **"Fracture Toughness: The Role of Identation Techniques,"** *Fracture Mechanics Applied to Brittle Materials, ASTM STP 678*, S. W. Freiman, Ed., American Society for Testing and Materials, 1979, pp. 112-135.

ABSTRACT: The quantitative measurement of the radial fractures that occur around hardness indentations in brittle materials has long been advocated as a measure of the fracture toughness. The evolution of the technique and the fundamental basis for toughness determination by indentation are described. The latest experimental results on a range of brittle materials are used to demonstrate the utility of the technique. Finally, the role of the technique, within the toughness testing repertoire, is discussed.

KEY WORDS: fracture (materials), brittle materials, crack propagation, indentation, toughness, residual stresses

The incidence of radial fracture around hardness indentations in brittle materials has been observed since the inception of hardness testing. Initially, the cracks were regarded as a nuisance and a detriment to effective hardness measurements on brittle materials. However, Palmqvist [*1,2*][2] recognized that the cracks must afford a measure of the toughness of the material. He then suggested that the average length of the cracks $<l>$, emanating from the corners of a Vickers' indent (Fig. 1*a*) might be a measure of the relative toughness. Palmqvist worked exclusively on carbides and found that the load P increased linearly with the crack length, often with an intercept P_o on the load axis. His toughness measure was the slope of this linear plot, which, he observed, varied considerably from one alloy to another. An important extension of Palmqvist's method was introduced

[1]Formerly, group leader, Science Center, Rockwell International, Thousand Oaks, Calif. 91360., and now with the Department of Materials Science, Hearst Mining Bldg., University of California, Berkeley, Calif. 94720.

[2]The italic numbers in brackets refer to the list of references appended to this paper.

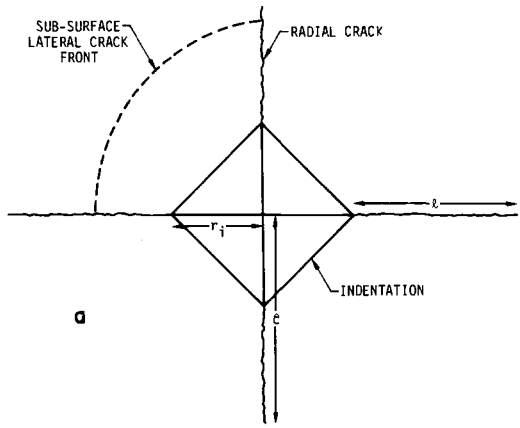

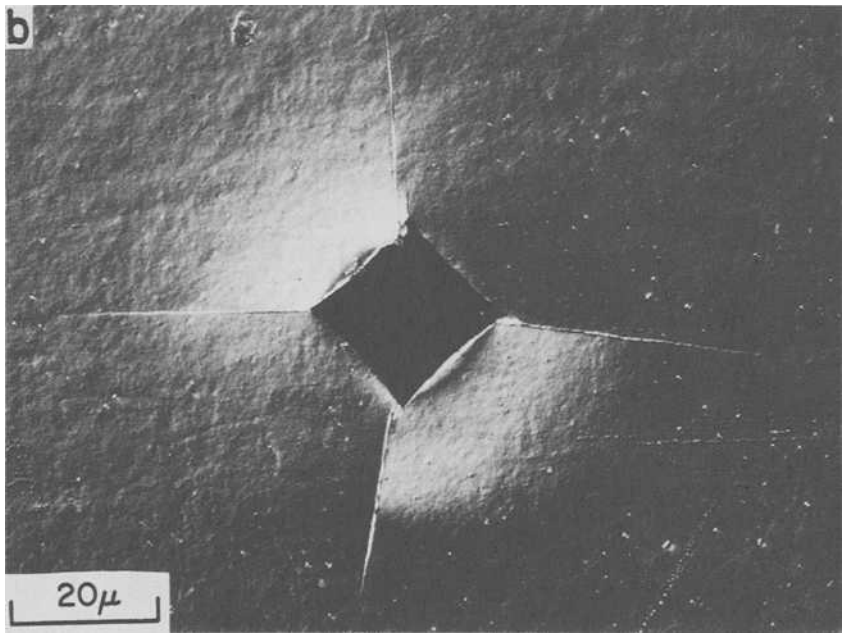

FIG. 1—*Indentation cracks introduced by a Vickers indenter* (a) *schematic showing the parameters used in the test.* (b) *a typical crack pattern obtained in* Si_3N_4 *(polarized light reflected micrograph).*

subsequently by Dawihl and Altmeyer [3]. They noticed that the dependence of the crack length on the load was influenced by the character of the surface. They correctly attributed this dependence to the presence of residual surface compression introduced by grinding, and eliminated the problem by performing their tests on specimens with carefully polished surfaces. The significance of residual surface stresses will be one of the important themes of this paper.

A resurgence of interest in indentation toughness occurred quite recently, following the pioneering work on the principles of indentation fracture by Lawn et al [4-6]. This paper intends primarily to demonstrate that, on the basis of these recent developments, the indentation technique has been established as a viable technique for the approximate determination of the toughness of many brittle materials.

The first of the recent studies was reported by Lawn and Fuller [6]. Working primarily on glass, they discovered that the crack radius $\hat{c}$ (Fig. 1*a*) increased with load as $P^{2/3}$, and that $\hat{c}$ depended on the profile of the indenter as well as the friction coefficient. These observations were rationalized by a dimensional fracture mechanics analysis of three-dimensional (conical or semicircular) cracks, forming under the influence of a localized force acting on the surface. However, there is an apparent disparity between the functional dependence of the crack length on load between the Palmqvist-Dawihl-Altmeyer data [1-3] and the Lawn-Fuller data [6]. This was recognized and verified by Evans and Wilshaw [7] in their indentation fracture studies on ceramic polycrystals. They suggested that the disparity could be resolved by recognizing the essential elastic/plastic character of the indentation field, and extending the dimensional fracture mechanics analysis from the elastic into the elastic/plastic regime. The ratio of the toughness K_c to the hardness, H, emerged from this analysis as the key parameter that dictates the indentation fracture. Extensive data obtained by Evans and Charles [8] confirmed these expectations and allowed a "universal" indentation fracture curve to be established (if, following Dawihl and Altmeyer [3], the role of surface compression stresses was recognized and their effect minimized). The essential details of the elastic/plastic fracture mechanics analysis were substantiated further by a sequence of analyses performed by the Cambridge group [9-12] and by results reported in this paper.

Analyses of identation stress fields, and of indentation fracture are described in this paper, in the detail needed to both rationalize the observed fractures and to develop characterization schemes for indentation fracture (that afford a suitable basis for fracture toughness determinations). The analyses are not rigorous, because of the extreme complexity of the indentation fracture process. They provide a knowledge of the parameters that are likely to be involved in determining the extent of the indentation fracture. Finally, the probable role of the indentation technique within the repertoire of available toughness techniques is developed.

Fracture Observations

Radial cracks can be obtained using spherical and sharp indenters [*7,11*]. However, the standard Vickers' indenter is the most suitable configuration for toughness determination, because four cracks are obtained consistently, emanating from the corners of the indentation (Figs. 1*a* and *b*).[3] The cracks frequently are observed to terminate without fully penetrating the contact zone [*7,11*] (Fig. 2*a* and *b*); especially in the softer materials or at small relative crack lengths. This observation clearly indicates the presence of substantial compressive stresses adjacent to the contact zone. Observations on transparent specimens [*7*] and on specimens fractured from the indentation precrack [*13*] indicate that the radial cracks are approximately symmetric about the indentation site. Also, direct crack evolution observations indicate that, often, much of the radial crack extension occurs during

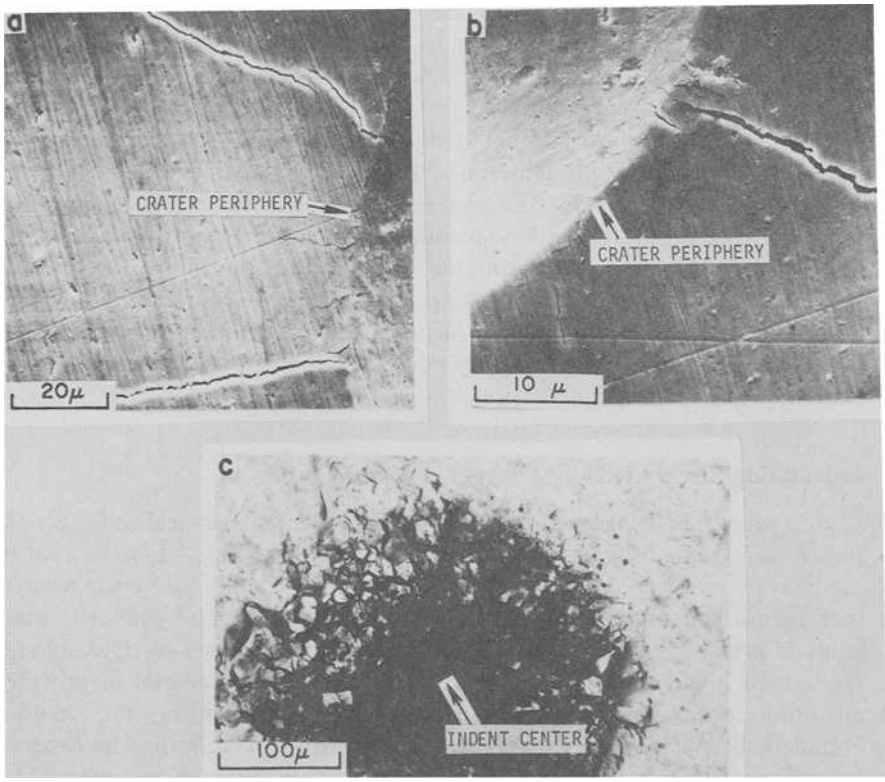

FIG. 2—(a, b) *Indentation cracks obtained in ZnS showing crack termination near the indentation interface,* (c) *indentation microcracking obtained in fully dense sintered* Al_2O_3 *(lucalox), transmitted light optical micrograph.*

[3]Knoop indenters also have been used [*8*], but these proved inappropriate for toughness determinations and will not be considered further.

load removal [*4,7,10*], indicating an important residual stress effect. The residual stresses also provide an appreciable crack opening at zero load that facilitates the observation of the cracks in the optical microscope. The indentation generally is accompanied by subsurface lateral fractures [*4,5,7, 10*] that can cause material elevation adjacent to the indentation (Fig. 1*b*) [*7,10*]. These cracks normally do not impede effective measurements of the radial crack extension.

The incidence of dislocation plasticity in the immediate vicinity of the indentation has been amply confirmed (in crystalline materials) by transmission electron microscopy [*14*] and by etch studies [*7*]. However, the latter also indicates that the plastic zone radius r_p along the surface (in isotropic polycrystals) is only slightly larger than the indentation radius, r_i (that is, $r_p \sim 1.1 - 1.3\, r_i$). A similar result has been obtained analytically [*15*], and by numerical results reported in the next section. Hence, despite the local plasticity, the surface extension of the radial cracks occurs primarily in material subjected only to elastic strains. This is important to the subsequent fracture analysis, which employs principles of linear elastic fracture mechanics.

Finally, it is emphasized that distinct radial cracks are not observed for at least one class of materials. These are relatively coarse grained materials ($\gtrsim 20\ \mu$m grain size), sintered to full density (translucency) with the aid of specific additives; these include, alumina sintered with magnesium oxide (MgO) (lucalox), MgO sintered with lithium fluoride (LiF). Identations in these materials are accompanied by extensive grain boundary fractures, in a symmetric pattern around the indentation site (Fig. 2*c*), for reasons that are not yet comprehended. The toughness of these materials cannot be obtained by indentation.

Indentation Stress Fields

This section is concerned with the development of generalized elastic/plastic stress fields pertinent to indentation problems. Elastic/plastic indentation stress fields are not known in complete detail. However, results that permit indentation fracture to be rationalized can be deduced from analytic pressurized cavity analyses and numerical analyses of rigid sphere indentation. The results for spherical indenters are considered to provide an appropriate conceptual framework for comprehending the results obtained for Vickers' indenters, because of strong similarities in experimental crack length measurements for spherical and Vickers' indenters [*7*]. The principal quantitative discrepancies will occur for very small cracks, which experience strong interactions with the corners of the indenter. The tangential stresses are of primary interest for radial fracture; hence, for conciseness, results will be presented only for this component of the stress field.

The elastic/plastic solution for a spherical cavity, radius r_i, subjected to an internal pressure p has been known for some time (Fig. 3) [*16*]. The tangential stress within the plastic zone in an infinite body at a distance r from the center is given for a perfectly plastic material by [*16*]

$$(\sigma_\theta{}^p/\sigma_y) = -2 \ln (r_p/r) + 1/3 \qquad (r < r_p) \tag{1}$$

where r_p is the plastic zone radius and σ_y is the uniaxial yield stress;[4] while the elastic stress is [*16*]

$$(\sigma_\theta{}^e/\sigma_y) = (r_p/r)^3/3 \qquad (r < r_p) \tag{2}$$

The peak tensile stress thus occurs at the elastic/plastic boundary (Fig. 3);

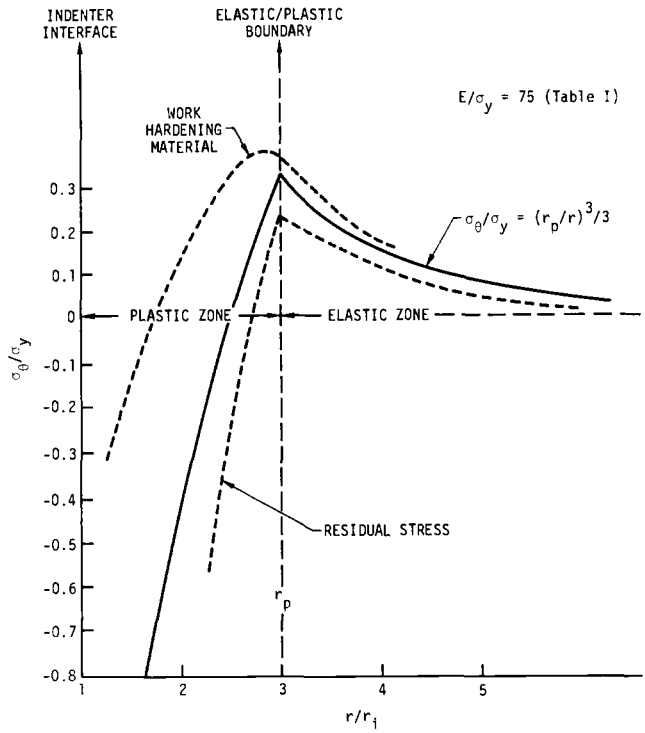

FIG. 3—*The elastic/plastic indentation field for a spherical cavity, plotted for a* E/σ_y (~ 75) *typical of ceramic polycrystals (Table I).*

[4]The uniaxial yield stress (compressive or tensile) is related to the hardness (see Eq 11), and in brittle materials is inferred from hardness measurements.

the stress at the cavity wall is compressive. This stress distribution is modified by work hardening. The principal effect of work hardening (by analogy with the crack tip problem [*17*]) will presumably be to displace the peak tension toward the cavity surface (Fig. 3), but, of greater significance for indentation fracture, the stresses in the elastic zone should be relatively unchanged.

Indentation fracture observations are performed after the indenter has been removed; hence, the residual stresses are of considerable interest. Since the outer layers elastically compress the inner layers during the unloading process, the residual stresses are obtained by subtracting the elastic unloading stresses [*16*]. Thus, in the elastic zone, the stress at a pressure p_u during unloading is

$$(\sigma_\theta{}^e/\sigma_y) = (1/r^3)\,[(r_p{}^3/3) - ((\hat{p} - p_u)/2\sigma_y)r_i{}^3] \qquad (r > r_p) \tag{3}$$

where $\hat{p}$ is the peak pressure. The elastic stresses exhibit consistent spatial characteristics throughout, and just decrease as the pressure decreases (Fig. 3). In the plastic zone

$$(\sigma_\theta{}^p/\sigma_y) = -2\ln(r_p/r) + 1/3 - [(\hat{p} - p_u)/2\sigma_y)]\,(r_i/r)^3 \qquad (r < r_p) \tag{4}$$

The stresses in the plastic zone decrease rapidly during unloading (Fig. 3), until reverse yielding ($\sigma_\theta - \sigma_r = \sigma_y$) occurs near the cavity surface.

Two other relations derived for the infinite medium are of interest. The pressure needed to expand the cavity (p_o) is found to be constant and related to the yield stress and Young's modulus, E, by [*16*]

$$\frac{p_o}{\sigma_y} = \frac{2}{3}\left[1 + \ln\left(\frac{E}{3\sigma_y(1-\nu)}\right)\right] \tag{5}$$

where ν is Poisson's ratio. The plastic zone radius also is found to be related to the ratio E/σ_y by [*16*]

$$\left(\frac{r_p}{r_i}\right)^3 = \frac{E}{3\sigma_y(1-\nu)} \tag{6}$$

In general, therefore, at any stage in the pressure cycle, the tangential stresses are given by the functions

$$(\sigma_\theta{}^e/p_o)\,R\,(r/r_i) = R_p\,(E/p_o,\nu) + P_1\,(p_u/p_o, E/p_o, \nu) \tag{7a}$$

$$(\sigma_\theta{}^p/p_o) = 1/3 + R_p{}'\,(E/p_o, r/r_i, \nu) + R\,(r/r_i)\,P_2\,(E/p_o, p_u/p_o, \nu) \tag{7b}$$

where R is a function that essentially determines the scale of the elastic stress field ($\equiv (r/r_i)^3$); R_p and R_p' are functions that reflect the influence of the plastic zone radius, and P_1 and P_2 are functions that dictate the stress adjustments that occur during unloading.

The limitation of the spherical cavity solution for detailed indentation analysis is exposed when it is recognized that the elastic stresses (Eq 2) at large r are not consistent with the point force indentation field obtained by Bousinesq [*18*] and, therefore, do not satisfy St. Venant's principle. For reference purposes, the point force solution is

$$\sigma_\theta{}^e = -\frac{P}{2\pi r^2}(1-2\nu)\left[1 - \frac{(z/r)}{[1+(z/r)^2]^{1/2}} - \frac{(z/r)}{[1+(z/r)^2]^{3/2}}\right] \quad (8)$$

where z is the depth below the surface and r is the distance along the surface. The primary features to note are the $1/r^2$ spatial dependence and the *compressive* character of the tangential stress.

However, interpolation between the elastic/plastic solutions (Fig. 3) and the elastic solution (Eq 8) can be used to construct the hypothetical tangential near-surface stress distribution shown in Fig. 4. The important features of the stress field are the peak tension ($\sim \sigma_y/3$) at the elastic/plastic boundary, the large compression in the plastic zone at the indenter interface, and the remote elastic compression. The large compression very close to the interface would restrict crack extension into the indentation surface, as

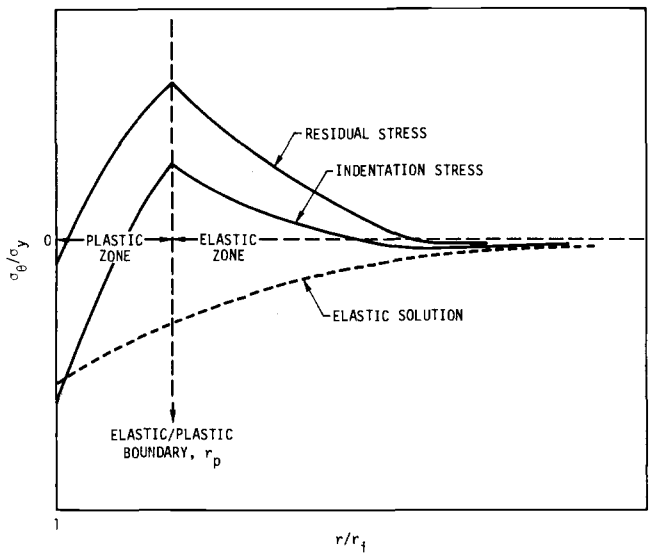

FIG. 4—*A hypothetical tangential surface stress distribution for indentation of a hard material.*

observed experimentally (Fig. 2*a* and *b*) while the compression in the elastic zone remote from the indentation would provide a restriction to outward radial crack extension. The finite element results of Hardy et al [*19*] obtained for a perfectly plastic material [*17*], although rather limited in scope, indicate similar behavior adjacent to the indentation site; and suggest, in addition, that the surface tension only develops when the plastic penetrations are appreciable (that is, at loads > 40 times the initial plastic penetration load). Experimental observations at large penetrations [*20*] also have confirmed the existence of tangential tension at the surface. However, the characteristics of the tangential stress field depicted in Fig. 4 have not been substantiated totally. A finite difference calculation of the stress field generated by rigid sphere indentation thus has been generated. The plastic properties of the material studied in the calculation were expressed in terms of a (linear work hardening) Meyers law relation

$$p = \sigma_y (r_i/r_o)^{2+n} \tag{9}$$

where n is the work hardening coefficient and r_o is an empirical constant. Specific plastic and elastic properties pertinent to polycrystalline MgO ($\sigma_y =$ 2 GPa and $n = 0.3$) were chosen for the calculation. A Lagrangian computational scheme was used to obtain the stresses [*21*]. The calculation was conducted by applying a force to the indenter at a constant velocity, sufficient to achieve a contact equal to half the sphere radius. Then, the force was held constant until the stresses approached equilibrium. The equilibrium plastic zone and the corresponding out-of-plane tensions are shown in Fig. 5*a*. The plastic zone shape and size are consistent both with observation [*7*] and with available analytic solutions [*13*]. The tangential tensions at the surface are plotted in Fig. 5*b*; a good correspondence with the postulated field (Fig. 4) is apparent. The only noteworthy difference is that the magnitude of the peak tension at the elastic/plastic boundary ($\sim 0.25\sigma_y$) is less than that predicted by the cavity solution.

The extension of the stress field analysis to unloading is particularly significant. As already discussed, residual stresses caused by the indentation plasticity are obtained by subtracting the unloading elastic stress field from the elastic/plastic field. In this instance, therefore, the unloading elastic stresses, given by the Hertz solution [*10*], would generate an *enhanced* tension at the surface

$$\sigma_\theta{}^e = \frac{1 - 2\nu}{2} (\hat{p} - p_u) (r_i/r)^2 \tag{10}$$

The maximum surface tension should thus pertain at zero load, as shown in Fig. 4. Tensile stress enhancement also is observed in the finite element solution [*19*], adding credence to the postulated form of the residual stress

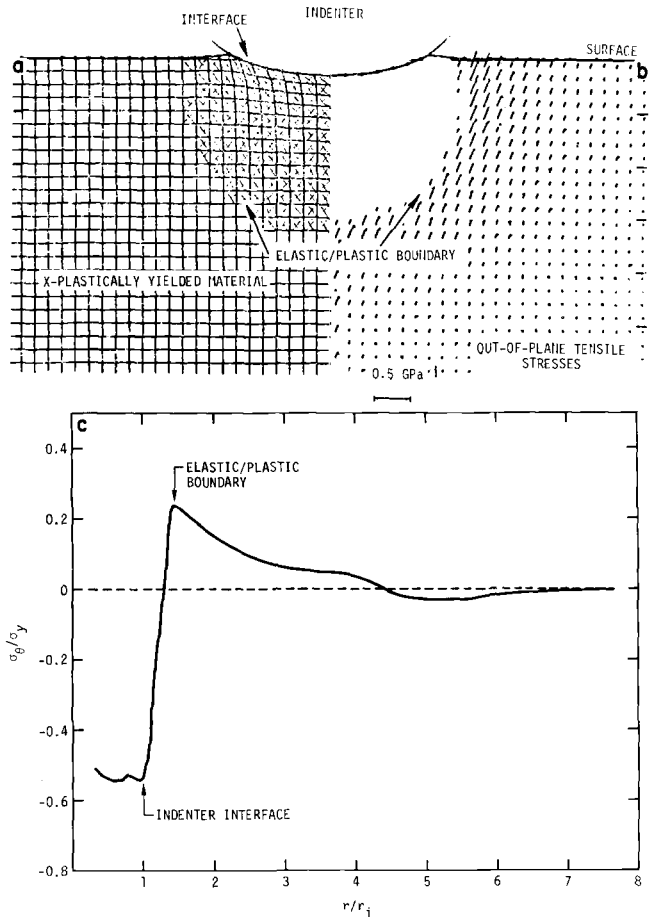

FIG. 5—*The solutions for the finite difference calculation of indentation by a rigid sphere.* (a) *The zone of plastic deformation,* (b) *the out-of-plane tensile stresses on a section through the impact center, the lines indicate the magnitude (with reference to the scale) of the maximum out-of-plane tensions at each grid point (the compressive stresses are not plotted),* (c) *the tangential stresses at the surface.*

distribution. The elevation of the tension in the elastic zone during unloading is quite different from the spherical cavity result (Fig. 3), but is consistent with the observations of radial crack extension during unloading [*7,10*].

Two related features of the indentation process that require brief mention are the influence of a fixed profile (rather than spherical) indenter—such as a Vickers' indenter—on the stress field, and the relation between the indentation pressure and the plastic properties of the material. The use of a fixed profile indenter leads to a constant state of plastic strain

at the indenter interface. Hence, even for work hardening materials, variation in the stress field amplitude with penetration should be relatively minor. The amplitude of the stress field will reflect the flow stress at the interface strain (~ 8 percent for a Vickers' indenter), and this flow stress should replace the uniaxial yield stress in the stress field equations. The indentation pressure is also modified by the indenter geometry. Solutions have been derived by extending the spherical cavity result [*9,22*] (Eq 5) to fixed profiles. No specific account has been taken of free surface effects that might influence the pressure distribution in a semi-infinite medium. Nevertheless, the solutions compare very well with experimental observations. The latest solution is the most complete [*22*], and yields the following relation for a fixed profile indenter

$$\frac{p}{\sigma_y} = 0.5 + \frac{2}{3}\left\{1 + \ln\left[\left(\frac{E}{\sigma_y}\right)\frac{\tan\beta}{3}\right]\right\} \tag{11}$$

where β is the contact angle.

Apparent divergence from this relation may occur in very hard materials, manifested as an indentation pressure that increases at low loads. This apparent divergence is the result of distortion of the indentation by elastic compression during unloading; this leads to reduced definition of the indentation diagonal. (Also, small inelastic recovery effects caused by reverse plastic flow might be involved.) Therefore, indentation toughness determinations normally must be performed at relatively *large loads*, well within the load independent regime, if valid results are to be obtained. When small loads need to be employed, it is important to obtain indentation measurements at high resolution (for example, in the scanning electron microscope) to minimize the errors introduced by recovery effects.[5]

To summarize, it is apparent that elastic/plastic indentation fields have been explained qualitatively in terms of available solutions, but the quantitative details have not been substantiated fully; a comprehensive numerical analysis is needed for this purpose. However, these results are not a prerequisite to interpretation of the indentation fracture behavior at the level needed to develop a toughness technique: the general expressions (Eqs 7*a* and *b*) suffice. These expressions emphasize that the amplitude of the stress field is dictated primarily by the uniaxial flow stress σ_y (or the pressure p_o), while the extent (or scale) of the stress field is determined by the contact radius r_i and, to a lesser extent, by the plastic zone radius (through the ratio E/σ_y). A possible influence of friction at the indenter interface also should be admitted, through a friction coefficient μ.

[5] For example, in the relatively hard/tough ceramics (Si_3N_4, SiC, Al_2O_3), loads between 100 and 500 N (10 and 50 kg) are required; for WC/Co, 300 to 1000 N loads are used; while for the softer or more brittle materials (ZnS, ZnSe, PZT), loads between 10 and 200 N are usually adequate.

Indentation Fracture

Parametric Analysis

This section uses the generalized stress analysis described in the previous section in conjunction with linear elastic fracture mechanics concepts to develop parametric relations for the indentation crack length. Brittle fracture problems in semi-infinite media can be solved conveniently by linear superposition methods [*23,24*]. These methods allow the stress intensity factor K to be computed from the prior stress field, using an appropriate Green's function. Then, K can be equated to the fracture toughness K_c, in order to provide a description of the crack extension behavior.

For a penny crack, radius c, in an infinite medium, the stress intensity factor K can be written explicitly as [*23*]

$$K_I\Big|_{\theta=0} = \frac{2}{(\pi c)^{3/2}} \int_0^c \int_0^\pi \frac{\sigma(\theta,r)\,[1 - (r/c)^2]^{1/2}}{[1 - 2(r/c)\cos\theta + (r/c)^2]}\, r dr d\theta \qquad (12)$$

where

r = distance from the crack center,
θ = angular location on the crack surface with respect to the position of interest, and
$\sigma(\theta,r)$ = stress normal to the crack surface.

Similar expressions obtain for the Modes II and III stress intensity factors [*23*]. It is convenient for subsequent analysis to rewrite Eq 12 in terms of dimensionless quantities. For this purpose, let the stress be given by

$$\sigma = \hat{\sigma}\, f(r,\theta) \qquad (13)$$

where $\hat{\sigma}$ represents the stress amplitude and f is a dimensionless function that represents the spatial characteristics of the stress field. Then, the dimensionless result is

$$\frac{K}{\hat{\sigma}\sqrt{c}} = \left(\frac{2}{\pi^{3/2}}\right) \int_o^1 \int_o^\pi \frac{f(\xi,\theta)\,[1 - \xi^2]^{1/2}}{[1 - 2\xi\cos\theta + \xi^2]}\, \xi d\xi d\theta \equiv \lambda \qquad (14)$$

where $\xi = r/c$ and λ is a dimensionless parameter that depends only on the spatial details of the stress field and the location on the crack front. For a surface crack in a semi-infinite solid, analogy with the two-dimensional result [*23*] indicates that K will be larger than the value predicted by Eq 14, by an unspecified dimensionless factor $F(\xi,\theta)$ in the integrand (the angular dependence of F must be small since indentation cracks are observed to be nearly semi-circular (section on Fracture Observations)).

This result can be used in conjunction with the generalized elastic/plastic stress field (Eq 7) to obtain a general relation between the toughness and the crack length. Since the radial cracks are confined largely to the elastic zone (section on Fracture Observations), the K solution initially will be derived in terms of the elastic stress field (Eq 7*a*), as

$$\frac{K}{p_o\sqrt{c}} = \left(\frac{2}{\pi^{3/2}}\right)\int_o^1\int_o^\pi \frac{(1-\xi^2)^{1/2}F(\xi)\,\xi}{[1-2\xi\cos\theta+\xi^2]} \left\{\frac{R_p(E/p_o,\nu)+P_1(E/p_o,\,p_u/p_o,\nu)}{R(c/r_i,\xi)}\right\} d\xi d\theta \qquad (15)$$

$$\equiv h(c/r_i,\,E/p_o,\,p_u/p_o,\,\nu)$$

where h is a dimensionless function. An equivalent, but more convenient, form of Eq 15 is

$$\frac{K}{p_o\sqrt{r_i}} = g(c/r_i,\,E/p_o,\,p_u/p_o,\,\nu) \qquad (16)$$

where g is another dimensionless function. Equating K to the critical value K_c, and noting that p_o is just the hardness H, the maximum radial crack length $\hat{c}$ becomes

$$\frac{K_c}{H\sqrt{r_i}} = \hat{g}(\hat{c}/r_i,\,E/H,\,p_u{}^c/H,\,\nu) \qquad (17)$$

where $p_u{}^c$ is the applied pressure at which $c = \hat{c}$. Now, suppose that, as most observations suggest, the maximum crack extension is attained at $p_u{}^c \sim 0$ (see section on Fracture Observations), and that the Poisson ratio influence is minor. Then, since the only remaining variables in Eq 17—the ratios $\hat{c}/r_i$ and E/H—are *independent*, the crack extension relation reduces to

$$\frac{K_c}{H\sqrt{r_i}} \quad g_1(\hat{c}/r_i)\,g_2(E/H) \qquad (18)$$

where g_1 and g_2 are independent dimensionless functions. Precisely the same result can be obtained by dimensional analysis (Appendix), once the variables that are expected to influence the fracture process have been defined by aforementioned stress/fracture analyses. However, it is important to recognize that the analysis indicates that the independence of g_1 and g_2 will be compromised if the stresses within the plastic zone exert

an important influence on the crack extension (a consequence of the interdependence of E/p_o and r/r_i in the term R_p in Eq 7*b*). Additional dependencies will be involved if Poisson's ratio exerts a significant influence, or if the frictional effects at the interface depend on material variables other than E/H. In the present scheme, the important influences must be ascertained by experiment: throughout, retaining an awareness of the variables that can be involved.

Before embarking on a detailed data analysis, it is instructive to examine a possible large crack length asymptote. By regarding the indenter as a wedge and applying the solution for a penny crack wedged by a force Q at the center [*23*], $K = Q/(\pi c)^{3/2}$, a crack extension relation can be obtained for a Vickers' indenter as

$$\frac{K_c}{H\sqrt{r_i}} = k(H/E)\,(\hat{c}/r_i)^{-3/2} \tag{19}$$

where k is a function. The important features to note are that $g_1 \equiv (\hat{c}/r_i)^{-3/2}$, and that no correlation terms appear.

Data Analysis

Indentation fracture data (with surface compression effects minimized either by careful polishing or by annealing) have been obtained by Dawihl and Altmeyer [*3*], Evans and Charles [*8*], and Lange [*25*]; but independent toughness measurements on the same material have not been obtained in all cases. Those materials for which both indentation fracture and toughness data are available are listed in Table 1.[6]

The data correlation is first attempted in terms of g_1, which would pertain if the roles of the residual stresses and the plastic zone radius were insignificant. The results are summarized in Fig. 6. The correlation is clearly inadequate. Also plotted on the figure are lines corresponding to the Lawn-Fuller [*6*] scheme ($P\alpha c^{3/2}$) and the Palmqvist [*1*] scheme ($P\alpha\hat{c}$). It is evident that the former affords a reasonable approximation at large $\hat{c}/r_i$, where the influences of the local elastic/plastic stress field around the indentation are minor; while the latter has limited utility at small $\hat{c}/r_i$, where the local elastic/plastic field begins to dominate. The apparent discrepancy between these alternate plotting schemes thus is explained.

The inadequate correlation based solely on g_1 suggests that the residual stresses the plastic zone radius, or all of these, may be exerting important influences, through g_2 (E/H). Since the analysis does not provide information about the functional form of g_2, the approach adopted is to assess

[6] It is re-emphasized that large indentation loads were used to obtain valid results.

TABLE 1—*Properties of materials used to construct indentation toughness curve.*

Material	K_c, MPa $\sqrt{m}$	H, GPa	E, GPa	ν
WC/Co (12 percent)	16.0	13.2	700	0.25
Si_3N_4 (hot pressed)	4.9	14.1	320	0.27
SiC (hot pressed)	4.0	19.3	420	0.22
B_4C (sintered)	6.0	32.2	500	0.27
ZnS (CVD)	1.0	1.9	103	0.3
ZnSe (CVD)	0.9	1.0	68	0.3
ZrO_2 (PSZ)	6.9	11.4	170	0.25

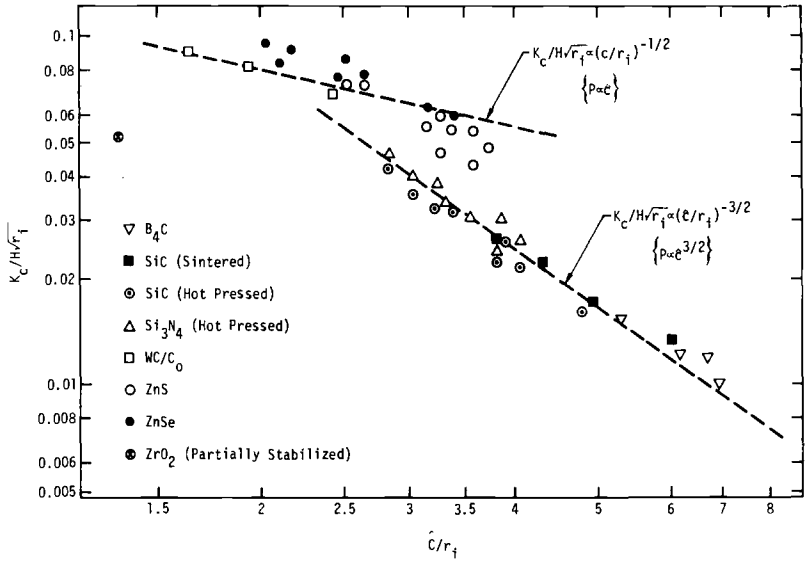

FIG. 6—*The variation of the toughness/hardness parameter* $K_c/H\sqrt{r_i}$ *with the relative crack length* $\hat{c}/r_i$, *for a range of brittle materials.*

various possible forms and to select the form that most effectively correlates the data. Proceeding in this way, an appropriate function for g_2 is found to be

$$g_2 = \left(\frac{E}{H}\right)^{2/5} \tag{20}$$

such that

$$\frac{K_c}{H\sqrt{r_i}}\left(\frac{H}{E}\right)^{2/5} \approx g_1(\hat{c}/r_i) \tag{21}$$

The resultant curve is plotted in Fig. 7.[7] The correlation is surprisingly good, considering the simple form of g_2 and the lack of any cross terms. It is important to recognize that only a limited set of possibilties has been explored, and that other functions are likely to afford a superior correlation. However, the present correlation is adequate for the indentation toughness testing scheme proposed in the following section.

Finally, it also is noted that the apparent lack of a Poisson's ratio effect in the data may reflect the relatively narrow range encompassed by typical brittle materials (for example, 0.2 to 0.3, see Table 1). Significant effects in materials with anomalous Poisson's ratios should not be discounted. The apparent absence of a friction coefficient terms should not be construed to imply that frictional effects are not involved, rather, it suggests either that the friction for a Vickers' indenter is material independent or that it depends primarily on E/H.

Role of Indentation Technique

The indentation technique has two unique advantages. It can be applied to very small specimens, and it is capable of measuring the local crack

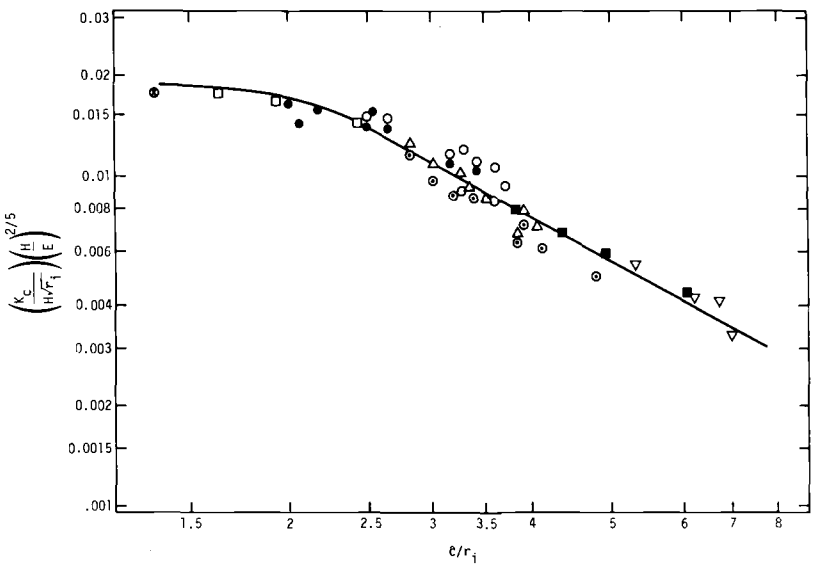

FIG. 7—*The data from Fig. 6 plotted using a plastic zone modification factor,* $(E/H)^{2/5}$.

[7] A convenient polynomial fit [26] is log $[(K_c/H\sqrt{r_i})\ (H/E)^{2/5}] = -1.59 - 0.34\ [\log (\hat{c}/r_i)] - 2.02\ [\log (\hat{c}/r_i)]^2 + 11.23\ [\log (\hat{c}/r_i)]^3 - 24.97\ [\log (\hat{c}/r_i)]^4 + 16.32\ [\log (\hat{c}/r_i)]^5$, where log refers to $\log_{10}$.

growth resistance $(K_c)_\ell$ of a material (for example, the microtoughness pertinent to cracks on the order of the microstructural dimensions). These attributes are the bases for the proposed role of the indentation technique. In all cases, it is reemphasized that residual surface compression effects due to surface grinding must be minimized and that relatively large loads must be used if realistic results are to be obtained. The former can be achieved either by employing a precise polishing sequence or by annealing out the dislocations after grinding.

Materials Development

In the development of materials on a laboratory scale, the fabricated samples are small. For conventional toughness techniques, only a few test specimens, at most, can be prepared from each sample. The monitoring of changes in toughness that can be affected by heat treatment (precipitation, grain growth, etc.), consolidation variables (temperature/pressure cycle), powder morphology, or second phase content and distribution would often be prohibitively expensive. However, the indentation technique allows many measurements on a single specimen so that detailed trends in toughness can be followed with quite small quantities of material. The technique becomes even more appealing when it is appreciated that precision is of secondary importance at the materials development stage.

This approach already has been adopted with considerable success for the development of toughness in partially stabilized zirconia and its alloys [*25*], aluminides, [*27*] and silicon nitride alloys [*25*].

Microtoughness Determinations

It has been recognized for some time that the crack growth resistance pertinent to naturally occurring flaws can be substantially different from the macrotoughness determined using conventional techniques [*28,29*]. An inability to obtain "microtoughness" values pertinent to natural flaws would be a considerable impediment to failure prediction, based on a nondestructive flaw size characterization. The indentation technique has an important role in this context, because it is capable of obtaining local toughness data that elucidate the primary microtoughness trends.

Two test schemes seem pertinent. Firstly, by varying the indentation load, the toughness can be measured as a function of the ratio $\hat{c}/d$, where d is the dominant microstructural dimension (grain size, precipitate spacing, etc.) to obtain K_c $(\hat{c}/d)$. It is expected that K_c will decrease from a polycrystalline asymptote at large $\hat{c}/d$ toward a single crystal value in the range $1 < \hat{c}/d \lesssim 10$ [*28,29*]. Approximate functional forms for K_c $(\hat{c}/d)$ could be obtained using the indentation technique. The techniques would be

most pertinent to brittle materials in which the threshold load for crack initiation at the indentation is small.

Second, the modified crack growth resistance in the vicinity of natural flaws [*29*] (as might result from, for example, a chemical reaction between an inclusion and the host material) can be estimated by forming indentation cracks in the vicinity of defects located on the surface. Changes in K_c as the crack tip approaches the defect can then be monitored, and used to estimate the local degradation in toughness.

Effective Surface Toughness

A number of brittle materials are subjected to surface treatments (tempering, ion exchange, etc.) in order to introduce surface compressive stresses; and, thereby, to improve the projectile impact resistance, the fracture strength, etc. The performance improvement that can be effected by these treatments is related directly to the indentation fracture characteristics. In particular, the relative extent of the damage created in as-fabricated and surface-treated specimens, by the impact of a solid projectile, is directly proportional to the extent of the indentation fracture in the two specimens. Specifically, impact studies have indicated [*21*] that the depth of damage C_r is given by

$$C_r \propto \left[\frac{(r_p v_o)^2}{K_{\text{eff}}}\right]^{2/3} \tag{22}$$

where r_p and v_o are the projectile semidiameter and velocity, respectively, and K_{eff} is the "effective toughness" of the surface layers of the target. This effective toughness is identically equal to the toughness deduced by indentation, at the equivalent crack size; and incorporates, in a single parameter, the influence of near surface stresses, chemical and microstructural changes, etc. No other technique is capable of evaluating this effective toughness. The indentation technique is thus indispensable for impace damage prediction.

Another tentative application of the indentation method is to invert the crack length measurements and, thereby, obtain estimates of the prepresent residual stresses [*30*]. Consider a residual stress given by

$$\sigma_R = \sigma_o \, \Omega \, (z/z_o) \tag{23}$$

where σ_o is the stress at the surface and $\Omega \, (z/z_o)$ is the depth dependence of the stress. The effective stress intensity factor is obtained by subtracting this residual stress from the indentation stress, and inserting the resultant

stress into the formulae discussed in the previous section. This procedure yields (see Ref 30)

$$K_{\text{eff}} - K_c = \frac{2\sqrt{\hat{c}}}{\pi^{3/2}} \sigma_o \int_0^1 \int_0^\pi \frac{(1-\xi^2)^{1/2} F(\xi)}{[1 - 2\xi\cos\theta + \xi^2]}$$

$$\Omega[z(\xi, \theta)/z_o]\, \xi d\xi d\theta \equiv \sigma_o \sqrt{\hat{c}}\, q(\hat{c}/z_o) \qquad (24)$$

where $q\ (\hat{c}/z_o)$ depends on the stress gradient, K_c is the material toughness (for example, obtained by indentation in the absence of residual stress), and K_{eff} is the effective toughness obtained on the surface compression strengthened specimen (using the relative crack length and Fig. 7 in the usual way). The approximate magnitudes of $a(\hat{c}/z_o)$ can be computed for specific stress profiles of practical interest by letting $F(\xi)$ be unity. For a uniform residual stress, the simple result is [*24*]

$$K_{\text{eff}} - K_c = \frac{2}{\sqrt{\pi}} \sigma_o \sqrt{\hat{c}} \qquad (25)$$

indicating that K_{eff} must increase as the crack length increases.

A residual stress distribution of more practical interest is the parabolic distribution obtained for tempering

$$\sigma = \frac{E\alpha\Delta T}{2(1-\nu)} \left[1 - 3(z/z_o)^2\right] \qquad (26)$$

where α is the expansion coefficient, ΔT is the quench temperature and $2z_o$ is the speciment thickness. Another important distribution is that obtained by mass transport processes (ion exchange, oxidation, etc.) which, for a cylinder, is given by

$$\sigma(t) = \frac{\beta E C_o}{(1-\nu)} \left\{ \left(\frac{1}{z_o{}^2}\right) \int_0^{z_o} \delta z dz + \left(\frac{1}{z^2}\right) \int_0^z \delta z dz - \delta \right\} \qquad (27)$$

where

$\delta = 1 - erf\,[(z_o - z)/\sqrt{2}Dt]$,
β = lattice dilation coefficient,
C_o = surface concentration of the diffusing species,
D = diffusion coefficient, and
z_o = cylinder radius.

To obtain the stress intensity factor on the surface, the angle Θ in Eq 26 must be taken with reference to the surface plane; hence, $z_o - z = r \sin \Theta$.

Making this substitution and inserting the stresses into Eq 26, the effective stress intensity factors become: for the tempering problem [*31*]

$$K_c - K_{\text{eff}} = -\frac{E\alpha\Delta T\sqrt{c}}{(1-\nu)\,\pi^{3/2}} \int_0^1 \int_0^\pi \frac{\xi[1-\xi^2]^{1/2}}{[1-2\xi\cos\theta+\xi^2]} \left[1-3(1-(\hat{c}/z)\xi\sin\theta)^2\right] d\xi d\Theta \qquad (28)$$

where $\sigma_o \equiv E\alpha\Delta T/(1-\nu)$; for the diffusion problem [*32*]

$$K_c - K_{\text{eff}} = \frac{2\beta EC_o\sqrt{\hat{c}}}{(1-\nu)\,\pi^{3/2}} \int_0^1 \int_0^\pi \frac{\xi[1-\xi^2]^{1/2}}{[1-2\xi\cos\theta+\xi^2]} \left[K_1 + \frac{K_2}{[1-(\hat{c}/z_o)\,\xi\sin\Theta]^2} - 1 + \textit{erf}\left[(z_o/\sqrt{2Dt})\,(\hat{c}/z_o)\,\xi\sin\Theta\right]\right] d\xi d\theta \qquad (29)$$

where

$$K_1 = \int_0^1 \{1-\textit{erf}\left[(z_o/\sqrt{2Dt})\,(1-x)\right]\}\,x dx,$$

$$K_2 = \int_0^{1-(\hat{c}/z_o)\,\xi\sin\theta} \{1-\textit{erf}\left[(z_o/\sqrt{2Dt})\,(1-x)\right]\}\,x dx, \text{ and}$$

$$\sigma_o = \beta EC_o\,(2K_1-1)/(1-\nu)$$

Integration of Eqs 28 and 29 yields the results plotted in Fig. 8. These curves, coupled with Fig. 7, can be used to obtain a measure of the residual stress from the relative indentation crack length. This is accomplished if results also can be obtained on a stress free sample, or that K_c values for the material are available. Otherwise, only approximate estimates of the residual stress and the fracture toughness may be deduced from the crack length dependence of K_{eff}.

Properties of Coatings/Layers

Ceramic coatings on metals and other ceramics, formed by chemical or vapor deposition or by sintering, have considerable practical potential. The *in situ* toughness and hardness characteristics of the coatings can be determined by indentation, following the aforementioned procedures for surface treated materials. Similarly, the properties of corrosion layers can be

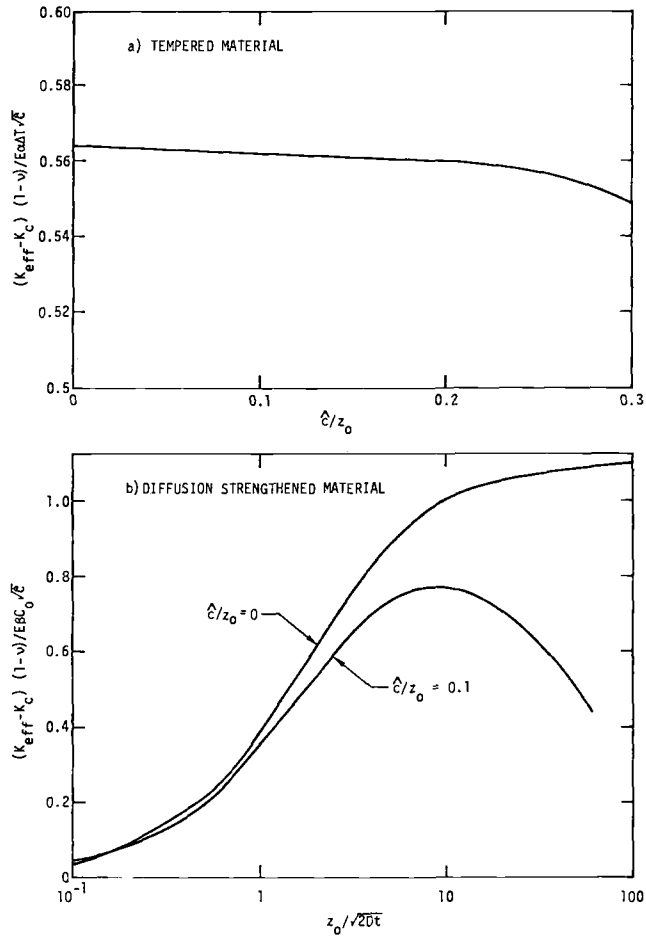

FIG. 8—*The relation between the effective toughness, indentation crack length and prior residual stress for two important residual stress distributions.*

deduced by indentation, as an important adjunct to studies of corrosion and corrosion/erosion phenomena. Again, none of the alternative methods can be applied to these problems.

However, the technique has one important limitation; a minimum coating thickness is needed to obtain quantitative data. This restriction must be invoked whenever the substrate has elastic or plastic properties that differ significantly from those of the coating. The minimum thickness is the thickness at which the elastic deflection of the coating, or the plastic deformation of the substrate, significantly perturbs the indentation stress field (over the crack trajectory). Systematic studies of the influence of the relative elastic moduli and plastic deformation properties on the minimum

thickness have not yet been conducted. It would thus be premature to formulate guidelines. However, we note that this restriction is not involved when the indentation test is being used to assess the relative improvement in impact damage resistance imparted by a ceramic coating (see section on Effective Surface Toughness).

Conclusion

A generalized analysis of indentation fracture suitable for toughness determination using indentation techniques has been outlined. The analysis is not a rigorous quantitative analysis of indentation fracture—a problem of extreme complexity—but provides a framework for identifying the parameters that dictate the extent of indentation fractures. The analysis indicated that the crack length would be dictated primarily by the toughness (the materials crack growth resistance), the hardness (the quantity that affects the amplitude of the elastic/plastic field), and the contact radius (which determines the scale of the stress field)—through the dimensionless parameter $K_c H \sqrt{r_i}$. A number of other possible influences were anticipated by the analysis: the residual indentation stresses and the plastic zone radius (through E/H), Poisson's ratio ν, the interface friction coefficient μ. Limited experimental data indicated that Young's modulus E is important, through the ratio E/H, but did not reveal any effects of ν or μ.

A discussion of the role of the indentation technique indicated several unique functions. These included microtoughness determination, the determination of the *in situ* toughness characteristics (or pre-existent residual stress levels, or both) of surfaces, coatings, layers, etc. Also, the technique appeared to be highly desirable in materials development studies and for routine (production) toughness monitoring purposes.

APPENDIX

Dimensional Analysis

The concept of crack formation in an elastic/plastic field identifies the following possible indentation fracture parameters (see section on Indentation Stress Fields): crack length ($\hat{c}$), indentation size (r_i), toughness (K_c), hardness (H), Young's modulus (E), Poisson's ratio (ν), friction coefficient (μ). It is instructive to obtain groupings of these variables, suitable for experimental characterization schemes, by using the methods of dimensional analysis [*33*].

Let the relative crack length be given by

$$\hat{c}/r_i = K_c{}^{\alpha} H^{\beta} E^{\gamma} \mu^{\delta} \nu^{\omega} r_i{}^{\lambda} \tag{30}$$

Expressing Eq 30 in terms of force (F) and length (L) dimensions, gives

$$0 = [F^{\alpha} L^{-3\alpha/2}]\,[F^{\beta} L^{-2}\beta]\,[F^{\gamma} L^{-2\gamma}]\,L^{\lambda} \tag{31}$$

and hence,

$$F \rightarrow \alpha + \beta + \gamma = 0 \tag{32a}$$

$$L \rightarrow -\frac{3\alpha}{2} - 2\beta - 2\gamma + \lambda = 0 \tag{32b}$$

If we let $\gamma = 0$, Eqs 32*a* and *b* give, $\beta = -\alpha, \lambda = -\alpha/2$. Therefore

$$\hat{c}/r_i = (K_c/H\sqrt{r_i})^{\alpha}\mu^{\delta}\nu^{\omega} \tag{33}$$

For $\gamma \neq 0$,

$$\hat{c}/r_i = (K_c/H\sqrt{r_i})^{\alpha}(H/E)^{\gamma}\mu^{\delta}\nu^{\omega} \tag{34}$$

Acknowledgment

The author wishes to thank the Office of Naval Research for financial support, under Contract N0014-75-C-0669, and F. F. Lange for many useful suggestions.

References

[1] Palmqvist, S., *Archiv Eisenhüttenwesen*, Vol. 33, 1962, p. 629.
[2] Palmqvist, S., *Jernkontorets Annalen*, Vol. 167, 1963, p. 208.
[3] Dawihl, V. W. and Altmeyer, G., *Zeitschrift für Metallhunde*, Vol. 55, 1964, p. 231.
[4] Lawn, B. R. and Swain, M. V., *Journal of Materials Science*, Vol. 10, 1975, p. 113.
[5] Lawn, B. R. and Wilshaw, T. R., *Journal of Materials Science*, Vol. 10, 1975, p. 1049.
[6] Lawn, B. R. and Fuller, E. R., *Journal of Materials Science*, Vol. 10, 1975, p. 2016.
[7] Evans, A. G. and Wilshaw, T. R., *Acta Metalurgica*, Vol. 24, 1976, p. 939.
[8] Evans, A. G. and Charles, E. A., *Journal of the American Ceramic Society*, Vol. 59, 1976, p. 371.
[9] Johnson, K. L., *Journal of Mechanics and Physics of Solids*, Vol. 18, 1970, p. 115.
[10] Swain, M. V. and Hagan, J. T., *Journal of Physics*, D, Vol. 9, 1976, p. 2201.
[11] Studman, C. J. and Field, J. E., *Journal of Physics*, D, Vol. 9, 1976, p. 857.
[12] Studman, C. J. and Field, J. E., *Journal of Materials Science*, Vol. 12, 1977, p. 215.
[13] Kinsman, K. R., Govila, R. K., and Beardmore, P., *Plasticity of Ceramics*, R. C. Bradt and R. E. Tressler, Eds., Plenum Press, New York, 1975, p. 465.
[14] Hockey, B. J., *Journal of the American Ceramic Society*, Vol. 54, 1971, p. 223.
[15] Shaw, M. C. and DeSalvo, G. J., *Transactions*, American Society of Mechanical Engineers; *Journal of Engineering for Industry*, May 1970, p. 480.
[16] Hill, R., *The Mathematical Theory of Plasticity*, Oxford University Press, Oxford, England, 1950.
[17] McMeeking, R. M., *Journal of Mechanics and Physics of Solids*, Vol. 25, 1977, p. 357.
[18] Bousinesq, J., see Timoshenko, S., and Goodier, J. N., *Theory of Elasticity*, McGraw-Hill, New York, 1950, p. 398.
[19] Hardy, C., Baronet, C. H., and Tordion, G. V., *International Journal of Numerical Methods in Engineering*, Vol. 3, 1971, p. 451.
[20] Johnson, K. L., *Engineering Plasticity*, Cambridge University Press, Cambridge, England, 1968, p. 341.
[21] Evans, A. G., Gulden, M. E., and Rosenblatt, M., *Proceedings, Royal Society*, A361, 1978, p. 343.
[22] Studman, C. J., Moore, M. A., and Jones, S. E., *Journal of Physics*, D, Vol. 10, 1971, p. 949.

[23] Sih, G. C., *Handbook of Stress Intensity Factors*, Lehigh University Press, Bethlehem Pa., 1973.
[24] Evans, A. G. and Charles, E. A., *Journal of the American Ceramic Society*, Vol. 60, 1977, p. 22.
[25] Lange, F. F., work performed at Rockwell Science Center, to be published.
[26] Davis, B. I., private communication.
[27] Rhodes, G. C., Evans, A. G., and Paton, N. E., work performed at Rockwell Science Center.
[28] Rice, R. W., *Fracture Mechanics of Ceramics*, R. C. Bradt, D. P. H. Hasselman and F. F. Lange, Eds., Plenum Press, New York, 1975, p. 323.
[29] Evans, A. G. and Langdon, T. G., *Progress in Material Science*, Vol. 21, 1976.
[30] Lawn, B. R. and Marshall, D. B., *Journal of the American Ceramic Society*, Vol. 60, 1977, p. 86.
[31] Kingery, W. D., *Introduction to Ceramics*, Wiley, New York, 1960.
[32] Richmond, O., Leslie, W. C., and Wriedt, H. A., *Transactions*, American Society of Mechanical Engineers, Vol. 57, 1964, p. 294.
[33] Wiederhorn, S. M., private communication.

J. J. Mecholsky[1] *and S. W. Freiman*[2]

Determination of Fracture Mechanics Parameters Through Fractographic Analysis of Ceramics

REFERENCE: Mecholsky, J. J. and Freiman, S. W., **"Determination of Fracture Mechanics Parameters Through Fractographic Analysis of Ceramics,"** *Fracture Mechanics Applied to Brittle Materials, ASTM STP 678,* S. W. Freiman, Ed., American Society for Testing and Materials, 1979, pp. 136-150.

ABSTRACT: Fracture surface analysis of brittle materials can be used as a quantitative tool to determine not only the size of the fracture initiating flaw but also the stress at failure and the critical fracture toughness of the material. The techniques for standardizing these fracture surface measurements and the influence of factors such as microstructure, internal stress, and loading rate are described. The sizes and geometries of fracture initiating flaws are correlated with the K_{Ic} of the material local to the flaw periphery and these are compared to the K_{Ic} obtained from fracture surface analysis. Failure under combined K_I and K_{II} loading is shown to become more amenable to analysis through the use of fractography. Static fatigue failures can be analyzed through the fracture surface features they generate. Not only the stress causing failure but also the time under stress can be determined quantitatively through measurement of flaw and "fracture mirror" sizes.

KEY WORDS: fracture (materials), fractography, ceramics, fracture mechanics, brittle materials, mechanical properties

Fracture of ceramic materials involves the extension of preexisting flaws. The primarily brittle propagation of cracks in these materials leaves a number of fracture surface features which, it will be shown, can be related to the fracture toughness and stress at failure.

There are basically two types of features which can often be observed on the fracture surface of ceramics. The first and most basic feature is the

[1]Technical staff member, Sandia Laboratories, Albuquerque, N. Mex. 87185. The work was performed at Naval Research Laboratory.

[2]Ceramic engineer, National Bureau of Standards, Washington, D. C. 20234.

preexisting flaw at the fracture origin. Whether the flaw is observed during fractography depends on a number of factors such as the direction of stress relative to the flaw and the microstructure. For ceramics with fine grains failing transgranularly, 80 to 90 percent of the flaws are found. In materials with large grains, such as zinc selenide (ZnSe), calcium fluoride (CaF_2), and large grained alumina (Al_2O_3) (Lucalox), observation is much more difficult. As will be discussed later, in cases where subcritical crack growth occurs due to environmental effects, the preexisting flaws may extend to some degree before a critical crack size is reached (Fig. 1). The initial flaw boundary is observable if the direction of stressing with respect to the flaw plane is different during a test than when the flaw was introduced. In glasses, no *critical* flaw size boundary should be visible because the stress direction does not change abruptly.

The second type of feature is caused by the propagation of the flaw subsequent to the application of a critical stress. The propagation of the flaw basically leads to the formation of four regions surrounding the original flaw. These are the following: a generally smooth region, commonly known as a fracture mirror which is bounded by a region of small radial ridges known as mist, followed by an even rougher area known as hackle, and finally by macroscopic crack branching, that is, the formation of two primary cracks. The latter two boundaries can be nearly coincident. However, the specimen size and strength will determine whether all boundaries actually occur. Many

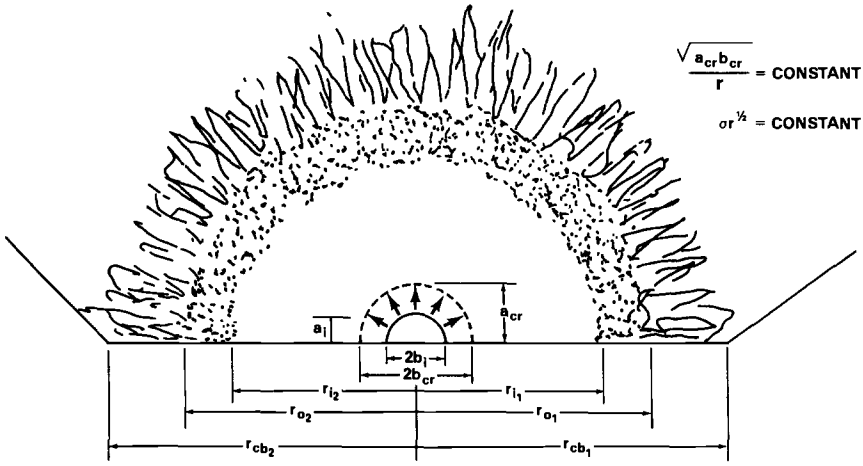

FIG. 1—*Schematic of fracture surface of brittle materials showing the idealized preexisting flaw of depth* a_i *and half-width* b_i *and the failure initiating critical flaw of depth* a_{cr} *and half-width* b_{cr}. *For rapid loading* a_i *and* b_i *should be nearly coincident with* a_{cr} *and* b_{cr}. *The fracture mirror radii boundaries are also shown in the figure:* r_i (*mirror-mist*); r_o (*mist-hackle*); *and* r_{cb} (*macroscopic crack branching*). *For some conditions* r_o *and* r_{cb} *cannot be distinguished.* σ *is the fracture stress* [32].

times specimens are too small to contain macroscopic crack branching. The distances from the fracture origin to the boundaries of each of these regions has been shown experimentally to be

$$\sigma r_j^{1/2} = A_j \tag{1}$$

where

σ = stress at fracture,
r_j = distance to a particular boundary, and
A_j = corresponding mirror constant (Fig. 1).

In this paper, we will discuss the relationship of both flaws and fracture mirrors to various fracture mechanics parameters and show the effect on these relationships of the microstructure of the material and other properties, such as intrinsic stresses or inhomogeneities.

Flaws

Although most defects are not regular in shape, they usually can be idealized in the manner described by Randall [*1*].[3] For an elliptical flaw, either in the interior or on the surface of a body, the maximum stress intensity occurs at the minor axis of the ellipse having axes a and b. The expression for the critical stress intensity factor, K_{Ic}, in terms of the fracture stress σ and critical flaw size c (the smaller of a and b) is given by

$$K_{Ic}^2 = \frac{z\pi\sigma^2 c}{\varphi^2 - 0.212(\sigma/\sigma_y)^2} \tag{2}$$

where

σ_y = yield stress of the material at the crack tip,
φ = elliptical integral of the second kind which accounts for the degree of ellipticity of the flaw, and
z = factor which depends on the flaw location, that is, on the surface or in the interior of a body.[4]

It should be pointed out that the flaw size in this relationship is the critical flaw size which can be somewhat larger than the actual flaw size observed on the fracture surface (Fig. 1). The difference between c_{initial} and c_{critical} is determined by the amount of subcritical crack growth and is a function of the material, loading rate, and the environment. For most materials tested under

[3]The italic numbers in brackets refer to the list of references appended to this paper.

[4]For most ceramic materials tested at room temperature, the correction for plastic flow $0.212(\sigma/\sigma_y)^2$ is negligible, as is the back surface correction often used with metals [*1*] because of the relatively small flaws.

relatively high loading rates, however, the $c_{critical}$ and the observed flaw size, $c_{initial}$, agree quite well [2–5].

Defect Types

The types of defects that cause mechanical failure of ceramic materials can be divided into three broad categories. Processing defects, such as pores or clusters of pores; machining and handling defects; and service or environmentally induced defects. Other sources of failure are foreign particles, single large grains or clusters of large grains which are associated with cracks or pores. It has been shown generally that failure from pores for rapidly loaded bars can be explained by the measurements of the pore diameter plus a grain size [6]. However, failure from pores is a current research topic that is being debated. In general, calculation of fracture energy from the minor dimension of inclusions or foreign particles, or both, is seen to give reasonable agreement with that measured [5,6].

The study of machining defects has been focused primarily on those from grinding and secondarily from polishing. Fractography of machining flaws [3] have been used to study the effect of grinding on strength and has shown that the strength anisotropy relative to perpendicular grinding directions [7] is related to two perpendicular flaw populations produced from grinding. Polishing itself introduces the same type of dual crack population as grinding [8]. Because the direction of most polishing operations is random, strengths are essentially isotropic and failure from polishing flaws invariably occurs from the elongated cracks which tend to form parallel with the local particle direction of motion.

Handling defects may occur either in the processing of the specimen or in subsequent service and take on a variety of forms such as scratches, spalls, and cracks, for example, that may be caused by localized impact contacts [9,10].

Corrosion or oxidation can result in surface pits. Correlations between calculated and measured values of K_{Ic} for hot pressed Si_3N_4 using the pit size and geometry as the flaw size, are quite good [11].

Microstructural Effects

The unique feature for the application of fracture mechanics to failure of ceramics compared to most metal failure is basically that the fracture toughness of ceramics is so low that critical flaw sizes are of the same order of magnitude as the microstructural features, for example, grain sizes in the range of 10 to 50 μm. This means that average values of fracture toughness measured using fracture mechanics techniques employing large flaws cannot always be applied to explain the failure from small defects which occur on fracture specimens or actual components. In fact, as shown in Table 1, when

TABLE 1—*Predicted and measured critical flaw size in ceramics.*

Material	Average Grain Size, μm	Flaw Size, μm	
		Predicted[a]	Observed
Silicate glasses[b]	...	82	80
Pyroceram 9606	<1	90	100
MgF_2	<1	57	60
$BaTiO_3$	5	30	27
Lucalox (Al_2O_3)	35	140(45)[c]	38
ZnSe	20-300	115(24)[c]	25

[a] $c = \varphi^2 K_{Ic}^2 / 1.2\pi\sigma^2$
[b] For example, borosilicate glass (Corning 7740).
[c] Values in parentheses calculated assuming single crystal K_{Ic}.

the flaw size becomes smaller than the grain size, the parameter controlling fracture of the body changes from the polycrystalline value of K_{Ic} to a value close to that for a single crystal of the particular material. This variation is quite reasonable, since a crack contained within a single grain sees an environment which is essentially that of a crack in a large single crystal [*5,12,13*]. Following this logic, the flaw can grow to critical size before the grain boundary is reached, that is, before there is any perturbation of the propagation characteristics in the single grain. As shown in Fig. 2, as the flaw size is increased in comparison to the grain size, there is a transition from single crystal K_{Ic} to polycrystalline K_{Ic} [*14,15*].

Internal Stress

Another factor which must be accounted for in analyzing fracture is that of

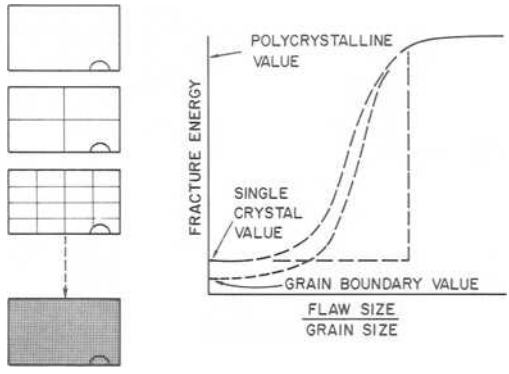

FIG. 2—*Schematic of the transition from a flaw within a large grain (near single crystal fracture energy initiation) to a flaw which encompasses many grains (polycrystalline behavior).*

internal stresses which can arise due to thermal expansion anisotropy or phase transformations. The maximum stresses which occur due to these phenomena arise at the grain boundaries. Since even a small flaw may encompass a number of grains, there will be some averaging of stresses around the flaw perimeter. Equation 2 can be modified[5] to account for these stresses as follows

$$K_{Ic} = \frac{\sqrt{z\pi}}{\varphi}(\sigma + <\sigma_i>)\, c^{1/2} \tag{3}$$

where $<\sigma_i>$ is defined as the effective internal stress around the flaw. $<\sigma_i>$ will depend on the ratio of the flaw to grain size. $<\sigma_i>$ approaches zero as the flaw size increases because the flaw averages more and more of the tensile and compressive components of the internal stress. On the other hand, as the flaw becomes smaller, $<\sigma_i>$ will increase because failure in ceramics occurs from the weakest region, or region of highest tensile stress. An example of the effect of internal stresses on failure [*16*] is shown in Fig. 3 for barium titanate. The internal stress calculated by inserting measured values of σ, K_{Ic}, and c in Eq 2 decreased from a value approaching the theoretical limit in the material to zero for very large flaws.[6]

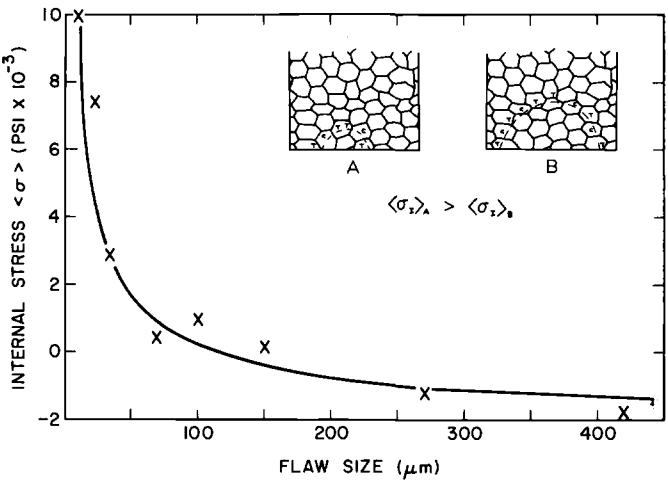

FIG. 3—*Internal stress as a function of flaw size for $BaTiO_3$ with a grain size of 1.0 to 1.5 μm. As flaw size increases (insert), the average of compressive and tensile regions approaches zero* [16].

[5]Neglecting plastic flow at the crack tip.

[6]The actual value in Fig. 3 is negative because of residual stress due to indentations that were made to produce the large cracks [*16*].

Compositional Variations

Another important consideration for many ceramic materials is the presence of compositional heterogeneities, [*17,18*]. As mentioned previously, failure in ceramics occurs from the weakest portion of the structure so that the presence of small regions of lower density can be very deleterious to strength. However, measurements of fracture toughness made using large cracks may not be influenced significantly by these regions because the cracks encompass much more of the "homogeneous" material. An example of this is the case of Si_3N_4 plus 15 percent yttria, wherein $K_{Ic} \approx 7$ MPa·m$^{1/2}$ was measured using a double cantilever beam test with a large crack; yet the strength of the material was equal to or less than that of a Si_3N_4 having a fracture toughness of 4 MPa·m$^{1/2}$ [*17*]. This discrepancy was shown to be due to the presence of regions of different chemical composition in the material of the order of the preexisting flaw sizes. These regions were observed on a polished surface under polarized light. It is failure from flaws within these lower toughness regions that governs the strength of this material [*17,18*].

Inelastic Deformation

While the complication of inelastic deformation usually can be ignored in the case of most ceramic fracture, failure at elevated temperature increases the probability of having some localized inelastic deformation. An example of this effect is shown in Fig. 4 for Si_3N_4 tested over a range of temperatures. At the lower temperatures (below 1300°C), the failure is basically brittle fracture, having the typical flaw and fracture mirror features described earlier [*19*]. At the higher temperatures, however, the flaw character changes to one whose appearance is more like that found in metals, apparently due to a combined creep-crack growth interaction which occurs due to viscous grain boundary sliding. In fact, the flaw itself extends over a large portion of the sample area. It has been shown [*20*] that by taking into account in Eq 2, the localized inelastic deformation of these materials at the grain boundaries which occurs before fracture, as well as a correction for the decrease in load bearing area due to the large flaw [*1*], reasonably good agreement between the fracture toughness predicted from these very large flaws and that measured in the material at corresponding temperatures can be obtained.

Nonplanar Flaws

A common impediment to the use of flaw sizes to predict both the stress of failure as well as the fracture toughness is the fact that many flaws are not wholly contained in the plane perpendicular to the maximum tensile stress [*3,21*] so that all portions of the flaw are not stressed in a typical K_I mode. This means that the use of the observed flaw sizes seriously underestimates

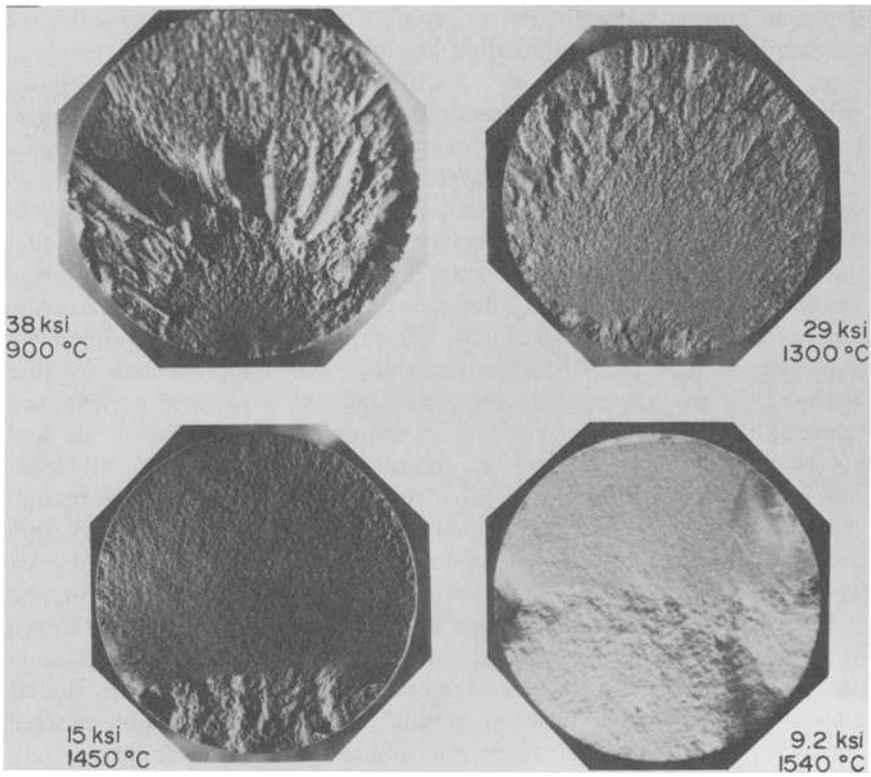

FIG. 4—*Fracture surfaces of hot pressed Si_3N_4 (HS-130) rods tensile loaded to the stresses and temperatures indicated showing brittle fracture (900°C) and regions of "slow crack growth-creep" for rods tested at 1300°C and above* [19].

the stress required to cause fracture. However, as will be discussed in the next section, the use of fracture mirror measurements is particularly useful in these cases, since the fracture mirror is contained in a plane essentially perpendicular to the applied tensile stress [*3,22*].

Fracture Surface Features

While observation of the fracture initiating flaw is important, flaws in many cases are nonplanar, too small, have unclear boundaries, or have been eliminated because of a chip removal so that one cannot determine the flaw size. One of the powers of fractography is in using the fracture surface features that form outside the flaw to describe fracture behavior. The mirror-mist and mist-hackle boundaries are easiest to discern in glasses and fine grain dense ceramics, and are much more difficult, if not impossible, to

detect in porous materials and materials with large grains. However, the crack branching radius (bifurcation location) is discernible in all ceramics when the sample is large enough relative to the fracture stress. Typically, either the initial flaw at the fracture origin or fracture surface features beyond this region are found in most ceramics, if not both these features. While we cannot be sure why the features (mist and hackle), described earlier, form on the fracture surface that is, whether this is due to a change in the direction of the principle stress as discussed by Yoffe [*23*] or whether these features occur due to the formation of excess kinetic energy [*24*]), we do know that they can be used to describe the stress (Eq 1) and the fracture toughness (Eq 2) of the material [*25*]. A basic assumption in estimating these parameters is that, to a first approximation, one can apply a static fracture analysis, neglecting dynamic factors associated with strain energy release and surface kinetic energy contributions. This assumption seems reasonable, and good correlation between measured and calculated values is obtained [*25*].

While one might think initially that the measurement of a mirror boundary using a microscope is quite a qualitative operation and would vary from observer to observer; in fact, experiments performed over a number of years by a large number of investigators have shown that the values of mirror constants obtained in different laboratories are quite nearly the same, as shown in Table 2. While there is a gradual transition from smooth regions to rougher regions on the fracture surface, measurements taken in a similar manner will yield quite consistent results. Thus, the demarcation between mirror and mist as well as between mist and hackle is a measure of a certain critical density of fracture features being formed. It appears that the most consistent values of mirror constants are obtained when fracture mirrors are measured at a magnification such that the fracture mirror radius is approximately 2 cm in the microscope. In measuring the mirror-mist and mist-hackle boundaries, these should be projected to the tensile surface to complete a circular arc, since there is curvature at the surface due to free surface effects. Mirrors approaching specimen boundaries can be subject to edge effects leading to deviations from the relationship shown in Eq 1 [*24,26*]. Because of (light-dark) contrast effects, the optical microscope

TABLE 2—*Fracture mirror constants for ceramics* ($MN/m^{3/2}$).[a]

Material	
Soda-lime glass	1.7 [*27*],[b] 1.7 [*36*], 1.9 [*6*], 1.9 [*37*], 1.9 [*38*], 2.0 [*35*], 2.1 [*6*]
Pyroceram 9606	5.7 [*36*], 6.5 [*6*]
HP Al_2O_3	9.8 [*36*], 10.3 [*35*], 12 [*6*]
Si_3N_4	9.2 [*35*], 12 [*6*]
SiC	10.7 [*6*], 11.5 [*35*]

[a]The value of A in Eq 1; all valves are constants for mist-hackle boundary except the top line.
[b]Italic numbers in brackets refer to list of references appended to this paper.

measurements are preferred over those from scanning electron micrographs for mirror radius measurements whenever possible. In addition, measurements should be taken in varying lighting since the appearance of the boundary can change depending on the angle of the reflected light. In this way, an average value of the radius for different conditions can be calculated. Shand [*26*] has shown that very large mirrors (low strength) can deviate from the expected relationship (Eq 1), probably because of edge effects. Also, there can be deviations from Eq 1 at very small mirrors (high stress) [*6*], possibly due to internal stress effects.

Most of the strength measurements from which the fracture mirror data are obtained have been performed using bend tests. One of the past errors made in fracture mirror analysis has been shown to result from measurement of the mirror into the thickness of the specimen and therefore into a varying stress field. Mecholsky et al [*2*] pointed out that if all the fracture mirror data are measured along the tensile surface, that is, under constant stress, then good agreement is obtained between the various investigators. While Abdel-Latif et al [*27*] have suggested that the mirror constant is actually a function of specimen size for flexural test measurements, there are little experimental data other than their work to corroborate this hypothesis; the large deflections associated with small specimens-large spans, which can explain the differences in their mirror constant values for different conditions, have not been accounted for in Ref *27*. It has been demonstrated recently by Freiman et al [*22*] in the case of the formation of mirrors which are asymmetric about the flaw on the tensile axis, that the larger radius is the correct measurement. They show that the mirror constant obtained from this radius agrees well with other measurements. The reason for the use of the larger radius is that it corresponds to the smallest stress and therefore the stress at which the crack first started to propagate.

Relation of Fracture Mechanics to Fractography

Fracture mechanics expressions, Eq 2, can be combined with fracture surface analysis, Eq 1, to relate the mirror boundary measurements to the stress at fracture and the fracture toughness of the material [*3,6*] as shown below for a surface flaw ($z = 1.2$), assuming no inelastic deformation

$$K_{Ic} = \frac{\sqrt{1.2\pi}\left(\frac{c}{r_j}\right)^{1/2}}{\varphi} A_j \tag{4}$$

where A_j is described by Eq 1 and $c = \sqrt{a_{cr}b_{cr}}$ [*3*] as defined in Fig. 1.

One of the important parameters in this expression is the ratio of the mirror size to the flaw size. Equation 4 suggests that if the ratio of mirror to flaw size is a constant, a plot of mirror constant versus fracture toughness should

yield a straight line for flaws of the same geometry. This relationship does seem to hold for a wide range of materials [*6*], and can be used to calculate (mist and hackle) mirror to flaw size ratios, the average of which was determined to be 13 to 1 for a wide variety of ceramics. This ratio is given to indicate a trend and is not an absolute number. The fact that the mirror-to-flaw size ratio is a constant for a particular material suggests that if the mirror size can be measured and the fracture toughness of the material is known, the flaw size can be calculated. In at least two cases, however, caution should be used in analyzing mirror data in this way. For large grain materials, the flaw may be contained in one, or a few, large grains and the K_{Ic} would correspond to near the single crystal value. Calculations made from the mirror measurements can overestimate the K_{Ic} by a considerable amount. There are also materials such as some glass-ceramics for which K_{Ic} is significantly larger than that predicted from their mirror constants [*6,28*]. Studies [*29*] have shown that microcracking occurs fairly extensively at the crack tips in these materials. This microcracking appears to be local to the flaw and does not contribute as greatly to A_j as to K_{Ic} [*6*]. Because of the possible errors in measurement of the mirror boundaries, K_{Ic} should be measured by other fracture mechanics techniques whenever possible. The use of mirror constants (Eq 4) to estimate K_{Ic} is recommended when other data are not available, or to study the interaction of flaws and microstructure. The measurement of the flaw will provide local behavior when the flaw is of the size of the microstructural feature, for example, the grain size, and the mirror provides the far field behavior.

Complex Flaws

As discussed previously, one of the problems arising in the analysis of fracture initiating flaws occurs when the flaw is not planar. It has been shown that the relationship between fracture mirror size and flaw size can be used to study, for instance, the effect of machining on flaw shape in soda-lime glass and that calculations based on mirror size measurements are accurate even though the critical flaw is either out of the plane of fracture or of a very complicated shape [*3,22*]. As shown in Fig. 5, Mecholsky et al demonstrated that for glass the fracture toughness is independent of flaw shape. It was further demonstrated that for complicated flaw shapes, the area of the flaw divided by the square of the mirror radius (ab/r^2) was a constant in agreement with the prediction of Bansal [*30*]. In addition, it was shown that the use of fractography explained strength differences produced by differences in grinding direction. A recent study [*22*] showed that the critical fracture toughness for flaw propagation in soda-lime glass, calculated from mirror boundaries was independent of the combined (K_I and K_{II}) mode loading. It was shown that the K_c calculated using various expressions for combined K_I and K_{II} on flaws oriented from 90 to 20 deg to the tensile axis could be significantly different

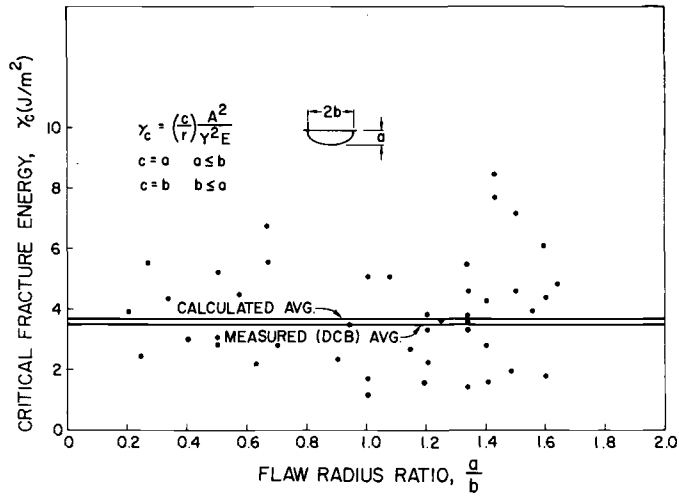

FIG. 5—*Critical fracture energy, γ_c, as a function of* a/b *ratio for soda-lime-silica glass; that is, Eq 3. Calculated average is arithmetic mean (3.83 J/m^2) with a 95 percent confidence limit of* ±0.48. *A least-squares fit to the data gives 3.81 J/m^2 at* a/b = *1 (semicircular flaw) and a slightly positive slope (0.17 J/m^2). These methods cannot be distinguished within the limits of the data. The agreement between calculated and measured fracture energy demonstrates that fracture mechanics can be used to determine* K_{Ic} *from fracture mirror data alone, regardless of flaw geometry* [3].

from the measured fracture toughness of the material, but that the K_c calculated using Eq 4 gave good correlations between fracture toughnesses regardless of the flaw orientation. This correlation appears quite reasonable since, as noted earlier, the fracture mirror is basically perpendicular to the loading direction regardless of the original direction of propagation of the flaw [*21,22*]. The mirror to flaw size ratio was also independent of flaw orientation.

Surface treatments, such as etching, will not in general, affect the strength-mirror relationship (Eq 1). However, due to local effects, such as residual stress, blunting, etc., near the flaw, the mirror/flaw ratio will not be constant [*8*].

Loading Rate

Because the effect of environment causes subcritical crack growth in ceramics [*31*], a variation in loading rate changes the size of the critical flaw relative to that of the initial flaw (Fig. 1). Increasing evidence [*25,32*] clearly indicates that the fracture mirror size is indicative of the stress at failure regardless of the loading rate. Thus, although slower loading rates (lower stresses), will result in a larger fracture mirror size, the fracture mirror constant is independent of loading rate. The mirror-to-critical-flaw size ratio will

remain a constant but the ratio of critical-to-initial-flaw size will be a function of loading rate (Table 3). Thus, using fracture surface analysis, one can calculate the life of a failed component. The case of rapid loading has been discussed elsewhere [*25,33,34*].

TABLE 3—*Effect of loading rate on fracture surface analysis.*

	A_i, MN/m$^{3/2}$	A_o MN/m$^{3/2}$	$R_i/\sqrt{a_i b_i}$	$R_o/\sqrt{a_i b_i}$
Rapid failure [*2*]	1.92	2.21	12.5	16.7
Delayed failure [*32*]	1.96	2.21	f(t)	f(t)

Stresses

Internal stresses resulting from thermal expansion anisotropy and phase transformation are important to flaw growth in ceramics. Little, if any, specific research has been performed to demonstrate the effect of internal stress on fracture mirrors. There may be an effect similar to but more complex than that for residual stresses. Residual stresses due to thermal or chemical treatments influence the fracture mirrors in these materials. An attractive approach to study the effect of residual stress is by plotting σ versus $\bar{r}^{1/2}$ as shown in Fig. 6 (rather than the more conventional log-log plot). This approach yields the value of residual stress contributing to failure. This type of analysis has been applied to glasses having various thermal treatments [*25, 26,35*]. Although these limited examples are not conclusive, they certainly are suggestive of a useful technique.

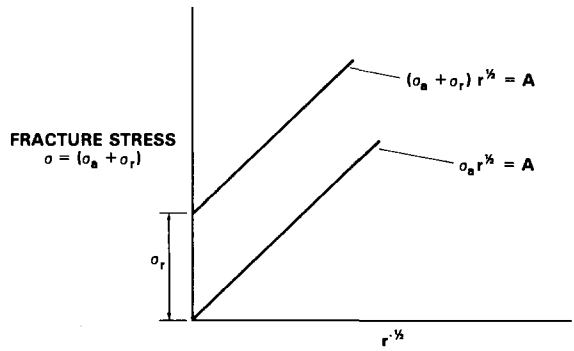

FIG. 6—*Schematic of the effect of residual stress, σ_r, on fracture surface analysis. Assuming the mirror constant, A, in Eq 1 is constant with and without residual stress, by measuring the mirror radius (say mist-hackle radius) for a particular specimen and knowing the applied stress, the amount of residual stress can be determined. A specific example of the analysis of data from Ref* 37 *is provided in Ref* 25.

Summary

In summary, fractographic analysis of ceramics is a powerful tool in determining both the conditions under which failure occurred as well as measuring the stresses at failure and the fracture toughness of the material. It was demonstrated that microstructural considerations such as grain/flaw size interaction and microcracking, as well as the possibility of residual and internal stresses must be accounted for in any analysis of brittle fracture in these materials.

Acknowledgments

The authors would like to thank R. W. Rice for reading the manuscript and offering helpful suggestions.

References

[1] Randall, P. N. in *Plain Strain Crack Toughness Testing of High Strength Metallic Materials, ASTM STP 410,* American Society for Testing and Materials, 1967, pp. 88-126.

[2] Mecholsky, J. J., Rice, R. W., and Freiman, S. W., *Journal of the American Ceramic Society,* Vol. 57, 1974, pp. 440-443.

[3] Mecholsky, J. J., Freiman, S. W., and Rice, R. W., *Journal of the American Ceramic Society,* Vol. 60, No. 3-4, 1977, pp. 114-117.

[4] Wiederhorn, S. M. in *Ceramics for High Performance Applications,* J. J. Burke, A. E. Gorum, and R. N. Katz, Eds., Brook Hill, Chestnut Hill, Ma., 1974, pp. 651-652.

[5] Mecholsky, J. J., Freiman, S. W., and Rice, R. W., *Journal of Materials Science.* Vol. 11, 1976, pp. 1310-1319.

[6] Rice, R. W. in *Proceedings,* Symposium on Fracture Mechanics of Ceramics, Vol. 2, Pennsylvania State University, Plenum Press, New York, 1973, pp. 323-345.

[7] Rice, R. W., "The Science of Ceramic Machining and Surface Finishing," NBS Special Publication 348, S. J. Schneider, Jr., and R. W. Rice, Eds., National Bureau of Standards, Washington, D. C., 1972, pp. 365-375.

[8] Mecholsky, J. J., Freiman, S. W., and Rice, R. W. in *Proceedings.* 11th International Congress on Glass, Prague, Czechoslovakia, July 1977, pp. 489-497.

[9] Kirchner, H. P. and Gruver, R. M. in *Proceedings,* Symposium on Fracture Mechanics of Ceramics, Vol. 3, Pennsylvania State University, Plenum Press, N. Y., 1978, pp. 365-378.

[10] Lawn, B. R. and Wilshaw, T. R., *Journal of Materials Science,* Vol. 10, 1975, pp. 1049-1081.

[11] Freiman, S. W., Mecholsky, J. J., McDonough, W. J., and Rice, R. W. in *Ceramics for High Performance Applications-II; Proceedings,* 5th Army Materials Technology Conference, Newport, R. I., 1977.

[12] Freiman, S. W., Mecholsky, J. J., Rice, R. W., and Wurst, J. C., *Journal of the American Ceramic Society,* Vol. 58, 1975, p. 406.

[13] Rhodes, W. J. and Cannon, R. M., *Bulletin of the American Ceramic Society,* Vol. 53, No. 4, 1974, p. 318.

[14] Freiman, S. W., Rice, R. W., Mecholsky, J. J., and Pohanka, R. C. in *Proceedings,* 14th Annual Meeting of the Society of Engineering Science, Inc., Lehigh University Publication, Bethlehem, Pa. 1977, pp. 357-368.

[15] Rice, R. W., Freiman, S. W., Pohanka, R. C., Mecholsky, J. J., and Wu, C. Cm., in *Proceedings.* Symposium on Fracture Mechanics of Ceramics, Pennsylvania State University, Plenum Press, New York, 1978, pp. 849-876.

[16] Pohanka, R. C., Freiman, S. W., and Bender, B. A., *Journal of the American Ceramic Society,* Vol. 61, 1978, pp. 72-75.
[17] Freiman, S. W., Williams, A., Mecholsky, J. J., and Rice, R. W., *Ceramic Microstructures '76,* R. M. Fulrath and J. A. Pask, Eds., Westview Press, Inc., Boulder, Colo., 1977, pp. 824-834.
[18] Rice, R., *Surfaces and Interfaces of Glass and Ceramics,* Plenum Press, New York, 1972, pp. 439-472.
[19] Rice, R. W., Freiman, S. W., Mecholsky, J. J., and Ruh, R., "Fracture Sources in Si_3N_4 and SiC," *Proceedings,* DARPA/NAVSEA-Garrett/Airesearch Ceramic Gas Turbine Engine Demonstration Program Review, Castine, Ma. Aug. 1977, to be published.
[20] Rice, R. W., Freiman, S. W., Mecholsky, J. J., Ruh, R., and Harada, Y., "Fractography of Si_3N_4 and SiC," *Ceramics for High Performance Applications-II; Proceedings,* 5th Army Materials Technology Conference, Newport, R. I., 1977.
[21] Petrovic, J. J. and Mendiratta, M. G., *Jounal of the American Ceramic Society,* Vol. 59, 1976, pp. 163-167, and Vol. 60, 1977, p. 463.
[22] Freiman, S. W., Gonzalez, A. C., and Mecholsky, J. J., "Mixed Mode Fracture in Soda Lime Glass," accepted by the *Journal of the American Ceramic Society.*
[23] Yoffee, E. H. in *The Philosophical Magazine,* Vol. 42, 1951, p. 739.
[24] *Dynamic Crack Propagation,* Sih, G. C., Ed., Nordoff International Publishing, Heyden, The Netherlands, 1973.
[25] Mecholsky, J. J., Freiman, S. W. and Rice, R. W. in *Fractography in Failure Analysis, ASTM STP 645,* American Society for Testing and Materials, 1978, pp. 363-379.
[26] Shand, E. G., "Breaking Stresses of Glass Determined from Fracture Surfaces," *The Glass Industry,* April 1967.
[27] Abdel-Latif, A. I. A., Tressler, R. E., and Bradt, R. C., *International Journal of Fracture Mechanics,* Vol. 13, 1977, pp. 349-359.
[28] Mecholsky, J. J. and Freiman, S. W. in *Proceedings,* 11th International Congress on Glass, Prague, Czechoslovakia, July 1977.
[29] Wu, C. Cm., Rice, R. W., Freiman, S. W., and Mecholsky, J. J., *Journal of Materials Science.* accepted for publication, 1978.
[30] Bansal, G. K., *Journal of the American Ceramic Society,* Vol. 59, 1976, pp. 87-88.
[31] Wiederhorn, S. M. in *Proceedings,* Symposium on Fracture Mechanics of Ceramics, Vol. 2, Pennsylvania State University, Plenum Press, New York, 1973.
[32] Mecholsky, J. J., Gonzalez, A. C., and Freiman, S. W., "Fractographic Analysis of Delayed Failure in Soda Lime Glass," submitted to *Journal of the American Ceramic Society,* 1978.
[33] Kirchner, H. P. and Gruver, R. M., Ceramic Finishing Company, Report No. 5, Jan. 1977.
[34] Pohanka, R. C., Smith, P. L., and Pasternak, J., "Report of NRL Progress," U. S. Naval Research Laboratory, Jan. 1975, p. 21.
[35] Kirchner, H. P. and Gruver, R. M., *Proceedings,* Symposium on Fracture Mechanics of Ceramics, Vol. 1, Pennsylvania State University, Plenum Press, New York, 1973.
[36] Bansal, G. K. and Duckworth, W. H., *Journal of the American Ceramic Society,* Vol. 60, 1977, pp. 304-310.
[37] Kerper, M. J. and Scuderi, T. G., *Bulletin of the American Ceramic Society,* Vol. 44, 1965, pp. 953-955.
[38] Johnson, J. W. and Holloway, D. G., *The Philosophical Magazine,* Vol. 14, 1966, pp. 731-743.

F. E. Buresch[1]

Fracture Toughness Testing of Alumina

REFERENCE: Buresch, F. E., **"Fracture Toughness Testing of Alumina,"** *Fracture Mechanics Applied to Brittle Materials. ASTM STP 678,* S. W. Freiman, Ed., American Society for Testing and Materials, 1979, pp. 151-165.

ABSTRACT: It is recognized that the plane strain brittle fracture of ceramics can be described in terms of a critical stress criterion of failure. Provided that fracture is induced by thermal or mechanical mismatch between anisotropic grains of equal or different phases, slip, or twinning, the microcracks propagate in an unstable manner when the local tensile stress ahead of a stress concentrator exceeds a critical value (σ_{mc}). If fracture loads are well below stresses leading to "intense microcracking," nonlinearity is confined to the vicinity of the notch. The σ_{mc}-concept establishes a local criterion for unstable cleavage fracture which is related to microstructural features using the model of the critical elastic energy density within the process zone proposed by the author. Similar to the case of metals, the stress state of specimen shape also has a strong influence on measured K_I-value of ceramics. For plane strain, the process zone is an autonomous region. The overall size depends on the grain/microcrack size distribution and the elastic interaction of the microcracks. For plane stress, the process zone is strongly related to the specimen thickness, hence, the grain size dependence also will change with specimen thickness.

KEY WORDS: alumina ceramic, fracture toughness, structure and notch sensitivity, stress state, specimen size, notch fracture mechanics, cyclic loading, slow crack growth, fracture (materials), crack propagation

It is recognized that the plane strain brittle fracture of ceramics at ambient temperature can be described conveniently in terms of a critical stress criterion of failure. Provided that fracture is induced by thermal or mechanical mismatch between anisotropic grains of equal or different phases, slip or twinning the microcracks propagate in an unstable manner when the local tensile stress (σ_{yy}) ahead of stress concentrator exceeds a critical value (σ_{mc}), which is assumed to be relatively independent of tem-

[1]Kernforschungsanlage Julich GmbH, Federal Republic of Germany.

perature and strain rate. This follows from the dependence of σ_{mc} on microstructural parameters [*1-3*].[2]

Values of σ_{mc} have been calculated mainly using Neuber's microsupport effect theory for notched bars loaded in plane strain bending. Here, the longitudinal stress (σ_{mc}) within the nonelastic deformed zone is described from mean value stress theory. If fracture loads are well below stresses for "intense microcracking", nonlinearity is confined closely to the notch root. Hence, if the notch is rounded, and if it is assumed that Neuber's microsupport effect theory adequately describes the stress state within the microcracked region σ_{mc} as a function of the stress intensity factor K_I and the notch root radius ρ is Fig. 1

$$\sigma_{mc} = \frac{2K_I}{\sqrt{\pi \rho}} \tag{1}$$

The σ_{mc}-concept establishes a local criterion for unstable cleavage fracture which can be related to microstructural features using the model of the critical elastic energy density within the process zone proposed by the author [*1-3*]. Here, microcracks are assumed to nucleate from thermal expansion mismatch at grain boundaries or from twinning and slip dislocation pile ups at brittle grain boundaries and the critical event is considered to be the growth of these nuclei into surrounding grains or grain boundaries thereby lowering Young's modulus inside the nonelastic deformed

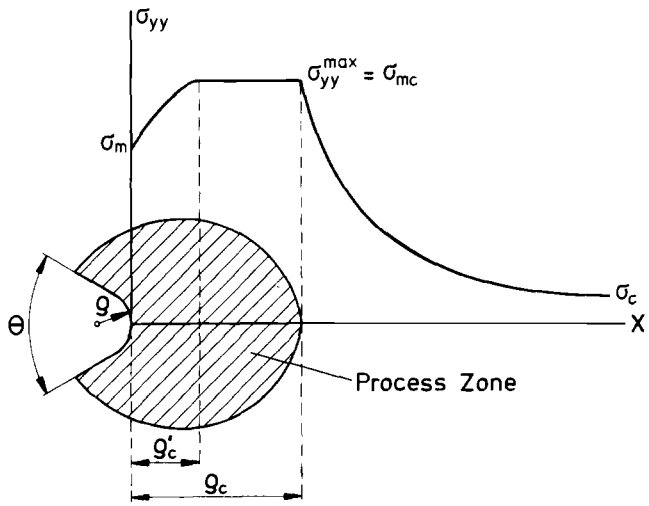

FIG. 1—*Estimate of non-linear stress distribution in front of a notch root.*

[2] The italic numbers in brackets refer to the list of references appended to this paper.

process zone to the value $E_\rho < E$. Then, using the critical microscopic elastic energy density criterion, the critical notch fracture strength is

$$\sigma_{mc} = 4 \sqrt{\frac{\gamma_s E}{d A(\mu)}} I_\rho \tag{2}$$

where I_ρ is the elastic microcrack interaction parameter which relates the density, length, orientation to the elastic interaction of the microcracks within the nonelastically deformed process zone of dimension ρ_c [*1,2*].

However, the theoretically predicted dependence of K_{Ic} on microstructural features can be masked by geometrical correlations. Literature data show an increase of K_{Ic}-values with grain size as well as a decrease specifically if SENB-, DCB- or DT-specimens are used [*5,6*]. In a preceding paper we have shown that in ceramics, as in the case of metals, the stress state of the specific specimen has a strong influence on the measured K_{Ic}-value. A real material specific K_{Ic}-value (predominantly plane strain) can be measured only if the notch root radius ρ is lower than a critical value ρ_c which must be small in comparison to other geometric parameters of the specimen, such as thickness or length of the macroscopic crack. ρ_c is the size of the region ahead of the root of the notch called the process zone in which stresses are reduced by microcracking [*1-4*].

Experimentally, it has been found that, as in the case of metals, the specimen dimensions must be multiples of the factor $(K_{Ic}/\sigma_{mc})^2$. K_{Ic}-values can only be measured for equivalent bend specimens of thickness B and width W with $B = W/2$ if the relation

$$B \geq 50\, \rho_c \tag{3}$$

holds. This is shown in the following sections.

Factors Influencing K_{Ic}-Measurements

Theoretical Background

Neuber's microsupport effect introduced in the failure of brittle materials form the foundation of notch analysis approach of fracture mechanics [*7,8*]. Within the framework of this theory the material toughness measured and reported as critical stress intensity at the onset of plane strain crack extension K_{Ic} is characterized by two parameters, the critical notch fracture stress σ_{mc} and the process zone ρ_c which is twice the Neuber microsupport effect constant p^+, namely

$$K_{Ic} = \frac{\sigma_{mc}}{2} \sqrt{\pi\, \rho_c} \tag{4}$$

Recent work by the author has led to further extension of notch analysis of fracture. A characterization of the fracture resistance (K_{Ic} or G_{Ic}) in terms of material specific properties was achieved [*1,2*]. Accordingly, brittle materials such as ceramics acquire their strength by dissipative processes which take place in the nonlinear elastic process zone ahead of a sharp notch or macrocrack tip. The dissipative processes generate microcracks. Thereby, we neglect other terms of dissipative processes like dislocation motion, glide of crack faces, or chemical reactions. It was shown by Hoagland et al [*9*] that the microcrack density of the potential microcrack cleavage planes is limited to about 50 percent thereby neglecting the elastic interaction of the microcracks. This state of material is attained when the stress strain curve of a notches bar reaches its maximum value meaning that the longitudinal tensile stress (σ_{yy}) ahead of the notch root equals the critical notch fracture stress (σ_{mc}) Fig. 1. At this stage, favorably oriented microcracks inside the process zone join to lengthen the macrocrack. However, it is well known from acoustic emission analysis that intense microcracking can occur at stresses well below the fracture stress ahead of a macrocrack. This stress level (σ_m) will not be discussed in further detail, but will be called "intense microcracking" (Fig. 1). It corresponds to the yield stress of metals.

By introducing the critical stored elastic energy density and the critical elastic energy release rate of the material inside the process zone as a consequence of a critical microcrack configuration in this region, a relationship for the critical stress intensity factor K_{Ic} in terms of material specific data, like Young's modulus E mean grain size d, specific fracture energy γ_s and the configuration of microcracks inside the process zone, has been derived [*1-3*]

$$K_{Ic} = 2\sqrt{\frac{\gamma_s E}{d\,A(\mu)}}\; I_\rho \sqrt{\pi\,\rho_c} \tag{5}$$

A (μ) denotes Poisson's ratio at the specific stress state. I_ρ is the elastic microcrack interaction parameter which denotes the change in stress intensity of one microcrack with respect to the elastic potential of the surrounding microcracks. The proposed model for the crack extension of ceramics correspond to the Dugdale Barenblatt model originally conceived for metals [*11*].

Concerning the resemblance between the plastic zone and the process zone, we must keep in mind correlations between the specimen dimensions of ceramics and the process zone size, especially the factor $(K_{Ic}/\sigma_{mc})^2$, to get valid K_{Ic}-measurements. This is shown experimentally in the following section.

Experimental Observations

Four-point bend specimens of two aluminas of different impurity level, which are 0.2 percent (denoted *A*) and 1 percent (denoted *F*) respectively are used with nominal sizes of 7, 14, and 135 mm as well as 3, 6, and 60 mm for thickness, width and length, respectively. The grain size and densities of the materials varied between 2 to 9 μm and 2.5 to 3.9 g/cm^3, respectively. Notches were diamond sawed in the range of 0.1 to 0.8 mm. It is assumed that half the notch width is equal to notch radius ρ. The K_I-values for the maximum load were measured, which shows a strong dependence on the square root of the notch radius as it was found for other brittle materials (see Eqs 1 and 4). This is shown in Figs. 2 and 3.

Only specimens with thickness $B = 7$ mm and notch root radius $\rho \leq \rho_c$ give specific material valid K_{Ic}-values. Thus, these values lie on a plateau. The $\sqrt{\rho}$ value of the intersection of this plateau with the line connecting the measured values of K_I for $\rho > \rho_c$ with zero gives the exact value of ρ_c. Compared to small specimens with thickness $B \leq 3$ mm, all K_I-values

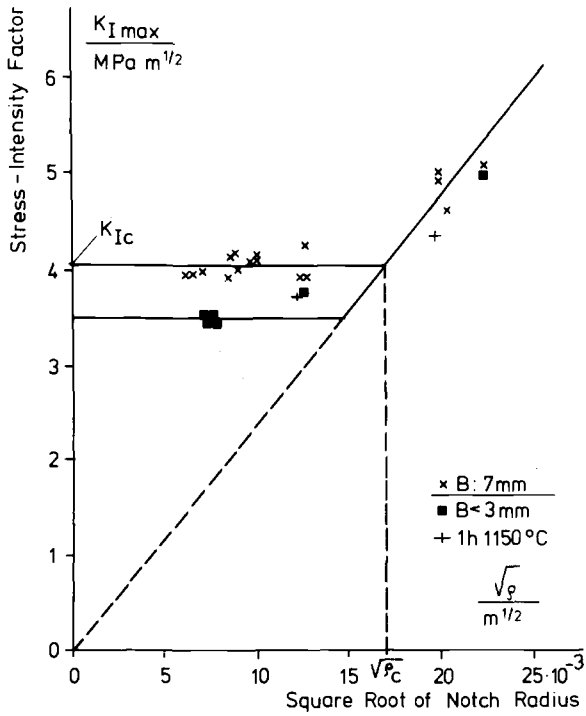

FIG. 2—*Correlation of stress-intensity factor* K_I *with notch radius* ρ *for four-point bend specimens with nominal thickness* B *of 3 and 7 mm of an alumina (A).*

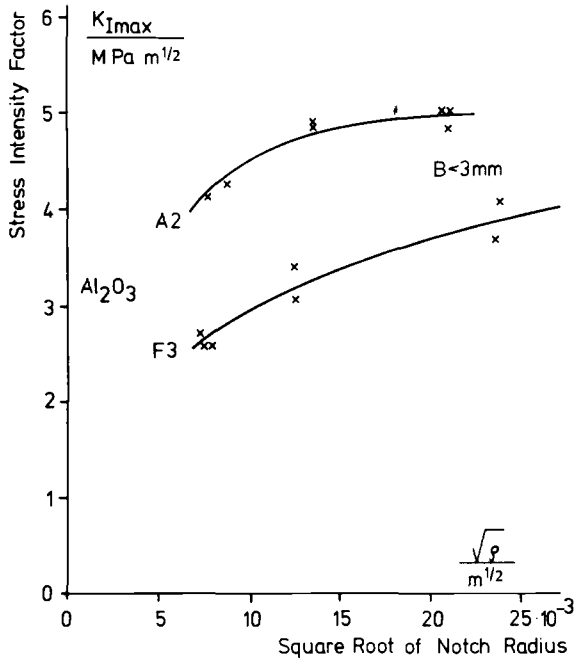

FIG. 3—*Correlation of stress intensity factor* K_I *with notch radius* ρ *of an alumina for four-point bend specimens with thickness* B *of less than 3 mm.*

are lower. This was also found in previous experiments using specimens with thickness $B = 1.5$ mm and 3.0 mm [*3, 10*[.

With these results, together with earlier measurements concerning K_{Ic}-values of an alumina with about 3 percent impurities [*3*], we conclude that the aforementioned relations must hold

$$(B,\ W/2,\ W - a) > 50\,\rho_c \tag{6}$$

and

$$\rho \leq \rho_c \tag{7}$$

However, the dimension of the process zone is related to microstructural features. Following an earlier paper [*1*] it was found that

$$\rho_c \approx d\,\frac{K_{Ic}^2}{\gamma_s\,\pi\,E}\,I_\rho^{-2} \tag{8}$$

Thus, with specimens having a notch root greater than ρ_c, $K_I > K_{Ic}$ will be measured.

Therefore, comparing Eqs 4 and 8, it must be concluded that distinct relations exist between the grain size and geometric parameters of the specimen to get real K_{Ic} measurement. This will be discussed in the next section.

Discussion

K_{Ic}-values of ceramics are characterized by the elastic energy release rate at instability of the material inside and outside the process zone. Specially the energy release rate of the material inside the process zone must be autonomous, that is, independent of geometric parameters of the specimen and the external loads. The autonomy is complete, but is approximated the better the smaller ρ_c is in comparison to geometrical parameters, as pointed out by Broberg [*11*]. However, ρ_c cannot be arbitrarily small, because the state of the region is associated with the concept of an elastic continuum. Therefore, ρ_c must be larger than the distance between the inhomogeneities, that is, grains or pores which signify departure from a continuum. Generally, ρ_c must be equal or greater in comparison to the notch root radius and small in comparison to all other specimen dimensions.

If fracture loads are well below "intense microcracking" the process zone is confined close to the notch root.

Microcracking during loading a random polycrystalline ceramic like alumina (Al_2O_3) is due to the anisotropy of the elastic constants and of the thermal expansion between the grains or between grains of different phases. Mainly high internal stresses are introduced in these materials during cooling from the sintering temperature which depends on the degree of thermal expansion anisotropy (TEA), the cooling rate and the grain size as pointed out by Blendell et al [*13*] and by Siebeneck et al [*14*]. The grain size dependence of these internal stresses also was pointed out by Buresch [*15*] concerning the stress concentration on intergranular pores. It was found theoretically as well as experimentally that a microscopic stress intensity factor K_I which is related to the TEA stresses increases with the square root of the grain size as well as linearly with the residual strain caused by TEA, and decrease with increasing intergranular porosity. Spontaneous intergranular microcracking during cooling from the sintering temperature will occur if the TEA K_I-value reaches the value of the critical microscopic stress intensity factor K_{Ic} which is related to the grain boundary energy [*15*]. In the high stress field ahead of a macrocrack, potential microcrack nuclei are activated by superposition with the TEA stresses, and intergranular microcracks will grow unstable up to a pinning point which may be an inclusion or a grain boundary. With increasing load, instability occurs when the elastic energy densities inside and outside of the microcrack-affected process zone reaches critical values. These are related

to the density, length, orientation, and elastic interaction of the microcracks inside the process zone. The elastic energy density inside the process zone is proportional to the square of the notch fracture strength σ_{mc} [3]. Thus, the critical elastic energy density criterion at instability is related to a critical stress criterion of failure.

Small Process Zone and Large Notch Root Radius

Physically, failure of specimen will occur if the maximum principal stress σ_{yy} exceeds σ_{mc} over a characteristic dimension and the process zone size reaches a critical value ρ_c, at a given crack length a_c. Following [1,2], the material specific notch fracture strength is given by

$$\sigma_{mc} = 2\,\sigma_c \sqrt{\frac{a_c}{\pi\,\rho_c}}\; y\left(\frac{a}{W}\right) \tag{9}$$

where y is a geometric parameter depending on the notch length to thickness ratio and σ_c is the critical fracture strength in the equation

$$K_{Ic} = \sigma_c \sqrt{\pi\, a_c}\; y\left(\frac{a}{W}\right) \tag{10}$$

normally used for the determination of K_{Ic} with critical crack of length a_c. With increasing notch root $\rho > \rho_c$, fracture strength increases to fulfill Eq 8. This is valid if σ_c is small in comparison to the strength for "intense microcracking."

Plane strain fracture toughness is naturally independent of B. Thus the fracture toughness K_{Ic} as a function of specimen thickness B will be approximately as shown in Fig. 4.

Large Process Zone in Plane Stress

If the fracture strength σ_c is comparable to the stress for "intense microcracking," microcracking will occur also far away from the notch root lowering Young's modulus in regions especially around the ligament of the specimen. Following Eq 2, the notch sensitivity is reduced in this case. The notch fracture strength will decrease, that is, K_{Ic} will decrease (Eqs 2 and 4). This is clearly shown in Figs. 2 and 3. This corresponds to plane stress.

For specimen thicknesses B not very much greater than ρ_c plane stress will exist. In some cases, a thin microcrack region will develop at a sharp notch. This region occurs for geometrical reasons (shearing). Obviously, by dimensional arguments, the linear size of the microcrack region is proportional to the specimen thickness, Fig. 5. Thus, G_{Ic} is proportional

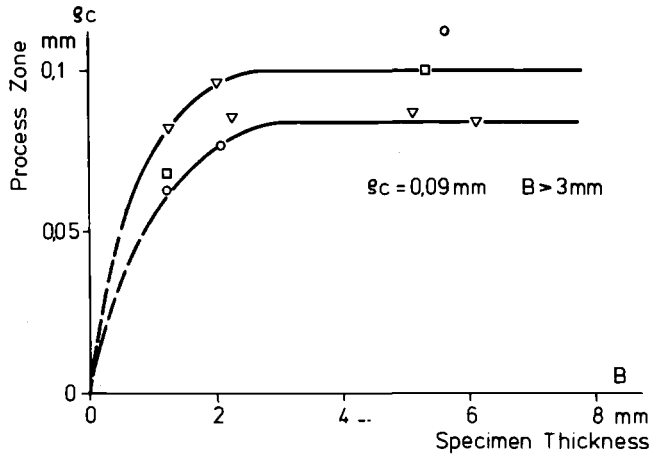

FIG. 4—*The dependence of stress intensity factor on thickness of four-point bend specimens of an alumina (plane strain for* B > *3 mm).*

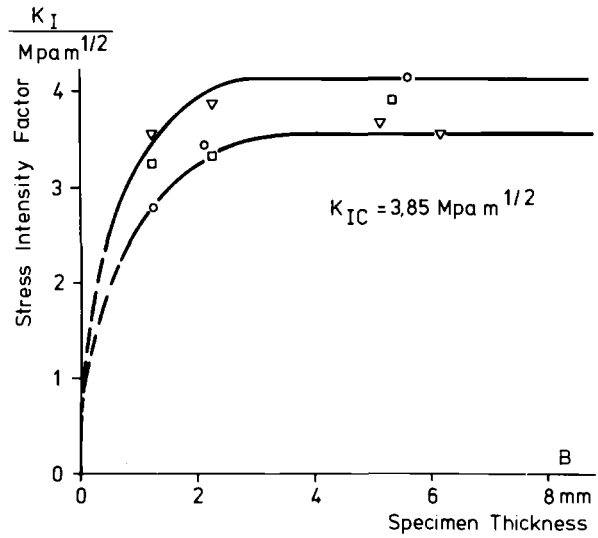

FIG. 5—*The dependence of process zone size on four-point bend specimens of an alumina (plane strain for* B > *3 mm).*

to B and the plane stress fracture toughness K_I which is proportional to $\sqrt{G_I}$ is proportional to $\sqrt{B}$. This is clearly shown in Figs. 4 and 5 in accordance with our experimental measurements. The aforementioned physical interpretation for the thickness dependence of toughness was first pointed out by Broberg [*11*].

Specimen Size and Grain Size Relationship for K_{Ic}

The stored elastic energy density inside ρ_c, which is proportional to the dissipative energy, depends on grain size, pore size, and phase distribution, as we have shown in a preceding paper [*1*]. For single phase alumina, ρ_c is proportional to the mean grain size d. The proportionality was found to be in the range

$$30\,d \leq \rho_c \leq 150\,d \tag{11}$$

However, the proportionality in general depends strongly on the ratio of the energy release rate G_{Ic} to the specific fracture energy γ_s and also on the Weibull modulus [*12*].

In the literature it is often found that, for measurements done to reveal the K_{Ic}-dependence on microstructural parameters, only a single small specimen size is used; therefore, following Eqs 3 and 11, the specimen size dependence of K_{Ic} is ignored. This means, for a specific specimen series of a ceramic with mean grain sizes in the range of 2 to 20 μm, the process zone size may vary, for, say $\rho_c = 30\,d$ between approximately 0.06 and 0.6 mm. Hence, for a material with a mean grain size of 2 μm, the thickness of SENB specimens may be $B = 3$ mm. Contrary, for specimens of a ceramic with a mean grain size of 20 μm, the thickness B must be $B = 30$ mm. The corresponding values of notch root radii to get K_{Ic}-values in plane strain are 60 μm and 0.6 mm, respectively.

If, in case of this specific example, only SENB specimens with thickness $B = 5$ mm and notch root radius $\rho = 0.15$ mm are used, typically for some literature data, an enhanced K_{Ic} will be measured for the fine grained material with mean grain size of 2 μm, because in this case $\rho > \rho_c = 60$ μm (see Fig. 2). Contrary for the coarse grained material with a mean grain size of 20 μm, a lowered K_{Ic}-value will be measured, because the specimen thickness equals $B < 50\,\rho_c$ (see Figs. 6 and 7). This misalignment often is found in literature.

The notch fracture strength σ_{mc} of the two aluminas measured in plane-strain conditon ($B = 7$ mm) shows a slightly different trend with respect of the grain size dependence as shown in Fig. 6 for the toughness (see Fig. 8). Contrary to the first term of Eq 2, σ_{mc} increase with increasing grain size. But concerning the second term this increase can be explained to be a measure of the elastic microcrack interaction parameter, Eq 2 [*1*]. It is often found in the literature that with increasing grain size transgranular fracture is more pronounced. The crack path becomes more tortuous as a consequence of microcracking. This will enhance the notch fracture strength σ_{mc} as predicted from Eq 2.

As in the case of fracture toughness the notch fracture strength decrease markedly with decreasing density (see Fig. 9). This decrease is in both

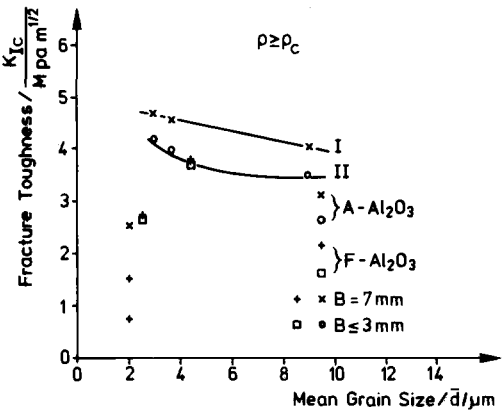

FIG. 6—*Dependence of fracture toughness on mean grain size for alumina of different densities (kg/m^3) (four-point bend specimens with thickness in the range of* B = *7 mm in plane strain and* B ≤ *3 mm in plane stress).*

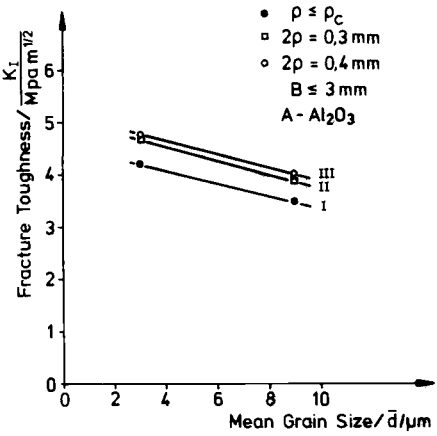

FIG. 7—*Dependence of fracture toughness on mean grain size for alumina of different densities (kg/m^3) (four-point bend specimens in plane stress with different notch radii).*

cases more pronounced as aspected from the decrease of Young's modulus with respect to increasing porosity. The drop is a measure of the low notch sensitivity of high porous alumina. Concerning the data scatter in the last figures one must consider that each single point in the Figs. 4 to 9 is a mean of about ten individual specimens (see Fig 2). As pointed up by Pabst and Buresch [*3, 16, 17*] the standard deviation of the K_{Ic} of a specific ceramic is better than 5 percent. The data scatter in Figs. 4 to 9 is related to changes in microstructure.

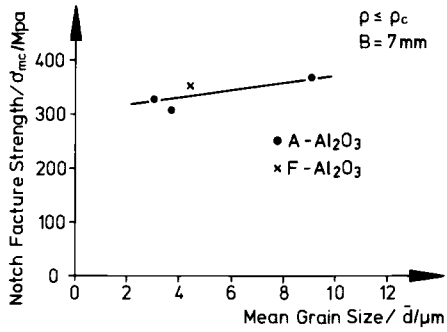

FIG. 8—*Dependence of notch fracture strength on mean grain size for aluminas of densities in the range of 3800 to 3850 kg/m*^{3} (B = 7 *mm*).

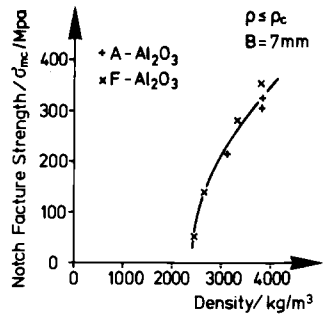

FIG. 9—*Dependence of notch fracture strength on density of aluminas of mean grain size in the range of 2 to 5 μm* (B = 7*mm*).

This reverse dependence, that is, the increase of the K_{Ic}-values with increasing notch root radius and their decrease with decreasing thickness of SENB-specimens, is shown in Figs. 6 and 7 for measured K_{Ic}-values of different specimen size, notch root radius, and microstructure. The grain size and density dependence of the measured K_{Ic}-values is in general agreement with Eqs 2 and 4. That means, K_{Ic} decreases with increasing grain size and decreasing density in the grain size range investigated.

Influence of Cyclic Loading and Unloading on K_{Ic}*-Measurements*

Another misinterpretation of K_{Ic}-values of ceramics often found in the literature concerns the precracking of specimens through slow crack growth. Generally sawing, drilling, or tooling of Al_2O_3 ceramics generate scratches, plastic deformation, and microcracking in the machine induced zone. The degree of distortion depends on the size and shape of the diamond grains used with the tools, the tooling velocity, and also on the pressure which

acts during the different machine processes. Normally, surface microcracks and scratches lower the strength of the material, and it was suspected that the scratches and microcracks which are generated at the root of the notch during sawing alter the K_{Ic}-value. It was found by Pabst and Buresch [*3,16,17*] that these scratches and microcracks can lower the K_{Ic}-value only for notch root radii $\rho > \rho_c$ by an amount up to about 10 percent. The decrease depends on the size of the diamond grains and probably on the cutting velocity and the pressure used. However for notch root radii $\rho < \rho_c$ a measurable change of K_{Ic} was not observed.

It is well known that scratches and microcracks can be healed or blunted during heat treatments. In the case of sawed notches it was found by Pabst and Buresch [*3,16,17*] that heat treatment does not influence K_{Ic}-values ($\rho < \rho_c$) whereas the K_I-values ($\rho > \rho_c$) are enhanced by an amount of about 10 percent. Physically, we believe that it is the radius of the strongest scratch or microcrack at the notch root which influences the K_I-value. For $\rho < \rho_c$ the K_{Ic}-value is independent on the notch-, scratch-, or microcrack radius, whereas in the case of K_I-values with $\rho > \rho_c$ this effect is more pronounced.

The annealing process is related to pore evolution and probably grain growth [*18*]. This change of microstructure can influence the strength. Nevertheless the K_{Ic} value is a real material-specific quantity unaffected by machining whereas σ_{mc} depends on this process and may be affected alternatively by change in microstructure during scratch blunting or microcrack healing, which must be clarified [*12*].

In the case of stable precracking a notched specimen by slow crack growth or load cycling microcracking is enhanced in the region surrounding the crack tip. This is accomplished by the activation of potential microcrack sources in the region of high stress concentration and the slow metastable growth of these nuclei up to a pinning point, in accordance with experimental observations [*19-21*].

During unloading of a precracked specimen, the resilience of the specimen disturbs the equilibrium of stresses inside the process zone which exists for the maximum external load. During one cycle the overall stress over the process zone changes from the tensile to the compression mode. The redistribution of stresses during cycling loading stabilizes existing microcracks through shearing and plastic deformation which cause crack tip blunting and generates new microcracks. The dissipative processes are evident from acoustic emission analysis and from the hysteresis of the load deflection curve. They also are thought to be related to frictional effects during microcrack opening and closure and are closely related to some microstructure features like pore and grain size distribution. In conclusion, it is thought that the dissipative processes during cyclic loading are responsible for the increase of fracture toughness through an increase of the microcrack density and their elastic interaction. Following Eq 5 the fracture

toughness will increase in accordance with experimental results [*5,6,19–22*]. This enhanced toughness must be considered in stable crack growth measurements for obtaining work-of-fracture data. The inelastic behavior of ceramic materials influences the compliance. This must be considered concerning the computations for stable crack growth of Bluhm [*23*].

Conclusion

For real materials specific K_{Ic} measurements of ceramics some rules must be kept in mind equivalent to that valid for metals. These rules refer to the correlations between geometric factors of the specimen, the notch width, and the process zone size, respectively. It was found experimentally, for single phase alumina with quarter point loaded four-point bend specimens with thickness B, width W and length L, equivalent to 1:2:20, that the thickness must follow, combining Eq 3 and 4

$$B \geq 60 \left(\frac{K_{Ic}}{\sigma_{mc}} \right)^2 \tag{12}$$

and the notch root radius, combining Eqs 4 and 7

$$\rho \leq \frac{4}{\pi} \left(\frac{K_{Ic}}{\sigma_{mc}} \right)^2 \tag{13}$$

Acknowledgment

I thank N. Claussen for fruitful discussions and G. Kleist for carefully reading the manuscript.

References

[*1*] Buresch, F. E. in *Fracture Mechanics of Ceramics*, Vol. 4, Plenum Press, N.Y., 1978, pp. 835–847.
[*2*] Buresch, F. E. in *Fracture 1977*, Vol. 3, 4th International Conference on Fracture, University of Waterloo Press, Waterloo, Canada, June 1977, pp. 929–932.
[*3*] Buresch, F. E., *Science of Ceramics*, Vol. 7, Société Française de Céramique, 1973, pp. 381–398.
[*4*] Pabst, R. F., Steeb, J., and Claussen, N. in *Proceedings*, Conference on *Fracture Mechanics of Ceramics*, Vol. 4, Penn State University, July 1977, pp. 921–933.
[*5*] Simpson, L. A., *Journal of the American Ceramic Society*, Vol. 56, No. 11, Nov. 1973, pp. 610–611.
[*6*] Pratt, P. L. in *Fracture 1977*, Vol. 3, 4th International Conference on Fracture, University Waterloo Press, Waterloo, Canada, June 1977, pp. 909–912.
[*7*] Neuber, H. in *Konstruktion*, Vol. 20, 1968, pp. 245–251.
[*8*] Weiss, V. in *Fracture*, Vol. 3, New York and London, 1971, pp. 227–264.
[*9*] Hoagland, R. G., Embury, J. D., and Green, D. J., *Scripta Metallurgica*, Vol. 9, 1975, pp. 907–909.
[*10*] Claussen, N., Pabst, R. in *Proceedings*, British Ceramic Society, Vol. 25, 1975, p. 139.

[11] Broberg, K. B., *Journal of the Mechanical Physics of Solids*, Vol. 19, 1971, pp. 407-418.
[12] Buresch, F. E., unpublished work.
[13] Blendell, J. E., Coble, R. L., and Charles, R. J., "On the Relaxation of Stresses Arising from Thermal Expansion Anisotropy During Cooling Polycrystalline Materials," *Ceramic Microstructure "76"*, pp. 721-730.
[14] Siebeneck, H. J., Cleveland, J. J., Hasselman, D. P. H., and Bradt, R. C., "Thermal Diffusivities of Microcracked Polycrystalline Ceramics," *Ceramic Microstructure "76"*, p. 753-762.
[15] Buresch, F. E. in *Science of Ceramics*, Vol. 7, 1973, p. 475.
[16] Buresch, F. E. and Pabst, R., in "Bestimmung von Festigkeitseigenschaften Keramischer Stoffe unter Verwendung bruchmechanischer Methoden, *Science of Ceramics*, Vol. 6, 1973, XVI/3.
[17] Pabst, R., "Bestimmung kritischer Spannungsintensitätsfaktoren keramischer Stoffe mit dem Biegeversuch," Dr.-Ing. thesis, Stuttgart, 1972.
[18] Gupta, T. K., *Journal of the American Ceramic Society*, Vol. 59, 1976, pp. 259-262.
[19] Hübner, H. and Illek, W., *Journal of Materials Science*, Vol. 12, 1977, pp. 117-125.
[20] Hübner, H. and Strobl, W., "Anwendbarkeit bruchmechanischer Verfahren auf keramische Werkstoffe," Ber. Dt. Keram. Ges. Vol. 54, 1977, pp. 401-404.
[21] Kriz, K, "Investigations of Microcrack Formation During Slow Crack Growth in Polycrystalline Alumina Using Acoustic Emission," ERAMS-I/TR 57 (April 1978).
[22] Hodulak, L. and Klein, G., "Spannungsanalyse von Mehrfachrissen," Wiss. Ber. JFKM 7/74 (Freiburg 1974).
[23] Bluhm, J. I., *Fracture 1977*, Vol. 3, 4th International Conference on Fracture,, Waterloo, Canada, June 1977, University of Waterloo Press, pp. 409-417.

R. A. Schmidt[1] *and T. J. Lutz*[1]

K_{Ic} and J_{Ic} of Westerly Granite—Effects of Thickness and In-Plane Dimensions

REFERENCE: Schmidt, R. A. and Lutz, T. J., "**K_{Ic} and J_{Ic} of Westerly Granite—Effects of Thickness and In-Plane Dimensions,**" *Fracture Mechanics Applied to Brittle Materials, ASTM STP 678,* S. W. Freiman, Ed., American Society for Testing and Materials, 1979, pp. 166-182.

ABSTRACT: An investigation is described in which tensile properties, fracture toughness, and critical J-integral are measured for Westerly granite, a rock that is used widely in rock mechanics studies. This was primarily a parameter sensitivity study in which the effects of specimen dimensions and testing techniques were assessed. It is hoped that this study will aid in establishing tentative standards and guidelines for fracture toughness testing of rock as well as indicate the feasibility of using a J-integral fracture criterion for this material.

ASTM standard specimen configurations of the compact and bend types were tested with compact specimens ranging in width from $W = 25.4$ mm to $W = 406.4$ mm (0.5T to 8T) and with thickness ranging from 13 to 100 mm. A series of 4T compact specimens were tested to assess the effects of thickness and fatigue precracking.

Techniques are described that enable several values of K_{Ic}, a complete J versus crack growth curve, and a J_{Ic} value to be obtained from each sample. Direct-pull tension tests on shaped specimens of Westerly granite are described which indicate a high degree of nonlinear, inelastic behavior. This fact raises questions about the use of linear elastic fracture mechanics, LEFM, but the J_{Ic} data presented appear to validate the K_{Ic} measurements.

KEY WORDS: fracture properties, fracture (materials), mechanical properties, fracture tests, size effect, fracture toughness, crack propagation, rock mechanics, rock (material)

The number of fracture mechanics investigations of rock materials has begun to increase rapidly in recent years. Prior to 1977, the U.S. Symposium on Rock Mechanics might have had at most one or two papers per year

[1]Member of technical staff and engineering and science assistant, respectively, Sandia Laboratories, Albuquerque, N. Mex. 87115.

dealing with fracture mechanics of rock, while in 1977 there were thirteen papers in two separate sessions devoted to the subject at the symposium.

Much of this interest in the fracture of rock stems from energy research. Resource recovery techniques such as stimulation of oil and gas wells by hydraulic fracturing, fragmentation of oil shale beds for *in situ* retorting, and thermal-stress induced fracturing of geothermal sources would benefit from a better understanding of the fracture process and requirements for crack propagation.

While a big step is required to apply fracture toughness measurements from intact, undamaged laboratory samples to large-scale field events such as the aforementioned, there are some small-scale field experiments being undertaken that may help bridge the gap. For example, Sandia Laboratories under contract to the Department of Energy is conducting hydraulic fracturing experiments at the Nevada Test Site that are aimed at testing various fracturing concepts. In these experiments hydraulic fractures of various sizes are created and marked with grout or dyed water and then, using an existing tunnel complex, the fractures are uncovered and examined directly by driving a tunnel to the fracture site [*1*].[2]

Several previous investigations on rock materials have examined the effect of specimen size on apparent fracture toughness, K_Q [*2-4*]. Indiana limestone, for example, was shown to have a K_Q versus crack length behavior that is similar to aluminum alloys. The ASTM requirement (ASTM Test for Plane-Strain Fracture Toughness of Metallic Materials) (E 399 - 76) for crack length, a,

$$a > 2.5\left(\frac{K_Q}{\sigma_y}\right)^2$$

was shown to apply reasonably well for this rock when σ_y was replaced with σ_{ult} [*2*]. However, much more fracture data are required on various rock types using a wide range in specimen dimensions before standards can be reliably set for fracture toughness testing of rock in general. The primary purpose of this investigation, then, is as a parameter sensitivity study to measure the fracture toughness of Westerly granite for a variety of thicknesses and in-plane dimensions using two specimen configurations.

However, it should be noted that the stress-strain behavior of this rock in tension is known to be rather nonlinear and, as a result, the use of a linear elastic parameter, K, may be questionable. Since the use of the J-integral fracture theory does not require linear-elastic behavior, additional measurements were made on these tests to determine the critical J-integral, J_{Ic}. Effects of specimen size on J_{Ic} will be addressed and correlated with

[2] The italic numbers in brackets refer to the list of references appended to this paper.

the K_{Ic} measurements. In addition, results from direct-pull tension tests will be presented and used for the J_{Ic}-K_{Ic} correlation, for crack length determination by compliance, and for evaluating the size effects on K_Q.

Material and Specimen Description

The rock used in this investigation, Westerly granite, comes from a quarry in Westerly, R.I., and is particularly well known to rock mechanics investigators. It is relatively fine-grained (average grain diameter of 0.75 mm) and is highly homogeneous on the macroscopic scale. A detailed description of this rock can be found elsewhere [*5,6*].

Specimens tested in this investigation consisted of 8 tension specimens and 26 fracture specimens. The tension tests were performed on direct-pull dogbone specimens as seen in Fig. 1. Accurate alignment of these specimens was obtained by grinding the reduced test section after threaded end caps had been bonded to the specimen ends. This reduced test section is 25 mm in diameter by 35 mm long. Two pairs of foil strain gages (gage length 6.4 mm) were bonded to opposite sides of the test section to measure axial and transverse strains.

The fracture tests were conducted on 20 compact specimens and 6 notched beam specimens of various sizes. The dimensions and tolerances of these specimens were in accordance with ASTM recommendations including the use of chevron notches to aid in establishing a well-behaved crack front (ASTM Method E399). All specimens ranged in width from 25 to 400 mm and thickness from 13 to 100 mm as depicted in Fig. 2. Notched beam specimens ranged in width from 25 to 100 mm and thickness from 13 to 50 mm.

Experimental Techniques

Tension Tests

All tension tests and fracture tests were performed in a 1.0 MN servo-controlled MTS[3] load frame. Data for all tests were digitized, reduced, and plotted in real time by means of a PDP11[4] computer, MTS interface, graphics display terminal, and appropriate software. (Information concerning this computer system and copies of the application programs can be obtained by contacting the authors.)

Tension specimens were pulled to failure at a constant stress rate of 220 kPa/s. Bending stresses were minimized by the combination of careful machining described previously and by including high strength alloy link

[3] MTS Systems Corporation, Minneapolis, Mn.
[4] Digital Equipment Corporation, Maynard, Mass.

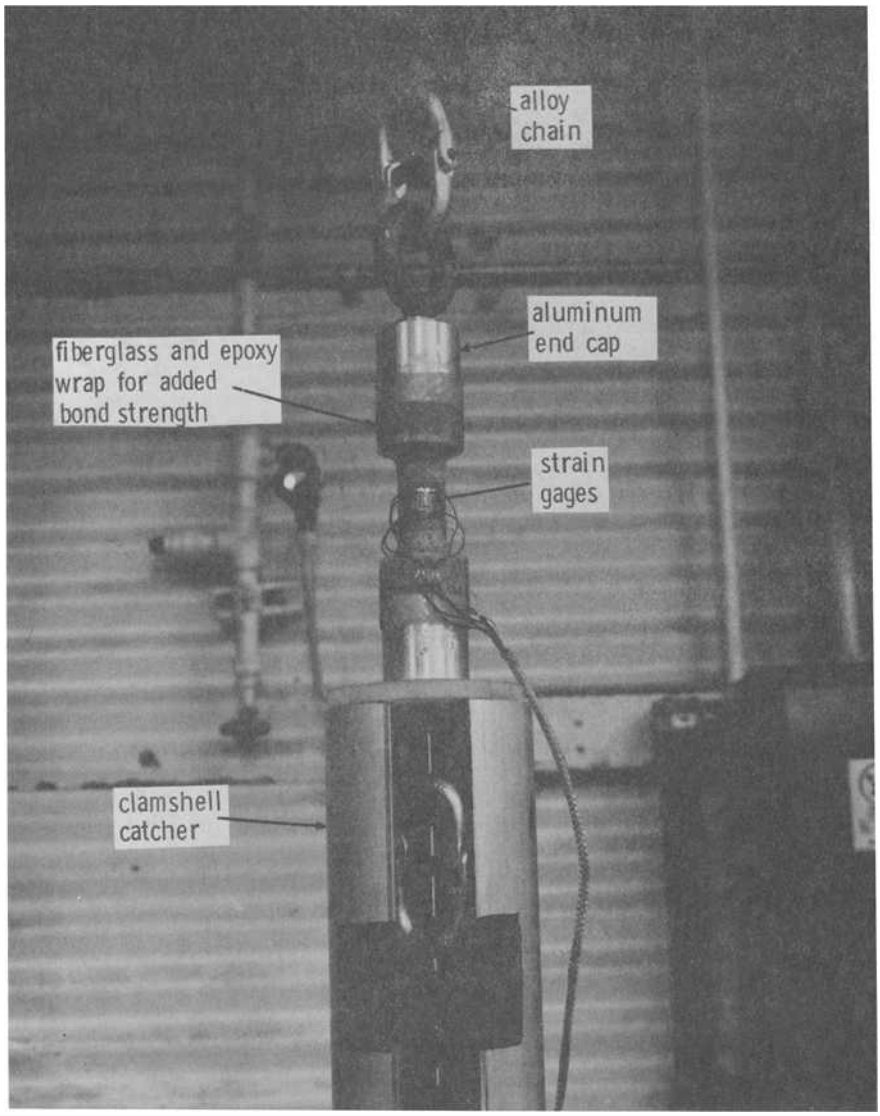

FIG. 1—*Direct-pull tension test of Westerly granite.*

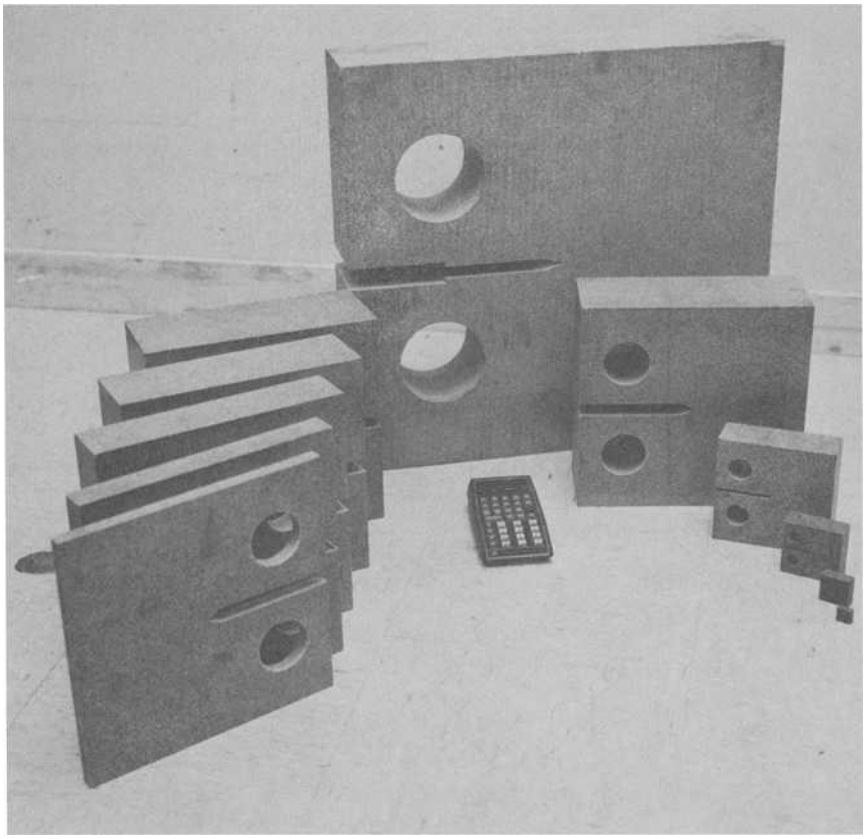

FIG. 2—*Compact specimens of Westerly granite.*

chain in the load train as recommended in ASTM Test for Direct Tensile Strength of Intact Rock Core Specimens (D 2936-71) (see Fig. 1). Since granite is a poor conductor of heat compared to metals, strain gage voltage was held to less than 3 V to minimize heating effects.

Fracture Tests

Fracture tests of compact specimens were performed using a clevis design following ASTM recommendations (ASTM Method E 399) but reduced in size somewhat due to the lower load requirements (Fig. 3). Specimens were precracked in fatigue and loaded to failure by using the crack mouth displacement (CMD) as the control parameter. Since CMD at fracture ranged from 0.5 mm to as low as 0.03 mm, the standard clip-in displacement gages (ASTM Method E 399) were replaced with a linear-variable differential transformer, LVDT, displacement transducer having a linear

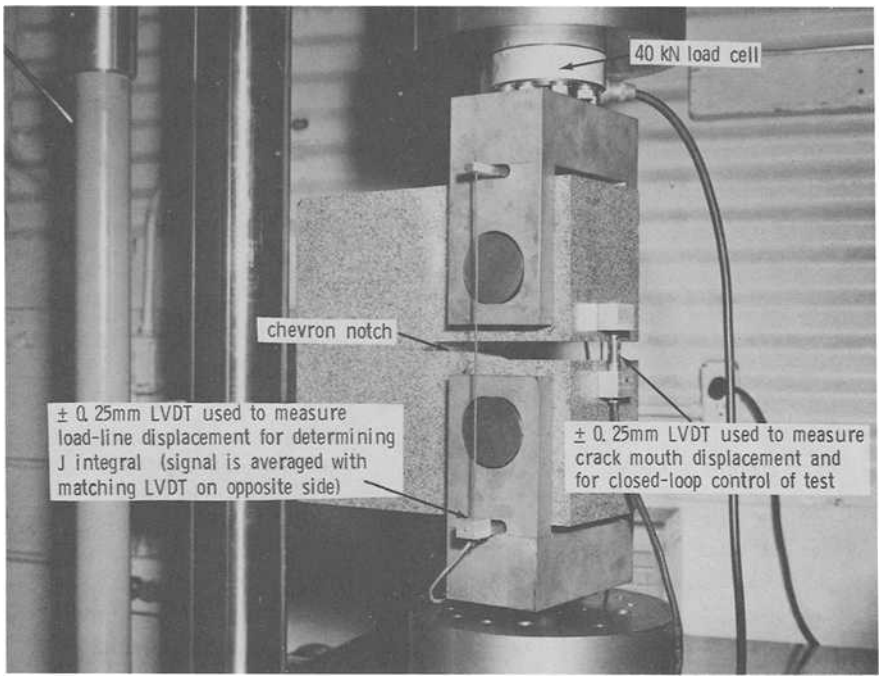

FIG. 3—*Test setup for compact specimen of Westerly granite* (W = *200 mm*, B = *100 mm*).

range of ±0.25 mm.[5] This particular LVDT, known as a precision gage head, was mounted so as to bridge the notch providing ample signal level for control and resolution to better than 0.01 μm.

Load-line displacement measurements were made on the compact specimen tests for J-integral determinations. The measurement technique employed here is similar to one tested by Mills et al [*7*] for J_{Ic} measurements of metals at elevated temperatures. As shown in Fig. 3, a fixture is mounted to the top and bottom of the specimen and allowed to extend through the clevises. This fixture holds a pair of LVDT's, one on each side, which are connected in series to obtain the load line displacement while ignoring any bending effects.

Notched bend tests were performed in a similar manner except that no attempt was made to determine J_{Ic} or to measure the displacement of the load point (Fig. 4). Loading was performed in three-point bending using a fixture that conforms to ASTM recommendations (ASTM Method E 399). Fatigue precracking and the final loadings were performed under CMD control using the same LVDT as for the compact specimens.

[5] Model No. PCA-220-010, Schaevitz Engineering, Camden, N.J.

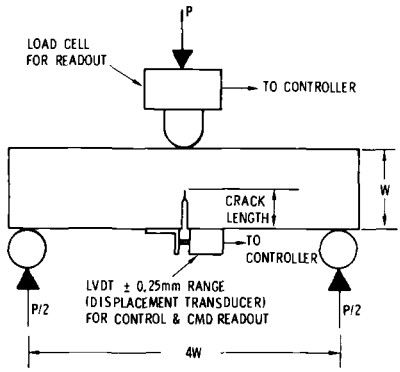

FIG. 4—*Fracture test schematic for bend specimen.*

Fatigue Precracking

A single fatigue crack was made to propagate from the machined notch in the fracture specimens by repeated loading to approximately 90 percent of the breaking load. (When the cyclic maximum load was less than 90 percent, all crack propagation appeared to cease). This loading actually was performed by a sinusoidal variation of the crack mouth displacement at a frequency of 2.2 Hz. By controlling CMD, the load automatically decreases as the crack grows providing the stability needed to fatigue crack this material.

Typical load versus CMD records from one test at various stages of fatigue cracking are shown in Fig. 5. Evidence of crack growth is seen as an increase in compliance for an increase in cycle number. (Compliance is determined from the inverse slope of the upper portion of these load-displacement records.)

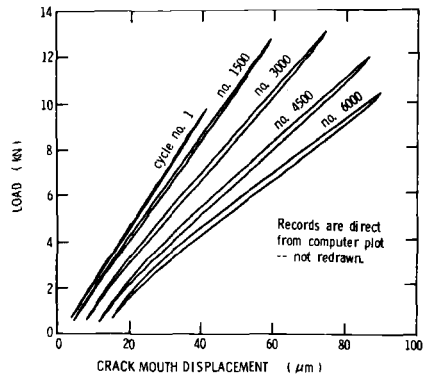

FIG. 5—*Load-displacement records of selected fatigue cycles for one compact specimen.*

It should be noted that these records show definitive evidence of crack surface interference, commonly called crack closure, as has been noted for other rocks [2,3]. Crack closure occurs when, upon unloading a cracked specimen, the crack surfaces contact each other before the load has been entirely removed. In other words, the crack is created in such a way that the two surfaces will no longer fit together perfectly as in a jigsaw puzzle. This is evidenced in Fig. 5 by records after the first cycle. The initial loading takes place with slope equal to that of the first cycle when there was no crack which indicates that the crack is completely closed initially. As the load increases, the crack gradually opens and the curve bends toward increasing compliance until the crack is fully open when the curve becomes linear, that is, compliance is constant. Also note that the linear portion of the curve extrapolates back to the origin indicating that no permanent set would occur were it not for this crack surface interference. This will be an important consideration later when using load to failure records to compute the J-integral from the total work done.

Load to Failure

All loadings were performed by increasing the crack mouth displacement at a constant rate of 0.6 μm/s which for these tests results in an increase in stress intensity at a rate of 10 to 30 kPa $\sqrt{m}$/s. Each specimen was loaded and unloaded several times. The maximum CMD for each run was varied randomly which resulted in differing amounts of crack growth for each cycle with the hope of obtaining a plot of J versus crack growth and several values of K_Q from each specimen.

The typical load-displacement records of Fig. 6 show the initial bending as the crack opens, a linear portion where the crack is fully open, bending again as inelastic behavior occurs in the crack tip process zone, followed by stable crack growth as the load drops, and finally unloading. In all cases the failure was steady and stable with no indications of pop-in or crack burst.

Crack Length Determination

It was initially felt that a direct measure of crack length and crack front shape in the fracture tests could be made by staining the crack with a dye penetrant after fatigue precracking but prior to the final load to failure. The relatively low permeability of undamaged Westerly granite should allow a dye to penetrate a crack without significant penetration of the rock itself. This approach seemed preferable to the indirect method of determining crack length from compliance (inverse slope of the load-displacement record) as was used in a previous study on Indiana limestone [2]. Knowledge of the crack front shape also would aid in determining a pos-

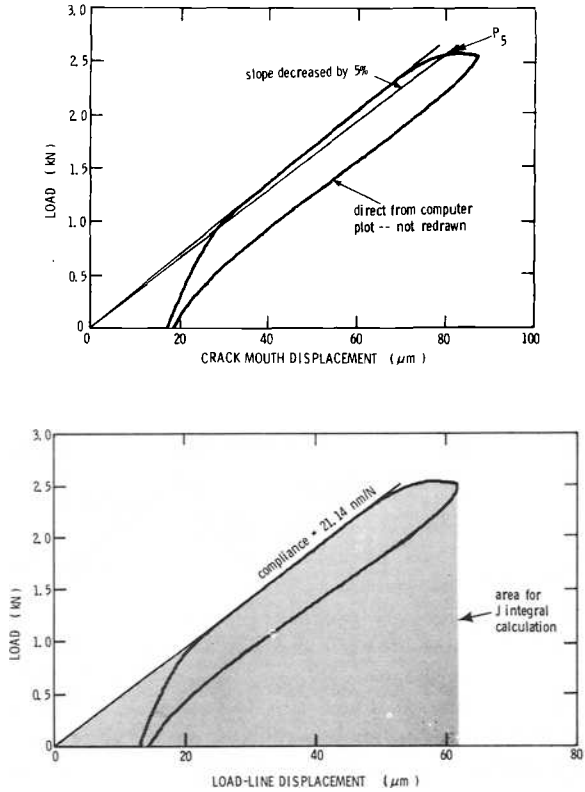

FIG. 6—(a) *Typical load-CMD record for load to failure of compact specimen,* (b) *load versus load-line displacement for same compact specimen as* (a).

sible thickness effect on K_{Ic} and might further our understanding of the mechanics of crack growth in rock.

Several dyeing techniques were attempted using a fluorescent dye penetrant known as Zyglo.[6] The techniques included (1) 30-min immersion in dye, (2) wetting the notch with dye while holding a load on the specimen, (3) fatigue cycling the specimen while wetting the notch, (4) 15-min immersion in a pressure vessel with dye pressurized to 35 MPa, and (5) combinations of these four. All procedures included a 30-min period in a vacuum chamber to remove excess dye before final loading. Techniques 1 to 3 gave crack length estimates that differed for specimens with the same compliance and technique 3 actually provided estimates that were longer than those obtained from a compliance calibration. An explanation of this was suggested from technique 4 when static pressure was found to

[6] A product of Magnaflux Corporation, Chicago, Ill.

cause the dye to penetrate 20 mm into uncracked rock. This implies that the cycling with technique 3 might create a pressure buildup near the crack tip that forces dye ahead of the tip. As a result, crack lengths were determined by the compliance calibration technique and the dyeing details were given here only to aid future investigators.

The compliance calibration technique involved measuring the slope of the load-displacement records of several specimens having a sharp machined notch of known length. The effective crack length of a specimen with a natural crack then was determined by a comparison of its compliance with those of the calibration specimens. Another determination of crack length was also obtained by using the specimen's compliance and the initial modulus from the tension tests along with the appropriate analytical formulas [*8*]. These crack length determinations along with direct observations of crack lengths on the specimen surfaces were found to be in reasonable agreement.

Results

Tension

A typical pair of stress-strain curves from one of the tension tests is displayed in Fig. 7 along with a summary of results from all eight tests. An unloading-reloading curve is also included. The stress-axial strain curve of this "brittle" material shows a large degree of nonlinear and inelastic response. The unloading cycle demonstrates that most of the nonlinear behavior is indeed inelastic but this inelastic behavior is generally recognized as growth of microcracks rather than plasticity *per se*.

The nonlinear and inelastic tensile behavior of some rocks was perhaps

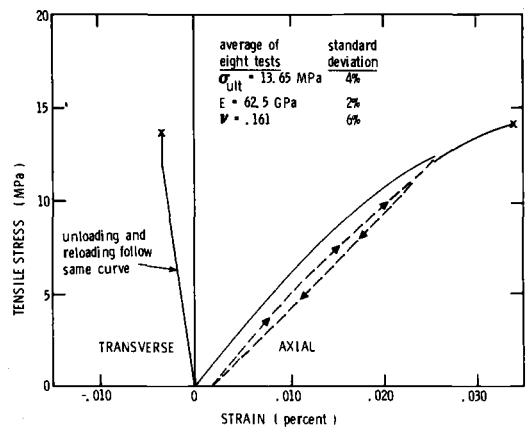

FIG. 7—*Typical stress-strain curve with unloading for direct-pull tension test.*

first recorded only 10 years ago by Wawersik [*9*]. In that study a charcoal gray granite sample was loaded in tension and unloaded just prior to failure. Sectioning of this sample indicated that stable crack growth had indeed occurred with the preferred orientation of cracks roughly perpendicular to the stress axis. This has been observed by others [*10*] and is substantiated by the rather linear-elastic behavior of the stress-lateral strain record in Fig. 7 since cracks with that orientation should have little effect on the lateral strain response.

Fracture Toughness

Values of apparent fracture toughness, K_Q, were calculated from load versus CMD records such as Fig. 6*a*. The compliance was established by fitting a straight line by the method of least squares through all the digitized data that fell between 50 and 90 percent of the maximum load. This compliance and the compliance calibration were used to establish the crack length. The load at "failure" was determined by the ASTM method using a 5 percent secant line constructed from the compliance line extrapolated to zero load. Crack length and failure load were then used to calculate K_Q from the ASTM formulas for compact and bend specimens (ASTM Method E 399).

Results from nineteen compact tests are summarized in Fig. 8. K_Q generally increases slightly with crack length[7] and appears to level off for long cracks. For all practical purposes the curve can probably be considered to have reached a constant value, K_{Ic}, for cracks longer than 2.5 (K_Q/

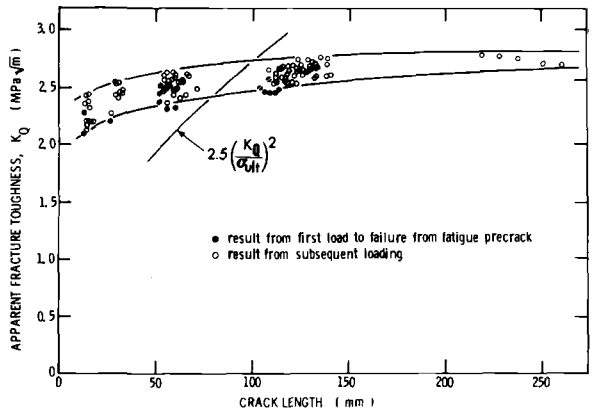

FIG. 8—*Apparent fracture toughness versus crack length for all compact specimens.*

[7] Similar behavior would be noted if K_Q were plotted versus remaining ligament and no inference should be drawn that the crack length is the only influential parameter.

$\sigma_{ult})^2$. (Ultimate stress is used in this calculation for convenience and for lack of a better well-defined strength parameter.)

Note that the data points in Fig. 8 for the initial loading of each sample generally fall on the lower portion of the scatter band. The increase in K_Q introduced by the use of the subsequent loadings is not large and these values may even be a better representation of the desired fracture toughness when consideration is given to the applications. A conservative design philosophy for metals dictates that K_{Ic} be the minimum value of fracture toughness and this approach may be entirely inappropriate for rock fracture applications.

To assess the effects of thickness on K_{Ic} nine of the compact specimens tested were of the 4T size (width equal to 203 mm, crack length approximately 100 mm) and varied only in thickness (Fig. 2). The average value of K_{Ic} for each specimen is plotted versus thickness in Fig. 9. No thickness effect is apparent from the figure. This result was not unexpected [*4*] since fracture toughness of concrete is known not to depend on thickness [*11*].

To assess the effects of fatigue precracking, a single 4T specimen was precracked by a single load cycle and then tested as usual. The results indicate little change in the values of K_{Ic}. In this test the data for the first load to failure cycle was consistent with subsequent points.

Figure 10 shows the results from the six bend tests. This data appears consistent with the compact data and helps to establish K_{Ic} as a material property for this rock.

J-Integral

Critical J-integral data were determined by the J-resistance curve technique [*12*] with the Merkle-Corten correction factors [*13*] for the compact specimen geometry. Using guidelines recommended by ASTM Subcommittee E24.08

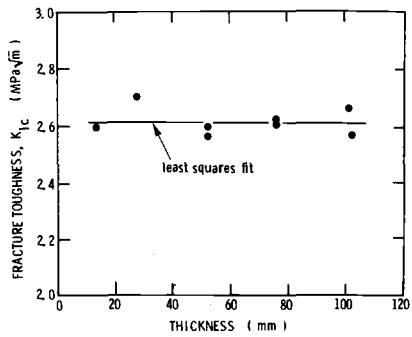

FIG. 9—*Effect of thickness on fracture toughness of Westerly granite.*

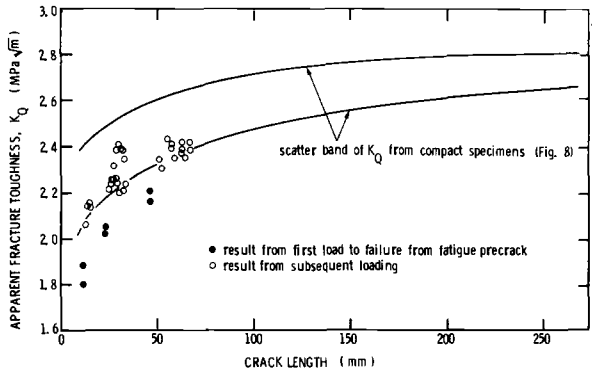

FIG. 10—*Apparent fracture toughness versus crack length for bend tests.*

on Elastic-Plastic Fracture Mechanics Terminology, the J-integral data were reduced using

$$J = \alpha_1 \frac{2A}{Bb} + \alpha_2 \frac{2P\delta}{Bb}$$

where

α_1, α_2 = Merkle-Corten coefficients,
A = the area under the load vs load-line displacement curve,
B = thickness,
b = remaining ligament,
P = final load value, and
δ = final displacement value.

To determine the total work done on the specimen the actual area, A, under the load versus load-line displacement curve was modified slightly to account for the energy stored at zero load due to crack closure. Since crack closure prevents a complete relaxation of stresses from occurring, the actual area used is the shaded area of Fig. 6*b*.

J_{Ic} is considered to be the intersection of the J versus crack growth line with a blunting line [*12*]. For all practical purposes the blunting line for these tests can be considered as a vertical line and J_{Ic} is then the J-integral extrapolated to the zero growth condition. The crack growth resulting from a single loading cycle was determined from the crack lengths calculated on the basis of the compliance of that loading cycle and the cycle immediately following. Crack growth that may occur during the unloading portion of each cycle is included here necessarily but, since the J_{Ic} point is the value extrapolated to infinitesimal crack growth, the only consequence would be

a change in the scale of the crack growth axis with little effect on J_{Ic}. A single value of J_{Ic} was determined for each specimen from a curve such as Fig. 11.

When linear elastic behavior predominates, J_{Ic} is directly related to K_{Ic} through

$$J_{Ic} = \frac{1 - \nu^2}{E} K_{Ic}^2 \text{ or } K_{Ic} = \sqrt{\frac{J_{Ic}E}{1 - \nu^2}}$$

With this in mind, $\sqrt{J_{Ic}E/(1 - \nu^2)}$ values are tabulated for comparison with average K_{Ic} values from the 4T compact specimens (Table 1).

Averaged values of $\sqrt{J_{Ic}E/(1 - \nu^2)}$ for each specimen size are plotted versus average crack length in Fig. 12. Note that a fairly constant value of fracture toughness is obtained even for crack lengths as small as 10 mm. The slight increase in toughness with crack length is probably within the

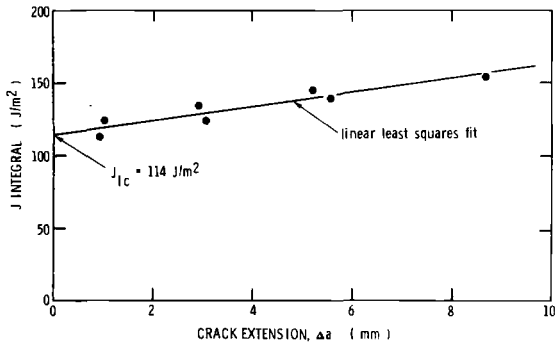

FIG. 11—*Typical J-resistance curve for one compact specimen.*

TABLE 1—*Comparison of* K_{Ic} *and* J_{Ic} *for 4T compact specimens.*

Thickness, mm	Number of Data Points	Average K_{Ic}, MPa $\sqrt{m}$	$\sqrt{\frac{J_{Ic}E}{1 - \nu^2}}$ MPa $\sqrt{m}$	Percent Difference
13.5	1	2.59	...	...
13.5	8	2.59	2.67	3
27.7	8	2.70	2.76	2
52.1	8	2.60	2.67	3
52.1	6	2.56	2.53	−1
76.5	8	2.62	2.73	4
76.5	2	2.61	...	...
101.6	7	2.66	2.70	2
102.9	5	2.57	2.51	−2

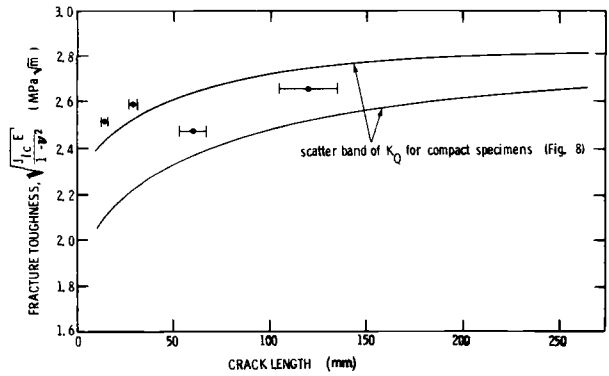

FIG. 12—*Fracture toughness versus crack length as determined from* J_{Ic} *calculations for compact specimens.*

experimental error. The fact that $\sqrt{J_{Ic}E/(1-\nu^2)}$ diverges from K_Q for small cracks lends some reassurance that the close agreement obtained in Table 1 is not a result of some redundancy in the data reduction schemes.

Discussion

At least one investigator has suggested that the general nonlinear stress-strain response of some rocks such as Westerly granite invalidates the use of LEFM and K_{Ic} [*14*]. However, empirical results presented here support previous studies that suggest K_{Ic} to be a material constant for rocks since measurements using different specimen configurations produce the same value of K_{Ic}. In addition, the J-integral data presented show K_{Ic} to be consistent with J_{Ic} values for which linear elastic behavior is not required.

Perhaps the successful application of LEFM to this nonlinear inelastic material is due to the fact that the load-to-failure tests are performed on precracked specimens that have a fully developed process zone at the crack tip. The unloading and reloading behavior of the tension tests suggest that the loading of each material element within the cracked fracture specimen takes place in a nearly linear elastic fashion with a spatially varying modulus. In addition, the bulk of material is under low strain conditions such that the overall resultant behavior is nearly linear elastic.

Future studies on fracture toughness of rocks should consider the attributes of both a J_{Ic} and K_{Ic} approach. J_{Ic} testing appears to be less restrictive of specimen size and needs less verification due to a nonlinear stress-strain behavior. K_{Ic} measurements on the other hand require fewer tests to be performed and data reduction follows a simpler procedure. However, a recent analysis by Ernst et al [*15*] indicates that a complete J versus crack

growth curve can be determined from a single load-displacement record with absolutely no measure of crack length.

One other aspect of rock fracture that needs attention at this phase is the micromechanics of crack propagation. Speculations of microcrack zones need direct substantiation in order to understand fully the material behavior. Crack front configurations need to be examined to understand the effects of plane stress and plane strain. Perhaps the most important reason for micromechanics models is that guidance is needed when extrapolating data from one or several rock types to the various rocks encountered in a particular application.

Conclusions

1. Tension test results of intact Westerly granite specimens display substantial nonlinear and inelastic response prior to failure. Tensile strength is 13.64 MPa, initial Young's modulus is 62.4 GPa, and initial Poisson's ratio is 0.161.

2. Crack surface interference or crack closure occurs in precracked fracture specimens of Westerly granite.

3. Apparent fracture toughness, K_Q, of Westerly granite increases with an increase in crack length, a, and appears to reach a practical limit of 2.70 MPa $\sqrt{m}$ for

$$a > 2.5 \left(\frac{K_Q}{\sigma_{ult}}\right)^2$$

4. K_{Ic} of Westerly granite is insensitive to changes in specimen thickness for thicknesses ranging from 13 to 103 mm.

5. Little difference in K_Q is detected between the first load to failure cycle and subsequent cycles.

6. K_Q data from bend tests are consistent with results from compact specimens.

7. J_{Ic} data from compact specimens do not vary with crack length as much as K_Q, indicating that valid toughness values can be obtained on smaller samples using a J-integral approach.

8. J_{Ic} and K_{Ic} values correlate remarkably well and help to verify the use of K_{Ic} for this nonlinear, inelastic material.

Acknowledgment

This work was supported by the U.S. Department of Energy (DOE) under Contract AT (29-1) 789.

References

[1] Northrop, D. A. and Schuster, C. L., Eds., "Enhanced Gas Recovery Program 2nd Annual Report, October 1976 through September 1977," Technical Report SAND77-1992, Sandia Laboratories, Albuquerque, N. Mex., 1977.

[2] Schmidt, R. A., *Experimental Mechanics*, Vol. 16, No. 5, May 1976, pp. 161-167.

[3] Schmidt, R. A. in *Proceedings*, 18th U.S. Symposium on Rock Mechanics, Keystone, Colo., June 1977.

[4] Schmidt, R. A. and Ingraffea, A. R., "On the Prediction of Tensile Strength of Rock from Fracture Toughness or Effective Surface Energy," Technical Report SAND77-0408, Sandia Laboratories, Albuquerque, N. Mex., 1978.

[5] Birch, F., *Journal of Geophysical Research*, Vol. 65, No. 4, April 1960, p. 1083.

[6] Brace, W. F., *Journal of Geophysical Research*, Vol. 70, No. 2, Jan. 1965, p. 391.

[7] Mills, W. J., James, L. A., and Williams, J. A., *Journal of Testing and Evaluation*, Vol. 5, No. 6, 1977, pp. 446-451.

[8] Gross, B., Roberts, E., and Srawley, J. E., "Elastic Displacements for Various Edge-Cracked Plate Specimens," NASA Technical Note TN D-4232, National Aeronautics and Space Administration, Washington, D.C., Nov. 1967.

[9] Wawersik, W. R., "Detailed Analysis of Rock Failure in Laboratory Compression Test," Ph.D. thesis, University of Minnesota, Minneapolis, Minn., 1968.

[10] Peng, S. S., *International Journal of Rock Mechanics and Mining Sciences and Geomechanics Abstracts*, Vol. 12, 1975, pp. 125-127.

[11] Mindess, S. and Nadeau, J. S., *Cement and Concrete Research*, Vol. 6, 1976, pp. 529-534.

[12] Landes, J. D. and Begley, J. A. in *Fracture Analysis, ASTM STP 560*, American Society for Testing and Materials, 1974, pp. 170-186.

[13] Merkle, J. G. and Corten, H. T., *Journal of Pressure Vessel Technology*, Vol. 96, Series J, No. 4, 1974, pp. 286-292.

[14] Wilkening, W. W., "Dilational Deformation and Fracture in Barre Granite," Ph.D. thesis, Massachusetts Institute of Technology, Cambridge, Mass., 1976.

[15] Ernst, H., Paris, P. C., Rossow, M., and Hutchinson, J. W., "The Analysis of Load-Displacement Relationships to Determine J-R Curve and Tearing Instability Material Properties," presented at 11th National Symposium on Fracture Mechanics, Blacksburg, Va., June 1978.

A. E. Naaman[1] *and S. P. Shah*[1]

Fracture and Multiple Cracking of Cementitious Composites

REFERENCE: Naaman, A. E. and Shah, S. P., **"Fracture and Multiple Cracking of Cementitious Composites,"** *Fracture Mechanics Applied to Brittle Materials, ASTM STP 678,* S. W. Freiman, Ed., American Society for Testing and Materials, 1979, pp. 183-201.

ABSTRACT: Cementitious composites consist essentially of a Portland cement paste, mortar or concrete matrix reinforced with steel (primarily) or mineral fibers. Compared to fiber reinforced polymeric and metallic matrices they form in a way a different class of composites. Their primary characteristics are: (1) that the ultimate tensile strain of the matrix is much lower than the yield or ultimate tensile strain of the fibers, and (2) the bond strength at the fiber matrix interface is relatively small (there is little adhesion in the chemical sense).

Attempts have been made to calculate some fracture properties of these composites, using linear elastic fracture mechanics approach, by testing notched beam specimens, notched tension specimens, or cleavage type specimens. The results have been only partly successful because these composites may not show a brittle type of failure depending upon the relative dimensions of the specimen and the length of the critical crack (in the Griffith's sense). Tests on double cantilever type cleavage specimens of Portland cement mortar reinforced with steel fibers showed that a pseudo-plastic zone develops in front of an advancing crack. In this zone the matrix is cracked but the fibers are in a state of pull-out. If the plastic zone is larger than the specimen cross section, then instead of a rapid crack propagation, multiple cracking and ductile failure may occur. The length of the pseudo-plastic zone can be determined from the results of the cleavage tests and depends on: (*a*) the length, aspect ratio, volume fraction, spatial distribution, and the pull-out behavior of the fibers, and (*b*) the properties of the matrix.

It is concluded that for cementitious composites for which no fracture testing standards exist, specific experimental techniques to measure fracture properties and analytical approaches to interpret their values, must be developed.

KEY WORDS: concrete, fiber concrete, fracture strength, crack propagation, notched beams, double cantilever beams, notched tensile prisms, multiple cracking, surface energy, size effects, fracture mechanics, reinforced concrete, fracture (materials)

[1]Associate professor of structural design and professor of civil engineering, respectively, Department of Materials Engineering, University of Illinois at Chicago Circle, Chicago, Ill. 60680.

Portland cement based matrices, mainly neat paste, mortar, and concrete, are generally considered brittle materials because of their low tensile strength and low tensile strain prior to fracture. Such materials are shown to contain inherent flaws and interfacial bond microcracks [*1–3*][2] which form numerous nuclei for potential crack propagation and fracture. Under tensile loading, existing microcracks grow, link together and form larger cracks. Eventually, one of these conglomerates reaches a size for which rapid crack propagation and fracture follows [*4*]. The fracture of these materials should be described in relative terms and is also dependent on the size of the specimen tested. It has been shown [*5*], for example, that for specimens of the same size, paste is more notch sensitive (in the Griffith sense) than mortar and concrete in which hard aggregate inclusions provide an effective crack arresting or retarding mechanism; similarly concrete tends to exhibit a pseudo ductile failure behavior if the size of the aggregate inclusion increases [*3*].

In recent years there has been increasing interest in overcoming the deficiencies of portland cement based matrices by reinforcing them with small diameter short fibers such as steel, glass, or asbestos fibers [*6, 7*]. Applications of these composites include highway pavements, surface bonded masonry construction, airport runways, underground tunnel linings, blast and earthquake resistant structures, and a variety of precast products for the construction industry. It is now recognized that, apart from enhancing the mechanical properties of the composite, the most significant improvements of fiber reinforcement are to delay the onset of "first visible" cracking, increase the extent of multiple cracking, control the post-peak-load behavior and improve ductility, energy absorption, impact, and toughness properties. Thus it has become increasingly important to determine the fracture properties of these composites. This study focuses mainly on portland cement based matrices reinforced with steel fibers and generally termed "fiber reinforced concrete." It describes the distinct behavior of fiber reinforced concrete under tensile loading, discusses some analytical models proposed to predict its fracture properties, and summarizes some of the testing techniques used to determine them.

Behavior of Fiber-Reinforced Cementitious Matrices

As compared to fiber-reinforced polymeric or metallic matrices, fiber-reinforced cementitious matrixes form, in a way, a different class of composites. Their primary characteristics are: (*a*) that the ultimate tensile strain of the matrix (ϵ_{mu}) is much lower than the yield or ultimate tensile strain (ϵ_{fu}) of the fiber (Fig. 1), and (*b*) the bond strength at the fiber-matrix interface is relatively small (there is little adhesion in the chemical sense). This implies that with increasing tensile stresses on the composite, the matrix will crack at

[2]The italic numbers in brackets refer to the list of references appended to this paper.

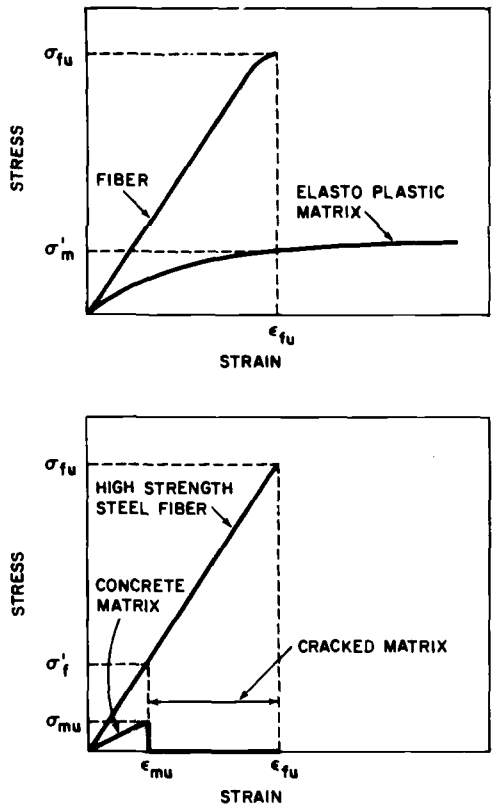

FIG. 1—*Typical stress-strain diagrams of fiber reinforced concrete as compared to most fiber reinforced plastics.*

some level of stress long before the fibers reach their failure strength. Furthermore, the composite response after matrix cracking and the efficiency of fiber reinforcement will greatly depend on the pullout resistance of the fibers (steel fibers). This is because the fibers are relatively short and, in practice, it is very difficult to obtain uniform dispersion of the fibers in the concrete if their length exceeds about 5 cm. Typical load-elongation curves of fiber reinforced concrete specimens are shown in Fig. 2. The upper figure is for a cement matrix reinforced with asbestos fibers whose length is less than a millimetre while the lower figure is for a mortar matrix reinforced with 2.5-cm long steel fibers. It can be seen that the shorter fibers provide in this case very little post-cracking (after peak load) resistance and ductility.

As in other composites, fiber reinforced concrete can suffer any of the modes of failures of its constituents together with a few modes arising from their combination. The use of continuous instead of discontinuous fibers,

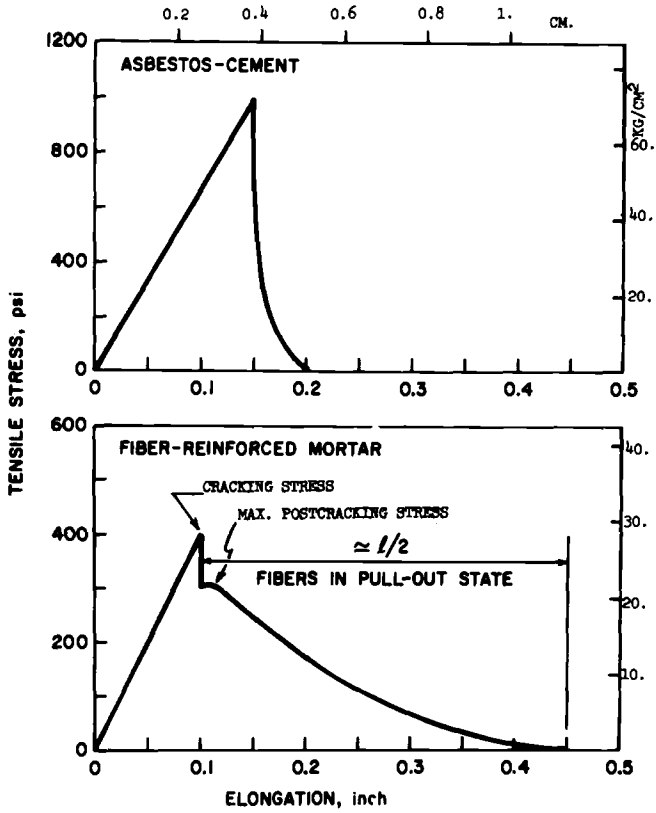

FIG. 2—*Typical stress elongation curves as influenced by fiber length.*

such as in reinforced concrete and ferrocement, adds some limiting failure modes of interest.

Qualitative load-elongation (or deflection) response curves of fiber-reinforced concrete specimens are plotted in Fig. 3. Understanding the types of behavior described in Fig. 3 is essential for understanding the work attempted in this research.

The ordinate axis of Fig. 3 represents the ratio of the load on the composite to the load at the first cracking of the matrix. It is defined as the load at which the deviation from the first linear portion *OA* of the curve occurs. Cracking may indicate a short crack or a crack that runs through the width of the specimen. Thus the ordinate is indicative of the composite stress, while the abscissa represents elongations, deflections or equivalently composite strains. Numbers have been associated with the curves. Shaded areas indicate various ranges of failure behavior.

A fiber-reinforced concrete specimen can show a load-elongation curve

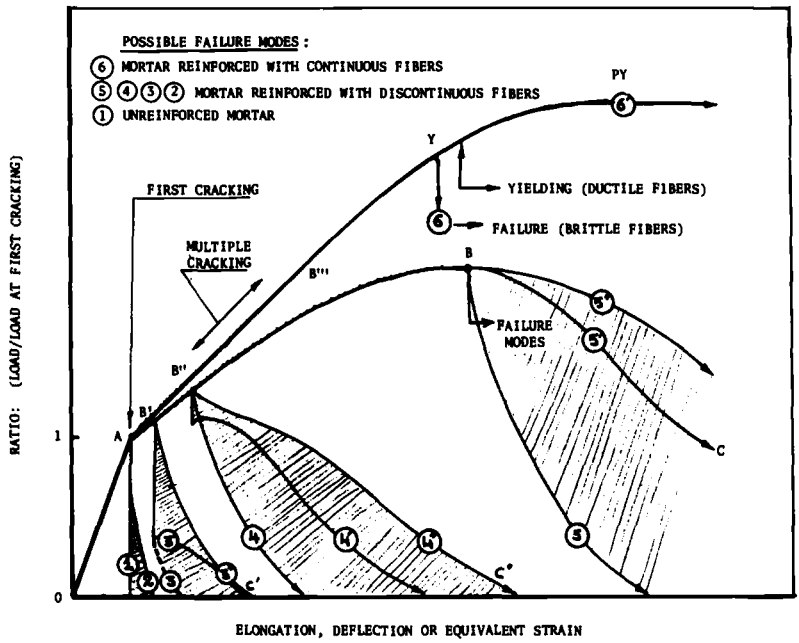

FIG. 3—*Qualitative load-elongation curves for fiber reinforced concrete.*

anywhere in the range between curve 1 and curve 6′. Curve 1 describes the behavior of unreinforced portland cement paste. It is essentially linear up to cracking which is accompanied by a brittle-like failure. Curve 6′ describes the behavior of a continuous fiber-reinforced concrete specimen such as ferrocement. Here at least three portions of the curve with decreasing slopes are identified: the first portion OA with the steepest slope represents the composite's response up to first cracking (no attempt is made to differentiate the slope of OA from the unreinforced or discontinuously reinforced case), then a relatively linear portion AY follows up to yielding of the steel, and the third portion PY corresponds to the post-yielding behavior of the steel and depends on its properties. Note that this description is generally applicable only to the cases where continuous aligned fibers are used.

The behavior of a discontinuous fiber-reinforced concrete specimen can be described by any of the curves between 1 and 6′. Here also up to three portions can be distinguished qualitatively: an essentially linear elastic portion OA up to first cracking, a possible "multiple cracking" portion such as AB', AB'', or AB, and a failure (descending branch) portion after maximum load, such as $B'C'$, $B''C''$ or BC. Note that multiple cracking may be inexistent, such as for curve 2, and failure may be brittle 2 or ductile 5″. It has been hypothesized that the substantially improved impact resistance and ductility of fiber-reinforced concrete and gypsum composites are related to the multi-

ple cracking of the matrix [*8–10*]. Possible modes of behavior seem to depend on many parameters including the reinforcement parameters, specimen geometry, type of loading and the like, and are not very well understood. Curve 2, for example, is typical of an asbestos cement specimen or of specimens reinforced with a relatively small volume fraction of steel or glass fibers (Fig. 2). Curve 3 or 4 can be observed if the volume fraction is increased substantially. For 3 and 4 the extent of multiple cracking is larger but failure is still brittle-like. Curves similar to 3′, 4′, 5′, or 5″ have been observed for steel and glass fiber-reinforced mortar specimens (see also Fig. 4). It can be seen that the extent of multiple cracking may in some cases be substantial and that failure can be fast (brittle) or gradual (ductile).

Examination of the fracture surfaces (Fig. 5) of steel fiber-reinforced concrete, as used so far, has shown that, practically speaking, the fibers never fail. Rather, they pull out from the fracture surfaces of the matrix on each side of a crack. It can also be shown analytically, using available experimental data on the bond strength at the fiber matrix interface, that for the fiber aspect ratios generally used, the failure stress of the fiber is seldom attained. The pullout process is beneficial and responsible for the added toughness of the material. Depending, however, on a number of parameters, failure, as mentioned previously, may be brittle or ductile. Although the exact reason is not well understood, an attempt is made here to provide a possible explanation. Among the cracks that develop, extend or coalesce, or all three, under

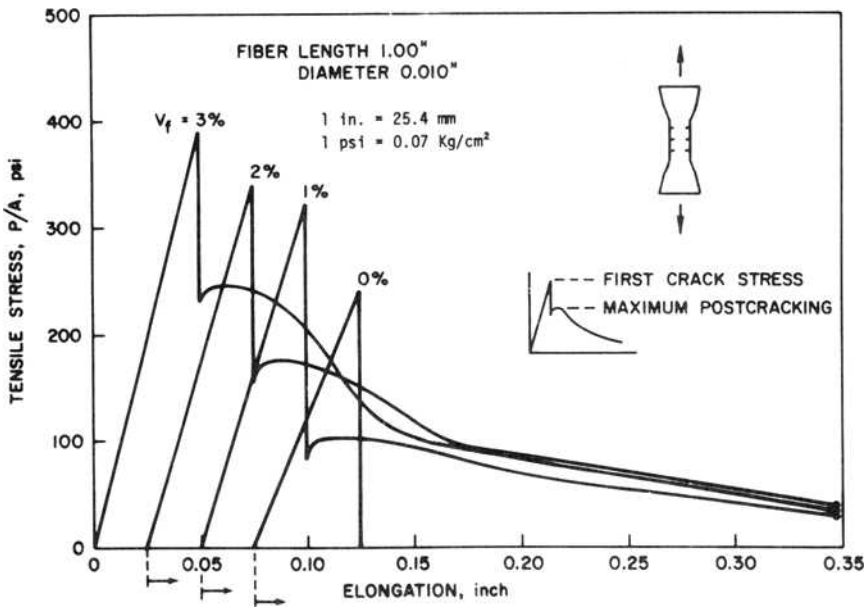

FIG. 4—*Load-elongation curves of fiber-reinforced concrete specimens in tension.*

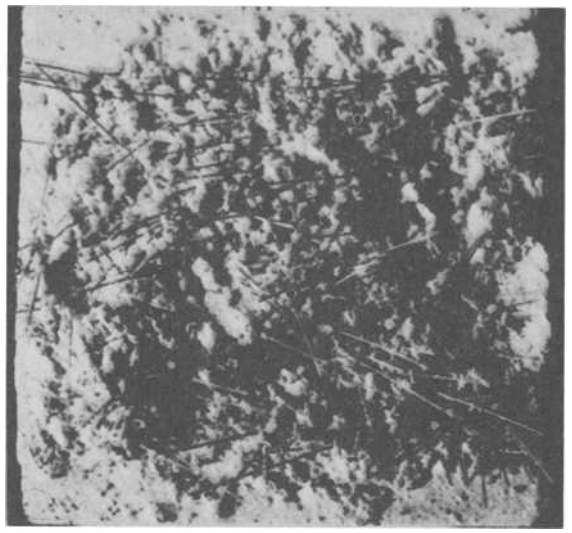

FIG. 5—*Typical fracture surface of fiber reinforced concrete.*

increased stresses during the multiple cracking process, a critical crack length in the Griffith's sense can form; the critical crack length for a given composite may be smaller or larger than the width of the specimen under test; if it is smaller, a rapid crack propagation can follow; however, if the critical crack length for the applied stress is larger than the width of the specimen, then essentially a three-step process seems to occur: (1) the largest cracks extend all the way through the matrix width, (2) the load is redistributed among the fibers bridging the cracked surfaces, and (3) the fibers pull out gradually under increasing elongation. Typical response curves are shown in Fig. 4.

Analytical Approaches and Related Background Information

The problem of crack propagation in a fiber-reinforced cementitious composite subjected to a uniaxial tensile stress along its longitudinal axis have been approached in two distinct ways: one deals primarily with the propagation of one critical crack in a transverse cross section, while the other deals mainly with the development of transverse cracks parallel to each other in the longitudinal direction, which is described here as part of the multiple cracking process. The transverse crack propagation problems have been treated primarily by using concepts of fracture mechanics [*11,12*], while the aspects of multiple cracking have been dealt with using classical mechanics. A substantial amount of experimental and theoretical work has been done to predict the spacing of transverse cracks in the longitudinal direction and

their widths for continuously reinforced and prestressed concrete structural members [*13,14*] and for ferrocement [*15*]. It will not be reviewed here.

Transverse crack propagation may be brittle (that is, unstable in the Griffith's sense) or may be stable from the point of view of the overall composite behavior. Multiple cracking for members subjected to uniaxial tension may consist of essentially parallel transverse cracks across the entire cross sections (such as with ferrocement and reinforced concrete) or across only part of the cross section (Fig. 6).

Whether a given fiber-reinforced composite exhibits one or more of these types of crack propagations depends on the fiber, matrix, and the specimen geometric parameters.

Brittle Crack Propagation

The classical fracture mechanics concept of brittle crack propagation in materials has been applied only relatively recently to cementitious matrixes such as paste, mortar, and concrete [*4,5,16–18*]. In 1963 Romualdi and Batson [*11*] proposed a model to explain how closely spaced discontinuous stiff fibers can increase the stress at which the crack appears in the concrete matrix. They essentially applied to fiber-reinforced concrete, the classical Griffith approach as modified by Irwin and described by

$$\sigma_c = \frac{K_{Ic}}{\sqrt{\alpha \pi a}} \tag{1}$$

where

σ_c = stress at onset of rapid crack propagation,
K_{Ic} = critical plane strain fracture toughness (opening Mode I) (it is equal to the stress intensity factor),
α = parameter depending on specimen and crack geometry, loading rate, crack-tip sharpness, etc., and
a = half-length of a penny-shaped internal crack or length of external crack.

The expression proposed by Romualdi and Batson for fiber-reinforced concrete is given by

$$\sigma_c = \frac{K}{\sqrt{s}} \tag{2}$$

where

K = constant related to the fracture toughness and
s = average fiber spacing.

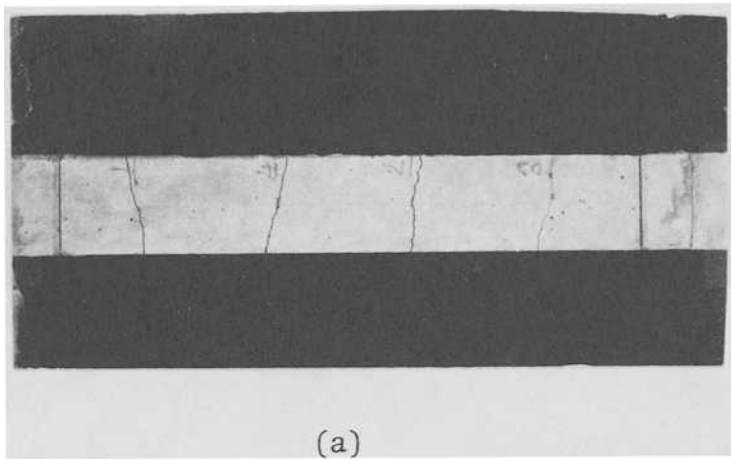

FIG. 6—*Multiple cracking in fiber reinforced concrete* (a) *tensile specimen with all the way cracks, and* (b) *flexural specimen.*

This formula, however, ignores the important effect of fiber debonding on both sides of the cracked surface. Fiber debonding and fiber pull out lead to substantial increase in energy absorption or toughness of the composite. This energy is, in a way, similar to the plastic surface p introduced by Orowan [*19*] as a modification to Griffith's equation to account for the plastic deformation around the tip of a crack. Naaman et al [*20*] have attempted to include

the effect of fiber debonding in the classical fracture mechanic's relation. They showed that due to the process of debonding in fiber-reinforced concrete, a pseudo-plastic zone of radius R (Figs. 7,8) develops at the tip of a crack. The pseudo-plastic zone represents an area where the matrix is cracked but where the fibers bridging the cracked surfaces are still debonding, thus providing a pullout resistance. This increases the assumed minimum critical internal flaw size for the composite by $2R$. Consequently, they proposed the following relation which applies in the three-dimensional case of a tensile prism

$$\sigma_c = \frac{K_{Ic}}{\sqrt{\frac{4(\delta + R)}{\pi}}} \tag{3}$$

where

K_{Ic} = fracture toughness at critical crack propagation (opening Mode I),
2δ = crack length; or diameter of largest weak area defined as that area having no or little amount of fiber crossings by probability analysis, and
R = length or radius of pseudo-plastic zone from crack tip.

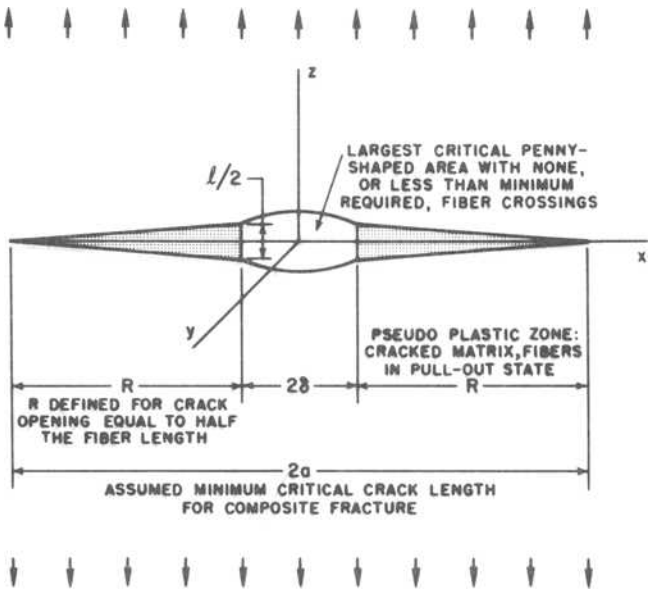

FIG. 7—*Assumed critical crack model controlling fracture of fiber-reinforced concrete composite.*

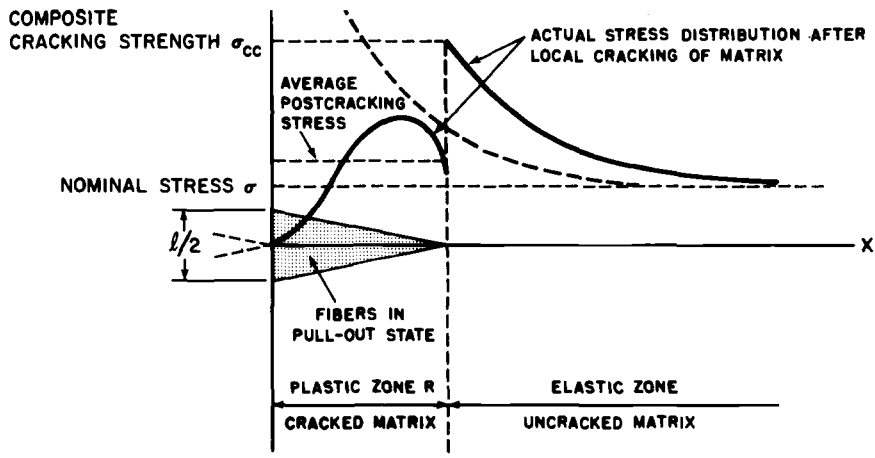

FIG. 8—*Distribution of longitudinal stress ahead of a crack in a fiber-reinforced concrete composite.*

By using double-cantilever type specimens and 12.5 mm long fibers, they observed that the pseudo-plastic zone radius R may be comparatively large (and for their parameters of the order of 50 cm). Thus, depending on the size of the specimen, brittle fracture may not occur. The question of the relative size of δ and R to the dimensions of the specimen becomes of major importance in determining the type of failure shown in Fig. 3.

If the specimen cross section is smaller than the plastic-zone area, brittle fracture will not occur. Rather a three-stage process will be observed (Figs. 4 and 9): a transverse matrix crack through the entire cross section, redistribution of forces among fibers bridging the crack, and a gradual pull out of fibers. For this case, the values of the first cracking stress (σ_{cc}), the postcracking stress (σ_{cu}) and the occurrence of multiple cracking can be predicted using classical mechanics. However, if the reinforcing fibers are such that the plastic zone is relatively small, then, as apparently happens for asbestos cement (Fig. 2), the crack propagation may be brittle and the fracture mechanics approach (Eq 3) may be more appropriate.

To determine the composite stress for brittle crack propagation by using Eq 3, one needs to know the fracture toughness K_{Ic} or its related value G_{Ic} (toughness). Some of the experimental tests undertaken to determine these values are described in the next section and some conclusions on their usefulness are drawn.

Experimental Program and Results

It is clear from the above discussion that due to a number of influencing parameters which include the very nature of cementitious matrixes, relative

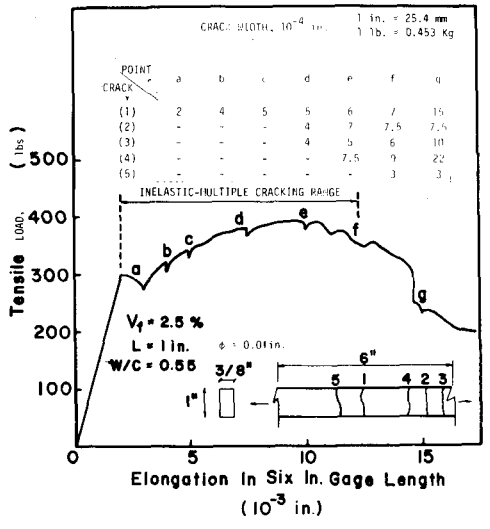

FIG. 9—*Size effect (fiber-specimen) on load-elongation curve.*

size effects, weak interfacial bond between matrix and fiber, and a non-conventional fracture behavior, the conventional concepts of linear elastic fracture mechanics are not directly applicable to fiber reinforced cementitious systems. Another difficulty is that, unlike fracture toughness testing of metals and polymers, little information exists on the fracture testing of fiber reinforced concrete and no standard procedures defining the types and dimensions of specimens, notch geometry, and testing variables have yet been defined.

This section describes several tests used by the authors to better understand the fracture properties of fiber reinforced concrete.

Tension Tests

Three types of tensile experiments were undertaken; the geometry of each type of specimen is described in Figs. 6*a*, 10 and inset of 9. The notched plates were used to clarify the load-elongation response of unreinforced mortar specimens [*5*]. They also give an indication of the response of matrixes reinforced with very small fibers (asbestos fibers) simulated here by sand particles. The matrix composition consisted of Type III portland cement with sand-to-cement ratio of 1 and water-to-cement ratio of 0.5 by weight.

Typical load elongation response of the unreinforced series of specimens is shown in Figs. 1*b*, Fig. 3 curve 1, and Fig. 4. It is representative of a brittle type of behavior. The results of such tests have been analyzed to obtain the values of the toughness and fracture toughness of the material [*5,17*].

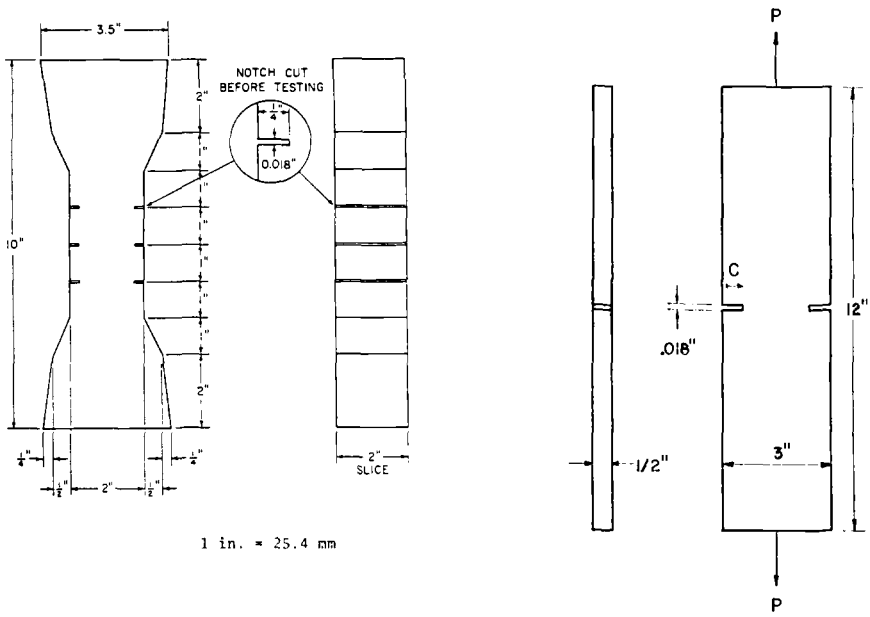

FIG. 10—*Notched tensile prisms and plates.*

However, it has been shown that a substantial amount of branch cracking and microcracking occur prior to the rapid crack propagation. As a result it is difficult to obtain accurate values of the real fracture area which is different than that of the major crack (net cross-sectional area at the notch).

The difficulty of using the results of the notched tension or flexural specimens to evaluate the fracture parameters is compounded when the load-elongation response is as shown in Fig. 4. Here notched tensile prisms (Fig. 9) were used to estimate the "toughness" of fiber reinforced concrete specimens as measured from the area under the load-elongation curve. Typical curves are shown in Fig. 4. The matrix composition consisted of Type III portland cement with water-to-cement ratio of 0.6 and sand-to-cement ratio of 2.5 by weight. The volume fraction of fibers and their length (aspect ratio) were varied as shown in the caption of Fig. 11 where the surface energy is plotted versus fiber parameters. The surface energy was assumed equal to half the material toughness. It can be seen that generally speaking the composite toughness increases with volume fraction and aspect ratio of the fibers. These values of the surface energy are only approximate and useful primarily for relative comparison. This is so because the individual contributions of the various mechanisms such as branch cracking, fiber debonding, and the stiffness of the testing system are not accounted for.

The small tensile plates (Fig. 6*a*) were used to clarify the effect of the

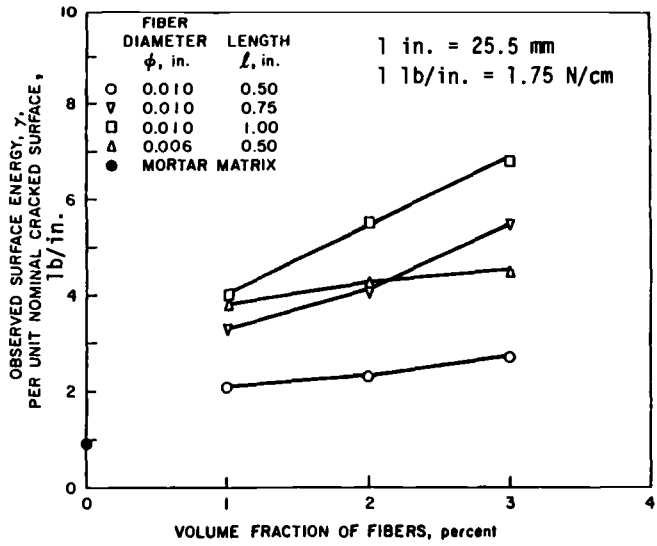

FIG. 11—*Variation of surface energy with fiber parameters.*

relative size of the fiber to that of the specimen on the stress-strain and load-elongation response in tension. The specimens were tested using an Instron testing machine, however the load-elongation was automatically recorded on an x-y recorder controlled by an LVDT directly attached to the specimen between a 15 cm gage length. Matrix composition consisted of portland cement Type III with a variable water-to-cement ratio (0.4 to 0.8) and a sand-to-cement ratio of 2.5 by weight. The fiber content was varied from 0 to 2.5 percent by volume and the fiber length was 12.5 and 25 mm. A typical load-elongation curve is shown in Fig. 9. It illustrates a ductile type of failure with occurrence of multiple cracking. Some other results are summarized in Table 1.

Although the response of these specimens indicates that the results cannot be used to obtain parameters for the application of elastic fracture mechanics theory, they are useful in determining the relations among ductility, multiple cracking, and matrix and fiber properties. Such relations are shown in Table 1. Note that the extent of inelastic strain is related to multiple cracking and increases with increasing the length and the volume fraction of fibers as well as decreasing the water-cement ratio of the matrix. Decreasing the water-cement ratio of the matrix increases significantly its tensile strength and the bond strength at the fiber-matrix interface. Increasing the bond strength tend to decrease crack spacing, thus increasing the amount of cracking and the corresponding extent of inelastic strain.

TABLE 1—*Some test results of tensile prisms illustrating multiple cracking.*

Series	Fiber[a]		Water-Cement Ratio	Average[b] Inelastic Strain 10^{-4}	Average[c] Number of Cracks
	V_f, percent	Length, mm			
A	1	12.5	0.55	4.79	1.5
B	1	12.5	0.4	6.18	1.5
C	2.5	12.5	0.55	7.41	2.0
D	2.5	12.5	0.4	11.33	4.0
E	1	25.0	0.55	8.12	2.5
F	1	25.0	0.8	4.58	2.0
G	2.5	25.0	0.55	13.67	3.5
H[d]	2.5	25.0	0.4	19.5	6.67

[a] Fiber cross section is square 0.025 by 0.025 mm.
[b] Average of four to six specimens—(see also Fig. 9); it corresponds to the multiple cracking range.
[c] In a 15 cm gage length.
[d] Paste only (no sand used.)

Double Cantilever Beam Tests

The purpose of the double cantilever beam test was to determine the fracture toughness and study the extent of the "pseudo-plastic" zone in a typical fiber reinforced concrete material. This zone is described as the area in which the matrix is cracked but the fibers bridging the cracked surfaces are still providing pullout resistance. Several cross-sectional shapes were used in preliminary series of tests. The most significant problem was to keep the crack from bifurcating from its preassigned path. Finally, continuous longitudinal rods were added and the specimen's cross section and the test set-up shown in Fig. 12 were selected. A typical load-opening curve is shown in Fig. 13. It shows a ductile type of behavior and is substantially different in shape from similar curves obtained with fiber reinforced polymetric matrixes. In its present form this curve does not seem to be useful in determining the material's toughness. Furthermore, as the plastic zone size was larger than the specimen length this test was not conclusive. However, it was estimated that for the fiber parameters used the plastic zone radius would be at least equal to 50 cm. This indicates that brittle fracture may occur only for relatively large specimens. The aforementioned tests are to be continued. However, smaller size fibers and larger size specimens must be used. Also as in a typical double cantilever cleavage specimen the compliance varies with the crack extension it may be advantageous to use a technique for double-cantilever beam testing in which the point of loading moves with the advancing crack front [*21,22*].

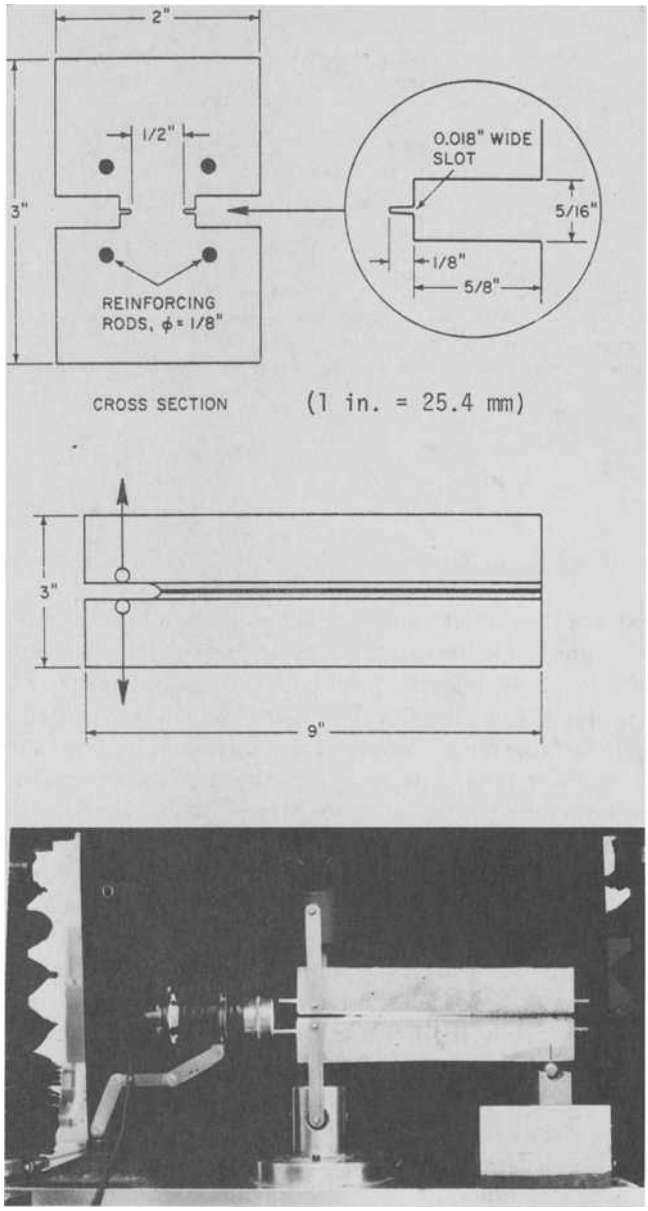

FIG. 12—*Double cantilever cleavage specimen and test set-up.*

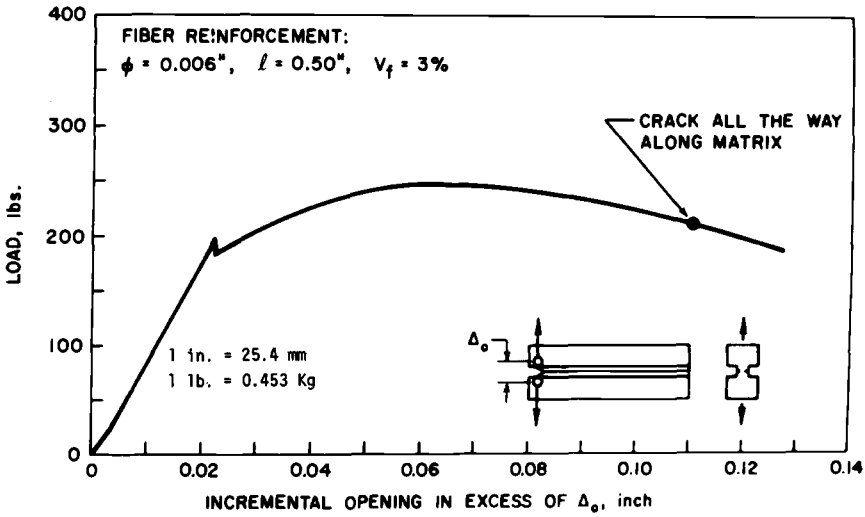

FIG. 13—*Typical load-displacement-response curve of cleavage specimen.*

Notched Flexural Beam Tests

Notched flexural beam specimens are being tested currently by the authors at the University of Illinois in order to determine the toughness properties of the composite. As fiber reinforced concrete does not behave as a linear elastic material it was felt that the application of elastic-plastic fracture mechanics techniques may prove more appropriate. Consequently not only the load-deflection curves of these beams are being recorded but all additional tests and measurements necessary to the application of the COD or J-integral technique are being taken. The test beams are 37.5 by 75 mm in cross section and 45 cm long. They are cast with a notch at midspan and tested in four-point bending. The variables under investigation include matrix composition, volume fraction of fibers, fiber length and notch depth. A typical load deflection and load-COD curve is shown in Fig. 14 with corresponding information on crack extension and crack opening displacement. No conclusion can yet be drawn as to the usefulness of these tests to determine the fracture properties of fiber reinforced concrete. However, it seems from the load-COD relationship that such criteria as critical COD cannot be applied simply to evaluate the fracture toughness for fiber reinforced concrete. Similarly, it was noted in Ref *18* that it was difficult to determine the critical value of J-integral for fiber reinforced concrete specimens.

Concluding Remarks

The results of this mostly exploratory investigation strongly indicate that

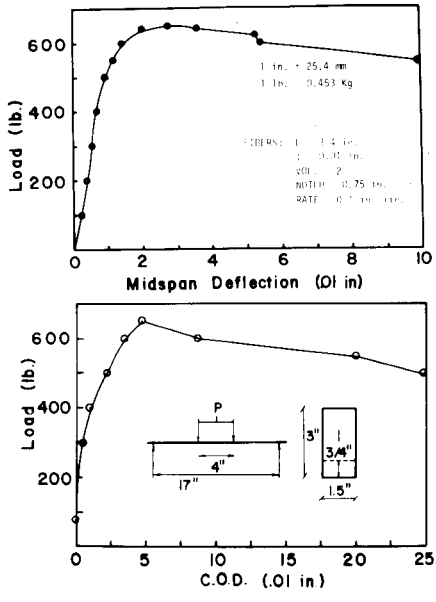

FIG. 14—*Typical load-deflection-COD curve of notched flexural beam.*

there are inherent difficulties in any type of fracture toughness testing procedure if used to determine the fracture properties of fiber reinforced concrete. This is due to the very nature of cementitious matrices, the presence of fibers and the failure behavior of the composite which, depending on the reinforcing parameters, can be very brittle, very ductile, or anywhere in between. There are increasing needs to identify most appropriate testing methods, establish standards for specimen sizes and geometry, and develop analytical techniques in order to evaluate the fracture properties of these composites.

Acknowledgment

This research is being supported by a grant from the National Science Foundation (ENG 77-23534, Structural Materials and Geotechnical Engineering Program) to the University of Illinois at Chicago Circle, Department of Materials Engineering.

References

[*1*] Hsu, T. T. C., Slate, F. O., Sturman, G. M., and Winter, G., *Journal of the American Concrete Institute*, Vol. 60, No. 2, Feb. 1963, pp. 209-224.

[*2*] Shah, S. P. and Slate, F. O., "Internal Microcracking, Mortar-Aggregate Bond and the

Stress-Strain Curve of Concrete," *Proceedings,* International Conference on the Structure of Concrete, London, Cement and Concrete Association, 1965.

[3] Lott, J. L. and Kesler, C. E., Symposium on the Structure of Portland Cement Paste and Concrete, Highway Research Special Report, No. 90, 1966, pp. 204-218.

[4] Glucklich, J., *Engineering Mechanics Division,* American Society of Civil Engineers, Vol. 89, No. EM6, Dec. 1963, pp. 127-138.

[5] Shah, S. P. and McGarry, F. J., *Engineering Mechanics Division,* Vol. 97, No. EM6, Dec. 1971, pp. 1663-1676.

[6] "Fiber Reinforced Concrete," American Concrete Institute, Special Publication SP-44, 1974; *Proceedings,* Fiber Reinforced Concrete Symposium, Ottawa, 1974.

[7] "Fiber Reinforced Cement and Concrete," The Construction Press, Ltd., 1975; *Proceedings,* RILEM Symposium, London, 1975.

[8] Shah, S. P. and Naaman, A. E., *Journal of the American Concrete Institute.* Vol. 73, No. 1, Jan. 1976, pp. 50-53.

[9] Shah, S. P. and Baehr, D., "Properties of Glass Fiber Reinforced Gypsum," Technical Report, U.S. Gypsum Co., Des Plaines, Ill., 1974.

[10] Oakley, D. R. and Proctor, B. A., "Tensile Stress-Strain Behavior of Glass Fibers Reinforced Cement Composites," Proceedings, RILEM Symposium, London, 1975, pp. 347-361.

[11] Romualdi, J. P. and Batson, G. B., "Mechanics of Crack Arrest in Concrete," *Engineering Mechanics Division;* American Society of Civil Engineers, Vol. 89, No. EM3, 1963.

[12] Harris, B., Varlow, J., and Elis, C. D., *Cement and Concrete Research,* Vol. 2, 1972, pp. 447-461.

[13] Gergeley, P. and Lutz, R., "Maximum Crack Width in Reinforced Concrete Structural Members," Special Publication SP-20, American Concrete Institute, July 1968.

[14] Nawy, E. G., "Crack Width Control in Welded Fabric Reinforced Centrally Loaded Two-Way Concrete Slabs," Special Publication SP-20, American Concrete Institute, July 1968.

[15] Naaman, A. E. and Shah, S. P., *Journal of the American Concrete Institute,* Vol. 68, No. 9, Sept. 1971, pp. 693-698.

[16] Naus, D. J. and Lott, J. L., "Fracture Toughness of Portland Cement Concrete," *Journal of American Concrete Institute,* June 1966.

[17] Moavanzadeh, F. and Kuguel, F., "Fracture of Concrete," *Journal of Materials,* American Society for Testing and Materials, Vol. 4, No. 3, Sept. 1969.

[18] Mindess, S., Lawrence, F. V., and Kesler, C. E., *Cement and Concrete Research,* Vol. 7, 1977, pp. 731-742.

[19] Orowan, E., "Fracture and Strength of Solids," Progress in Physics, Vol. 12, 1949.

[20] Naaman, A. E., Argon, A. S., and Moavenzadeh, F., *Cement and Concrete Research,* Vol. 3, 1973, pp. 397-411.

[21] Weitzmann, R. H. and Finnie, I., "Measuring Fracture Toughness: A Simplified Approach Using Controlled Crack Propagation," Department of Mechanical Engineering, University of California, Berkeley.

[22] Pujari, V. K., "An Improved Method for Fracture Toughness Evaluation in the Linear Elastic Range and a Comparison with Elastic-Plastic Data Obtained with Smaller Specimen," unpublished Ph.D. thesis, Department of Mechanical Engineering, University of California, Berkeley, Spring 1977.

S. M. Wiederhorn[1] *and J. E. Ritter, Jr.*[2]

Application of Fracture Mechanics Concepts to Structural Ceramics

REFERENCE: Wiederhorn, S. M. and Ritter, J. E., Jr., **"Application of Fracture Mechanics Concepts to Structural Ceramics,"** *Fracture Mechanics Applied to Brittle Materials, ASTM STP 678,* S. W. Freiman, Ed., American Society for Testing and Materials, 1979, pp. 202-214.

ABSTRACT: Techniques of improving the reliability of ceramic materials in structural applications are described. Based on fracture mechanics concepts, these techniques use strength, or fracture mechanics methods of measurement to characterize the delayed failure behavior of ceramic materials. The techniques have been tested experimentally; for several materials, agreement between theory and experiment is satisfactory. For other materials agreement is not satisfactory, suggesting that additional experimentation is needed to evaluate the limits of the theory fully and to identify those materials for which the theory is applicable.

KEY WORDS: ceramics, crack growth, delayed failure, fracture mechanics, mechanical reliability, strength, fracture (materials), crack propagation

Methods of dealing with design problems involving ceramic materials have been developed over the past 10 years through the application of the techniques and concepts of fracture mechanics [*1-3*].[3] Since fracture mechanics techniques can be used to characterize both the conditions for subcritical crack growth and the conditions for crack instability, they also can be used for purposes of design to estimate the allowable applied stress and the expected lifetime for a given component. This is accomplished by estimating the initial crack size in a ceramic component and the time required for the crack to grow from its initial size to a final critical size. Several mutually independent techniques have been developed recently to

[1] Assistant division chief, Fracture and Deformation Division, National Bureau of Standards, Washington, D.C. 20234.

[2] Professor, Mechanical Engineering Department, University of Massachusetts, Amherst, Mass. 01003.

[3] The italic numbers in brackets refer to the list of references appended to this paper.

provide these types of estimates. Since these techniques promise to revolutionize the way in which structural components made of ceramic materials are designed, a complete understanding of these techniques and their limitations will be necessary to use them correctly.

While the relationship between crack velocity and stress intensity factor can be rather complicated because of environmental effects, it has been found that at low velocities, the crack velocity (v) and the stress intensity factor (K_I) can often be related by the following empirical relation [*4*]

$$v = A K_I^n \tag{1}$$

where A and n are empirically determined constants that depend on environment, temperature, and material. Assuming that delayed failure results only from subcritical crack growth, the failure time (t) at a constant stress can be derived from Eq 1 [*1-3*]

$$t = B S_i^{n-2} \sigma_a^{-n} \tag{2}$$

where $B = 2/[AY^2 (n-2) K_{Ic}^{n-2}]$, Y = constant that depends on the flaw shape; it is usually assumed to be $2/\sqrt{\pi}$,[4] K_{Ic} = critical stress intensity factor, and S_i = fracture strength in an inert environment. The time-to-failure in Eq 2 is simply the time required for a flaw to grow from an initial, subcritical length to the critical length for catastrophic crack propagation. B and n are constants that characterize the subcritical crack growth; the initial flaw size is characterized in Eq 2 by the strength of the ceramic material in an environment where subcritical crack growth is absent.

It can be shown similarly that the minimum lifetime after proof testing (t_{min}) is given by [*1-3*]

$$t_{min} = B \sigma_p^{n-2} \sigma_a^{-n} \tag{3}$$

where σ_p = proof stress. From a fracture mechanics viewpoint, proof testing characterizes the largest effective flaw possible since a larger flaw would have caused failure during the proof test. Thus, t_{min} is the time it takes for this maximum length flaw to grow to dimensions critical for spontaneous fracture.

From Eqs 2 and 3 it is seen that lifetime predictions for ceramics depend on the crack growth parameters B and n. To be relevent for lifetime prediction purposes, these parameters must be measured in the service environment. They can be determined either by crack velocity, stress rupture, or stressing rate experiments. Regardless of which technique is used to measure B and n, the same values should be obtained for a given material

[4] This is the value of Y for a penny-shaped crack.

and environment. Experimental studies show that the same value of B and n, in fact, are obtained for some materials, but not for others. From the discussion it will become clear that additional experimentation is needed to evaluate the limits of the theory fully and to identify those materials for which the theory is applicable.

Techniques for Characterizing Delayed Failure

Subcritical crack velocity can be measured as a function of the stress intensity factor on specimens specifically designed for fracture mechanics experiments. These specimens contain macroscopic cracks that allow accurate measurement of the crack velocity and the stress intensity factor. A regression analysis of these data using Eq 1 gives A and n, their variances and their covariance. By determining K_{Ic} in a separate experiment, B can be determined from its definition (Eq 2). Predictions of lifetime can then be made using Eq 2 and 3. The errors in the lifetime prediction as a result of uncertainties in A, n, and K_{Ic} also can be determined by standard statistical techniques using either the Monte Carlo method of error prediction, [5] or the normal statistical method of error propagation [6].

A second method of evaluating B and n is by measurement of time-to-failure as a function of applied load. Stress rupture measurements of this type are made on a large number of specimens at several constant applied stresses. From these data the median value of the failure time ($\bar{t}$) is determined as a function of the applied stress. By measuring the median inert strength ($\overline{S_i}$) on a group of specimens statistically identical to those used in the stress rupture test, B and n can be determined from [3]

$$\ln \bar{t} = \ln B + (n - 2) \ln \overline{S_i} - n \ln \sigma_a \tag{4}$$

A linear regression analysis of $\ln \bar{t}$ versus $\ln \sigma_a$ allows n and B and their related statistical quantities to be determined. Again standard statistical techniques can be used to evaluate the error in the predicted failure time which result from experimental uncertainties in $\overline{S_i}$, B, and n.

The third techniques for evaluating delayed failure in a ceramic involves measuring the strength as a function of stressing rate. The analysis of these data is similar to that carried out on stress rupture data since the median strength ($\overline{S}$) is related to stressing rate ($\dot{\sigma}$) by [3]

$$\ln \overline{S} = \frac{1}{n + 1} [\ln B + (n - 2) \ln \overline{S_i} + \ln \dot{\sigma} + \ln (n + 1)] \tag{5}$$

From a regression analysis of $\ln \overline{S}$ on $\ln \dot{\sigma}$, n and B on their statistical variates can be determined. The failure time and its uncertainty can then be predicted as before.

Although the analysis of stress rupture and stressing rate data based on median values is straightforward, it does not make most efficient use of the data. Alternate procedures that use all of the data in the regression analysis have been developed to analyze this type of data. The reader is referred to Ref 7 for further discussions of this point.

The three experimental techniques for evaluating the parameters n and B each have their advantages and limitations. Crack velocity measurements have been used widely to determine the fatigue behavior of ceramics. The experimental techniques are relatively simple, and relatively few specimens are needed to collect large quantities of data. Because the behavior of cracks are observed directly, the technique has been used to generate much fundamental data on subcritical crack growth. This fundamental information is often missed when strength techniques are used to evaluate delayed failure because only the average crack propagation behavior can be inferred from the data. On the other hand, strength techniques use specimens that more closely resemble structural parts so that failure results from microscopic rather than macroscopic cracks. Because of this, cracks in strength specimens are likely to behave in the same way as those in the structural component. The same cannot always be said for the macroscopic size cracks that are used in fracture mechanics tests. In fact, recent evidence (to be discussed in the following section) indicates real differences in lifetime prediction for some materials, depending on which technique is used for the prediction. Obviously, when such differences occur, lifetime estimates made from strength data are to be preferred over those made from fracture mechanics data.

Data Extrapolation for Long Term Lifetime Predictions

For many applications structural reliability is required for periods that range from 1000 to 50 000 h ($\sim$40 days to $\sim$6 years.) Because of the expense involved in long-term mechanical strength testing, it would be valuable if long-term lifetime predictions could be made from relatively short-term tests. The fracture mechanics based theory discussed in this paper offers a framework within which these predictions can be made. Aside from the expected problem of error propagation due to experimental uncertainties in the values of n, B, and S_i, two additional factors must be considered in predicting extended lifetimes: one factor involves the assumed relation between K_I and v (Eq 1), the other involves the efficiency of obtaining delayed failure data for lifetime predictions.

In Eq 1 we assumed that the crack velocity can be expressed as a power function of the applied stress intensity factor. This equation was selected because it fits experimental data over a wide range of crack velocities and because it permits other equations for reliability predictions to be handled by relatively simple mathematics. However, because of the strong

dependence of crack velocity on stress intensity factor, other equations can be shown to fit the crack propagation data equally well [8]. A similar conclusion may be drawn for both stress rupture and stressing rate data in which a number of analytic expressions may be used with apparently equal accuracy to represent the strength properties of ceramic materials. If failure predictions are made within the range of experimental data, all of the possible equations give similar predictions of lifetime. However, if the strength or crack propagation data has to be extrapolated beyond the time period over which the data were collected, then large differences in predicted failure time can occur.

The effect of the form of the crack propagation equation on the predicted failure time has been demonstrated for glass [8]. Minimum lifetime predictions based on crack propagation data obtained on an ultra low expansion glass [92.5 weight percent silicon dioxide (SiO_2); 7.5 weight percent titanium dioxide (TiO_2)] are plotted in Fig. 1 for three different representations of the crack propagation equation. The vertical line on this graph marks the lower velocity limit of the crack propagation data. Points to the left of this line reflect crack propagation data taken in the laboratory; points to the right of this line reflect extrapolation of the crack propagation data to long-term failure conditions. We note that to the left of the vertical line, all three representations of the crack propagation data give equivalent predictions of failure time, which is consistent with the fact that the crack propagation data are represented equally well by the three equations. To

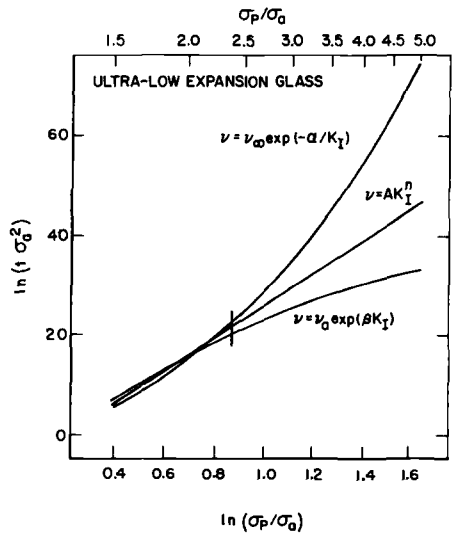

FIG. 1—*Proof test diagram comparing three representations of the crack propagation data of an ultra-low expansion glass* [8].

the right of the vertical line, however, the three predictions of failure time are divergent, indicating the danger in extrapolating data.

Requirements for accurate long-term lifetime predictions necessitate the collection of data for slowly moving cracks, since it is these cracks that cause failure after they have been subjected to loads for extended periods. Data of the type needed can be collected by either of the three methods discussed earlier. Crack velocity techniques require measurements to be made to very low crack velocities. Stressing rate measurements require the use of very low stressing rates, while stress rupture measurements require relatively low stresses and correspondingly long failure times. Regardless of which technique is used, experimental times involved in collecting such data will be long, and as a consequence, some consideration must be given as to which of the three techniques is most time efficient.

An upper limit of experimental data (on Figs. 1 through 5) can be determined by each of the techniques under consideration.[5] For the crack velocity technique the limit is given by $\sigma_p/\sigma_a = K_{Ic}/K_I$, where K_I is the stress intensity factor that corresponds to the lowest crack velocity measurement made. Since K_I is determined from the lowest practical crack velocity that can be measured, its value will depend on the stress corrosion properties

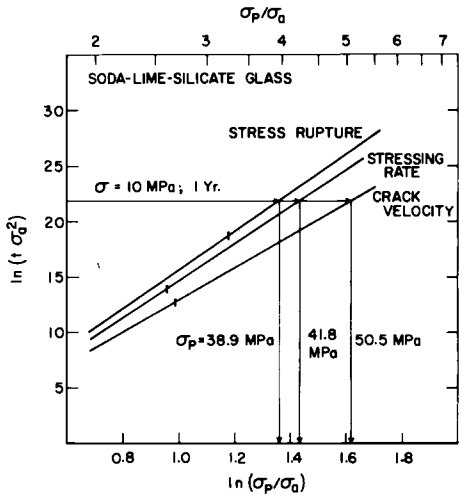

FIG. 2—*Proof test diagram comparing crack velocity stress rupture, and stressing rate techniques used in determining crack growth constants for soda-lime silicate glass (data from Ref 3).*

[5]The upper limit of the experimental data on Figs. 1 through 5 is defined by the minimum K_I in a crack velocity experiment, or by the minimum breaking stress in either a stress rupture or stressing rate experiment. Higher values of σ_p/σ_a on these diagrams represent extrapolation of experimental data.

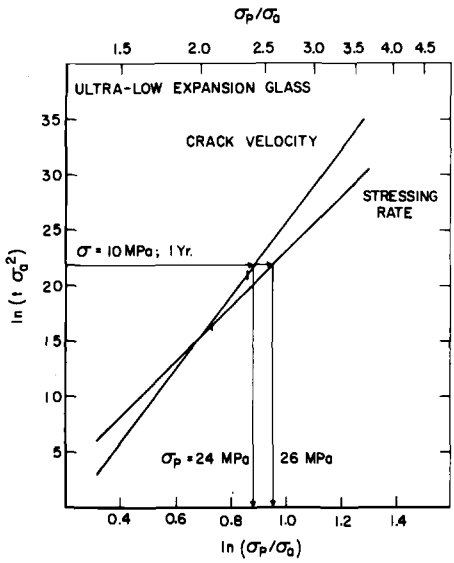

FIG. 3—*Proof test diagram comparing crack velocity and stressing rate techniques used in determining crack growth constants for an ultra-low expansion glass (data from Ref* 10).

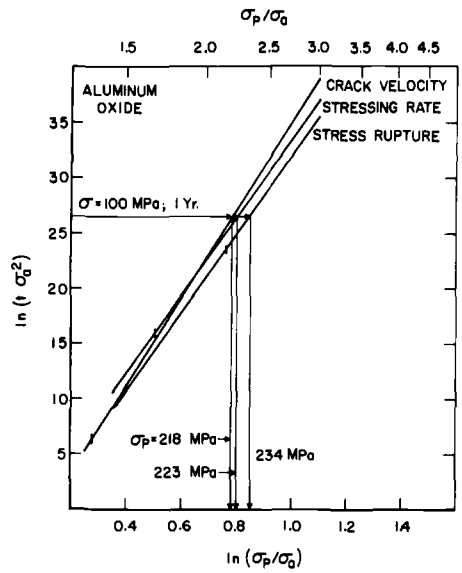

FIG. 4—*Proof test diagram comparing crack velocity, stress rupture, and stressing rate techniques used in determining crack growth constants for* Al_2O_3 *(data from Refs* 11 *and* 12).

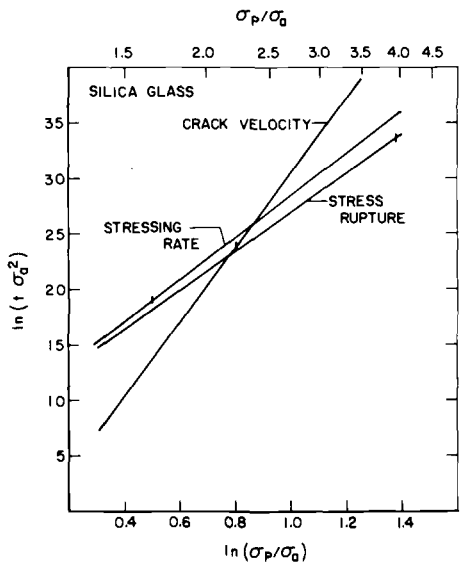

FIG. 5—*Proof test diagram comparing crack velocity, stress rupture, and stressing rate techniques used in determining crack growth constants for fused silica (data from Refs* 13 *and* 14).

of the material studied. In general higher values of K_{Ic}/K_I are obtained for materials that are more susceptible to stress corrosion cracking, that is, low value of n in Eq 1. For the stress rupture technique, the limit is given by $\sigma_p/\sigma_a = S_i/\sigma_1$ where σ_1 is the lowest stress used in the experiment. Again, larger values of S_i/σ_1 are obtained with materials that are more susceptible to stress corrosion cracking. Similarly, for stressing rate experiments the limit for the laboratory data is given by $\sigma_p/\sigma_a = S_i/S_1$ where S_1 is the lowest strength measured experimentally. As in the case of a static fatigue experiment, larger values of S_i/S_1 are obtained with materials that are more susceptible to stress corrosion cracking.

The times required to conduct stress rupture and stressing rate experiments for samples at the same failure stress level are related by [*3,9*]

$$t_d = (n + 1)\, t_s \tag{6}$$

where t_s and t_d are respectively the failure time in a stress rupture and stressing rate experiment. Since values of n for ceramic materials range from ~15 for soda-lime-silica glass to ~100 for some types of aluminum oxide, one to two orders of magnitude more time would be required at the same breaking stress level for dynamic fatigue testing than for static fatigue testing. As a consequence, it may be concluded that static fatigue testing

is superior to dynamic fatigue testing when long lifetimes, that is, low velocity data, are important.

A comparison between stress rupture and crack velocity techniques can be obtained by regrouping the terms of Eq 2 in the form

$$t_s = 2a_i/[v_i(n-2)] \tag{7}$$

where a_i is the initial crack size and v_i is the crack velocity at first application of the service stress. Therefore, if the initial crack size, a_i, can be determined, then the initial crack velocity, v_i also can be determined by measuring the time to failure, t_s. However, the initial crack velocity also can be determined from crack velocity techniques by simultaneously measuring the amount of crack growth, Δa, and the time, t_{cv}, required for the growth. Substituting $v_i = \Delta a/t_{cv}$ into Eq 7, we obtained

$$t_{cv}/t_s = (n-2)\,\Delta a/(2a_i) \tag{8}$$

We see from Eq 8 that t_{cv}/t_s depends on n, the initial crack size, a_i, and the accuracy with which the change in crack size, Δa, can be measured. By definition, if $t_{cv}/t_s > 1$, then stress rupture techniques are more time efficient; conversely, for $t_{cv}/t_s < 1$, crack velocity techniques are more time efficient. The effectiveness of these two techniques for characterizing the delayed failure of soda-lime glass ($n = 17$) can be determined as follows. The lower limit for measuring Δa by optical techniques is approximately 10 μm. Substituting this value into Eq 8 shows that stress rupture techniques are more time effective for cracks less than ~75 μm; whereas, crack velocity experiments are more appropriate for larger cracks. Given an estimate of n and the accuracy with which Δa can be measured, a similar calculation can be made for any material.

Experimental Verification of the Basic Equations

In previous sections of this paper we have developed and discussed a theory of predicting the lifetime of structural ceramics. The theory is based on fracture mechanics and takes into account both the initial flaw size and the rate at which the flaw will grow when subjected to stresses. Since the theory gives quantitative predictions of failure time as a function of the applied stress, the theory can be checked in the laboratory on model systems that cover a wide range of materials and material microstructures. In this section the theory will be compared with available experimental data to determine validity and limitations of the theory. Particular attention will be paid to the three experimental techniques for determining the delayed failure behavior of the material.

Glass is one material/environment system for which several techniques

have been applied to characterize fatigue parameters. The results of these studies have been varied somewhat in character; sometimes excellent agreement is obtained among the three test procedures, while at other times agreement is less than satisfactory. Soda-lime-silicate glass is one material that seems to give consistent results regardless of which technique is used to evaluate the fatigue parameters [*3*]. Figure 2 illustrates minimum lifetime predictions for soda-lime-silicate glass based on Eq 3. The upper limit of the experimental data is indicated in each case by a vertical line. We see that the three techniques are represented by nearly parallel lines, corresponding to the fact that slopes n of the data are nearly the same for the three techniques. For a lifetime of 1 year at an applied stress of 10 MPa ($\sim$1400 psi), the ratio σ_p/σ_a to obtain this lifetime ranges from 4 to 5, which is satisfactory considering the fact that this prediction is made from an extrapolation that extends well beyond the range of all the data. A similar study [*10*] comparing stressing rate and crack velocity data on a low expansion glass gave closer predictions of σ_p/σ_a ranging from 2.4 to 2.6, for the same lifetime and stress (Fig. 3). For this glass, the slopes of the curves differ more than for the soda-lime glass, but because the data overlaps in the region it was collected, excellent lifetime predictions are obtained.

Stress rupture and stressing rate data [*11*] collected in a moist environment on the same grade of aluminum oxide are compared in Fig. 4 with crack growth data [*12*] that were collected on a similar but not identical grade of aluminum oxide tested in water. For a lifetime of 1 year, at a stress of 100 MPa ($\sim$14 000 psi) the value of σ_p/σ_a ranges from 2.2 to 2.3. Therefore, the agreement between the three methods for this material is better than obtained for glass.

Based on the aforementioned results it can be concluded that soda-lime glass and aluminum oxide fail by subcritical crack growth from preexisting flaws in moist environments, and that this crack growth can be characterized by crack velocity, stress rupture, or stressing rate experiments. Unfortunately, crack growth parameters determined by the various techniques are not always self consistent. Figure 5 gives a comparison of strength data on pristine silica fibers [*13*] with crack velocity data for silica [*14*]. The figure shows that the crack growth parameters determined from strength experiments differ significantly from those obtained from crack velocity experiments. This lack of agreement probably results from the extreme difference in size of cracks in the fibers, $\sim$3 nm, versus those in the crack velocity specimens, $\sim$1 cm. In addition, the chemical environment at the crack tips of the two types of specimens probably differs, resulting in a difference in crack growth behavior. Furthermore, one must question the underlying assumption of an elastic continuum for cracks as small as 30 nm. It is possible that cracks this small are affected by molecular scale inhomogeneities in the glass.

Interactions between the microstructure and the crack also can affect crack growth behavior and thus influence lifetime predictions. Tables 1 and 2 summarize crack velocity and strength data obtained for various grades of aluminum oxide. Values of n obtained from crack velocity studies ranged from ~ 20 to ~ 40, a variation that is believed to be significant. Similarly, values of n obtained from stressing rate experiments vary from ~ 30 to ~ 70, which also is believed to be significant. These results indicate an effect of microstructure and small differences in chemical composition on the crack propagation parameters, whether they be obtained by stressing rate or by crack velocity techniques. Unfortunately, this area of research has not yet been explored in sufficient detail, so that the full implications of microstructure in relation to the crack size are not fully understood.

Further indications of the importance of microstructure to crack propagation parameters have been obtained on two grades of glass ceramics using both crack velocity and stressing rate techniques [*15*]. The presence of small particles (~ 2 by $\sim 8\mu$m) in a magnesium aluminosilicate glass-ceramic causes crack branching and bifurcation in fracture mechanics specimens. Differences in the propagation behavior for small cracks in bend specimens and large cracks in fracture mechanics specimens resulted in differences in n depending on the measurement technique used to measure n. Crack velocity techniques gave values of ~ 84 for n, whereas biaxial

TABLE 1—*Fatigue parameters for polycrystalline alumina, crack velocity data.*

Relative Density, percent	Grain Size, μm	Environment	N	ln B	Reference
99.3	20	air	27.8	9.84	*18*
95.0	20	air	27.8	8.76	*18*
99.9	large	air	27.8	8.25	*18*
99.5	4	air	20.5	8.93	*18*
99.9	8	air	20.5	8.93	*18*
95	not reported	air	31	−1.6	*19*
96	5	H_2O	42	−5.0	*12*

TABLE 2—*Fatigue parameters for polycrystalline alumina, stressing rate data.*

Relative Density, percent	Grain Size, μm	Environment	N	ln B	Reference
99	6	air	46.1	−0.618	*20*
95	10	air	42.7	−3.46	*21*
95	19	H_2O	35	...	*22*
97.5	8	H_2O	39	...	*22*
99.3	4	H_2O	61	...	*22*
97.5	4	H_2O	68	...	*22*

bend strength techniques gave values of ~51. By contrast, a lithium aluminosilicate glass-ceramic with a more homogeneous structure gave values of ~46 for the fracture mechanics study and ~37 for the stressing rate study. The difference in n obtained for the magnesium aluminosilicate was attributed to crack-size dependent interactions between the microstructure and the propagating cracks in the glass ceramics. Other recent studies on foamed glass [*16*] and porous alumina [*17*] also indicate the importance of microstructure and test method in establishing the correct crack propagation parameters for improving component reliability. This research indicates that the crack propagation parameters depend not only on the test technique (fatigue strength versus crack velocity), but also on the particular strength test used (flexure, biaxial tension, or compression) to characterize delayed failure. An important conclusion to be drawn from this research is that when there are possible microstructural interactions the test to be chosen to characterize delayed failure should be one that most closely simulates the stress condition in service.

Summary

This paper reviews techniques that have been developed recently to improve the reliability of ceramic components in structural applications. To date, the theory has been tested experimentally with mixed results. For soda-lime-silicate glass and one grade of aluminum oxide, the three methods of determining the crack propagation parameters gave self-consistent results. For other ceramics, the results were not self-consistent. Crack size and microstructure strongly influenced the value of the crack propagation parameters. The fatigue behavior of pristine silica glass fibers, which contain 3-nm flaws, differs from that of silica glass which contains large preexisting cracks such as are used in fracture mechanics specimens. In polycrystalline ceramics, microstructural parameters such as porosity and grain size can influence the crack propagation parameters, n and B, for both fracture mechanics and fatigue techniques. Furthermore, the type of stress field to which the specimens are subjected has a significant effect on these parameters. Because of these discrepancies, additional experimentation is needed to fully evaluate the limits of the theory. Until a deeper understanding of the fracture process and its effect on the failure prediction equations is developed, precautions must be taken in using the theory. When possibilities of microstructural interference exist, the test chosen to determine design diagrams should be the one that most closely simulates the stress condition in service.

Acknowledgments

Author J. E. R. is grateful for the support of National Science Founda-

tion Grant DMR 77 05647; author S. M. W. is grateful for the support of the Office of Naval Research.

References

[1] Evans, A. G. and Wiederhorn, S. M., *International Journal of Fracture*, Vol. 10, 1974, pp. 379-392.
[2] Wiederhorn, S. M. in *Ceramics for High Performance Applications*, Book Hill Publishing Co., Chestnut Hill, Ma. 1974, pp. 635-665.
[3] Ritter, J. E., Jr. in *Fracture Mechanics of Ceramics*, Vol. 4, Plenum Press, N.Y., 1978, pp. 667-685.
[4] Wiederhorn, S. M. in *Fracture Mechanics of Ceramics*, Vol. 2, Plenum Press, N.Y., 1974, pp. 613-646.
[5] Jacobs, D. F. and Ritter, J. E., Jr., *Journal of the American Ceramic Society*, Vol. 59, 1976, pp. 481-487.
[6] Wiederhorn, S. M., Fuller, E. R., Jr., Mandel, J., and Evans, A. G., *Journal of the American Ceramic Society*, Vol. 59, 1976, pp. 403-411.
[7] Jakus, K., Coyne, D. C., and Ritter, J. E., Jr., to be published in Journal of Material Science, 1978.
[8] Wiederhorn, S. M., "Dependence of Lifetime Predictions on the Form of the Crack Propagation Equation," *Fracture 1977*, University of Waterloo Press, Waterloo, Canada, 1977, pp. 893-901.
[9] Davidge, R. W., McLaren, J. R., and Tappin, G., *Journal of Materials Science*, Vol. 8, 1973, pp. 1699-1705.
[10] Wiederhorn, S. M., Evans, A. G., Fuller, E. R., Jr., and Johnson, H., *Journal of American Ceramic Society*, Vol. 57, 1974, pp. 319-323.
[11] Ritter, J. E., Jr. and Humenik, J. N., to be published in *Journal of Materials Science*, 1978.
[12] Bansal, G. K., Duckworth, H., and Niesz, D. E., *Journal of the American Ceramic Society*, Vol. 59, 1976, pp. 472-78.
[13] Proctor, B. A., Whitney, I., and Johnson, W., *Proceedings*, Royal Society, London, Series A, Vol. 297, 1967, pp. 534-557.
[14] Wiederhorn, S. M., Evans, A. G., and Roberts, D. E. in *Fracture Mechanics of Ceramics*, Vol. 2, Plenum Press, New York, 1974, pp. 829-842.
[15] Pletka, B. J. and Wiederhorn, S. M. in *Fracture Mechanics of Ceramics*, Vol. 4, Plenum Press, New York, 1978, pp. 745-759.
[16] Conley, P. H., Chandan, H. C., and Bradt, R. C., "Stressing Rate Effects on the Tensile, Compressive and Flexural Strengths of Foam Glass," Paper No. 19-CG-77F, 1977 Fall Meeting of Glass Division, American Ceramic Society, Bedford Springs, Pa.
[17] Gesing, A. J. and Bradt, R. C., "Effects of Porosity on Room Temperature (K_i, V) Behavior of Polycrystalline Al_2O_3," paper No. 141-B-77, 1977 Annual Meeting of American Ceramic Society, Chicago, Ill.
[18] Freiman, S. W., McKinney, K. R., and Smith, H. L. in *Fracture Mechanics of Ceramics*, Vol. 2, Plenum Press, New York, 1974, pp. 659-676.
[19] Evans, A. G., *Journal of Materials Science* Vol. 7, 1972, pp. 137-146.
[20] Ritter, J. E., Greenspan, D. C., Palmer, R. A. and Hench, L. L., to be published.
[21] Ritter, J. E., Jr., to be published.
[22] Rockar, E. M. and Pletka B. J., in *Fracture Mechanics of Ceramics*, Vol. 4, Plenum Press, New York, 1978, pp. 725-735.

Summary

The papers in this volume are basically of three types: papers that are concerned with testing techniques both from a theoretical as well as an experimental point of view; those concerned with the application of these techniques to particular brittle materials; and papers dealing with the use of fracture mechanics techniques to predict the fracture behavior of actual components.

The first two papers are concerned with the double torsion technique. This technique is particularly important because it represents a test configuration in which stress intensity is independent of crack length. This technique is widely used for determining fracture mechanics parameters of ceramic materials and is particularly useful at elevated temperatures because crack growth parameters can be obtained without the need for actually viewing the crack. In the first paper, Fuller discusses the assumptions made in the analysis of the double torsion specimen regarding the crack profile, the deflections beyond the crack tip, and possible influences of side grooves in the specimen, to guide the crack. He describes possible consequences of the invalidity of the assumptions, since many of these assumptions have yet to be proved for different specimens geometries. Pletka, Fuller, and Koepke discuss the procedures for actually conducting subcritical crack growth tests using the double torsion specimen. They recommend a particular specimen design for collecting valid data and discuss the precracking procedures needed to obtain good data. They show that the validity of the constant K_I conditions may be affected by the interaction of the crack with the microstructure.

The notched bend test is another widely used procedure because of the small specimen size, making it quite useful for examining experimental quantities of brittle materials. Bansal and Duckworth discuss the use of the notched bend technique to obtain both critical fracture toughness as well as work of fracture data on glass and ceramics. They point out the importance of the way in which the notch is introduced on the value of K_{Ic} that is obtained. They also show that notched bend test data can be significantly different than data obtained by other fracture mechanics techniques as shown by the findings of several investigators. Microcracking or residual stresses were suggested as being possible reasons for this difference. Flaw size microstructure interactions also may be a significant factor.

The double cantilever beam technique continues to be used extensively to

obtain K_{Ic} as well as crack growth data in many varieties of brittle materials. Fourney and Kobayashi report on the effect of the loading system on crack jump lengths in a double cantilever beam system. Stress intensity factors were determined as a function of crack velocity in a birefringent polymer using high-speed photography of the isochromatic fringe patterns associated with the propagating and arresting crack. The stiffness of the loading system was shown to have an important effect on the crack propagation parameters for this material. In another paper, Champomier compares double torsion and double cantilever beam measurements of K_{Ic} as well as crack growth rates in glasses. Although he obtains equivalent values of K_{Ic} from the two techniques, he finds discrepancies in crack velocity-K_I curves obtained by the techniques. Possible reasons for these discrepancies are discussed. Barker discusses a modification of the double cantilever beam configuration in the recently developed short rod and short bar specimens. He presents K_{Ic} data for aluminum, alumina, and fused quartz that is in good agreement with that obtained by other experimental techniques.

One recently developed fracture mechanics technique involves the use of a hardness indentation to provide a well characterized flaw which can then be propagated to failure. Unlike other fracture mechanics techniques, this flaw is of the same size as the microstructure and is similar to flaws in actual components. Petrovic and Mendiratta discuss both the advantages and disadvantages of this controlled flaw technique. In their procedure a crack is introduced into a test bar using a hardness indentor; the bar is then fractured in bending; K_{Ic} is calculated from the fracture stress and the measured size and geometry of the initial crack introduced during indentation. Problems associated with the technique such as residual stress effects, flaw healing, etc., also are discussed. Petrovic and Mendiratta show that localized residual stresses due to the indentation are the most serious problems but that these can be eliminated by polishing off the indentations or annealing in vacuum. A variation of the controlled flaw technique uses the indentation process itself and the flaws it produces to determine fracture toughness. Two primary advantages of this variation are that only small amounts of material are required for testing and point-to-point variations in properties within a specimen can be determined. In the paper by Marion, the author examines effects of indentor geometry and specimen surface preparation on the fracture toughness measured by the indentation technique. Tests were performed on both polycrystalline ceramics and glasses. He concludes that one should use a Vickers indentor and fast loading rates in order to minimize effects of subcritical crack growth. The use of large loads reduces surface effects including residual stresses. Good correlation with other techniques for low toughness materials is obtained but the correlation between K_{Ic} values in higher toughness materials such as alumina (Al_2O_3) is not as good. Evans examines the basis for the use of

indentation techniques to determine the fracture toughness of brittle materials. He derives expressions relating the formation of cracks under a hardness indentation to both the hardness and fracture toughness of the material, and shows the relationship between the fracture toughness and both the crack and indentation sizes formed on the surface. He shows that K_{Ic} can be determined from the size of the crack seen on the tensile surface without the need for fracturing the specimen as in the other indentation technique just discussed. Evans also shows that the relationship between K_{Ic} and indentation size seems to be valid for a wide range of materials, but the precision to which K_{Ic} can be obtained by this techniques has not yet been established. He also suggests that this technique might be used to obtain a measure of the residual stresses in a surface. Both Marion and Evans suggest that the indentation technique provides a good relative ranking of the fracture toughness of materials.

The final paper in the section on test procedures deals with an indirect method of obtaining fracture mechanics information by fracture surface analysis. Mecholsky and Freiman show that the features formed on the fracture surfaces of brittle materials are quantitatively related to both the fracture stress and the fracture toughness of the material and describe the experimental procedures for obtaining reproducible results. They point up that microstructural and residual stress effects must be accounted for in the determination of K_{Ic} by a fractographic technique and examine effects of combined K_I and K_{II} loading on fracture.

The next three papers emphasize the use of fracture mechanics techniques to study the fracture behavior of various brittle materials. Buresch reports results of K_{Ic} measurements on a number of aluminum oxide bodies using the notch bend test. He shows that only specimens having a certain thickness and notch root radius give a valid K_{Ic}. He suggests that the required geometry is related to the grain size of the alumina and invokes the concept of a process zone to explain the results. Microcracking is proposed to occur within this zone. He suggests that the ratio of the process zone size to the specimens thickness is important for the determination of K_{Ic}. He also shows that the grain size can be important in establishing the value of fracture toughness for a particular material.

Schmidt and Lutz conducted fracture toughness tests on Westerly granite, a material used frequently as a model for brittle rocks because of its fine grain, homogeneous nature. They used both direct tension and compact tension specimens comparing K_{Ic} and J_{Ic}. J_{Ic} data indicates the validity of the K_{Ic} measurements despite observed nonlinear inelastic behavior. They find that K_{Ic} is insensitive to changes in specimen thickness ranging from 13 to 103 mm.

Naaman and Shah discuss the various fracture toughness tests techniques applicable to cement reinforced with steel fibers. This material behaves as a composite rather than an homogeneous material. The authors

could not come to a conclusion regarding the validity of any one particular test and made no recommendations as to which test might be the best.

The final paper in this volume deals with the use of the fracture mechanics obtained by various test techniques for the prediction of failure of components in service. In this paper, Wiederhorn and Ritter discuss the use of fracture mechanics data to predict time to failure of ceramic structural components, through knowledge of the subcritical growth of intrinsic flaws. By assuming that crack growth follows a particular form, they are able to derive expressions for the probability of failure of a material in service given knowledge of the crack growth parameters, and the initial flaw size distribution. The use of proof testing to guarantee lifetimes also is discussed. They show that while theory and experiment agree quite well for some materials such as glasses, and some aluminum oxides, in others, agreement is not very good. In some cases, three different test procedures for determining crack growth parameters do not give self consistent results. The authors point out that the crack size and microstructure of the material have a significant influence on the values of the fracture mechanics parameters that will be applicable to the prediction of lifetimes.

In summary, while this volume cannot be considered to contain references to all of the various techniques used to measure fracture mechanics parameters of brittle materials it does provide a reasonable state-of-the-art review of many test procedures, as well as the use of fracture mechanics principles to determine the strength of these materials and to predict their behavior under long term loading. It is hoped that this volume will provide a basis for further experimentation and development of test techniques as well as increasing our understanding of the mechanism of brittle fracture.

S. W. Freiman

Fracture and Deformation Division, National Bureau of Standards, Washington, D.C. 20234; editor.

Index